Fluid Dynamics of Suspension Bioreactors

by

Mohd Zulhilmi Paiz Ismadi

A dissertation
submitted in fulfillment of the requirements for the degree of
Doctor of Philosophy

Department of Mechanical & Aerospace Engineering
Monash University

August 2014

To my family,
and bleeding disorder community
around the world.

PART A: General Declaration

Monash University

Declaration for thesis based or partially based on conjointly published or unpublished work

General Declaration

In accordance with Monash University Doctorate Regulation 17.2 Doctor of Philosophy and Research Master's regulations the following declarations are made:

I hereby declare that this thesis contains no material which has been accepted for the award of any other degree or diploma at any university or equivalent institution and that, to the best of my knowledge and belief, this thesis contains no material previously published or written by another person, except where due reference is made in the text of the thesis.

This thesis includes three original papers published in peer-reviewed journals and one unpublished publication. The core theme of the thesis is the fluid mechanics in bioreactors. The ideas, development and writing up of all the papers in the thesis were the principal responsibility of myself, the candidate, working within the Department of Mechanical & Aerospace Engineering, and Division of Biological Engineering under the supervision of Associate Professor Andreas Fouras and Professor Kerry Hourigan.

The inclusion of co-authors reflects the fact that the work came from active collaboration between researchers and acknowledges input into team-based research.

In the case of Sections 3.1, 4.1, 5.1 and 6.1, my contribution to the work involved the following:

Thesis chapter	Publication title	Publication status	Nature and extent of candidate's contribution
3.1	Experimental Control of Vortex Breakdown by Density Effects	Published	Conceived, designed and performed experiments. Analysed the data and wrote the manuscript. (75%)
4.1	Experimental Characterisation of Fluid Dynamics in Spinner Flask Bioreactor	Published	Conceived, designed and performed experiments. Analysed the data and wrote the manuscript. (80%)
5.1	Flow Characterisation of Spinner Flask for Induced Pluripotent Stem Cell Application	Published	Conceived, designed and performed experiments. Analysed the data and wrote the manuscript. (80%)
6.1	Optimisation of a Stirred Bioreactor through the Use of a Novel Holographic Correlation Velocimetry Flow Measurement Technique	Published	Conceived, designed and performed the experiments, analysed the data, co-wrote the analytical software and wrote the manuscript (35%)

I have renumbered sections of submitted or published papers in order to generate a consistent presentation within the thesis

Signed:

Date:

Abstract

THE successful engraftment of pluripotent stem cells has revolutionised regenerative medicine in the treatment of many degenerative diseases and injuries. For many years, bioreactors have been widely used to improve cell culturing efficiency. Although the importance of mechanical stresses on cell culture has been often reported in the literature, little attention has been given to understanding the fluid dynamics aspect of the bioreactor. This thesis demonstrates the use of experimental fluid dynamics in uncovering the underlying physics of the flow mechanics in bioreactors.

The first section of the study comprised the flow visualisation in a rotating-top disk cylindrical bioreactor, with the height-radius ratio of 2. Qualitative analysis determined the effect on the flow when the density of the dye injection was varied. The injection of a relatively denser fluid created a buoyancy force downward, which counteracted the meridional recirculation in the cylinder and thus enhanced the formation of a vortex breakdown bubble. On the other hand, the injection of a lighter fluid did not destroy the vortex breakdown. However, for large enough density differences (larger than 0.03%), the lighter fluid was able to pierce through the bubble and led to a new structure of the vortex breakdown. Translating this knowledge to the use of microcarriers in a rotating lid bioreactor, it is expected the microcarriers will accumulate and thicken at the centre of the container. Then, the behaviour is followed by destabilisation of the flow with an oscillatory effect creating a phenomenon similar to dense dye experiments.

The flow field within a spinner flask at varying speeds (10RPM to 80RPM) and impeller positions was characterised experimentally. Particle Image Velocimetry (PIV) was employed to visualise the fluid flow and calculate the stresses and vorticities associated with the flow within the flask. The highest shear stress region was observed at the base of the spinner flask due to fluid-wall interaction. The study provides an overview of the fluid structure within the spinner flask in the meridional and azimuthal planes. Furthermore, the quantitative results of this study gave an accurate numerical stress margin for the given impeller speeds. The optimum flow condition for culturing mouse induced pluripotent stem cells (iPSCs) was investigated. It was found that the mouse iPSCs achieved the optimum number of cells over 7 days in a 25RPM suspension culture. This condition translated to a 0.0984 Pa maximum shear stress caused by the interaction of the fluid flow with the bottom surface. However, negative cell growth

was obtained in the 28RPM culture condition. Such a narrow margin demonstrated that mouse iPSCs cultured on microcarriers are very sensitive to mechanical forces. This study provides insight to biomechanical parameters, specifically the shear stress distribution, for a commonly-used spinner flask over a wide range of Reynolds number. Additionally, these results provide estimates of the biomechanical properties within the type of spinner flask used in many published cell studies.

In an effort to measure three-dimensional (3D) velocity fields in biological flows, a correlation-based approach, termed Holographic Correlation Velocimetry (HCV), was developed. The direct flow reconstruction approach developed here allows for measurements at high seeding densities. Moreover, because the system is based on in-line holography, it is very efficient with regards to the use of light, as it does not rely on side scattering. This efficiency makes the system appropriate for high-speed flows and low exposure times, which is essential for imaging dynamic systems. The method was rigorously tested, validated and applied to measure flows in a cuvette and a spinner flask bioreactor.

This thesis provides invaluable information and deep insight into flow behaviour within bioreactors. Furthermore, the wide range of variables covered in the study will allow the estimation of the magnitude of mechanical forces to be made, thus improving the understanding of the relations between mechanical forces and the culture outcome. The proposed imaging technique will allow thorough characterisation of the biomechanical parameters and define the design criteria for future bioreactor development.

Acknowledgements

Publications

Constituent publications of this thesis

Ismadi, M.-Z., Meunier, P., Fouras, A., & Hourigan, K. (2011) Experimental Control of Vortex Breakdown by Density Effects. *Physics of Fluids.* **23**, 034134.

Ismadi, M.-Z., Higgins, S., Samarage, C. R., Paganin, D., Hourigan, K., & Fouras, A. (2013) Optimisation of Stirred Bioreactor through the Use of Novel Holographic Correlation Velocimetry Flow Measurement Technique. *PLoS ONE.* **8** (6), e65714.

Ismadi, M.-Z., Gupta, P., Fouras, A., Verma, P., Jadhav, S., Bellare, J., & Hourigan, K. (2014) Flow Characterisation of Spinner Flask for Induced Pluripotent Stem Cell Culture Application. *PLoS ONE.* **9** (10), e106493.

Ismadi, M.-Z., Hourigan, K., & Fouras, A. (2014) Experimental Characterisation of Fluid Dynamics in Spinner Flask Bioreactor. *Processes.* **2** (4), 753-772.

Gupta, P., **Ismadi, M.-Z.**, Verma, P., Fouras, A., Jadhav, S., Bellare, J., & Hourigan, K. (2014) Optimisation of Agitation Speed in Spinner Flask for Microcarrier Structural Integrity and Expansion of Induced Pluripotent Stem Cells. *Cytotechnology.* (Available online).

Contents

Chapter 1

Introduction

SINCE the development of pluripotent stem cells, the focus on regenerative medicine has shifted from organ transplantation to cell therapy. The self-renewing ability that the stem cells possess offers the greatest advantage in the treatment of degenerative diseases. However, a large number of cells are required before any cell therapy can be realised. Thus, finding the best method to culture and harvest stem cells in large quantities has become a primary focus for many research groups.

Bioreactor development has been one way to optimise the cell culturing procedure. The fluid dynamics within the bioreactor plays a crucial role in promoting the cell growth. Yet, due to the lack of fluid mechanic specialists involvement in this research area, there is limited literature on flow characterisation of stirred bioreactors, which has become a constraint in the advancement of bioreactor design. Studies that were conducted to determine impact of certain input parameter on the cell yield have not been able to adequately quantify the mechanical parameters associated to the flow within the bioreactor. Therefore, it is important to gain thorough insight into the underlying flow mechanics in bioreactors and how it affects the cells; which in turn may reestablish design requirements for bioreactors.

In this thesis, flow characterisation studies within a rotating-lid cylinder and a spinner flask bioreactor are presented. The study is primarily aimed to gain insight into the flow environment within the bioreactors. Studies described in this thesis are intended for broad applicability, focusing on the fluid mechanics perspective rather than the conventional biological perspective. Reynolds number, which is the inertia-viscous forces ratio, is widely used to generalise the flow characteristics and ensure the wide practicality of the study.

Several flow characterisation techniques were utilised in the study, which include

dye visualisation and Particle Image Velocimetry (PIV). Dye visualisation is simple and it provides quick insight into the understanding of flow behaviour. Although the flow is characterised qualitatively, the simplicity of this technique is useful to enhance the appreciation of fluid dynamics in cell studies and promote the collaboration between engineers and biologists. On the other hand, PIV provides an accurate quantification of the flow parameters in the bioreactor. Measurements were conducted at several imaging planes and velocity vectors were determined. These measurements could then be used to calculate other mechanical parameters, such as stresses and vorticity. The analyses performed in this study offers detailed parametric characterisations of the flow in the spinner flask.

Chapter 2 provides general overview of stem cells, their source of engraftment and application. The background information of previous studies that utilise commercially -available bioreactors are presented in detail. Furthermore, this chapter includes the basics and background of fluid stress and characterisation methods. The flow in a rotating lid bioreactor and how microcarriers affect the flow are described in Chapter 3. Chapter 4 focuses on the flow mechanics and mechanical parameters in the general use of spinner flask bioreactor over a wide range of speed, as a reference to previous and future studies with similar setup. Similarly to Chapter 4, Chapter 5 explains a parametric study specifically for culturing mouse induced pluripotent stem cells (iP-SCs). In addition, the impact of stresses towards microcarrier structure and cell yield are analysed and included in this chapter. Chapter 6 outlines a novel volumetric imaging technique called Holographic Correlation Velocimetry which was developed to improve the laser-imaging measurement technique capability towards 3-dimensional and 3-component imaging tool. The technique was then demonstrated in the characterisation of flows in a cuvette and a spinner flask bioreactor. Finally, Chapter 7 highlights the final conclusions and future work recommendations.

Chapter 2

A Review of the Literature

2.1 Introduction

R EPAIRING and replacing damaged or absent tissues and organs has been a major interest for centuries to improve human life quality for those in need. This interest has led to the development of various solutions ranging from cosmetics to surgery. Successful implementation of organ transplantation has given a new hope. However, it was later realized that the procedure incurred a few major problems: the rejection caused by the immune system, and the low availability of donors (Cabrita *et al.* 2003). Additionally, transplantation has raised a number of bioethical and economic issues regarding consent, payment of organs for transplantation, expense of the procedure and the cost of long-term monitoring and support of the patient. The recipient also carries the risk of safety pertaining to the graft itself. This includes the source of the graft, its collection, preservation and transport to the recipient (Paya *et al.* 2004; Fishman & Rubin 1998).

Scientists have been culturing tissue in order to tackle issues related to organ transplantation. Depending on the type of tissue required, tissue graft can be derived *in vitro* from either the patient's body or stem cells, which makes the source of graft readily available, as well as lowering the risk of rejection by the immune system. There have been a significant number of tissues engineered in previous studies. These include skin, cartilage, bones, muscle, heart valve, tendon, lung, pancreas, cornea, spinal cord and many more (Martin 1981). These studies proved the reliability of this technique in treating patients who require tissue implantation.

Although tissue engraftment from the patient's body has claimed many successes, tissue engrafted from stem cells offers a wider application. Stem cell therapy application is not just for tissue repair, it could also offer contribution to clinical treatment of genetic

diseases.

The advent of stem cell research has opened a new world in cell therapy and revolutionized regenerative medicine (Hentze *et al.* 2007; Ho & Li 2006; Hoffman & Carpenter 2005; Lyon & Harding 2007; Mountford 2008) for many degenerative diseases or injuries (Smith 2003). The stem cell's unlimited ability for self-renewal (Shenghui *et al.* 2009; Conti *et al.* 2005) and to differentiate to various cell types (Keller 2005) make it an effective option as the basic material for various potential treatments. Furthermore, the possibility of obtaining large amounts of these cells, making full use of its self-renewal nature, could lead to substantial advancement for scientific research and therapy purposes.

Prior to implantation of the graft, the extracted tissue or cells have to proliferate to a certain extent to ensure success in the implantation. Thus, it is important to be able to culture tissue in a fast, reliable and safe manner. Bioreactor systems are used to assist the *in vitro* growth process of the cells. Apart from being able to support the cell growth, it is also important that bioreactor systems are automated, which would allow the scale-up process to be realised. Due to the cell's vulnerability, control over environment serum such as pH, oxygen dissolution rate, temperature, nutrient transfer, and mechanical stimulation in terms of shear stress and hydrodynamic stress, is highly desired to ensure repeatability and reproducibility of the cells (Cormier *et al.* 2006; zur Nieden *et al.* 2007).

Although tissue-engineering research is strongly dominated by biologists or tissue culturists, researchers have to understand more than just the biochemistry side of the system in order to develop a suitable bioreactor. Mechanical stimulation involved in the system design is a very important parameter for the cells. However, biologists may have limited knowledge in quantifying this parameter to be incorporated in the design constraints. With these complex design requirements, engineers have become involved in the development of bioreactor systems, making tissue and cell engineering a multidisciplinary research. As there are still many cell mechanisms yet to be understood, current bioreactor design is far from complete. By having engineers collaborate with cell biologists, new discoveries in the area of cell mechanisms as well as that of bioreactor design can be achieved.

Before designing a bioreactor for cell therapy, it is crucial for an engineer to learn and understand more about cells. This includes their morphology, behaviour, and more

importantly the process and environment required for optimum growth. Different cells will behave differently in various environments imposed on them. As for stem cells, the process normally consists of two steps. The first step is to proliferate the cells. In this stage, the bioreactor needs to provide a certain environment to promote the self-renewal nature of the cells, causing the cells to multiply their number, and producing similar types of cells. The second step is differentiating the cells to a certain tissue type. It is crucial for the bioreactor to mimic the exact local environment of the engrafted tissue to stimulate the cells to differentiate and stabilize to the specific required tissue before implantation. The requirements for bioreactor design of these stages are often very specific to the type of cell. Sections 2.2 and 2.3 brief the type of stem cells as the source of engraftment and their application.

It is also important for an engineer to learn the importance of the dynamic system that is a bioreactor. As every cell has a different morphology, each also has different sensitivity towards mechanical stimulation. In an effort to control the differentiation process, it is also crucial for the bioreactor to supply enough nutrients for the cell's needs. Section 2.4 describes background information of some of the previous studies in on growing stem cells using commercially-available bioreactors. Next, fluid stress theory is presented in section 2.5 to appreciate the importance of the stress parameter in biological experiments. Section 2.6 details various characterisation techniques used to measure the flow in a bioreactor. Finally, section 2.7 and 2.8 describe the research motivation and aims of present study.

2.2 Stem Cells

Stem cells serve as an internal repair system due to their potential to proliferate and differentiate into diverse cell types without limit to replenish damaged cells. The products of stem cell division are either similar stem cells or cells with specific lineage capability (Ying *et al.* 2003; Conti *et al.* 2005; Keller 2005). Stem cells are different from other cell types because of two distinct unique characteristics. First, they are unspecialized cells capable of renewing themselves through cell division, and secondly, under certain physiological and experimental conditions, they can be induced to differentiate into tissue- or organ-specific cells with special function (Reubinoff *et al.* 2000; Ohgushi & Caplan 1999). The potential of stem cells to divide into specific cell types is determined by the stem cell's potency. This section is a review of three main stem cell types - pluripotent, multipotent and unipotent- which describes the source of engraftment and progression in stem cell research.

2.2.1 Pluripotent Stem Cells

Pluripotent cells have the widest range of ability to differentiate into any of the three germ layers, which are endoderm, mesoderm and ectoderm, apart from its unlimited, undifferentiated proliferation ability. Being able to differentiate into any of the germ layers means that one could have access to any type of tissue of any lineage from a single cell when it is used as the engraftment source. The breakthrough study of pluripotent stem cell establishment derived from the blastocyst of mouse embryo (Evans & Kaufman 1981) has revolutionized regenerative medicine and tissue repair research. The cells obtained with this harvesting technique are known as Embryonic Stem Cells (ESCs) (Martin 1981). Figure 2.1 illustrates a colony of ESCs imaged using a light microscope.

Although the process of ESCs derived from mouse blastocysts was established in 1981 by Evans & Kaufman, it took more than a decade before the first success of human ESC isolation (Thomson *et al.* 1998). Nevertheless, the long study in mouse ESCs provide crucial knowledge about the biological behaviour as well as the cultivation method of these cells (Torres 1998). The parameters and technique for culturing ESCs without differentiating to any lineages, as well as for initiating the cells to differentiate into specific cell types while retaining the normal functions, have been studied extensively. To date, ESCs have been the dominant interest in research as they demonstrated capabili-

ties for the generation of a variety of cell types including cardiomyocytes (Maltsev *et al.* 1993; Mummery *et al.* 2003), hematopoietic cells (Keller *et al.* 1993; Kaufman *et al.* 2001), neuronal cell types (Bain *et al.* 1995; Okabe *et al.* 1996; Dhara & Stice 2008; Li *et al.* 2005), skeletal myocytes (Kehat *et al.* 2001; Rohwedel *et al.* 1994), adipocytes (Dani *et al.* 1997), osteoblasts (Buttery *et al.* 2001; zur Nieden *et al.* 2003), chondrocytes (Kramer *et al.* 2000; zur Nieden *et al.* 2005), and hepatocytes (Hamazaki *et al.* 2001).
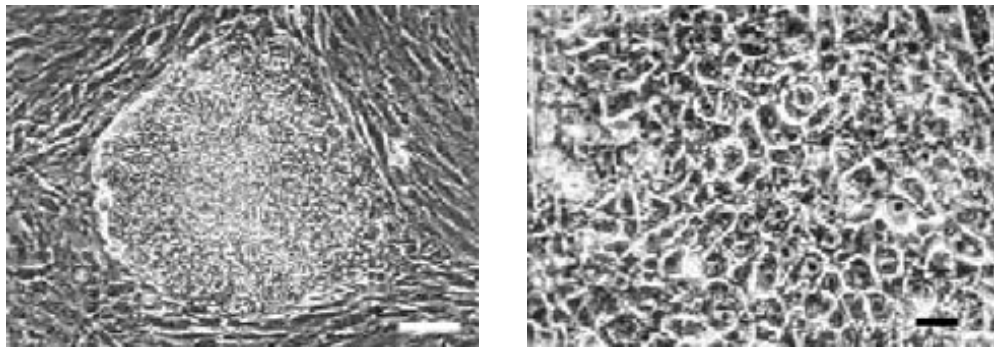
FIGURE 2.1: (Left) Embryonic stem cells colony, scale bar: 100μm. (Right) Embryonic stem cell colony at higher magnification, scale bar: 25μm (Reubinoff *et al.* 2000).

The knowledge gathered from mouse ESC studies provide a solid background required for proliferating and differentiating human ESCs despite the fact that the source of the cells are different, and thus behave differently. Mouse ESCs require a biochemical known as leukemia inhibitory factor (LIF) to proliferate without any sign of differentiation and maintain pluripotency *in vitro* (Chambers 2004; Amit *et al.* 2010). However, human ESCs require an inactivated feeder layer in culture medium mixed with serum, in addition to LIF, as part of the culture conditions to provide a platform for growth. The feeder layer normally is in the form of animal fibroblasts (Thomson *et al.* 1998; Xu *et al.* 2005b), such as mouse embryonic fibroblast (MEF). It produces growth factors that support the living stem cells. The *in vitro* proliferating technique may impose some risk to the use of stem cells for human therapy due to the exposure to animal cells or proteins. It is possible that viruses from the animal can be transmitted to human during implantation. Thus, recent development has focused on the protocol that eliminates the use of animal feeder layer by replacing it with MEF-conditioned medium (Ludwig *et al.* 2006; Xu *et al.* 2001; Amit *et al.* 2004; Xu *et al.* 2005a) or human feeder layer (Richards *et al.* 2002; Amit *et al.* 2003).

Once the cells are removed from the feeder cells, the cells are grown in suspension with the help of a bioreactor. Human ESCs then form aggregates of cells known as Embryonic Bodies (EBs) (Cameron *et al.* 2006). Embryonic Bodies consist of a combination of cell types of all three germ layers for tissue development (Itskovitz-Eldor *et al.* 2005). The cells are then isolated and sorted based on the evidence of differentiation expression of genetic markers. Normally, the pluripotency markers used are SSEA-1, Oct3/4A, Nanog, rex-1, TRA-1-81 and alkaline phosphatase (zur Nieden *et al.* 2007). As for the differentiated cells, they are marked with different markers that detect the genes associated with the product cells. Cells from EBs have proven to be able to produce cardiomyocytes, epithelial cells, and neural cells (Odorico *et al.* 2001). Functional cells of liver and pancrease have also been obtained in a separate study (Schuldiner *et al.* 2000).

A significant amount of research has been undertaken to continually improve the culture and differentiation protocols of the stem cells. Most of the research has involved the development of various biochemicals for cell maintenance, such as the culture medium, the serum, as well as the feeder layer. Additionally, studies have also focused on additives to inhibit unnecessary spontaneous differentiation of pluripotent stem cells. Due to the sucess of these studies, the main structure of the protocol has not significantly changed. Thus, the procedure explained before is valid and practicable.

ESCs have also been cultured in *in vivo* conditions. In this method, the cells are injected into mice. The mice then become a host to growing teratomas. Teratoma is a benign tumor made up of three germ layers. It is similar to EBs. Teratomas were shown to give arise to epithelium, bone, muscle, cartilage and neural cells (Thomson *et al.* 1998). A few studies showed promising results when mouse ESCs are implanted in other animals. Insulin was partially restored in diabetic mice when mouse ESCs were transplanted (Lumelsky *et al.* 2001). In a separate study, neural function was restored in animals with spinal-cord injuries using mouse ESCs in the transplantation therapy (McDonald *et al.* 1999).

The experiments described above demonstrated that ESCs are able to produce a wide range of tissue for regenerative therapy for both *in vivo* and *in vitro* settings. It was also shown that the cells are very sensitive and complex, making it difficult to grow them to a specific tissue. Abnormal behaviour and morphology of the cells are also expected if they are placed in an unnatural environment. Despite the fact that a

lot of factors that control the growth and differentiation of ESCs remain unknown, the success achieved by growing ESCs *in vitro* advances the application of ESCs one step closer to successful regenerative therapies in the future. *In vitro* studies will provide thorough understanding in terms of genetic controls for tissue differentiation (Duncan *et al.* 1998), as well as excellent opportunity for the development of biochemicals, refined to cellular level, which could induce the cells to differentiate, to migrate to damaged tissue, and to adapt into tissues (Schuldiner *et al.* 2000).

If pluripotent stem cells could be proliferated without any sign of differentiation, one could have unlimited access to spare tissue for later use. Cell therapies could also improve the success rate of implantation without the use of immunosuppressive drugs. The recipient would not reject the specific treatment tissue developed with the stem cells because the immune cells produced in the recipient's body would see the new tissue as part of them.

It is important to note that no study has shown any positive *in vivo* development of a full functioning organ derived from human ESCs. The availability of human ESCs is very limited. Due to the fact that ESCs derived from the blastocyst of an embryo, ethical issues are a major concern in the derivation process, as the embryo will not survive once ESCs are harvested. Additionally, funding for such research is limited and the cost involved in ESC maintenance is very high, which caused most of the physiological testings to be done on animals.

In an effort to eliminate the ethical constraint related to ESCs, the derivation of human induced pluripotent stem cells (iPSCs) from adult tissue (Takahashi *et al.* 2007; Yu *et al.* 2007) with similar ESC abilities has sparked great interest and represents a breakthrough in stem cell research. The two separate research groups, Yu *et al.* and Takahashi *et al.*, successfully reprogrammed adult human fibroblasts to pluripotent stem cells, thus eliminating embryo dependency in pluripotent cell harvesting process. A simplified reprogramming process is illustrated in Figure 2.2. Since the breakthrough, the derivation of iPSCs has expanded from a variety of sources such as human blood (Loh *et al.* 2009), pancreatic cells (Stadtfeld *et al.* 2008) and adult neural stem cells (Kim *et al.* 2008). These studies proved that generating patient-specific pluripotent stem cells will be possible in the future and that pluripotent cells can be created from a sample of adult cells. With successes in developing iPSCs from various sources, it is important to measure the performance of the cells by creating a specific and fully

functioning cell. Zhang *et al.* (2009a) and Mauritz *et al.* (2008) successfully differentiated iPSCs into fully functioning cardiomyocytes. Other studies were able to derive human hepatic endoderm (Sullivan *et al.* 2010), retinal-pigmented epithelium (Buchholz *et al.* 2009), dopaminergic neuron (Switowski *et al.* 2010) and recently neuron (Oki *et al.* 2012), in an effort to improve recovery of stroke-damaged brains, from the iPSCs. Apart from ESCs and iPSCs, umbilical cord blood showed ESC-like and pluripotential
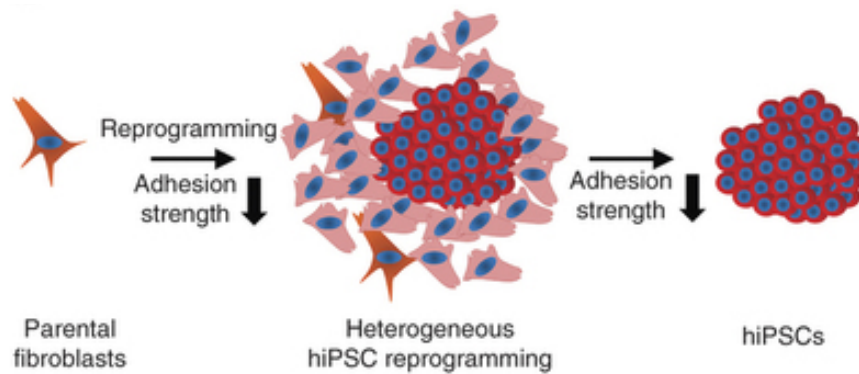
FIGURE 2.2: Schematic representation of iPSC reprogramming (Singh *et al.* 2013)

cell behaviour, being able to differentiate to hematopoietic, epithelial, endothelial and neural tissues (Harris & Rogers 2007). On the other hand, Jiang *et al.* (2002a) showed the pluripotentiality of adult marrow. The mesenchymal stem cell in adult marrow was able to differentiate to endothelium, endoderm and ectoderm on top of mesenchymal lineage in *in vitro* and *in vivo* settings from mouse marrow cells (Jiang *et al.* 2002a).

Irrespective of the source, pluripotent stem cells and the developments in this area have definitely opened a new world in regenerative medicine. Due to several constraints, such as cost and availability, in pluripotent cell research, a lower potency and more viable source like multipotent stem cell has attracted a lot of interest for research and therapy.

2.2.2 Multipotent Stem Cells

Multipotent stem cells have the basic stem cell features, like self-renewal and differentiation abilities into specialized cells. Unlike pluripotent cells, multipotent cell differentiation ability is limited to a certain lineage within a closely related family. For example, multipotent cells in the brain can differentiate into various neural cells but

will not be able to give rise to blood cells. In short, multipotent stem cells are pluripotent stem cells that have undergone specialized differentiation, to give rise to cells with more specific function.

Adult stem cells, obtained from living mammals, are considered multipotent stem cells as their differentiation ability is specialized and limited. They serve a purpose of replenishing damaged or aged cells throughout the life. Thus, multipotent cells can be found in tissues, which make the access to these cells more viable than pluripotent cells.

One of the benefits of using multipotent stem cells is that there is no termination of embryos involved, such as for the case of pluripotent stem cells. These cells are also particularly suitable for transplants. As they are partially differentiated, they could be isolated and guided to differentiate to a specific function within the same family before being transplanted into the same patient. Immunological repercussions could be avoided after the transplantation.

There are several known sources for multipotent stem cells. Unlike pluripotent cells, multipotent cells are more available and can be obtained from living mammals. Human adipose (fat) (Rodriguez *et al.* 2005; Zuk *et al.* 2002), dermis (Toma *et al.* 2001), human term placenta (Miao *et al.* 2006; Yen *et al.* 2005), amniotic membrane (Alviano *et al.* 2007) and umbilical cord blood (Lee *et al.* 2004; Kern *et al.* 2006) have been the few sources of multipotent cells in the form of mesenchymal stem cells. Mesenchymal stem cells have been known to be able to differentiate into bone-like cells such as chondrocytes (Day *et al.* 2005; Robins *et al.* 2005) and osteoblasts (Day *et al.* 2005). Studies have also shown that mesenchymal progenitor cells are the source of smooth muscle (Galmiche *et al.* 1993; Grigoriadis *et al.* 1981), myocytes (Li *et al.* 2007; Zhang *et al.* 2007) and fat cells, also known as adipocytes (Grigoriadis *et al.* 1981).

On the other hand, bone marrow is a unique source of multipotent cells. It is able to provide several types of multipotent cells. Reyes *et al.* (2002) showed that bone marrow contains multipotent adult endothelial progenitor cells on top of multipotent mesenchymal cells (Miao *et al.* 2006; Kern *et al.* 2006; Pittenger *et al.* 1999). Additionally, marrow- and umbilical cord blood-derived cells also contain multipotent hematopoietic cells (Morrison *et al.* 1997; Broxmeyer *et al.* 1989), which differentiate to blood cells such as red blood cells, platelets, monocytes, granulocytes and lymphocytes (Krause 2002).

Another progenitor that has multipotent characteristics is the multipotent neural precursor cell. It provides repair ability to brain and central nervous system cells such as neurons, astrocytes and oligodendrocytes (Arsenijevic *et al.* 2001). The cells can be harvested from bone marrow (Jiang *et al.* 2002b) and brain tissue specifically from the temporal and frontal cortex (Arsenijevic *et al.* 2001).
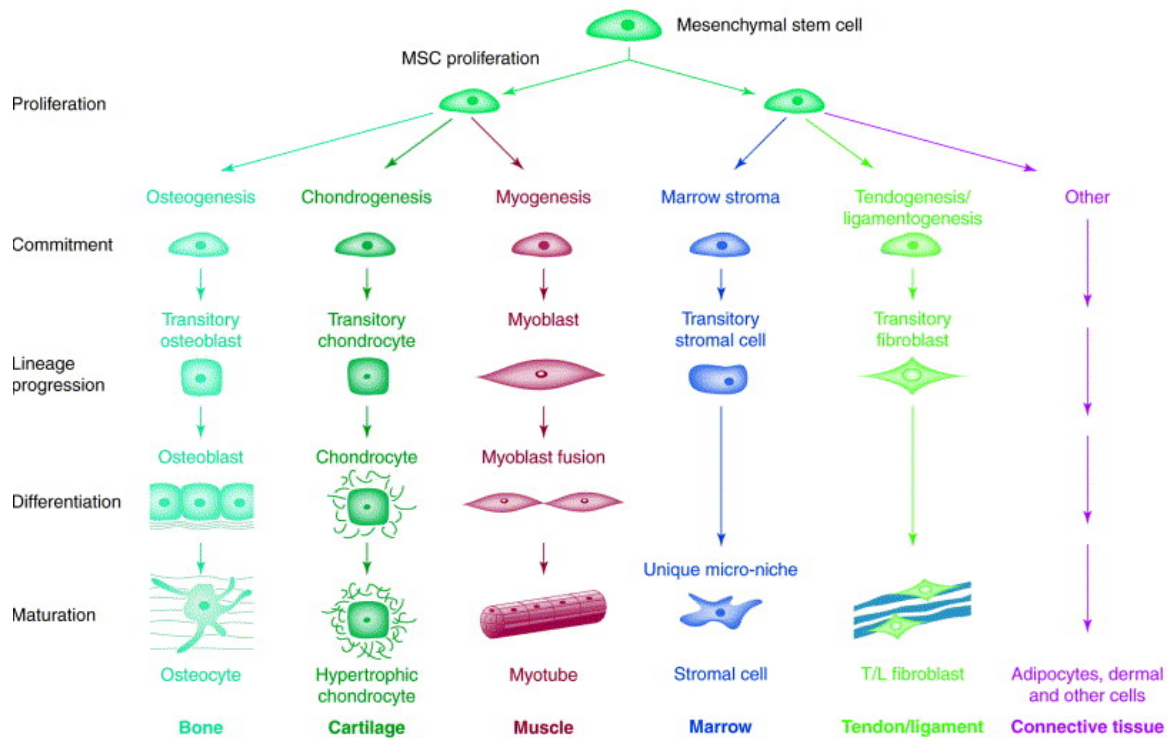
FIGURE 2.3: Mesenchymal stem cells (MSCs) are able to proliferate and differentiate into several different lineages to generate bone, muscle, tendon and connective tissue (Caplan & Bruder 2001)

As determined in previous studies, bone marrow consists of multiple types of progenitor cells, which makes it the most common source for multipotent stem cells. Although multipotent cell differentiation ability is limited to close familial line, it is more practical to obtain the cells due to their availability from various sources. Having said that, the cells have to go through a similar complex procedure as for plutipotent cells to induce differentiation to a specific lineage. Multipotent cells can be used as the graft source to replenish damaged cells and tissues. Mesenchymal cells have been shown to be able to provide therapies for damaged or injured tissues like bone (Bruder *et al.* 2004), cartilage (Ponticiello *et al.* 2000), tendon (Awad *et al.* 1999), muscle (Galmiche *et al.* 1993), dermis (skin) (Baksh *et al.* 2007) and also heart (Silva *et al.* 2005). The differentiation abilities of mesenchymal stem cells are summarised in Figure 2.3.

Hematopoietic phenotype cells could provide therapy for immunodeficiency-related diseases (Buckley *et al.* 1999) through their differentiation ability to various blood cells, as depicted in Figure 2.4. On the other hand, neural progenitor cells can be the graft material for central nervous system (CNS) disorders (Carpenter *et al.* 1999). In addition to being the sources of aforementioned therapies, multipotent cells, commonly mesenchymal-type cells, are also the source for iPSCs through *in vitro* gene reprogramming (Hanna *et al.* 2007), as discussed in previous subsection.
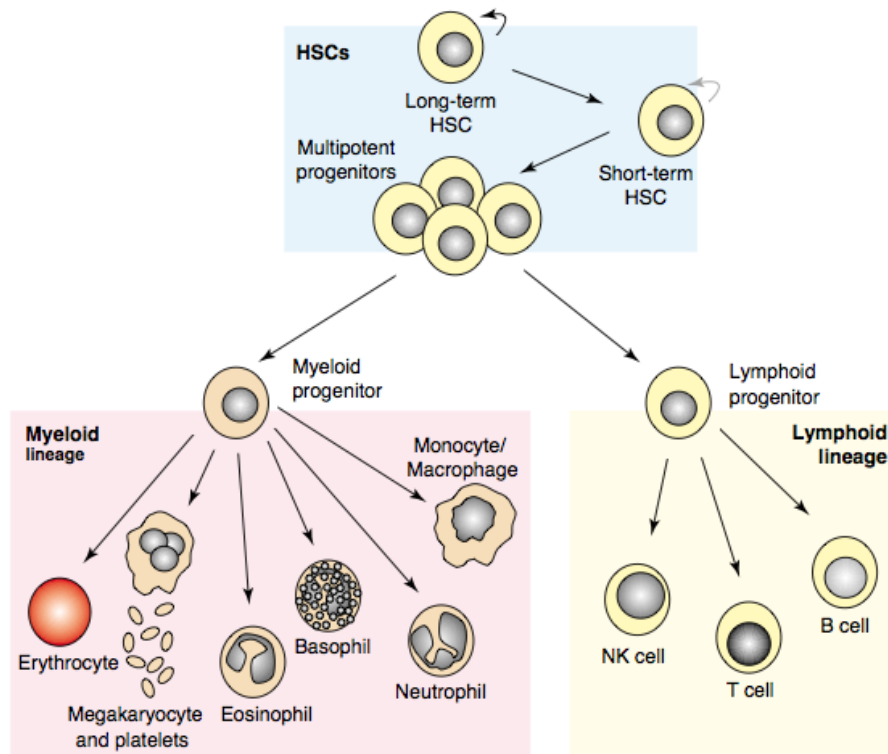
FIGURE 2.4: Differentiation lineage of hematopoietic stem cells (Cabrita *et al.* 2003).

Due to its practicality and availability, multipotent cells have attracted a lot of interest from research groups with various backgrounds in expanding the future of cell therapy. Another type of stem cell with lower potency, known as the unipotent stem cell, is described in the following section.

2.2.3   Unipotent Stem Cells

Unipotent cells have potential for therapeutic purposes, despite the fact the cells have not received similar attention in research compared to more potent cells like pluripotent and multipotent cells. The unipotent stem cell, discovered in adult tissues, has the

lowest potential of all stem cells. The cells show more progenitor-like behaviour and are only capable of differentiating into a very specific type of cell. This type of cell arises from differentiated multipotent stem cells, being closer to a target cell. However, it still has the self-renewal capacity, like any other stem cell. Despite the limited differentiation product, unipotent cells can make significant impact in regenerative medicine due to their proliferation ability.

Skin stem cells have unipotency ability, which constantly heal and repair the skin within a strict equilibrium of proliferation and differentiation in a fine lineage at a slow rate (Brouard & Barrandon 2003). The epithelial section of the human epidermis requires three weeks for complete renewal. Disturbance of the balance can cause scaring and cancers, which tend to develop on chronic cutaneous wounds (Owens & Watt 2003). The importance of skin therapy to treat injuries as well as the common occurrence of skin carcinomas has attracted a lot of attention to epidermis stem cell research. Evidence showed that unipotent stem cells could be found specifically in the basal layer of human epidermis (Watt 2001) and at the bulged section of hair follicles under normal conditions (Blanpain & Fuchs 2006). These cells tend to grow in the form of colonies, also known as clonogenic in culture procedure (Barrandon & Green 1987). The bulge serves as a reservoir for unipotent follicle stem cells, but in incidence of injury, Blanpain & Fuchs (2006) asserted that it acts as a multipotent stem cell reservoir in repairing interfollicular epidermis. The ability to reconstruct the epithelial section of the epidermis from a single cell promoted healing for burn victims during therapy (Gallico *et al.* 1984).

Cardiac and cranial neural crests are able to give rise to single phenotype, unipotent neural cells (Ito & Sieber-Blum 1991; Crane & Trainor 2006). A study in zebrafish showed that neural crest cells comprise a heterogeneous population of unipotent cells (Raible & Eisen 1994). Unipotent neuroblasts can give rise to 3-17 neuronal precursors (Weiss *et al.* 1996). Central nervous system neurons and glia are two examples of unipotent neural cell products. A study by Weiss *et al.* (1996) showed that basic Fibroblast Growth Factor (bFGF) can enhance neuroblast proliferation rate.

2.3   Examples of Cell and Culture Applications

2.3.1   Cardiomyocytes

Heart disease is the primary cause of mortality in developed countries. Infarction in myocardium can cause tissue loss and reduce cardiac performance and functionality. Furthermore, the post-infarcted heart weakens over time (Pfeffer & Braunwald 1990), which could consequently lead to heart failure (Xu *et al.* 2004). As the heart has low regenerative capability, previous treatment focuses on replacing the organ by transplantation (Laflamme *et al.* 2007). However, donor shortage and complications due to the immune system have been challenging issues for treatment (Cannizzaro *et al.* 2007). The emergence of cell research has demonstrated that cardiomyocytes, shown in Figure 2.5, are the ideal type of cell for therapy due to their integral electrical and physiological properties (Bauwens *et al.* 2005). This section is a summary of the previous works related to cardiomyocytes, with the focus mainly on the source of the cells and their approach to obtaining cardiomyocytes.
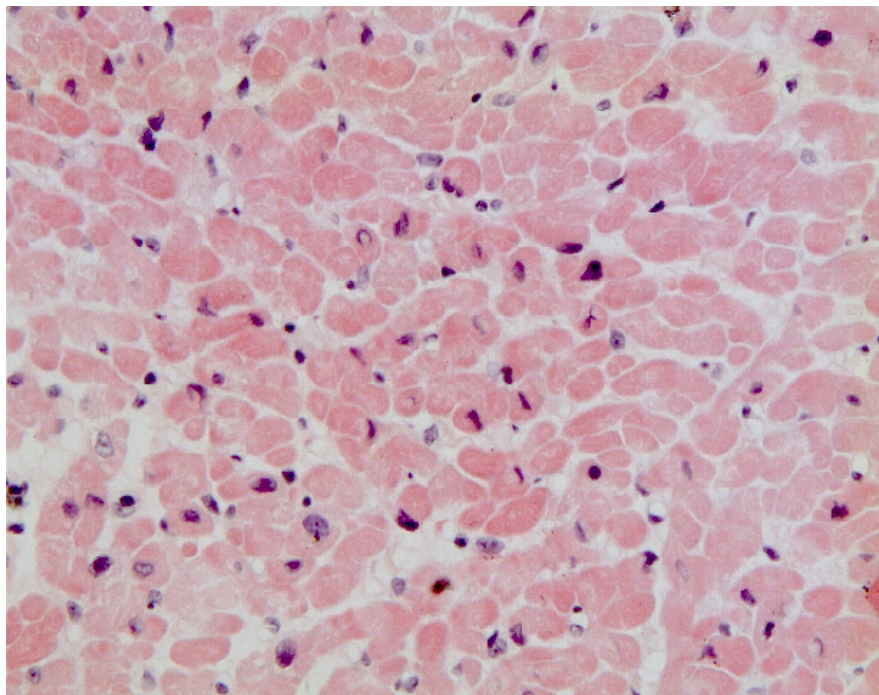

FIGURE 2.5: Light microscopy image of normal cardiomyocytes

2.3.1.1   Bone marrow-derived cardiomyocytes

One of the early works involving cardiomyocyte was conducted by Toma *et al.* (2002). Human mesenchymal stem cells (MSCs) were extracted from adult bone marrow aspirate. Then, the stem cells were transplanted into the left ventricle (myocardium) of adult mice. Fourteen days after the transplantation, the cells began to take the properties of surrounding cardiomyocytes. Out of 16 animals, 4 of the animals did not show any sign of MSCs in the myocardium, from which they concluded that the transplantation into the beating myocardium was not successful. No bioreactor was used in this study. Basically, cardiomyocytes were grown *in vivo* from human MSCs. This study was very closely related to a study by Orlic *et al.* (2001), where the authors transplanted bone marrow cells in infarcted myocardium in mice. Toma *et al.* (2002) suggested that bone marrow MSCs and cardiomyocytes came from similar lineage of early mesoderm, although they form in different parts of embryo. *In vitro* MSCs differentiation into cardiomyocytes was then investigated (Xu *et al.* 2004). Xu *et al.* also suggested that there is approximately 0.001-0.01% of MSCs in bone marrow aspirate and they successfully proliferated and differentiated these cells *in vitro* to obtain cardiomyocytes.

Although it was proven cardiomyocytes could be derived from bone marrow cells, the viability of this method was questioned. There is no doubt bone marrow is a promising source of multipotent stem cells, such as MSCs and hematopoietic stem cells (Pittenger *et al.* 1999). However, the ability to obtain cardiomyocytes from bone marrow cells after myocardial transplantation was doubted. It is unclear which bone marrow cells contributed to myocardium (Balsam *et al.* 2004). Balsam *et al.* reported that three different populations of bone marrow cells differentiated into haematopoietic lineages instead of cardiac muscle or vascular-type cells when injected into myocardium. Even if MSCs are able to differentiate to cardiomyocytes, the differentiating ability and number of cells reduce with age (Lee *et al.* 2004). A study done by Kattman *et al.* (2006) proposed that cardiomyocytes came from multipotent FLK-1+ cardiovascular progenitor cells. Cardiomyocyte, endothelial and vascular smooth muscle colonies were found in culturing process (Kattman *et al.* 2006). Unfortunately, the study did not report any possible source for the particular progenitor cells. As there are a lot of missing puzzles in cell research, many cell studies prefer to use higher potency cells as the graft source to eliminate uncertainties and controversies.

2.3.1.2   Embryonic stem cells (ESCs) as the source of cardiomyocytes engraftment

Zandstra *et al.* (2003) represent the pioneer group that used ESCs to obtain cardiomyocytes. The study successfully obtained cardiomyocytes from mouse ESCs cultured in a 250mL Bellco spinner flask at 60 revolutions per minute (RPM) with initial density of 5×10^5 cells/mL. Half of the culture medium was exchanged every second day of the process. A total of 6×10^5 cardiomyocytes/mL was achieved at the end of the study. This result was achieved by undertaking the differentiation process in culture dishes for 4 days to avoid the cells from clumping together. The result can be further improved by optimizing parameters such as ESC line, cell density, and medium supplementation (Zandstra *et al.* 2003).

Bauwens *et al.* (2005) used mouse ESCs in their study. These ESCs were encapsulated and inoculated in a 250mL Bellco spinner flask at a density of 4000 cells/mL. Unfortunately, no spinning rate was given and the study compared the feeding method by either changing the culture medium via perfusion (culture medium was exchanged over time), or by stopping the agitation and change 50% of the culture medium manually every 2 days. It was demonstrated that encapsulated ESCs yielded 19.8 times more cardiomyocytes compared to unencapsulated ESCs. Moreover, the cells preferred hypoxic condition at 4% of oxygen level as 1.47 fold more cardiomyocytes were obtained compared to normal oxygen condition (Bauwens *et al.* 2005). No results of cardiomyocyte output were mentioned for different feeding methods.

Mouse ESCs were also used by Schroeder *et al.* (2005) to engraft cardiomyocytes. Comparison was made between a 250mL Bellco spinner flask (agitated at 40, 50, 80 RPM) and a 250mL Integra bulb-shaped stirrer spinner flask (agitated at 40, 50 RPM). Half of the culture medium was exchanged daily to maintain the concentration of nutrient and waste in the system. It was found that the cells clumped and aggregated more in the Bellco spinner flask than the Integra bulb spinner. The aggregations of the cells resulted from stagnation regions under the Bellco impeller. Yields of 0.6×10^5 cardiomyocytes/mL and 2.1×10^5 cardiomyocytes/mL were acquired from Bellco and Integra spinner flasks, respectively. Another experiment was conducted using a 2L stirred bioreactor equipped with pitch blade turbine, agitated at 35, 65, 80 and 125 RPM. Cells were seeded at a concentration of 2×10^5 cells/mL into 1L of culture medium for the first 48 hours. The highest number of EBs was recorded at 24 hours,

when the impeller was spinning at a rate of 80 RPM. However, after 9 days of culturing, cells grown in 65 RPM bioreactor showed the most promising results with a total cells of 12.5×10^6 cells/mL. At the end of the differentiation process (18 days), 6.38×10^5 cardiomyocytes/mL were attained, a total of 6.4 fold increment to the number of cells.

Instead of using mouse ESCs, Laflamme *et al.* (2007) derived cardiomyocytes from human ESCs *in vivo*. Only 6 out of 34 infarcts contained myocardial grafts, which makes the success rate of transplantation to injured hearts at only 18%. They were able to increase the success rate by creating a mixture of chemicals to provide a better environment for cell survival called pro survival cocktail. The chemicals did not only improve the survival rate, they also increased the growth rate of myocardial graft in infarcted heart.

In 2008, a group studied the production of cardiomyocytes in a suspension culture system (Niebruegge *et al.* 2008). Using mouse ESCs as the graft source, the cells were grown in a 250mL Integra bulb-shaped glass with the impeller spinning at a rate of 60 RPM. Cells were seeded at 2×10^5 cells/mL with an initial culture medium volume of 125mL for the first 48 hours, and 250mL onwards. In terms of feeding protocol, by replenishing 50% of the culture medium every 2 days, more cardiomyocytes (2.4 cardiomyocytes per ESC) were obtained compared to replacing it every day (0.7 cardiomyocytes per ESC). The authors suggested that frequent change in culture medium caused severe dilution of cell-secreted factors that influence cell proliferation and differentiation. These tests were translated to a 2L bioreactor system at similar cell seeding density. Prolonging the proliferation time from 9 days to 11 days yielded more viable cells. The highest yield was 23×10^5 cardiomyocytes/mL under the perfusion feeding method.

While these studies focused on the optimum protocol in suspension bioreactor systems, a group studied the ESC growth in polymer scaffolds with a variation of fabrication method (Fromstein *et al.* 2008). Murine ESCs were grown in polymer scaffolds, either fabricated by electrospinning, or by thermally-induced phase separation (TIPS). A 1L round bottom bioreactor with a working volume of 500mL was used to culture ESCs. Cells were seeded at 5000 cells/mL and half of the culture medium was exchanged every 2 days. However, no spinning speed was given in the article. It was found that electrospun scaffolds produces elongated cardiomyocytes whereas TIPS produced rounded cardiomyocytes. It was concluded that cardiomyocyte growth is affected

by the surface roughness and porosity of the polymer (Fromstein *et al.* 2008).

2.3.1.3 Other sources of cardiomyocyte graft

Although most of cardiomyocyte studies were derived from pluripotent stem cells, there were a few efforts that used MSCs, obtained from skeletal muscle and mesenchymal stem cells from umbilical cord blood, to obtain cardiomyocytes.

Clause *et al.* (2010) utilized rat skeletal muscle-derived stem cells. The cells were proven to have multipotent properties that allowed differentiation to smooth muscle, bone, tendon, nerve, endothelial, and hematopoietic cells. The study showed that the stem cells were able to differentiate to cardiomyocytes in a 3-dimensional gel bioreactor. Even with a known ability to differentiate into cardiomyocytes, the efficiency of differentiation was unclear as it was limited to functional characterisation.

Recently, multipotent MSCs were harvested from human umbilical cord (Hua *et al.* 2011). Umbilical cord blood and umbilical cord cells are younger than other adult stem cells, which makes them a very good alternative source. The young age of the cells are less prone to rejection in transplants as these cells have not developed the features that can be recognized and attacked by recipients' immune systems. The self-renewal ability of these cells is expected of multipotent stem cells (Hua *et al.* 2011). Umbilical cord-derived cells were reported to differentiate into mesoderm cell types such as osteoblasts, chondrocytes, and adipocytes (Lee *et al.* 2004; Pittenger *et al.* 1999), but little work and controversial evidence have been reported in the isolation, characterisation and differentiation of MSCs from umbilical cord into functional neural, cardiomyocyte and germ cells, which raises the question of real MSC existence in umbilical cord (Lee *et al.* 2004). Hua *et al.* (2011) isolated hematopoietic cells to harvest MSCs from umbilical cord; the cells were differentiated *in vitro* to osteoblasts, adipocytes, neural, cardiomyocyte-like and germ cells. Traditional static culture was used in this study.

2.3.2 Neurons

Neurodegenerative diseases such as Parkinson's disease affects 550,000 people in North America, which translates to 20 billion dollars in healthcare cost every year (Sen *et al.* 2001). Parkinson's disease is caused by the degradation of nigrostriatal dopaminergic neurons which causes the bearer's movement to be shaky and slow (Lindvall *et al.* 2004). This disease is one of many other neurodegenerative diseases, such as Alzheimer's

disease, spinal injuries and Huntington's disease. While stroke is the prominent root of disability in the world (Poungvarin 1998), 10,000 Americans endure spinal cord injuries each year (Teng *et al.* 2002). The damage to the spinal cord results in reduction of its functional ability due to the loss of neurons, glia and axons. Example neurons are shown in Figure 2.6. Functional recovery can be considerably improved with conservation of a small percentage of tissue (Teng *et al.* 2002). Due to the severe effect imposed on the patients, both physically and mentally, caused by neurodegenerative diseases, extensive research has been conducted *in vivo* and *in vitro* in effort to provide treatment based on neural cells.
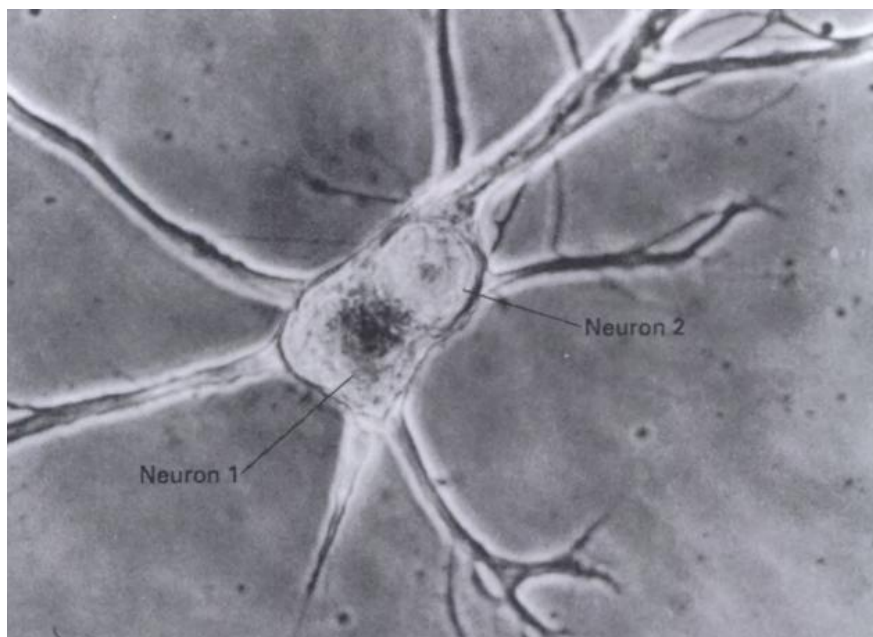
FIGURE 2.6: Figure of two adjoining neurons injected with the fluorescent dye Lucifer yellow (Kaczmarek *et al.* 1979)

2.3.2.1   Pluripotent stem cell-derived neurons

Using ESCs as the graft source, Fraichard *et al.* (1995) and Okabe *et al.* (1996) managed to differentiate the embryonic cells to neuroepithelial precursor cells before differentiating them further to functional neurons and glia. The latter research group developed the *in vitro* protocol, which produces central nervous system using a mixture of serum-free culture and growth factor (Okabe *et al.* 1996). In a separate study, Parkinsonism of a mouse model was reduced based on ESCs experiments (Björklund *et al.* 2002). The stem cells were propagated *in vitro*, which produced embryonic bodies. The embryonic bodies were later transplanted into right striatum of Parkinson model mouse. It was

found through functional neuroimaging that the cells in the *in vivo* experiments successfully differentiated into mesencephalic dopaminergic phenotypes, which integrated well with the host and reduced the Parkinson's effect (Björklund *et al.* 2002). In 2005, Muotri *et al.* (2005) cultured human ESCs *in vitro* on inactivated mouse embryonic fibroblast and implanted the cells into the brain ventricle of mice embryos. The *in vivo* environment conditions induced the differentiation process to give rise to neuronal and glial lineages with good integration with the host. While these studies showed success developing neuron phenotypes *in vitro* and *in vivo*, Shen *et al.* (2004) found that the neural stem cell proliferation could be enhanced by introducing soluble factors derived from endothelial cells. The soluble factors act as a stimulant to neural stem cells which enhances neuron production and inhibits their differentiation, allowing efficient growth of neural stem cells. Neural progenitor cells were also derived from human iPSCs using a microcarrier system (Bardy *et al.* 2013). An expansion of 20 fold was obtained as a result of the cells being proliferated in a static microcarrier culture before they were grown more extensively in spinner flasks (Bardy *et al.* 2013).

2.3.2.2 Multipotent stem cell-derived neurons

A few studies have shown that neural cells can be derived from adult stem cells such as bone marrow-derived stem cells. Zhao *et al.* (2002) implanted the stem cells in the affected rodents' brains due to stroke, which later successfully showed positive markers for neurons, astrocytes and oligodendroglia. The study also showed improvement of neurological function. On the other hand, Wislet-Gendebien *et al.* (2005) and Tropel *et al.* (2006) derived neurons effectively *in vitro* from MSCs in the bone marrow. Using Nestin as the main neural marker, it was suggested that basic Fibroblast Growth Factor (bFGF) could act as an inducer to enhance differentiation to neuron phenotype (Tropel *et al.* 2006). In order to increase the growth rate further, polymer scaffolds can be seeded with neural cells and implanted in the patient. By designing the scaffold to universally fit in various cavities, the functional recovery rate was optimised compared to direct cell transplantation (Teng *et al.* 2002). An image of cultured neural cells is depicted in Figure 2.7.

Neuron phenotypes can also be grown from adult neural cells, which are believed to have multipotent characteristics (Westerlund *et al.* 2003). The cells were obtained from the neurogenic region of the adult brain through tissue biopsy. Preliminary exper-
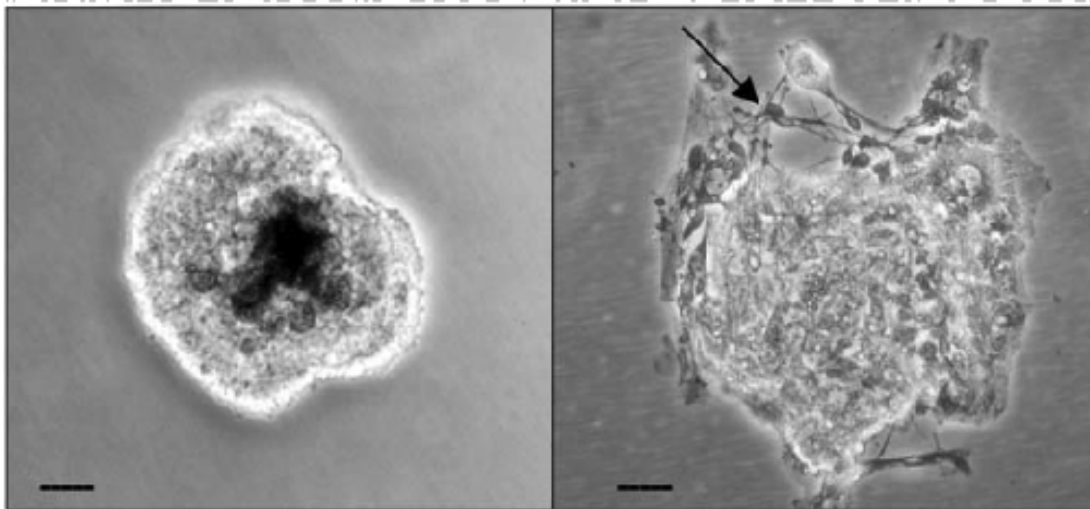
FIGURE 2.7: (Left) Human neurosphere derived from brain tissue of 8-week old human embryo after 4 days of culture. (Right) The spheres flattened out and showed neural characteristics at the marked arrow. Bar = 50μm (Kennea & Mehment 2002).

iments *in vitro* showed that the cells gave rise to cells with neuron and glia behaviour (Akiyama *et al.* 2001). Akiyama *et al.* (2001) transplanted adult human neural cells into the glial-free spinal cord tract of a rat which successfully restored the normal function in the axons. After proliferating the adult neural cells *in vitro* for 48 hours, the cells were transplanted into the hippocampus or the cortex of a developing or adult brain in allowing the cells to adopt morphological features (Englund *et al.* 2002). The resultant cells expressed positive for mature neurons in the adopted host (Englund *et al.* 2002). Additionally, cells harvested from four temporal lobes at the wall of the lateral ventricle of an adult brain displayed astrocytes, oligodendrocytes and neurons phenotypes in *in vitro* experiments (Westerlund *et al.* 2003). These studies could provide a novel therapeutic strategy to counter neurodegenerative disorders through stimulating neurogenesis in the affected area.

2.3.3   Chondrocytes

Cartilage is one of the avascular connective tissues. It delivers a near frictionless surface at the diarthrodial joints for load transmission (Erickson *et al.* 2002). The difference between bone and cartilage in an MRI image is shown in Figure 2.8. Due to low cell density, cartilage has low healing ability which makes it prone to injury and diseases (Betre *et al.* 2006). The common injuries involving cartilage are osteoarthritis and cartilage disorders. In the United States alone, more than 40 billion dollars were spent to treat cartilage disorders (Praemer *et al.* 1999). Normally, to treat cartilage disor-

der, microfractures are introduced in the subchondral bone which promotes cartilage regeneration through the use of local endogenous bone marrow stromal cells (Gillogly *et al.* 1998). However, this type of clinical treatment produces significant variance in biomechanical properties, causing converse effect to the joint (Minas & Nehrer 1997). Another treatment involves an invasive procedure by harvesting chondrocytes from undamaged joints and implanting them into the damaged area. This treatment could affect the undamaged area and initiate osteoarthritic modification to the joint (Lee *et al.* 2000a). Due to the repercussions involved in the treatments, a cell therapy is introduced using chondrocytes as graft source for tissue repair.
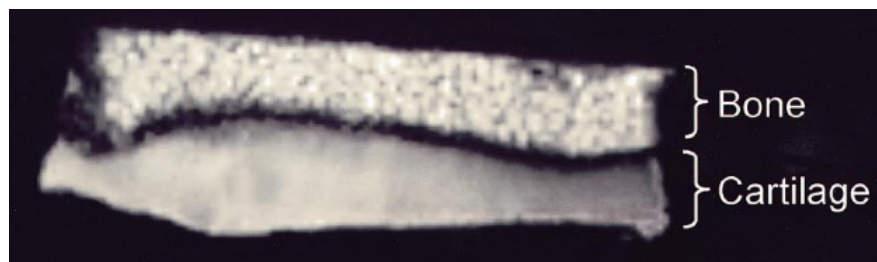
FIGURE 2.8: MRI image of bone and cartilage (Bashir *et al.* 1999)

2.3.3.1   Bone marrow cell-derived chondrocytes

Bone marrow has attracted significant interest in deriving chondrocytes for tissue repair. Most studies have made full use of multipotent mesenchymal stem cells that exist in bone marrow, and successfully gave rise to chondrocytes (Fortier *et al.* 1998; Mackay *et al.* 2007; Mauck *et al.* 2006) as shown in Figure 2.9. Initially, chondrocytes were grown in pellets from bone marrow-derived mesenchymal cells (Mackay *et al.* 2007). Mackay *et al.* (2007) also made a breakthrough discovery to enhance chondrocyte growth *in vitro* by including dexamethasone and transforming growth factor-$\beta3$ (TGF-$\beta3$) in the medium. Using similar engraftment source, Barry *et al.* (2001) defined the chemicals and proteins in the cartilage and managed to determine the steps of chondrogenesis. The team deduced that the extracellular matrix of cartilage contains aggrecan, decorin, biglycan, fibromodulin, cartilage oligomeric matrix protein and leucine-rich protein chondroadherin (Barry *et al.* 2001). By understanding chondrogenesis, it could be concluded that chondrocyte derivation is highly dependent on the evocation of the appropriate differentiation pathway by the implanted cell (Barry *et al.* 2001).
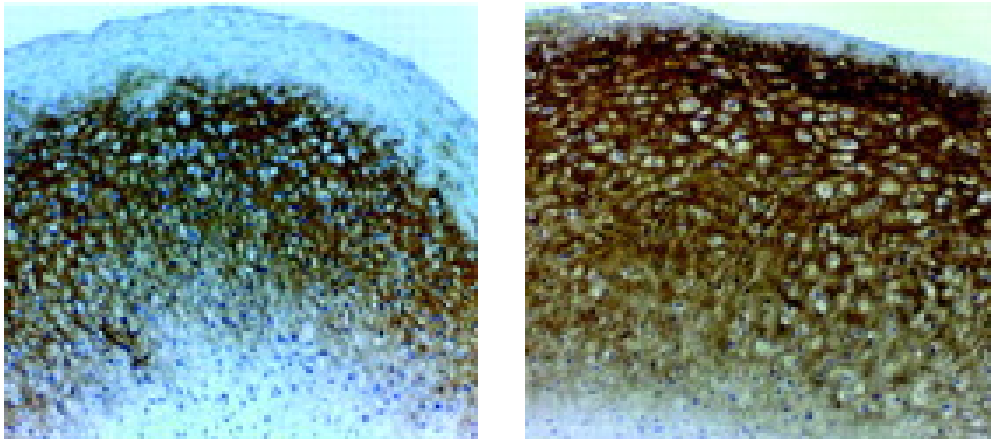
FIGURE 2.9: Marrow-derived stem cells showed chondrogenic morphology by staining with the C4F6 monoclonal antibody to type II collagen (Pittenger *et al.* 1999).

2.3.3.2   Pluripotent cell-derived chondrocytes

A few studies have used pluripotent ESCs as the graft source (Hegert *et al.* 2002; Kramer *et al.* 2000; Hwang *et al.* 2006). Chondrocytes were derived *in vitro* with aid of TGF-β3 medium and fibroblasts (Hegert *et al.* 2002). To eliminate the tumorigenic behaviour in the derived cells due to the ESCs' nature to differentiate spontaneously, the cells were selected to keep the culture in pure condition and any non-chondrocytes-like cells were discarded. Hegert *et al.* (2002) managed to develop growing and calcifying chondrocytes from mouse ESCs. In a separate study, Hwang *et al.* (2006) derived chondrocytes by growing embryonic bodies in hydrogel. The hydrogel enhanced the chondrogenic gene in the culture process to give rise to chondrocytes (Hwang *et al.* 2006).

2.3.3.3   Other source of chondrocytes engraftment

Although positive results were obtained in deriving chondrocytes from bone marrow-derived cells and ESCs, the source of engraftment imposed several challenges. Embryonic stem cells are surrounded with ethical issues whereas marrow-derived cells impose challenges related to donor site morbidity, low cell numbers, and reduced potential with increasing age (Banfi *et al.* 2002). It is important to have a source that is plentiful, has chondrogenic potential, and is highly accessible to and compatible with the patient (Hunziker 2001). A new source, adipose-derived cells emerged as the source for chondrogenic phenotype. Research has shown that multipotent cells can be found in adipose tissue (fat) (Zuk *et al.* 2001; Guilak *et al.* 2006). This source attracted a lot

of interest, as it is abundant and could be extracted by liposuction. Erickson *et al.* (2002) produced cartilage matrix in both *in vitro* and *in vivo* settings. Apart from dexamethasone and TGF-β medium, 3-dimensional round morphology is important to maintain chondrocytic behaviour. This could be obtained using a three-dimensional (3D) construct to support the growth (Erickson *et al.* 2002). On the other hand, Betre *et al.* (2006) utilized polypeptide gel to promote and support the differentiation process of adipose-derived stem cells to chondrocytes. Additionally, the growth of chondrocytes was improved by growing the cells at 5% oxygen tension on top of chondrogenic media supplement (Betre *et al.* 2006).

In an effort to improve the cell growth, biomaterial scaffolds, cellular supplement and biologically active molecules have been extensively studied (Langer & Vacanti 1999; Solchaga *et al.* 1999). It is important that the treatment is able to provide mechanical function, is bio- and immune-compatible, as well as having the ability of resorb/ remodel depending on the type of injury (Hubbell 2003).

Mechanical forces induced by compression, fluid flow, hydrostatic pressure have been found to regulate matrix metabolism in cartilage and *in vitro* chondrocyte culture (Sah *et al.* 1989; Gray *et al.* 1989; Lee *et al.* 2000b; Lee & Bader 2005). Fluid-induced shear in 2D and 3D cultures could regulate the matrix metabolism (Uchio *et al.* 2000). The shear stress is produced through the use of a perfusion bioreactor at varying flow rate. For chondrocyte development, by putting the culture in a perfusion bioreactor at a flow rate of 0.05mL/min (or 11μm/s) for 3 days, an increment of 80% cell count was obtained relative to the static culture method (Davisson *et al.* 2002). This result showed that shear stress is an important parameter in cell culture protocol. Section 2.4 explains various types of bioreactor that can promote and enhance cell growth.

2.4   Bioreactors

A bioreactor is a device used in biological processes that allows control of the environment and operating variables (Ellis *et al.* 2005). It is used to aid and accelerate the process while maintaining the sterility of the procedure in a closed system. Bioreactors have been widely used in tissue and cell engineering with promising results. Bioreactors used for such applications involve static culture systems, perfusion, rotating wall and spinner flasks. The subsequent subsections discuss the details of each type of bioreactor.

2.4.1   Static culture

Traditionally, stem cell expansion is done by using static culture systems since the pioneering work by Dexter *et al.* (1973). Well plates, petri dishes and T-flasks are examples of static culture system and have been extensively used in various culture procedures. An image of a T-flask is shown in Figure 2.10. The flasks or dishes, containing the cells and growth media, were placed inside an incubators that control most of the parameters such as oxygen level, temperature and humidity. Media were replenish after a certain amount of time to provide continuous nutrients supply, required for cell growth, as well as to control waste level within an acceptable range.
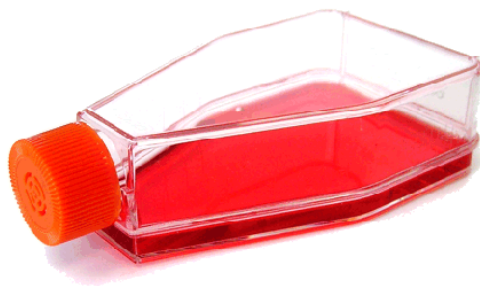
FIGURE 2.10: T-flask for static culture

Although static culture is the most prominent method in cell culture, there are several limitations including lack of mixing, causing significant concentration variance in pH, oxygen dissolving, and nutrients; high level of difficulty in online monitoring and control over culture environment; laborious process to feed the cultures and retrieve data on culture progress; and limited expansion due to the small surface area to sup-

port the number of cells in the system (Collins *et al.* 1998; Cabral 2001). The change of culture media introduced a counter-productive shock environment to the cell in the protocol.

2.4.2 Perfusion bioreactor

Perfusion bioreactors aim to provide the cells with a continuous nutrient supply over the culture period. The general perfusion bioreactor setup consists of a pump, media reservoir, circulation tubes and culture dishes or flask. Some perfusion reactors consist of an extra component of chamber to house the cells or scaffold seeded with cells. By having fresh media constantly pumped to the cells, this bioreactor is superior in terms of nutrients delivery and waste removal compared to static culture. The flow of the media induces mechanical stress, with mainly shear stress to the cells. Some studies have shown that the stress could be a stimulus to the cell growth and differentiation process. Furthermore, the shear stress could be easily varied by changing the flow rate to provide different cell stimulation.

To minimize the limitations imposed by static culture, Schwartz *et al.* (1991) experimented on the effect of perfusion rate on the productivity of the human bone marrow culture system. The cells were found to be doubling every 2.1 weeks when the system was perfused with medium at a rate of 50% volume exchange every day. Another perfusion culture was developed by Palsson and colleagues (1993) based on increasing the medium transfer rate. The perfused medium used in the study was restricted to fresh medium pumped continuously to the system using a syringe pump. An outstanding 10-fold expansion of total cell count was obtained in the bone marrow culture; the cells were later differentiated to hematopoietic cells (Palsson *et al.* 1993; Koller *et al.* 1993).

More recent studies have focused on the use of a porous construct tightly secured in a chamber to enhance the nutrient diffusion as well as to allow 3-dimensional cell growth. Ideally, as the cells grow around the construct and become tissue, they will replace the construct which will degrade automatically (Meinel *et al.* 2004).

Bancroft *et al.* (2003) perfused medium continuously through the interconnected porous network in the scaffold, placed in a chamber as illustrated in Figure 2.11. The characteristics of the scaffold allowed optimum nutrient transport when the medium was forcefully pumped throughout the scaffold both internally and externally. Moreover,
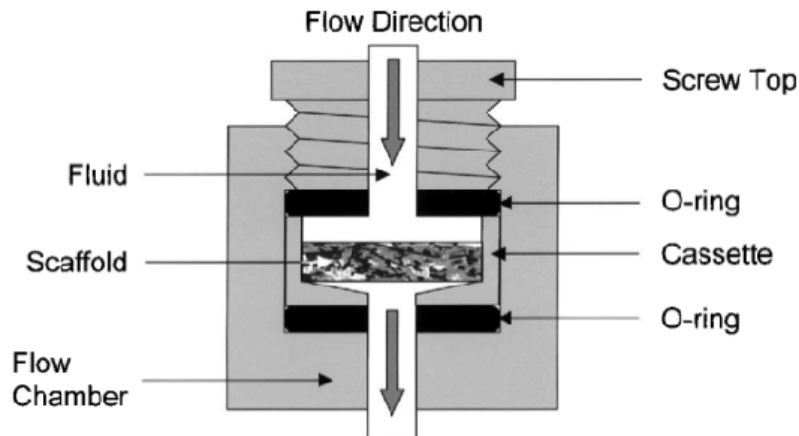
FIGURE 2.11: Diagram shows the flow chamber in the perfusion culture system designed by Bancroft *et al.* (2003). The scaffold, seeded with cells, is tightly secured in the cassette. The medium is pumped from the top of the chamber, flows through the scaffold and exits at the bottom of the chamber.

this design utilized two separate reservoirs (one to receive, and one to supply) interconnected to each other for ease of purging and medium replenishment (Bancroft *et al.* 2003). In a separate study, a perfusion bioreactor was used to produce chondrogenic- and osteogenic-cells from human MSCs (Meinel *et al.* 2004). Using a highly porous protein scaffold placed in 1.5mL chamber, the medium was perfused at a rate of 0.2mL/min. The flow and construct properties enabled the mimicking of some critical aspects of the native environment for bone tissue (Meinel *et al.* 2004). Zhao & Ma (2005) managed to integrate a cell-seeding procedure in the perfusion reactor. Forcing the cells in a suspension medium to perfuse into the matrix was an effective way to simplify and to maintain sterility in the protocol. The matrix was made from non-woven poly-ethylene terephthalate (PET) placed in a polycarbonate chamber. At 0.1mL/min flow rate and medium reservoir replaced every 5-8 days, the reactor was found to improve the structure, function and molecular properties of engineered cartilage as well as providing a physiochemical environment for tissue formation. The experiment yielded a high cell density of 4.22×10^7 cells/mL with uniform 3D cell growth (Zhao & Ma 2005). In a study by Oh *et al.* (2005) for culturing murine ESCs in a static perfusion culture system, an automated feeding system was utilized which yielded higher cell expansion compared to a normal static culture flask. The system was then adopted by Fong *et al.* (2005) in their research to expand human ESCs.

Even with the proven efficiency of this design, it was later deemed inadequate, as there was no computer- controlled features over culture condition (Cormier *et al.* 2006).

Reproducibility was also a significant issue as variability between cultures was expected. Furthermore, the application of a static culture perfusion system to culture stem cells to an adequate number of cells would only be relevant for a one patient treatment basis as the system is limited by the size of the chamber and scaffold (zur Nieden *et al.* 2007).

2.4.3 Rotating Wall bioreactor

The rotating wall vessel bioreactor, also known as the high aspect ratio vessel (HARV) and slow turning lateral vessel (STLV), is a bioreactor developed by the National Aeronautics and Space Administration (NASA). HARV and STLV, shown in Figure 2.12, were originally formulated to simulate microgravity conditions. This design is more complex, particularly when compared with the other bioreactor configurations. The space between the outer and inner cylinders is filled with cell culture medium. Oxygen is supplied to the culture medium through perfusion from the inner cylinder. Rotation around the horizontal axis of the vessel keeps the cells in suspension at low shear laminar flow. The vessels are available at various sizes depending on the scale of culture.
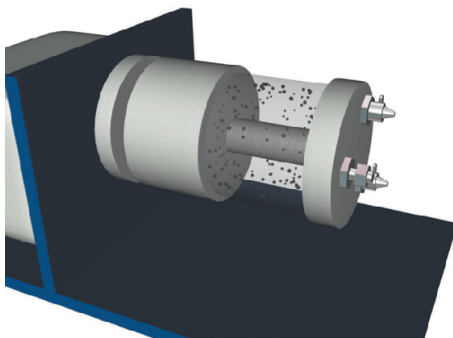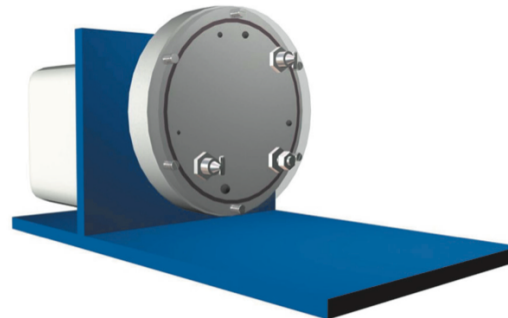
(a) Slow turning lateral vessel (STLV)   (b) High aspect ratio vessel (HARV)

FIGURE 2.12: Diagram of rotating wall bioreactors. The oxygen is delivered through perfusion from the inner cylinder. The cells are suspended in the medium as the vessel is continuously rotated (Reproduced from Gerecht-Nir *et al.* (2004)).

Early work using STLV was conducted in small intestine epithelium, hamster kidney and MSC culture experiments (Goodwin *et al.* 1993a,b). The group managed to obtain 3D growth of the cells with the aid of microcarriers, which provide a platform for the cell growth (Goodwin *et al.* 1993b). Later work by Freed & Vunjak-Novakovic

(1997) used STLV to culture chondrocytes as well as cardiomyocytes, seeded in construct, for 2 and 3 weeks, respectively. The low shear and efficient mass transfer in hydrodynamically-active environment in STLV enable the enhancement of chondrogenesis and chondrocyte maintenance. The bioreactor was also used in human ESC culture protocol which gave rise to EBs (Gerecht-Nir *et al.* 2004). STLV was able to yield 4 times- and 3 times- higher cell densities in 7 and 28 days, respectively, compared to traditional static culture procedure. This value translated to an overall 70 fold increase in cell number relative to the original number of cells seeded (Gerecht-Nir *et al.* 2004). The EBs obtained were more consistent in terms of size as the suspension of the cells inhibited large cell aggregation.

2.4.4   Spinner Flask bioreactor

The most widely used suspension bioreactor is the magnetic- or motor-driven impeller spinner flask. Microbial and mammalian cells have been extensively grown in stirred culture systems. The agitation or mixing rate can be easily controlled by changing the speed of the driving motor or the magnetic stirrer. The system offers a dynamic environment that is crucial in providing homogeneous nutrient distribution, which has been proven to improve cell production. Furthermore, spinner flasks are available in various sizes and impeller shapes depending on the culture size. Figure 2.13 shows examples of commercially-available spinner flasks.

Schroeder *et al.* (2005) and Zandstra *et al.* (2003) demonstrated the usability of suspension bioreactors for large-scale production of cardiomyocytes of murine ESCs. Using a 2L stirred bioreactor equipped with pitch-blade- turbine, Schroeder was able to yield high density cardiomyocytes. Recently, Lock & Tzanakakis (2009) were able to acquire endoderm progeny differentiation of human ESCs. Even though these studies did not maintain the pluripotency of the cells, it proved that suspension bioreactors are suitable and efficient for ESC differentiation. The development of suspension bioreactors for ESC expansion will advance the generation of relevant ESC and differentiated cells in a single bioprocess system.

Previous studies have demonstrated the efficiency of suspension bioreactors for undifferentiated mammalian stem cell expansion (Cabrita *et al.* 2003; Kallos *et al.* 2003; Mukhopadhyay *et al.* 2005; Cormier *et al.* 2006). Kallos *et al.* (2003) and Sen *et al.*

(a) Corning Proculture spinner flask   (b) Wheaton Magna-Flex spinner flask

Figure 2.13: Diagram shows the spinner flask bioreactor for stem cell culture manufactured by Corning Incorporated (USA) and Wheaton. A magnetic stirrer is required to drive the magnetic bar attached to the impeller.

(2001) achieved success in neural stem cell expansion, whereas recently, Zhang *et al.* (2009b) managed to expand fetal mesenchymal stem cells in their study. Hematopoietic stem cells were also deemed suitable to be expanded with this type of reactor (Cabrita *et al.* 2003; Mukhopadhyay *et al.* 2005).

The expansion of ESCs utilizing a suspension culture system was started by Fok & Zandstra in 2005 in murine ESCs culture protocol. In 2006, Cormier *et al.* developed a successful large-scale expansion of an undifferentiated murine ESCs procedure with a shorter doubling time. In this study, the cell agglomeration rate was closely controlled by agitation rate and inoculation density. The study was then extended and demonstrated that it is possible to obtain undifferentiated ESCs over extended periods of time (zur Nieden *et al.* 2007). Although positive progress and results have been acquired since the study done by Fok & Zandstra (2005), all of these research projects focused on the culture of murine ESCs in suspension bioreactors. Due to significant biological differences between murine and human ESCs, it is expected that human ESCs may behave differently in suspension culture reactors, and thus compromise the undifferentiated state and viability of human ESCs. It was demonstrated that human ESC differentiate excessively when cultured as aggregates compared to murine ESCs (Kehoe *et al.* 2010).

In early attempts to culture human ESCs in suspension bioreactors, the stem cells were cultured to form aggregates or EBs. Due to the nature of EBs, the pluripotentiality of the cells was compromised even though no specific cell lineage differentiation was obtained. EBs are also able to hinder efficient differentiation to specific lineage as it contains various types of cells (Kehoe *et al.* 2010).

Recently, a new technique, microcarrier suspension cell culture, has emerged that revolutionizes cell culture protocol. The microcarriers are microspheres made from either dextran, glass, polystyrene plastic, acrylamide or collagen, with typical size ranging between 125 to 250 μm in diameter (van Wezel 1967; Varani *et al.* 1983, 1985, 1986). There are several types of commercially available microcarriers including collagen-based (Cultispher, Percell), dextran-based (Cytodex, GE Healthcare) and polystyrene-based (SoloHill Engineering) microcariers. The surface can be coated with extracellular matrix proteins, recombinant proteins, enzymes as well as positive or negatively charged molecules. With different surface coating or treatment, cellular behaviour, morphology and proliferation can be manipulated (Varani *et al.* 1983, 1985, 1986). Moreover, one can also have control over their porosity, density, and optical properties to support different types of cells. Microcarriers are typically used in spinner flasks or rotating wall bioreactors to put them in suspension.

Microcarriers provide a platform for cells to grow in smaller clumps, thus reducing their tendency to grow as EBs and limiting the loss of pluripotency. Additionally, microcarriers provide high surface-to-volume ratio, accommodating more area for cell growth, thus improve the efficiency of cell culture procedure. The effectiveness of microcarrier use to culture mammalian (Hu *et al.* 1985; Kuriyama *et al.* 1992) and adult progenitor cells (Frauenschuh *et al.* 2007; Schop *et al.* 2008) in suspension bioreactors has been shown in previous studies. The idea was then adopted to culture ESCs. Earlier tests were conducted on murine ESCs on microporous collagen-coated dextran beads, glass microcarriers and macroporous gelatin-based beads (Fok & Zandstra 2005; Abranches *et al.* 2007; Fernandes *et al.* 2009). Positive cultivation of cells was acquired in all tests.

However, human ESCs are not as robust as murine ESCs or any progenitor cells. Additionally, any changes of conditions may cause the loss of pluripotency (Fok & Zandstra 2005; Oh & Choo 2006; Phillips *et al.* 2008).

Human ESCs have also attachment issue in microcarrier culture protocol. It is rela-

tively difficult to ensure physical attachment of human ESCs to microcarriers, especially microcarriers in suspension. Specially conditioned medium or coating was required to solve adherence problems. Phillips *et al.* (2008) showed that human ESCs are able to grow in stirred systems when the cells were attached to feeder-free polystyrene microcarriers with murine embryonic fibroblast (MEF) conditioned medium. Recently, Nie *et al.* (2009) managed to culture human ESCs with additional pre-treatment of dextran (Cytodex 3) beads by coating with Matrigel or MEF. The use of cellulose-based microcarriers, coated with Matrigel, was able to yield better expansion of human ESCs in suspension culture (Oh *et al.* 2009). However, the use of MEF and Matrigel introduced additional animal-derived compounds into the system and increased the overall cost. Dextran (Cytodex 3) beads were also used by Fernandes *et al.* (2009) in conjunction with denatured collagen as adherence has been proven to promote the expansion of human ESCs in a suspension system compared to conventional static culture. 23 - 30% human ESC clonal efficiency was acquired at 5×10^4 to 20×10^4 cells/mL seeding density with the use of Matrigel-coated beads as opposed to about 7% efficiency in static culture (Forsyth *et al.* 2006). There was minimal or absent lineage differentiation present in the cultured cells (Forsyth *et al.* 2006).

Successes on human ESCs culture and differentiation with microcarriers are due to several attributes. Microcarrier cultures provide high surface area-to-volume ratio and thus are able to accommodate higher cell densities as well as increase the efficiency of nutrient transfer. The flexibility of microcarrier types for culturing cells, either within macroporous or on compact microcarriers, is an important factor for human ESCs expansion or directed differentiation. Macroporous beads were demonstrated to direct murine ESCs to differentiate towards cardiomyocytes (Akasha *et al.* 2008), whereas compact microcarriers were able to preserve the self-renewal capacity of human ESCs due to direct exposure to the medium (Kehoe *et al.* 2010). Microcarriers also provide flexibility of cell growth area by varying the amount of microcarriers. Low local density may limit the loss of pluripotency in human ESCs culture observed in EBs (Kehoe *et al.* 2010). Control and monitoring over the microenvironment in suspension systems at high cell concentration are crucial for culture as well as directed differentiation purposes, especially after changes are made to the medium. Furthermore, the use of microcarriers has been expanded into the cryopreservation process to improve the recovery of undifferentiated cells in the large-scale culture development and to improve

the efficiency of current cryopreservation methods (Nie *et al.* 2009).

2.4.5 Challenges

Fluid flow is necessary to keep the culture medium homogeneously mixed to maintain nutrient supply and keep concentration of waste at low level around the cells. The mixing mechanism introduces shear stress in the system. Shear stress is important to prevent agglomeration of the cells which can cause cell death due to low nutrient, particularly oxygen, supply. In suspension bioreactors, shear provides lift to put the microcarriers in suspension. A certain amount of shear is needed for them to be suspended, as they tend to sink due to their denser nature compared to the fluid. On top of that, the introduction of shear stress can promote the differentiation process by providing stimulating shear environment that mimic the condition in the cells' natural environment (Yamamoto *et al.* 2005). However, a large amount of shear could be damaging to the cell membrane, thus altering the morphology of the cells.

Although the importance of mechanical stresses in cell culture has been reported often in the literature, the optimum stresses to promote cell growth remains unknown. Additionally, in most of the studies, details of the agitation rate, shear stress and aspect ratio were not emphasised. Studies detailing the properties of the flow in bioreactors, both qualitatively and quantitatively are very limited. The knowledge gained from flow characterisation studies could improve our understanding of shear role in cell culture, highlight the optimum stress for cell growth and define the design parameters that are essential to advance the bioreactor technology. With better understanding and refined design criteria, the efficiency of the cell culture process can be improved.

2.5 Fluid Stresses

As mentioned in the previous section, hydrodynamic forces played an important role in cell culture and biotechnology applications. Due to the significant knowledge gap between biologists and engineers, the effects of hydrodynamic forces in biological experiments were not well studied and understood. Minimum attention has been given in characterising the parameters until now. Thus, it is important to understand the concept of mechanical stresses from the basic fundamental principles for greater impact. In most biological flows, the flow profile and stresses involved have various magnitudes and in three-dimensional profiles. This section focuses on the fundamental stress theory of fluid elements in three-dimensional space. The principles of stress are the vital factor in understanding the mechanics of culture protocols, a topic which previously has not been appreciated by most biologists. It is hoped that this theory is able to close the knowledge gap between biological and mechanical scientists, as well as enhancing an appreciation towards the importance of characterising the mechanical parameters.

Stress tensor theory was developed by the French mathematician, Augustin Louis Cauchy, in 1829. The theory was derived from continuum mechanics, assuming the kinematic behaviour of an infinitesimal fluid element can be modelled as a continuous mass. In a three-dimensional space, arbitrarily given as x, y and z components, there are 3 stress components acting at each surface. In each surface, one component acts perpendicular to the surface, known as normal stress, and two components act along the surface, known as shear stress. For example, S_x has normal stress, σ_{xx} acting along the axis direction and shear stresses, σ_{xy} and σ_{xz} acting along the surface plane. The stress tensor can be represented in matrix form as follows:

$$T = \sigma_{ij} = \begin{bmatrix} \sigma_{xx} & \sigma_{xy} & \sigma_{xz} \\ \sigma_{yx} & \sigma_{yy} & \sigma_{yz} \\ \sigma_{zx} & \sigma_{zy} & \sigma_{zz} \end{bmatrix} \tag{2.1}$$

In general, stress can be represented as σ_{ij}. The first index, i, denotes the surface at which the stress acts whereas the second index, j, denotes the direction of the stress. The diagonal components in the matrix are the normal stress acting normal to each surface. As the matrix is symmetric, although there are 6 components of shear stress, there are only 3 independent magnitudes.

The normal stresses, σ_{xx}, σ_{yy} and σ_{zz}, are caused by dynamic as well as hydrostatic

pressure acting on the fluid elements. On the other hand, shear stress for Newtonian fluids can be defined as:

$$\sigma_{ij} = \tau_{ij} = \mu \left(\frac{\partial \mathbf{V_i}}{\partial \mathbf{X_j}} + \frac{\partial \mathbf{V_j}}{\partial \mathbf{X_i}} \right) \tag{2.2}$$

where $\mathbf{V}$ are velocity components, $\mathbf{X}$ is the position of the velocity component and μ is the dynamic viscosity of the fluid. The term $\left(\frac{\partial \mathbf{V_i}}{\partial \mathbf{X_j}} \right)$ is also known as the velocity gradient whereas the term $\left(\frac{\partial \mathbf{V_i}}{\partial \mathbf{X_j}} + \frac{\partial \mathbf{V_j}}{\partial \mathbf{X_i}} \right)$ can also be cited as shearing strain rate, commonly denoted as $\dot{\gamma}$. Arbitrarily, in Cartesian coordinates, the equation can be rewritten as:

$$\sigma_{xy} = \tau_{xy} = \mu \left(\frac{\partial V_x}{\partial y} + \frac{\partial V_y}{\partial x} \right) \tag{2.3}$$

$$\sigma_{xz} = \tau_{xz} = \mu \left(\frac{\partial V_x}{\partial z} + \frac{\partial V_z}{\partial x} \right) \tag{2.4}$$

$$\sigma_{yz} = \tau_{yz} = \mu \left(\frac{\partial V_z}{\partial y} + \frac{\partial V_y}{\partial z} \right) \tag{2.5}$$

In order to calculate the shear stresses, a reliable measurement technique to characterise the velocity field is required. As the flow involves a biological sample, sterility is the utmost priority in the measurement procedure. Many velocity measurement methods have been developed over the years through research and experimentation. However, the number measurement techniques is still growing to image various applications in more accurate, efficient and reliable ways. The next section highlights the current progress in measurement technique research.

2.6   Imaging Techniques

Despite the progress in stem cell research in recent years, technical limitations in scaling-up stem cell cultures represent a challenge in stem cell applications. A controlled, reproducible culture system is needed to expand the cells to adequate quantities for successful clinical implementation of stem cells. Cells are commonly grown in a spinner flask bioreactor. This provides a homogeneous culture environment, thus reducing culture variability. Hydrodynamic shear stress is a significant parameter to be considered in a suspension culture bioreactor. High shear could damage the cell membrane whereas low shear could cause agglomeration, which reduces the culture efficiency. In a suspension bioreactor, hydrodynamic shear stress is varied by the agitation rate and the type of impeller. In order to characterise this parameter, a non-intrusive measurement technique is highly desirable to maintain the sterility of the sample. This section highlights several imaging techniques, that include both qualitative and quantitative methods used in fluid mechanics research.

2.6.1   Dye/ Smoke Visualisation

FIGURE 2.14: Dye visualisation for flow in a closed vessel.

Dye/ smoke visualisation is a classical technique in characterising a flow. It is widely used in various fluid mechanics experiment due to its quick and easy preparation. Smoke is normally used for air or gas flow whereas dye is used for liquid flow. A small amount of dye/smoke is introduced upstream of a flow. The dye will then follow the flow, leaving a trail along the streamline, as demonstrated in Figure 2.14. Although

this technique will not be able to provide quantitative results, it qualitatively provides a quick feedback of the experiments. Due to the nature of this visualisation technique which introduces a foreign fluid into the flow, this technique is unsuitable for online cell imaging. However, it is a useful technique in visualising and unveiling the flow structure in a bioreactor.

2.6.2   Particle Image Velocimetry

Velocimetry techniques are widely used for various applications. In particular, Particle Image Velocimetry (PIV) is one of the techniques used for characterising flow profiles. Particle Image Velocimetry is a useful and well-established optical-based measurement technique to observe and study fluid flows that has been gaining popularity over the last two decades (Adrian 2005). Tracer particles are introduced into the flow, and the region of interest is illuminated using a laser source (typically a pulsed Nd:YAG laser). A very bright light source is required because the method relies on side scatter of light caused by the particles. Assuming that the particles faithfully follow the flow, consecutive images of the illuminated region are captured using a high-speed digital camera, placed in the paraxial position. The images are discretised into sub-regions and a cross-correlation analysis is performed in each sub-region (Willert & Gharib 1991). The cross-correlation is representative of the probability distribution for the displacement of the underlying particle images within the sub-region, and the maximum signal is the most probable displacement between image frames. Since the time between image frames is known, the velocity of the flow captured in the region can be determined. Processing each of the discretised sub-regions results in a detailed velocity field of the flow. In many cases, it is sufficient to collect these data from a single plane in the flow. In this traditional form, the method provides no out-of-plane flow information. The principle of PIV is summarised in Figure 2.15.

It is important to note that PIV is a non-intrusive velocity measurement tool because it does not use any probe such as pressure tube or hot wires (Raffel *et al.* 2007). All the data required in PIV are obtained optically by using a high-speed camera. Therefore, there is no direct contact between the flow and the probes used in assessing the flow. As the flow is not disturbed, the application of PIV is able to provide high accuracy data in analysing high speed flows with shocks or in boundary areas close to the wall,
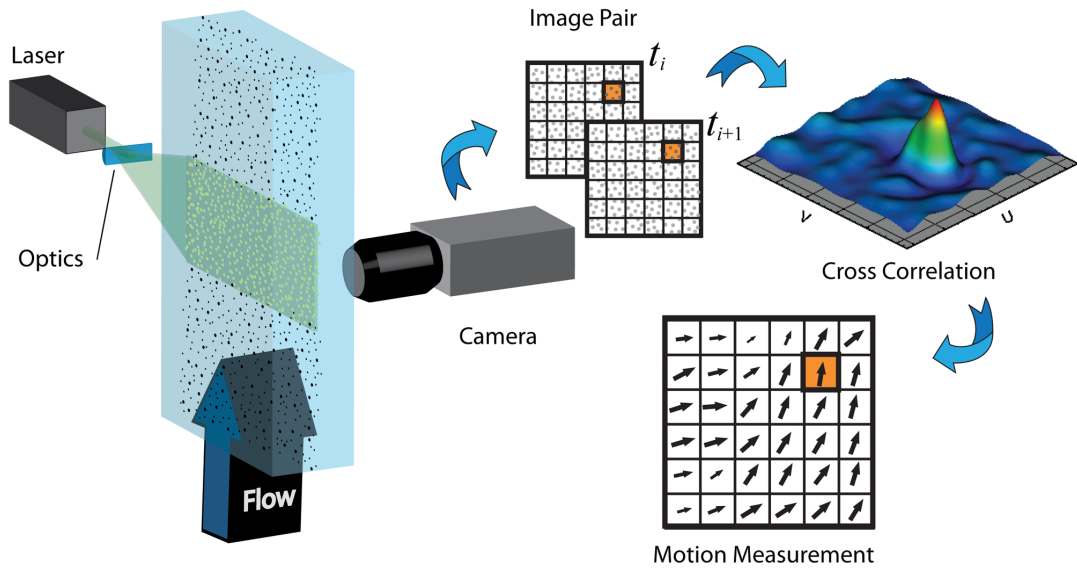
FIGURE 2.15: Principle of 2D PIV.

where the flow may be disrupted due to the presence of probes (Raffel *et al.* 2007).

The long-term development of two-dimensional PIV (2D PIV) has built a strong base in various principles that aid 3D-PIV development. The extended measurement of fluid flow velocity using 3D-PIV techniques provides in-depth understanding by uncovering the complete topology of unsteady flow. Scanning multi-plane PIV, stereoscopic PIV and tomographic PIV are introduced to characterise 3D flow.

2.6.2.1 Scanning Multi-plane PIV

Scanning multi-plane PIV uses multiple light sheets, parallel to each other, to characterise the 3-dimensional flow. The flow is recorded by multiple cameras and the analysis is conducted independently before combining the sets of data to simulate the original flow. As a laser sheet is the main light source, only one plane of the velocity field could be measured at a time. In order to acquire full volumetric flow profile, the position of the light sheet has to be adjusted throughout the volume as shown in Figure 2.16. This method is not capable of generating exact instantaneous data in 3D flow measurement due to the fact that the scanning procedure requires the interrogated flow to be stationary in time (Ooms *et al.* 2008; Fouras *et al.* 2007b). Additionally, the dynamics of the flow and depth of field are restricted by the time consumed for successive scans and focus requirements, respectively (Arroyo & Hinsch 2008).
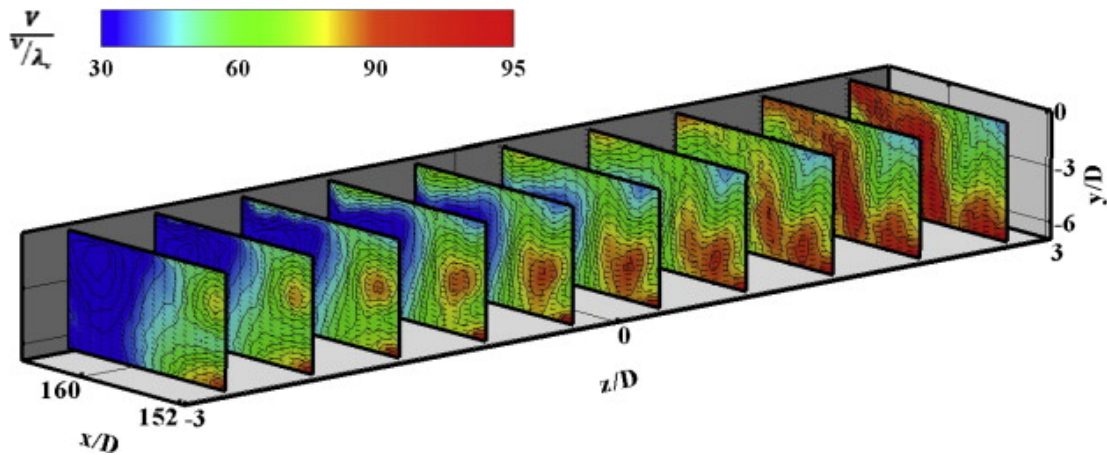
FIGURE 2.16: Diagram shows the example of scanning PIV results to characterise the turbulent structure in a jet. 2D PIV analyses are conducted at varying depth to characterise the volume (Cheng *et al.* 2011).

2.6.2.2 Stereoscopic PIV

Stereoscopic PIV, also known as stereo-PIV, utilises multiple cameras, placed at a specific angle of the light sheet. Due to the camera sensor not being perpendicular to the light sheet, the images captured are skewed. Mathematical formulations derived from calibration process are used to recalibrate the distorted images (Willert 1997; Fouras *et al.* 2008). This setup allows the measurement of the out-of-plane displacement component, providing 2D- 3-component (2D3C) characterisation of the flow (Willert 1997). However, the depth information is restricted by the small thickness of the light sheet. Due to such limitation, stereo-PIV is highly suitable for axisymmetric flow where a small section of the flow is similar along the axis of rotation as proven by Dusting *et al.* (2006) using a setup depicted in Figure 2.17. Using this technique, Dusting *et al.* (2006) mapped the velocity profile of a base-driven closed cylinder.

2.6.2.3 Tomographic PIV

Tomographic PIV was developed as an improvement to stereo-PIV. Kim & Chung (2004) were the first to introduce the term tomographic PIV in analysing the flow in a nasal cavity. The term *tomography* in this article refers to the cross-sectioning of the object. The flow in the nasal cavity was characterised using planar PIV at different locations. Although the article provided 3D velocity field distribution, the current tomographic PIV technique is quite different and refers to the reconstruction method.
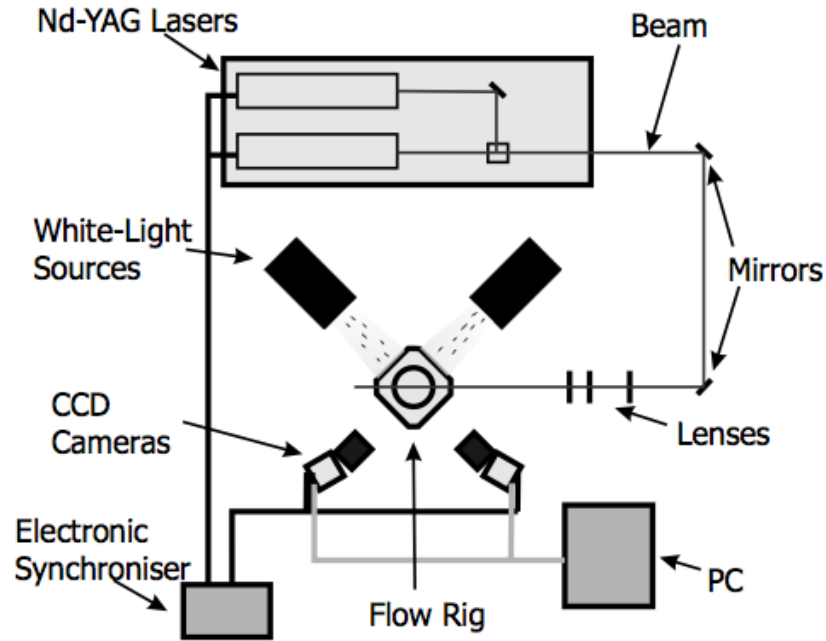
FIGURE 2.17: Schematic diagram of bioreactor visualisation experiment utilising stereoscopic PIV method by Dusting *et al.* (2006).

Elsinga *et al.* (2006) pioneered tomographic PIV, also known as tomo-PIV, by using a thicker light sheet and four cameras, as shown in Figure 2.18. By having the light sheet thickness 0.25 of the in-plane field of view and placing the cameras imaging the region-of-interest from different angles, it allows a full 3D3C measurement to be made. Larger focal depth is required to ensure the flow is in-focus throughout the depth. Similar to stereo-PIV, this technique requires a calibration procedure by placing a plate at several depths in order to correct the distorted images. Additionally, before PIV analysis is conducted, the volume is reconstructed using a multiplicative algebraic reconstruction technique (MART) and the 3D intensity distribution is recovered (Elsinga *et al.* 2006). This technique is superior to stereo-PIV due to the extra depth information captured in the measurement. Since the introduction of this technique, more research groups have been involved in the progression of this area such as Schröder *et al.* (2008) and Buchanan *et al.* (2011). The main motivation in the development of tomo-PIV is the need to characterise flow structure in turbulent flow (Elsinga *et al.* 2007; Worth & Nickels 2008; Atkinson *et al.* 2011). In 2010, Novara *et al.* was able to simplify the setup and reduce the number of cameras used to two or three cameras, while improving the measurement precision by integrating motion tracking enhancement (MTE), which

improved the reconstruction of individual intensity field.
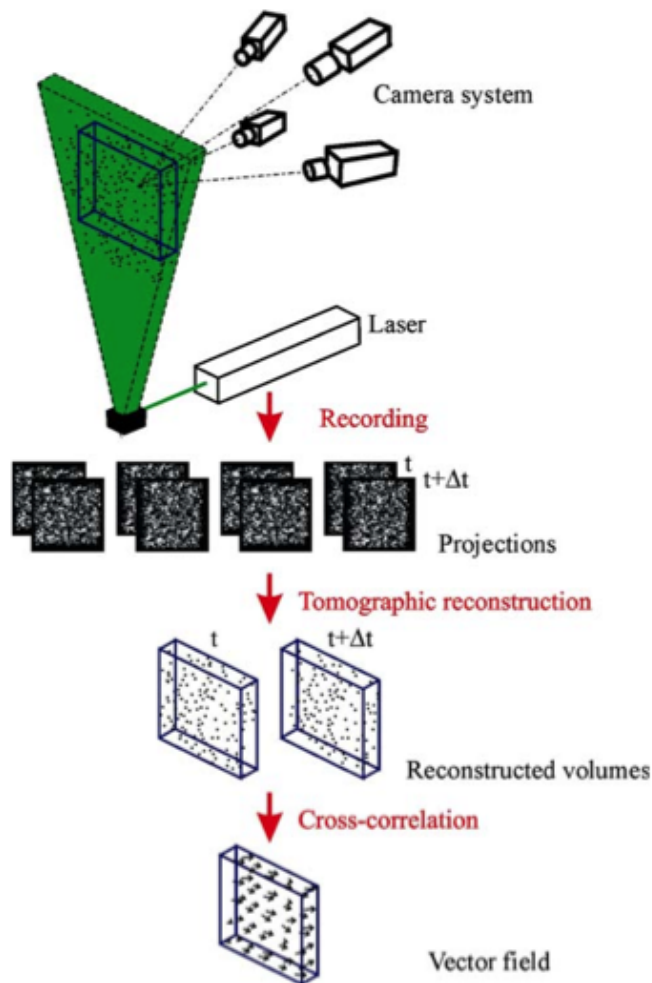
FIGURE 2.18: Schematic diagram of tomographic-PIV principle. Four cameras arranged at specific angles are used to image the illumination of tracer particles at a distinct point. The recorded images are analysed using tomographic reconstruction and cross-correlation to obtain vector field of the flow (Elsinga *et al.* 2006)

Recently, by rotating the sample and changing the light source to synchrotron X-ray beam, Dubsky *et al.* (2010) developed simpler method of 3D imaging. Computed tomography (CT) reconstruction was implemented to reconstruct an object in 3D space from 2D projections taken from different angles, using the Fourier back-projection method (Kak & Slaney 1988). To minimize the error, the estimated flow model and measured cross-correlation for every interrogation window were compared in iteration. This technique eliminates the need of multiple cameras and calibration process, thus providing significant advantage over previous approach.

This technique allows the measurement of velocity field of a flow. With the velocity

field, velocity gradients and shear stress can be calculated. Knowing this parameter, it would provide crucial information in cell culture and bioreactor design. On top of that, it could promote more inter-disciplinary research between cell culturists and engineers.

2.7   Summary and Research Motivations

Stem cell and tissue cultures have attracted much research interest, driven by the need to provide therapies to various diseases including congenital and degenerative disorders. Bioreactors have been utilised to promote cell proliferation and obtain sufficient number of cells within the required culture period. There have been many studies related to cell and tissue culture protocol using various types of bioreactors. In most cases, a dynamic bioreactor system is able to produce better cell counts compared to conventional static culture protocols. However, static culture protocols are still being frequently used as a benchmark of the process performance. Despite the fact that a dynamic bioreactor system produces better yields than static culture, there is limited literature related to the desired design requirements for optimum culture efficiency. Thus, there has not been much progress in dynamic bioreactor optimisation process.

There are several factors that cause the impediment of dynamic culture optimisation development. The factors are presented below.

1. The wide range of cell types.

   Each cell type requires a specific culture condition. Due to the variety of cell phenotypes, along with other variables such as the chemicals used, types of bioreactors and culture speed, it is a challenge to find the starting ground in defining the culture requirement for each cell type. Furthermore, depending on the phase of the culture, the conditions to maintain the potency of specific cells and to induce cell differentiation to particular lineages will be very different to each other.

2. The lack of a systematic approach in the culturing process.

   Most cell studies have very limited variable space with significant emphasis on chemical inductions rather than mechanical parameters, such as agitation speed, that would define the design criteria. Without detailed explanation of the bioreactor setup and reasoning to the speeds used, it is difficult to eliminate the parameter region that produces inefficient culture results and also to pinpoint the positive parameter region. Although the development of novel bioreactors may have produced positive results, the long-term improvement of dynamic culture could be impeded without knowing the appropriate flow conditions and mechanical properties that support the growth of the cells.

3. The dynamic culture performance is measured relative to static culture.

The performance in cell studies is often measured relative to static culture. With dynamic culture systems proven to have better performance than static systems, emphasis should be given to comparison between dynamic cultures. It is necessary to have a standard dynamic culture procedure as a baseline performance standard. Comparison between various dynamic culture systems will enable the required parameters to be critically defined and more effort focused in enhancing the efficiency of dynamic system.

4. The lack of design and fluid mechanics knowledge in culture process.
Cell culture is a research area that has been largely dominated by biologists. The complex flow structures in the dynamic culture cannot be easily understood without prior knowledge in fluid mechanics. Due to the lack of collaboration between biologists and fluid dynamicists, how certain flow, stress conditions and design modifications alter the culture performance is an area that has not been explored by many. The complexity and sensitivity in culture protocols, which may cause some variance in results, makes it difficult to determine the optimum protocol.

Stem cell research has opened a wide range of potential applications that includes cell therapy and tissue engraftment treatments, as well as provided contributions to the advancement of genetic research. Although the research subject has attracted much interest in recent years, there are very few studies in characterising the required mechanical parameters and their distributions, specifically in terms of stress, despite frequent acknowledgement of their importance in the dynamic culturing process. With increasing applications and possibilities yet to be discovered, design parameter characterisation is necessary to optimise the culture process and to contribute to the innovation of current bioreactor technology. By defining the required environment for cell growth, a new generation of bioreactors can be thoroughly developed from ground up to meet design requirements, on top of minimising the possible cause of non-uniformity in the cell yield. The knowledge gained from this research will bridge the knowledge gap, specifically in the area of mechanical forces induced to the cell within the dynamic culture system.

2.8   Research Aims

This research is driven by the need to fill the knowledge gap existing in bioreactor design. Due to the immense research area that is in bioreactor technology, the bioreactor with which the analyses are conducted has to be carefully chosen so as to make significant impact to reactor design. This work focuses on a novel rotating lid bioreactor and a conventional spinner flask bioreactor, which has been extensively used in cell studies.

The primary emphasis of the study will be the mechanics of the flow in spinner flask, focusing on the fluid mechanics perspective rather than the conventional biological perspective. For the purpose of this study, the chemical and thermodynamic properties, oxygen diffusion and nutrient transport are not the primary significance. To illustrate the fundamental flow and biomechanics for cell growth, the experimental fluid dynamics is the principal approach in the study. Velocity profiles, stress and vorticity are the focal parameters in understanding how these parameters affect the mixing and culturing performance. Additionally, non-dimensional parameters, such as Reynolds number, can generalise the geometry of the reactor and ensure the wide practicality of the outcome of the study. By linking the generalised parameter to cell response, more refined and new types of bioreactors can be established. On top of that, due to the growing interest in microcarrier culture, further prominence is given to see how the flow affects the microcarriers. To achieve the primary aim, the work is divided into the following objectives:

1. Investigation of flow characteristics in rotating lid bioreactor.

   - To qualitatively visualise the flow in the novel rotating lid bioreactor

   - To investigate the effect of introducing denser and lighter materials, which simulate the microcarriers in the system

2. Flow characterisation in conventional spinner flask.

   - To quantify the velocity profile, shear stress and vorticity in a conventional spinner flask bioreactor

   - To determine the effect of impeller position and rotational speed on the mechanical parameters

   - To create a fluid dynamics datasheet for many published cell studies that used similar bioreactors

3. Investigation of the biomechanics parameter for induced pluripotent stem cell culture.

   - To examine the effect of fluid mixing on the microcarriers

   - To determine the optimal biomechanics environment for induced pluripotent stem cell growth

4. Towards 3-dimensional and 3-component flow measurement technique.

   - To propose a volumetric imaging technique to characterise 3D velocity vectors in biological flows

   - To investigate its feasibility in quantifying full field flow in spinner flask bioreactors

Chapter 3

Flow Profile in A Rotating Lid Disk Bioreactor

THIS chapter discusses the analysis of flow in a high aspect ratio rotating lid bioreactor for cell application. Many numerical and experimental studies have been conducted based on the rotating bottom cylinder model due to its confinement and its simple boundary condition. They confirmed the stability diagram established by Escudier (1984) and highlighted the role of negative azimuthal vorticity. However, the rotating lid cylinder has several advantages for bioreactor purposes over the rotating bottom bioreactor. By having a driving disk at the top to promote mixing and recirculation, the manufacturing method can be simplified. Sealant can be eliminated, thus ensuring the sterility of the system as well as ease of maintaining the cleanliness of the bioreactor. Additionally, cell culturists may readily transport the product along with the container after cell culture procedure, whereas for a bottom-driven disk bioreactor, the cells with the culture medium have to be transferred into another container before the next test. Due to these advantages, the rotating lid bioreactor is chosen for analysis.

Previously, a spinning lid disk bioreactor was used to grow colonies of EL-4 mouse lymphoma cell *in vitro* by Thouas *et al.* (2007). In a stirred disk bioreactor, circular and disc-like cells were achieved with average diameter of 800μm compared to 200μm in an unstirred environment. Furthermore, it was also found that the cell growth was dependent on the agitation rate whereby the highest growth rate was achieved at Re = 600. Overall, the bioreactor was shown to be able to support the growth of cancer cell *in vitro*, on top of producing a comparable result to standard culture (Thouas *et al.* 2007). With increasing popularity of microcarriers use to promote culture efficiency,

this study is aimed to visualise the effect of microcarriers in the spinning lid bioreactor.

An article describing the microcarrier behaviour in a spinning lid bioreactor is presented. In this study, the flow in the rotating lid bioreactor is characterised using dye visualisation to ensure reliability of the setup. A new parameter, a ratio of density difference to density of water, $\Delta\rho/\rho_0 = (\rho - \rho_0)/\rho_0$, is introduced to characterise the dye density in the experiment. Then, the relative density is varied to simulate the effects of microcarrier on the flow inside the bioreactor between -0.9 $\times$ 10^{-3} and 0.2 $\times$ 10^{-3}. Characterisation plots were created for various Reynolds numbers. The article concludes by discussing the application of a rotating lid container and its potential use for alternative applications outside of cell culture.

This study provides invaluable information and a great insight for closing the gap between engineers and biologists due to the simplicity of the dye visualisation method.

3.1 Article I: Experimental Control of Vortex Breakdown by Density Effects

The following manuscript was published in 2011 in *Physics of Fluids*. This work was co-authored by P. Meunier, A. Fouras, and K. Hourigan. The article reproduced in this thesis is directly taken from the published version without alteration.

Declaration

Monash University

Declaration for Thesis Section 3.1

Declaration by candidate

In the case of Section 3.1, the nature and extent of my contribution to the work was the following:

Nature of contribution	Extent of contribution (%)
Conceived, designed and performed experiments. Analysed the data and wrote the manuscript.	75%

The following co-authors contributed to the work. If co-authors are students at Monash University, the extent of their contribution in percentage terms must be stated:

Name	Nature of contribution	Extent of contribution (%) for student co-authors only
P. Meunier	Treatment of experimental data and co-wrote the manuscript	NA
A. Fouras *	Revised manuscript	NA
K. Hourigan	Revised manuscript	NA

The undersigned hereby certify that the above declaration correctly reflects the nature and extent of the candidate's and co-authors' contributions to this work*.

Candidate's Signature		Date 01 AUG 2014

Main Supervisor's Signature		Date 01 AUG 2014

Experimental control of vortex breakdown by density effects

Mohd-Zulhilmi Paiz Ismadi,[1,2,a]) Patrice Meunier,[1,3] Andreas Fouras,[1]
and Kerry Hourigan[1,2]
[1]*Division of Biological Engineering, Monash University, Melbourne, Victoria 3800, Australia*
[2]*Department of Mechanical and Aerospace Engineering, Monash University, Melbourne,
Victoria 3800, Australia*
[3]*Institut de Recherche sur les Phénomenes Hors Equilibre, Aix-Marseille University, 13384 Marseille,
France*

The vortex breakdown inside a cylinder with a rotating top lid is controlled experimentally by injecting at the bottom a fluid with a small density difference. The density difference is obtained by mixing a heavy dye or alcohol with water in order to create a jet denser or lighter than water. The injection of a heavy fluid creates a buoyancy force downward, which counteracts the meridional recirculation in the cylinder and thus enhances the formation of a vortex breakdown bubble. The stability diagram shows that even a very small density difference of 0.02% is able to decrease by a factor of 2 the critical Reynolds number of appearance of the breakdown. On the other hand, the injection of a lighter fluid does not destroy the vortex breakdown. However, for large enough density differences (larger than 0.03%), the lighter fluid is able to pierce through the bubble and leads to a new structure of the vortex breakdown. Finally, a parallel is drawn between a light jet and a vortex ring generated at the bottom of the cylinder: strong vortex rings are able to pierce through the bubble, whereas weak vortex rings are simply advected around the bubble. © *2011 American Institute of Physics*. [doi:10.1063/1.3560386]

I. INTRODUCTION

Vortex breakdown usually refers to a recirculating bubble that appears on a swirling jet past a stagnation point. The goal of this paper is to analyze the sensitivity of this flow to a small injection of dense or light fluid in the core of the vertical swirling jet.

Vortex breakdown is a surprising and practically important phenomenon which can be observed in many different swirling flows. It appears as a rapid expansion of a thin vortex into a much broader vortex with an axisymmetric or spiralling recirculating pattern.[1] The phenomenon is of interest for various disciplines due to its occurrence in geophysical as well as in industrial swirling flows. Vortex breakdown was first observed over the delta wings of aircraft[2–4] where it creates a sudden drop in the lift and an increase in the drag, possibly leading to a loss of aircraft control.[5] By contrast, it can be advantageous in geophysical applications since it largely decreases the swirl of the vortex and thus limits the destructive power of tornadoes.[6,7] It is also beneficial in combustion devices since the presence of vortex breakdown can be used as a flame holder.[8] Additionally, vortex breakdown is of interest in bioengineering applications for the growth of cells inside bioreactors. New bioreactors made of cylinders with a rotating top disk have been proposed recently.[9,10] They create a smooth and efficient mixing inside the cylinder which brings more oxygen to the cells and thus accelerate their growth. On one hand, the presence of vortex breakdown might prevent the mixing of oxygen in the whole cylinder and thus decrease the efficiency of these bioreactors. On the

other hand, the vortex breakdown bubble could be used to localize the cells in a region far from the boundaries in order to prevent their adhesion to the wall and to reduce the destructive shear that they experience at the boundaries.

Vortex breakdown is also of great interest on a fundamental level. Despite a large amount of research in the past five decades, the destabilizing mechanism is not well understood. Early experiments have focused on flows in a tube, where the swirl is created by adjustable vanes located upstream of the tube.[11–13] They have shown that the bubble can be axisymmetric, helical, or contain a double helix, depending on the swirl parameter and the Reynolds number, with a strong hysteresis between these three regimes.

Theoretically, the early explanation of vortex breakdown as a helical instability[14] has been dismissed due to the presence of axisymmetric bubbles. Since these axisymmetric bubbles are observed for flows with no axisymmetric instability, another mechanism has to be found. Benjamin[15] explained vortex breakdown as a transition from a supercritical flow (without waves propagating upstream) to a subcritical flow (with waves propagating upstream) analogous to a hydraulic jump. This theory validates the criterion proposed by Squire[16] on the swirl parameter and has been recently extended to pipes with finite sizes by Wang and Rusak.[17]

Vortex breakdown has later been observed in a more simple configuration consisting of a closed cylinder with a rotating bottom.[18,19] This confined swirling flow has the great advantage of having very weak disturbances and well-defined boundary conditions. However, this flow does not have a constant swirl parameter in the volume of the cylinder and Benjamin's theoretical criterion is thus harder to apply.

23, 034104-1

The stability properties of this flow have been measured accurately by Escudier:[20] vortex breakdown appears in a finite band of the Reynolds number if the height to radius ratio H/R of the cylinder is larger than 1.5. Spohn *et al.*[21] later showed that this behavior is quantitatively but not qualitatively modified by the presence of a free surface.

Many numerical studies[22–24] have focused on the vortex breakdown inside a cylinder with a rotating bottom due to its confinement and its simple boundary conditions. They confirmed the stability diagram established by Escudier[20] and highlighted the role of negative azimuthal vorticity.[25] Furthermore, simulations confirmed that breakdown bubbles can become unsteady and asymmetric[26] as had been found experimentally.

Despite its interest for applications, there have been very few attempts to control vortex breakdown. Numerically, vortex breakdown was controlled by the corotation of the end walls[27,28] or by using the theory of optimal control in a closed loop system.[29] It has also been controlled numerically by applying a small temperature difference[30] between the bottom and the top disk, which leads to small density differences sufficient to stabilize or destabilize the vortex breakdown by gravitational and centrifugal convection. More recently, vortex breakdown was controlled by the rotation of a small rod,[31] a small lid,[32] or a small disk[33] opposite to the driving disk. Finally, it was shown that the use of a conical lid strongly influences the stability of vortex breakdown.[34]

Experimentally, there are few publications of control of vortex breakdown. One idea tested was the rotating of a small rod at the center of the cylinder.[35] This intrusive technique was replaced by a nonintrusive one where a small disk is rotated at the other end of the cylinder.[36] The authors reached a variation of 15% of the critical Reynolds number when the small disk is rotated twice faster than the driving disk. Other examples of control are axial pulsing[37] and lid tilting.[38]

In this paper, we apply experimentally the idea of Herrada and Shtern[30] to control the vortex breakdown by density effects. We use a slightly different setup since the density is introduced by injecting a fluid with a different density than the fluid inside the cylinder at the center of the motionless disk. We will show that this jet has a strong effect on vortex breakdown even for small injection rates and small density differences. After describing the experimental setup in Sec. II, we recover the literature results for a neutrally buoyant jet in Sec. III. We then describe the effect of a dense and a light jet in Secs. IV and V, respectively. Finally, we draw a parallel between the injection of a lighter jet and the generation of a vortex ring impacting the vortex breakdown in Sec. VI. Conclusions follow in Sec. VII.

II. EXPERIMENTAL SETUP AND METHODS

We study the flow inside a circular cylinder with a rotating top disk. Figure 1 shows the experimental setup, consisting of a cylindrical Plexiglas container with internal radius $R = 32.5$ mm, filled with water. This inner cylinder is placed inside an octagonal housing, which is also filled with water and which has flat exterior faces to prevent the refraction
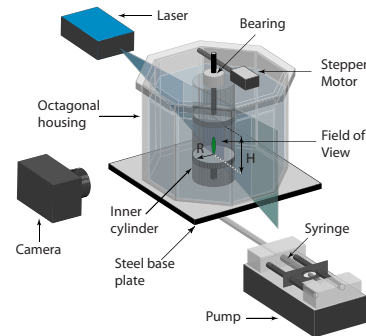

FIG. 1. (Color online) Diagram of the experimental setup used for the vortex breakdown inside the inner cylinder with a rotating top disk and with injection of dye at the bottom.

deformation of the images during the acquisition process. The whole setup is mounted on a steel base plate which is secured to a precision optical table to eliminate mechanical vibrations.

The flow under study is located inside the inner cylinder between two disks separated by a height H. For all the experimental cases, the aspect ratio H/R is maintained constant at 1.98, measured to an accuracy of 0.02%. In most previous experimental studies,[20,39] the bottom disk is rotated in order to drive the flow. Here, the bottom disk is fixed instead and the top disk is rotated at an angular velocity Ω varying from 0.6 to 3.6 rad/s. This top disk is driven by a stepper motor (Sanyo Denki America, Inc., USA) run through a motion controller (National Instruments Australia, North Ryde, NSW, Australia), enabling 5.12×10^4 steps per revolution. The velocity of the motor is further reduced by a factor 30 through the use of a worm wheel gear, which allows a smooth rotation of the disk at all speeds.

The flow is visualized by injecting some dye mixture at the center of the bottom disk through a 0.5 mm hole. The disturbance created by the hole itself is negligible. The hole is connected by a small plastic tube to a 1 ml syringe, filled with dye mixture, and driven by a syringe pump (Harvard Apparatus, Massachusetts, USA) at a volumic rate Q varying between 0.001 and 0.2 ml/min. In most experiments, the injection rate is equal to 0.02 ml/min, which gives a velocity of the jet equal to 1.7 mm/s, i.e., much smaller than the velocity of the disk periphery varying from 20 to 120 mm/s. Moreover, the characteristic time of variation of the mean density in the cylinder $(\tau = \pi R^2 H / Q)$ is on the order of 10^4 min, which is much larger than the duration of the experiments, which is on the order of a few minutes. This means that the mean density inside the cylinder can be assumed to be constant.

The fluorescein dye is illuminated by a blue laser (CVI Melles Griot, New Mexico, USA) so that it fluoresces very brightly with a green color. As illustrated in Fig. 1, the laser is expanded into a vertical sheet which is carefully placed at the center of the inner cylinder to visualize the flow pattern in a longitudinal section. A digital camera, Nikon D2X fitted
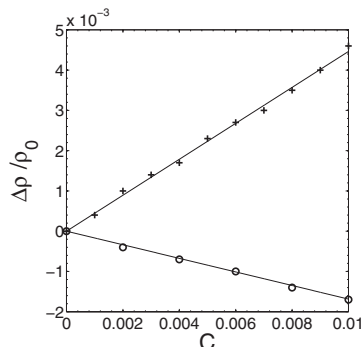
FIG. 2. Relative density difference $\Delta\rho/\rho_0=(\rho-\rho_0)/\rho_0$ of a fluorescein mixture (+) and of an alcoholic mixture (○) compared to water as a function of the mass concentration. Solid lines correspond to linear fit shown in Eqs. (1) and (2).

with Nikkor 17–55 mm f2.8G lens (Nikon Corporations, Japan) is used to capture the images of the dye during the experiments.

The temperature of the water is measured with an accuracy of 0.5 °C, which gives an accuracy of 1% on the viscosity. The average temperature of the room is fairly constant (less than 1°/day) such that thermal gradients can be ignored due to the small working fluid volume inside the inner cylinder (213.5 ml) and good forced mixing effect in the working area.

To study the effect of the density of the dye on the vortex breakdown, we have changed the density by varying the concentration of the dye (for heavier dye) and by adding alcohol (for lighter dye) in the mixture. A specific amount (usually 0.2 g) of fluorescein powder ($C_{20}H_{12}O_5$) is weighed using a precision balance (CP153, Sartorius Mechatronics, Australia) (with an accuracy of 0.001 g) and diluted in 100 ml of water, then diluted again to reach the desired mass concentration C, i.e., the weight of fluorescein divided by the weight of water. A similar protocol is conducted for the alcohol mixture except that a specific volume of 99.99% pure liquid ethanol is added into 100 ml of water and then diluted to the desired mass concentration. Although both mixtures are kept in closed flasks, a new mixture of ethanol is used for each experiment to eliminate the possibility of density change as a consequence of evaporation.

The density ρ of the dye and alcohol mixtures can be measured for large enough concentrations C using a density meter (Densito 30PX, Mettler Toledo, USA) accurate up to 0.0001 g/cm^3. The relative density difference $\Delta\rho/\rho_0=(\rho-\rho_0)/\rho_0$ with respect to the density of water ρ_0 is presented in Fig. 2 as a function of the concentration C at 20 °C. We recover the fact that the fluorescein mixture is denser than water and the alcohol mixture is lighter than water. It is also clear that the density difference depends linearly on the mass concentration of these dilutions, which allows one to fit the measurements by linear laws for the fluorescein,

$$\Delta\rho_{\text{Fluo}}/\rho_0 = 0.447 C_{\text{Fluo}}, \tag{1}$$

and for the alcohol,

$$\Delta\rho_{\text{alcohol}}/\rho_0 = -0.169 C_{\text{alcohol}}, \tag{2}$$

when the mass concentration is smaller than 0.01. These empirical laws are accurate to within 5% and are quite insensitive to the temperature because it is the difference with respect to the density of water which is given and not the absolute density. These formulas allow the creation of a mixture with the desired relative density difference down to 10^{-5}, even though it would be impossible to measure the density difference accurately below 10^{-3}. This is why these preliminary calibrations are extremely useful because it will be shown later that density differences on the order of 10^{-4} are sufficient to change the behavior of the flow dramatically. Moreover, by mixing the correct amount of fluorescein and alcohol (with densities of $+10^{-5}$ and -10^{-5}, respectively), it is possible to make a neutrally buoyant mixture that will be used as a test case.

The flow under consideration depends on three main dimensionless parameters. The aspect ratio H/R is kept constant at a value of 1.98. The Reynolds number Re=$\Omega R^2/\nu$, ν being the kinematic viscosity of the water, is varied between 700 and 4000. The relative density difference $\Delta\rho/\rho_0$ between the mixture and the water is varied between -1×10^{-3} and 2×10^{-4}. There are three additional dimensionless parameters that are small in the experiments. As defined by Herrada and Shtern,[30] the Froude number $F=\Omega^2R/g$ (where $g=9.81$ ms^{-2} is the gravity) varies between 0.001 and 0.04. The Schmidt number Sc=ν/κ, κ being the molecular diffusivity in water, is on the order of 2000 for the fluorescein and on the order of 800 for ethanol. Finally, the volumic injection rate Q dimensionalized by $R^3\Omega$ varies between 8×10^{-5} and 0.02.

III. VORTEX BREAKDOWN VISUALIZATION WITH NEUTRALLY BUOYANT DYE MIXTURE

A test case has first been studied with neutrally buoyant dye by mixing alcohol and dye in order to have a density difference as small as possible. The flow is initiated and allowed to evolve for about 200 rotation periods before the dye injection in order to eliminate the transient effects. Then, the injection is started; the visualizations for various Reynolds numbers are shown in Fig. 3. For small Reynolds numbers [see Fig. 3(a)], the dye injected at the bottom is simply advected toward the top along the centerline. This is due to the recirculation which appears because the fluid is centrifugally pushed outward by the rotating top. It can be noted that the recirculation is opposite to that usually obtained in the literature[20,21,30] where rotating bottom lids are used instead of rotating top lid. When the Reynolds number is increased above a critical value of 1400, a bubble appears on the center axis of the cylinder as a consequence of the vortex breakdown. This bubble has an axial velocity opposite to the recirculation (i.e., toward the bottom), thus creating a stagnation point at the bottom of the bubble. This structure is very clear in Fig. 3(b) where a large bubble is surrounded at the
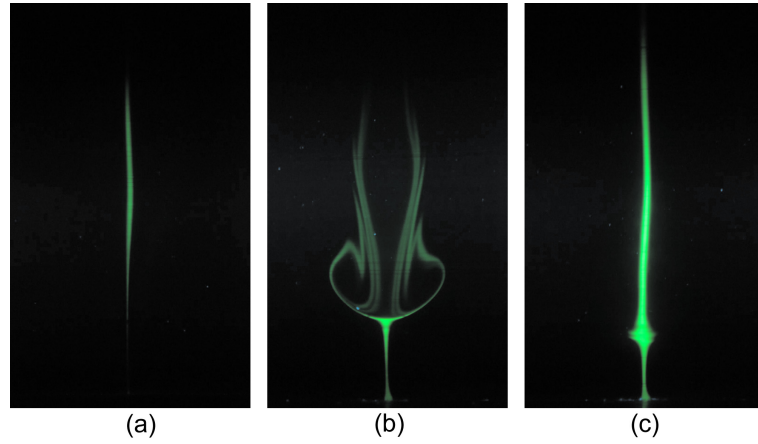
FIG. 3. (Color online) Dye visualization of vortex breakdown in the meridional plane with a neutrally buoyant dye ($\Delta\rho/\rho_0=0$) for a Reynolds number equal to (a) Re=1400, (b) Re=2060, and (c) Re=3030.

bottom by a saddle point and at the top by a smaller more elongated bubble. The presence of two bubbles is in excellent agreement with previous experimental results,[20] where two bubbles were observed above $H/R=1.95$ and even three bubbles around $H/R=3.35$. The size of the vortex breakdown bubble increases with the Reynolds number until Re$\sim$2000 and then decreases gradually up to Re=3000, where the bubble disappears completely. This is illustrated in Fig. 3(c) where the bubble has been replaced by a small undulation along the centerline, which is simply a consequence of small asymmetries in the experimental setup. These results are in excellent agreement with the literature where vortex breakdown has been observed for a Reynolds number between 1440 and 3000.

The temporal evolution of the dye after injection is shown on Fig. 4. The dye is first advected rapidly from the bottom to the stagnation point and slowly diverges radially [see Fig. 4(a)]. It is then advected around the bubble and exhibits large vertical undulations when it converges radially [see Fig. 4(b)]. These asymmetries are due to flow structural instability and experimental imperfections in the location of the injection hole and in the alignment of the rotating top disk.[38,40,41] At late stages, the dye slowly fills the two bubbles and becomes thicker due to the molecular diffusion [see Fig. 4(c)]. The structure observed in this experiment is similar to the structure found previously with a rotating bottom[20] except that it is upside down. This is because there
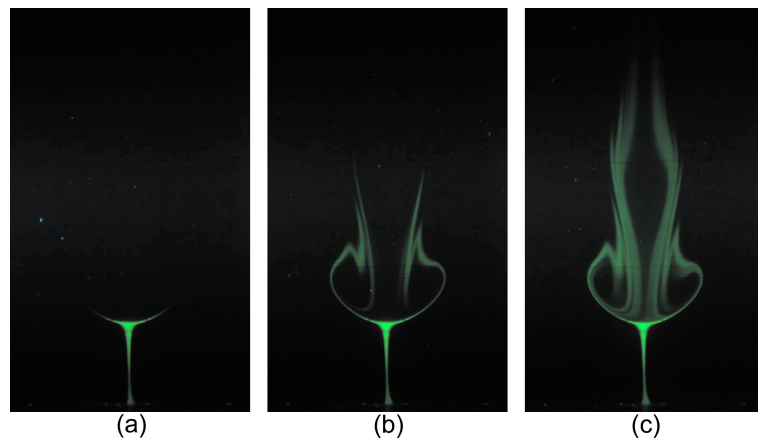

FIG. 4. (Color online) Temporal evolution of a neutrally buoyant dye ($\Delta\rho/\rho_0=0$) injected into the vortex breakdown at (a) $t\Omega=10$, (b) $t\Omega=60$, and (c) $t\Omega=140$ at Re=2060.
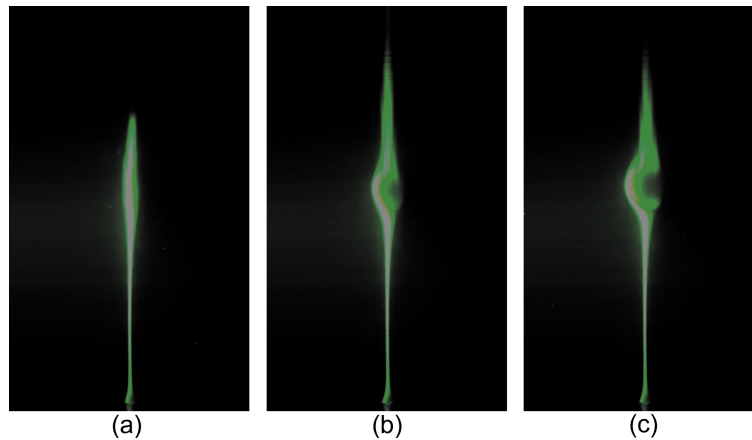
FIG. 5. (Color online) Temporal evolution of a dense dye ($\Delta\rho/\rho_0 = 0.75 \times 10^{-4}$) injected into the recirculating flow at a low Reynolds number (Re=1300). The images, taken approximately at (a) $t\Omega = 100$, (b) $t\Omega = 300$, and (c) $t\Omega = 400$ show the clear formation of a bubble.

are no density effects. We are now going to study the case of a nonbuoyant dye mixture.

IV. DESTABILIZATION OF THE FLOW BY INJECTION OF DENSE DYE

Figure 5 shows an experiment for a Reynolds number (Re=1300) below the critical Reynolds number of vortex breakdown appearance (Re$_c$=1400). Before injection of the dye, the flow is stable without any vortex breakdown. Heavy dye is then injected and a pattern similar to Fig. 3(a) can be seen at early stages, as shown in Fig. 5(a): the dye flows upward along the centerline from the injection point. However, this behavior is only transient. After about 50 rotation periods, the dye accumulates and thickens, as shown in Fig. 5(b). After about 60 rotation periods, Fig. 5(c) shows the clear formation of a bubble at the center of the cylinder, characteristic of vortex breakdown. The destabilization of the flow can be easily understood because the heavy dye tends to sink due to gravity and thus counteracts the global recirculation and axial flow velocity, which enhances the bubble formation. It is striking to see that this destabilization occurs for a very small density difference: in this case $\Delta\rho/\rho_0$ is smaller than 10^{-4}. This may be understood because the sinking velocity of the dye needs to counteract the upward velocity at the center of the cylinder, which, close to the critical Reynolds number, is smaller than the global meridional recirculation, which is itself much smaller than the rotation induced by the disk. A very small density difference is thus sufficient to create a sinking velocity comparable to the upward recirculating velocity along the center axis of the cylinder.

The destabilization due to the heavy dye can be quantified by plotting the critical Reynolds number of vortex breakdown appearance as a function of the density difference $\Delta\rho/\rho_0$. This is plotted on the stability diagram of Fig. 6 where the vortex breakdown is present between the two solid lines. The unstable band of the Reynolds numbers increases

rapidly when the density difference increases: the lower critical Reynolds number drops by a factor of 2 (from 1400 to 720) when the density difference increases up to 2×10^{-4}. This control by density effects is much more efficient than the use of a small rotating disk at the bottom which only modifies the critical Reynolds number by 15% when it rotates twice as fast as the top disk.[36] However, this control is limited to small density differences because the dye is not advected by the flow and simply spreads on the bottom of the cylinder if $\Delta\rho/\rho_0$ is larger than 2×10^{-4}. Finally, it should be noted that the bubble loses its steadiness if the dye is heavy enough (above a density difference of approximately 10^{-4}). The bubble was observed to lean off axis and then started to precess around the axis of the cylinder. This unsteadiness is very different from the axial periodic oscillation of the bubble that appears without dye injection at the high Reynolds numbers (larger than 2600 for this aspect ratio), as was found experimentally[20] and numerically.[42]
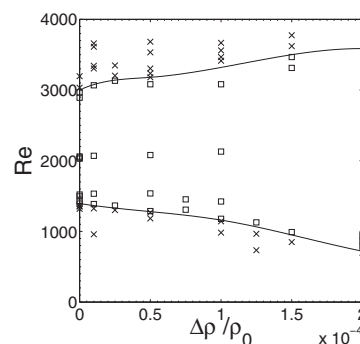

FIG. 6. Stability diagram of formation of vortex breakdown for a heavy dye. Experiments are represented by squares (□) to indicate the presence of a bubble and as crosses (×) when the flow is recirculating without a bubble. Solid lines are a fit of the experimental results.
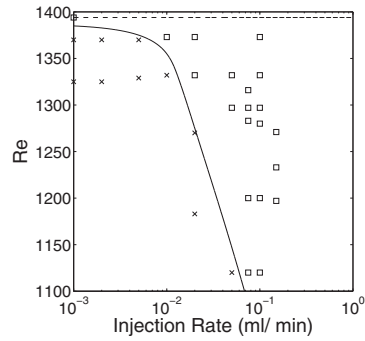
FIG. 7. Stability diagram of formation of the vortex breakdown as a function of the volumic injection rate Q for a fixed density difference $\Delta\rho/\rho_0 = 0.5 \times 10^{-4}$. Squares ($\square$) represent experiments with vortex breakdown and crosses ($\times$) without vortex breakdown. The solid line is a fit to the experimental data. The dashed line corresponds to the critical Reynolds number for a neutrally buoyant dye.

As noted by Herrada and Shtern,[30] there is another effect due to the density difference $\Delta\rho/\rho_0$. Since the flow is rotating close to the top spinning disk, there is a centrifugal acceleration $\mathbf{a_c}$ which creates a centrifugal force on the heavy dye. The dye tends to flow radially outward at the top of the cylinder, which enhances the global recirculation and thus reduces the formation of the vortex breakdown. This effect has been observed in the numerical simulations of Herrada and Shtern[30] in the absence of gravity, but it seems to be negligible in our experiments. In fact, it can be inferred from their results that the effect of the centrifugal convection counteracts the effect of the gravitational convection when the Froude number F (which is the ratio between the centrifugal force ΩR^2 and the gravity g) is roughly equal to 100. In our experiments, the Froude number is on the order of 0.01 and the effect of the gravitational convection is thus

10 000 times larger than the effect of the centrifugal convection. This is why our results can be explained by the effect of the gravity alone.

Finally, we measure the sensitivity of the flow with respect to the injection rate. Figure 7 shows the stability diagram of the vortex breakdown as a function of the injection rate for a fixed density difference $\Delta\rho/\rho_0 = 0.5 \times 10^{-4}$. At small injection rates, the critical Reynolds number is almost constant until $Q = 0.01$ ml/min, where it starts to decrease rapidly. This means that when the injection rate increases, the flow becomes more sensitive to the density difference $\Delta\rho/\rho_0$. It might thus be possible to decrease by more than a factor of 2 the critical Reynolds number of appearance of the vortex breakdown. This once again emphasizes the strong effect of the density difference on the destabilization of the flow.

V. A NEW VORTEX BREAKDOWN STRUCTURE FOR LIGHT DYE

We now present the effect of a dye which is lighter than the surrounding fluid. The temporal evolution of the flow after injection of a light dye ($\Delta\rho/\rho_0 = -2.3 \times 10^{-4}$) is presented in Fig. 8(a). The Reynolds number is chosen above the critical Reynolds number ($Re_c = 1400$) such that the flow contains a strong vortex breakdown bubble before the injection of dye. When the dye is injected, it is advected rapidly by the flow up to the stagnation point, as shown in Fig. 8(a). While the mixture accumulates at the stagnation point, some dye flows around the bubble. The accumulation of the dye increases its buoyancy force and thus allows the dye to pierce through the bubble, as shown in Fig. 8(b). At late stages, the dye creates a thin jet along the centerline, which goes through the whole bubble up to the top disk [Fig. 8(b)]. It is striking to see that this jet does not disrupt the vortex breakdown, which is still present as a leaf shape, although the visualization is not as clear because less dye is advected
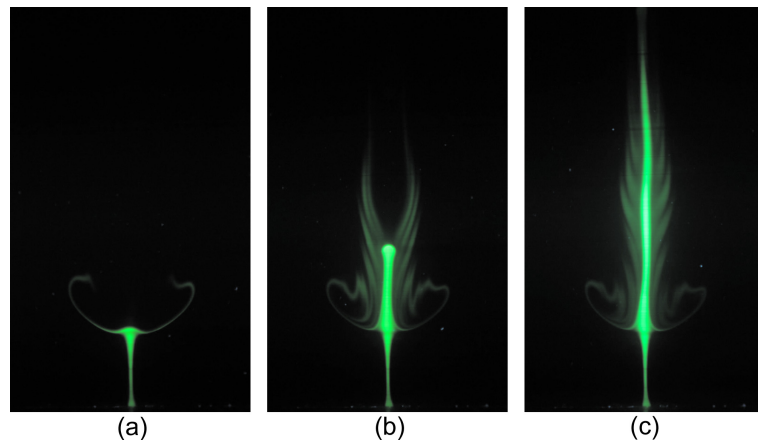

(a)   (b)   (c)

FIG. 8. (Color online) Temporal evolution of a light dye $\Delta\rho/\rho_0 = -2.267 \times 10^{-4}$ injected in a vortex breakdown at $Re = 2423$. The pictures are taken approximately at (a) $t\Omega = 25$, at (b) $t\Omega = 60$, and at (c) $t\Omega = 110$.
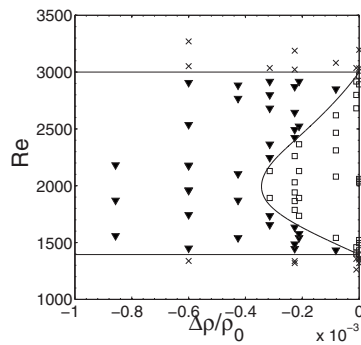
FIG. 9. Stability diagram of formation of vortex breakdown for a light dye. Experiments are represented by squares (□) to indicate the presence of a bubble and as crosses (×) when the flow is recirculating without a bubble. Solid lines are a fit of the experimental results. A new regime represented by solid triangles depicts the formation of vortex breakdown with a jet piercing through the bubble as shown in Fig. 8.

around the bubble. It can be noted that this evolution is very rapid: it happens after approximately ten rotation periods, whereas the destabilization of the flow by the dense dye happened in 50 rotation periods.

This new structure of the vortex breakdown is plotted in the stability diagram of Fig. 9 as solid triangles. It is observed for all Reynolds numbers when the dye is light enough ($\Delta\rho/\rho_0 < -3 \times 10^{-4}$). When the dye is not light enough, the mixture accumulates at the stagnation point but does not gain enough buoyancy force. It is thus advected around the bubble and leads to the well-known structure of the vortex breakdown found in Fig. 4. This classical regime is indicated by squares on the stability diagram. It is surprising to see that the light jet is not able to destroy the vortex breakdown bubble: the transition between the stable flow and the vortex breakdown with a buoyant jet is independent of the density difference. To conclude, even if the presence of a light dye is not able to destroy the vortex breakdown, a small variation of the dye density is able to create a radical change of the structure of the flow.

The sensitivity of the flow with respect to the dye density poses a major question concerning the results of the literature.[5,39] Indeed, most of the experimental results have been obtained by dye visualizations, where the dye was probably heavier than the working fluid. However, since these experiments have been done with a rotating bottom instead of a rotating top, the density effects are reversed: the heavy dye enhances the recirculation and thus tends to prevent the vortex breakdown. As was mentioned in this section, the breakdown bubble cannot be destroyed by the dye and this is why the results of the literature (for a rotating bottom) are not influenced by the injection of a dense dye.

VI. VORTEX RING INTERACTION WITH VORTEX BREAKDOWN

We wish to study the interaction of a vortex ring generated at the bottom with the vortex breakdown. It is similar to an injection of light dye because the vortex ring contains some momentum and pushes the fluid toward the top. In these experiments, a Reynolds number of 2000 is selected such that a strong breakdown bubble is formed in the cylinder. Additionally, a neutrally buoyant dye is used to ensure that the visualization process does not modify the flow. Before the vortex ring is created, a small amount of fluorescein mixture is injected to visualize the breakdown bubble. The vortex ring is then created by mechanically pinching the tube connected to the injection hole.

In the first experiment, a strong vortex ring is produced and its interaction is visualized in Fig. 10. The vortex ring rapidly reaches the stagnation point and penetrates through the breakdown bubble. As the vortex ring travels through the breakdown region, the ring decelerates and its diameter in-
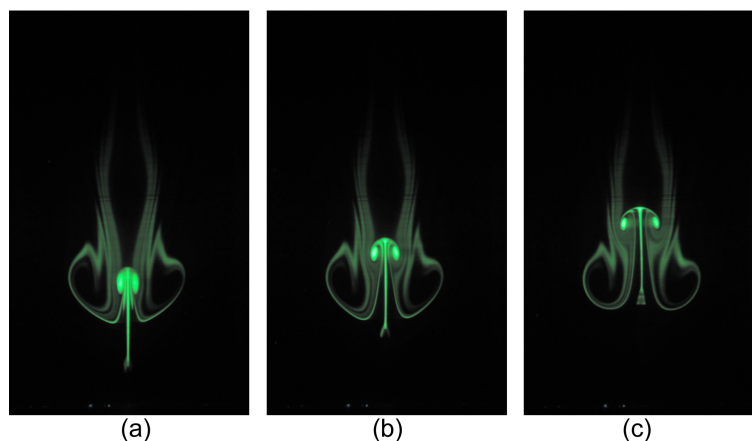

FIG. 10. (Color online) Temporal evolution of a strong vortex ring impacting the vortex breakdown at Re=2000, visualized with a neutrally buoyant dye ($\Delta\rho/\rho_0=0$).
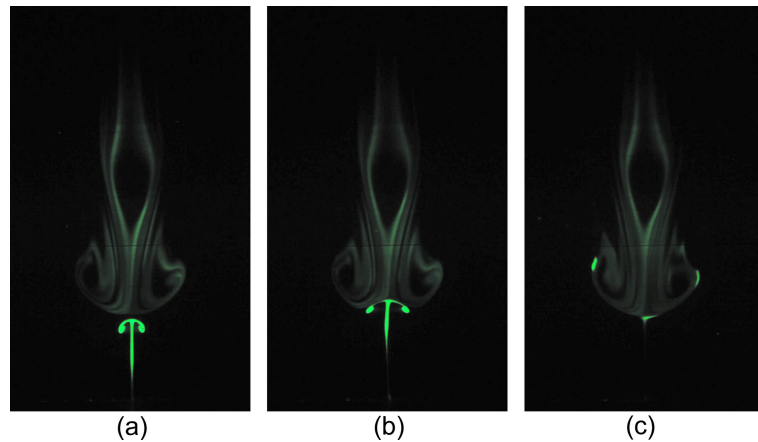
(a)   (b)   (c)

FIG. 11. (Color online) Temporal evolution of a weak vortex ring impacting the vortex breakdown at Re=2000, visualized with a neutrally buoyant dye ($\Delta\rho/\rho_0$=0).

creases. The breakdown bubble is very weakly modified by the presence of the vortex ring. This shows once again the robustness vortex breakdown to disturbances. This behavior is very similar to the one shown in Fig. 8, where the light jet pierces through the bubble. Although the characteristics of the vortex ring were not measured accurately by particle image velocimetry (PIV) measurements, they were estimated using the position and the size of the ring on the dye visualizations. The vertical velocity of the vortex ring decreases rapidly due to viscous effects and due to the interaction with the vortex breakdown but it was approximately equal to 4.4 cm/s (or 0.7 in dimensionless units) before reaching the stagnation point (i.e., for $z/H \approx 0.15$). The diameter of the ring increases slowly and is on the order of 2.5 mm (i.e., $0.07R$) before the impact with the vortex breakdown.

A second experiment is conducted for a weak vortex ring interacting with the vortex breakdown, as visualized in Fig. 11. The vortex ring travels upward along the centerline and decelerates at the stagnation point. Instead of penetrating through the breakdown bubble, the ring widens and is advected around the breakdown. The strength of the vortex ring decreases very fast, leading to a simple blob of scalar without any vorticity at late stages. The velocity of the vortex ring was estimated to be equal to 2.2 cm/s (or 0.35 in dimensionless units) and its diameter is equal to 2.5 mm (or $0.07R$) before the impact with the vortex breakdown (i.e., for $z/H \approx 0.15$).

These two experiments show that the behavior of a vortex ring impacting a vortex breakdown is similar to a jet of light dye. If the vortex ring is strong enough (or if the dye is light enough), the vortex ring (or the dye) will pierce through the bubble. If the vortex ring is too weak (or if the dye is not light enough), the vortex ring (or the dye) will be advected around the bubble. However, in no cases investigated could the vortex ring (or the light jet) destroy the vortex breakdown bubble.

VII. CONCLUSIONS

We have shown that the density of the dye used for visualizations has a significant effect on the vortex breakdown structure and stability. This effect has been observed and measured experimentally in a cylinder with a rotating top lid when the dye is injected at the bottom. On one hand, a denser dye is able to induce vortex breakdown and thus widens the range of critical Reynolds numbers for which the bubble appears. This can be explained by the sinking velocity of the dye which counteracts the global recirculation and thus favors the formation of a stagnation point and creation of the bubble. This dramatic effect can reduce the critical Reynolds number by a factor of 2 for the extremely small density difference of 0.02% at a very small injection rate. On the other hand, a light dye does not destroy the vortex breakdown but leads to a new structure where the jet of dye pierces through the breakdown bubbles. This new structure appears above a critical density difference on the order of 0.03%, which is also extremely small. Finally, we have shown that a vortex ring impacting the vortex breakdown has the same behavior as a light jet: it can either penetrate through the bubble or be advected around it depending on the momentum of the vortex ring.

These results indicate that a very small density difference can be used to control the vortex breakdown in a very efficient way. This effect might have great implications in geophysical flows where the presence of water vapor at the bottom of the tornadoes (e.g., tornadic waterspouts) might have a large effect on the structure of the tornadoes. Unfortunately, it might not be very suited to aeronautical or combustion applications since it occurs only for a vortex with a vertical axis. In bioengineering, this effect can be important for bioreactors since the injection of a dense or light nutrient might have a large effect on the structure of the flow inside the bioreactor. Moreover, the new structure of a light jet

Fluid Dynamics of Bioreactors

034104-9   Experimental control of vortex breakdown by density effects   Phys. Fluids **23**, 034104 (2011)

penetrating through the vortex breakdown could be used to feed the cells located in the bubble without having to put a probe close to the cells. This is of great interest for suspension cells which need to grow far from any boundary. Finally, the sensitivity of the flow to the density difference could be used to control the shear stress experienced by the cells, which is known to induce differentiation for stem cells.

[1] S. Leibovich, "The structure of vortex breakdown," Annu. Rev. Fluid Mech. **10**, 221 (1978).

[2] D. L. Kohlman and W. H. Wentz, "Vortex breakdown on slender sharp-edged wings," J. Aircr. **8**, 156 (1971).

[3] M. G. Hall, "Vortex breakdown," Annu. Rev. Fluid Mech. **4**, 195 (1972).

[4] M. V. Lowson and A. J. Riley, "Vortex breakdown control by delta wing geometry," J. Aircr. **32**, 832 (1995).

[5] M. P. Escudier, "Vortex breakdown: Observations and explanations," Prog. Aerosp. Sci. **25**, 189 (1988).

[6] O. R. Burggraf and M. R. Foster, "Continuation or breakdown in tornado like vortices," J. Fluid Mech. **80**, 685 (1977).

[7] R. P. Davies-Jones, "Tornado dynamics," in *Thunderstorms: A Social, Scientific, and Technological Documentary*, edited by E. Kessler (University of Oklahoma Press, Nolan, 1983), Vol. 2, p. 297.

[8] A. K. Gupta, D. G. Lilley, and N. Syred, *Swirl Flows* (Abacus, Kent, England, 1984).

[9] J. Dusting, J. Sheridan, and K. Hourigan, "A fluid dynamics approach to bioreactor design for cell and tissue culture," Biotechnol. Bioeng. **94**, 1196 (2006).

[10] G. A. Thouas, J. Sheridan, and K. Hourigan, "A bioreactor model of mouse tumor progression," J. Biomed. Biotechnol. **9**, 327 (2007).

[11] J. K. Harvey, "Some observations of the vortex breakdown phenomenon," J. Fluid Mech. **14**, 585 (1962).

[12] T. Sarpkaya, "On stationary and travelling vortex breakdowns," J. Fluid Mech. **45**, 545 (1971).

[13] J. H. Faler and S. Leibovich, "An experimental map of the internal structure of a vortex breakdown," J. Fluid Mech. **86**, 313 (1978).

[14] H. Ludwieg, "Zur erklarung der instabilitat der uber angestellten delta-flugeln auftretenden freien wirbelkerne," Z. Flugwiss. **10**, 242 (1962).

[15] T. B. Benjamin, "Theory of the vortex breakdown phenomenon," J. Fluid Mech. **14**, 593 (1962).

[16] H. B. Squire, "Analysis of the vortex breakdown phenomenon. Part 1," Department of Aeronautics, Imperial College Report No. 102, 1962.

[17] S. Wang and Z. Rusak, "The dynamics of a swirling flow in a pipe and transition to axisymmetric vortex breakdown," J. Fluid Mech. **340**, 177 (1997).

[18] H. U. Vogel, "Experimentelle ergebnisse über die laminare strömung in einem zylindrischen gehaüse mit darin rotierender scheibe," Max-Planck-Institut für Strömungsforschung Technical Report Bericht 6, 1968.

[19] B. Ronnenberg, "Ein selbstjustierendes 3-komponenten-LDA nach dem vergleighstrahlverfaren, angewendt für untersuchungen in einer stationären zylindersymmetrischen drehströmung mit einem rühckströmgebiet," Max-Planck-Institut für Strömungsforschung Technical Report Bericht 20, 1977.

[20] M. P. Escudier, "Observations of the flow produced in a cylindrical container by a rotating endwall," Exp. Fluids **2**, 189 (1984).

[21] A. Spohn, M. Mory, and E. J. Hopfinger, "Observations of vortex breakdown in an open cylindrical container with rotating bottom," Exp. Fluids **13**, 70 (1993).

[22] H. J. Lugt and M. Abboud, "Axisymmetric vortex breakdown in a container with a rotating lid," J. Fluid Mech. **179**, 179 (1987).

[23] G. P. Neitzel, "Streak-line motion during steady and unsteady axisymmetric vortex breakdown," Phys. Fluids **31**, 958 (1988).

[24] J. M. Lopez, "Axisymmetric vortex breakdown. Part 1: Confined swirling flow," J. Fluid Mech. **221**, 533 (1990).

[25] G. L. Brown and J. M. Lopez, "Axisymmetric vortex breakdown. Part 2: Physical mechanism," J. Fluid Mech. **221**, 553 (1990).

[26] J. M. Lopez and A. D. Perry, "Axisymmetric vortex breakdown. Part 3: Onset of periodic flow and chaotic advection," J. Fluid Mech. **234**, 449 (1992).

[27] S. Bhattacharyya and A. Pal, "Axisymmetric vortex breakdown in a filled cylinder," Int. J. Eng. Sci. **36**, 555 (1998).

[28] D. T. Valentine and C. C. Jahnke, "Flow induced in a cylinder with both ends walls rotating," Phys. Fluids **6**, 2702 (1994).

[29] F. Gallaire, J. M. Chomaz, and P. Huerre, "Closed-loop control of vortex breakdown: A model study," J. Fluid Mech. **511**, 67 (2004).

[30] M. A. Herrada and V. Shtern, "Control of vortex breakdown by temperature gradients," Phys. Fluids **15**, 3468 (2003).

[31] D. Lo Jacono, J. N. Sørensen, M. C. Thompson, and K. Hourigan, "Control of vortex breakdown in a closed cylinder with a small rotating rod," J. Fluids Struct. **24**, 1278 (2008).

[32] B. Jørgensen, J. Sørensen, and N. Aubry, "Control of vortex breakdown in a closed cylinder with a rotating lid," Theor. Comput. Fluid Dyn. **24**, 483 (2010).

[33] B. T. Tan, K. Y. S. Liow, L. Mununga, M. C. Thompson, and K. Hourigan, "Simulation of the control of vortex breakdown in a closed cylinder using a small rotating disk," Phys. Fluids **21**, 024104 (2009).

[34] P. Yu, T. S. Lee, Y. Zeng, and H. T. Low, "Effects of conical lids on vortex breakdown in an enclosed cylindrical chamber," Phys. Fluids **18**, 117101 (2006).

[35] H. Husain, V. Shtern, and F. Husain, "Control of vortex breakdown by addition of near-axis swirl," Phys. Fluids **15**, 271 (2003).

[36] L. Mununga, K. Hourigan, and M. C. Thompson, "Confined flow vortex breakdown control using a small rotating disk," Phys. Fluids **16**, 4750 (2004).

[37] S. Khalil, K. Hourigan, and M. C. Thompson, "Effects of axial pulsing on unconfined vortex breakdown," Phys. Fluids **18**, 038102 (2006).

[38] M. C. Thompson and K. Hourigan, "The sensitivity of steady vortex breakdown bubbles in confined cylinder flows to rotating lid misalignment," J. Fluid Mech. **496**, 129 (2003).

[39] A. Spohn, M. Mory, and E. J. Hopfinger, "Experiments on vortex breakdown in a confined flow generated by a rotating disc," J. Fluid Mech. **370**, 73 (1998).

[40] M. Brøns, W. Z. Shen, J. N. Sørensen, and W. J. Zhu, "The influence of imperfections on the flow structure of steady vortex breakdown bubbles," J. Fluid Mech. **578**, 453 (2007).

[41] M. Brøns, M. Thompson, and K. Hourigan, "Dye visualization near a three-dimensional stagnation point: Application to the vortex breakdown bubble," J. Fluid Mech. **622**, 177 (2009).

[42] A. Y. Gelfat, P. Z. Bar-Yoseph, and A. Solan, "Three-dimensional instability of axisymmetric flow in a rotating lid-cylinder enclosure," J. Fluid Mech. **438**, 363 (2001).

3.2   Discussion and Conclusion

From this research, it was found that by having the driving disk at the top, a structure, similar to the structure found previously with a rotating bottom-disk container, is obtained except that it is inverted. The results are also in excellent agreement with previous experimental results found by Escudier (1984), which demonstrates the accuracy of the apparatus.

The density of the dye used for visualisations has a significant effect on the vortex breakdown structure and stability. This effect has been observed and measured experimentally when a dye has been injected into the bottom of a rotating top lid cylinder. On one hand, a denser dye is able to induce vortex breakdown and thus widens the range of critical Reynolds numbers for which the bubble appears. This can be explained by the sinking velocity of the dye which counteracts the global recirculation and thus favours the formation of a stagnation point and the creation of the bubble. This dramatic effect can reduce the critical Reynolds number by a factor of two for an extremely small density difference of 0.02% at a very small injection rate. On the other hand, a light dye does not destroy the vortex breakdown but leads to a new structure where the jet of dye pierces through the breakdown bubbles. This new structure appears above a critical density difference of 0.03%, which is also extremely small.

Translating this knowledge to the use of microcarriers in a rotating lid bioreactor, the microcarriers are expected to accumulate at the centre of the container. As the microcarriers have higher density than the working fluid, they tend to sink due to the negative buoyancy effect, which counteracts the upwards axial flow at the middle of the cylinder. This occurrence is followed by some fluctuations which cause destabilisation of the flow, creating phenomenon similar to dense dye experiments. The low shear and high mixing rate in a vortex breakdown bubble would possibly be an ideal condition for cell growth. Injecting the microcarriers and cells into the bubble will place the cells into the recirculation bubble and enable the cells to grow optimally. On the other hand, the new structure of a light jet penetrating through the vortex breakdown could be used to feed the cells located in the bubble without having to place a probe close to the cells. This is of great interest for suspension cells which need to grow far from any boundary. This study gives insight of the flow characteristics in the rotating lid bioreactor. Moreover, it is known that the density of the dye or microcarriers can stabilise or destabilise the flow. For a known microcarrier density, the required

spinning rates can be manipulated to achieve a specific flow behaviour during the culture procedure.

Dye visualisation is a simple and quick technique used to characterise the profile of a flow. This study also showed the effect of microcarriers on the flow behaviour in the spinning lid bioreactor. Although the results are mainly qualitative, it is a useful method to enhance the appreciation of fluid dynamics in cell studies and also promote the collaboration between engineers and biologists. The next chapter describes quantitative characterisation of a commercially-available spinner flask.

Chapter 4

Fluid Dynamics of the Conventional Stirred Bioreactor

T HE flow characterisation in the conventional spinner flask is outlined in this chapter. Although the suspension bioreactor has been proven to yield superior cell count to a static culture, flow characteristics in spinner flask bioreactors are poorly understood. There have been limited studies that analysed the underlying flow mechanics in the spinner flask. As cell research is dominated by biologists, little appreciation has been given to hydrodynamic force in cell culture protocols and bioreactor design aspects, thus limiting the progression of the bioreactor development.

Using PIV, Sucosky *et al.* (2003) previously measured the flow characteristics around arrays of construct for cartilage culture. Furthermore, Dusting *et al.* (2006) presented an extensive flow profile in a disk-driven bioreactor, Meunier & Hourigan (2013) investigated the mixing properties, and Mununga *et al.* (2004) studied the control of flow in such bioreactors. The characterisation of commercial bioreactors has not been conducted until recent years (Kaiser *et al.* 2012; Liovic *et al.* 2012); furthermore, only limited results were shown in these studies.

There are a number of variations in cell culture procedures as the protocol is commonly tailor-made for specific cell types. However, commercial of-the-shelf spinner flask bioreactors are widely used due to ease of setup. Generally, the rotational speeds are varied to culture different cell types. The article presented in this chapter provides a detailed quantitative investigation of velocity, shear stress and vorticity in the spinner flask through the use of the PIV measurement technique. Additionally, by varying the impeller position and rotational speed, a wide-range of experimental variables are cov-

ered that can be of benefit to many research groups. The study is aimed at providing a mechanical property datasheet as a reference for previous and future works. The insight gained through the extensive flow characterisation, together with published cell experiment results, would provide an estimate to the bioreactor design parameters and, therefore, accelerate the development of more efficient bioreactors.

4.1   Article II: Experimental Characterisation of Fluid Dynamics in Spinner Flask Bioreactor

The following manuscript was published in 2014 in *Processes*. This work was co-authored by Andreas Fouras, and Kerry Hourigan. The article reproduced in this thesis is directly taken from the published version without alteration.

Declaration

Monash University

Declaration for Thesis Section 4.1

Declaration by candidate

In the case of Section 4.1, the nature and extent of my contribution to the work was the following:

Nature of contribution	Extent of contribution (%)
Conceived, designed and performed experiments. Analysed the data and wrote the manuscript.	80%

The following co-authors contributed to the work. If co-authors are students at Monash University, the extent of their contribution in percentage terms must be stated:

Name	Nature of contribution	Extent of contribution (%) for student co-authors only
K. Hourgan	Technical advice and revised manuscript	NA
A. Fouras *	Technical advice and revised manuscript	NA

The undersigned hereby certify that the above declaration correctly reflects the nature and extent of the candidate's and co-authors' contributions to this work*.

Candidate's Signature		**Date:** 01 AUG 2014
Main Supervisor's Signature		**Date:** 01 AUG 2014

Article

Experimental Characterisation of Fluid Mechanics in a Spinner Flask Bioreactor

Mohd-Zulhilmi Ismadi [1,2,*], Kerry Hourigan [1,2] and Andreas Fouras [1,2]

[1] Division of Biological Engineering, Monash University, Melbourne, VIC 3800, Australia;
███

[2] Department of Mechanical and Aerospace Engineering, Monash University, Melbourne, VIC 3800, Australia

* Author to whom correspondence should be addres████████████████████
███████████████████████████████

External Editor: Michael Henson

Abstract: The spinner flask bioreactor has been widely used in *in vitro* cell culturing processes due to its superiority in providing a homogeneous culture environment compared to traditional culturing methods. However, there is limited understanding of the flow fields in these bioreactors, and optimum culture conditions are yet to be determined. This article presents the experimental characterization of the flow field within a spinner flask at varying speeds (10 RPM to 80 RPM) and impeller positions. An optical, non-invasive measurement technique, Particle Image Velocimetry (PIV), was employed to illustrate the fluid flow and calculate the stresses and vorticity associated with the flow within the flask. The largest recirculation structure was observed in the meridional plane at the highest impeller position while the highest shear stress region was observed at the base of the spinner flask. The study provides an overview of the fluid structure within the spinner flask in the meridional and azimuthal planes. Furthermore, the results presented in this study give an accurate quantification of the range of stresses for the given impeller speeds. These results provide estimates of the biomechanical properties within the type of spinner flask used in many published cell studies.

1. Introduction

Stem cells have great potential in regenerative medicine due to their ability to differentiate to multiple lineages. The self-renewal ability possessed by these cells is highly suitable to replenish damaged cells, which could be caused by injury or degeneration due to age. When the cells divide, they could produce either a similar cell type or differentiated cells [1].

Stem cells inherently exist in all organisms and serve as an internal repair mechanism for damaged tissue. However, the number of stem cells present in organisms is very low. Before any cell therapy can be realized, an optimized cell culture system is required to increase the number of cells for clinical treatment. A high-throughput bioreactor is essential to ensure that optimum level of cell expansion can be achieved while maintaining its genetic stability at the end of the culture process.

The static culture system using petri dishes and T-flasks has been the classical method for cell expansion since the early work by Dexter *et al*. [2]. The simplicity of the setup is the main attraction for many research studies. Media were replenished after a specific time to allow continuous nutrient supply. Although being the most prominent method in cell culture, this technique nevertheless has several limitations including lack of mixing, which causes concentration variance in culture condition, and limited surface area to support the number of cells in the system [3,4].

The dynamic culture system offers homogeneous culture environment and enhanced mass transfer. The lower oxygen and nutrients gradient in the system provide cell culture results superior to the static culture system. Additionally, the reduced waste concentration prevents cell damage due to waste intoxication. Many cell studies have used a dynamic culture system that includes the rotating wall bioreactor [5–7] and more commonly, the spinner flask bioreactor [8–10]. Several novel dynamic culture bioreactors have also been developed such as spinning lid [11], spinning base [12] and bi-axial rotating bioreactors [13], to name a few, in an effort to obtain maximum number of cells at the end of the culture period.

The most widely used suspension bioreactor is the magnetic- or motor-driven impeller spinner flask. Microbial and mammalian cells have been extensively grown in stirred culture systems. The agitation or mixing rate can be easily controlled by changing the speed of the driving motor or the magnetic stirrer. The culture medium is partially replenished after a number of days to maintain nutrient supply and keep the waste concentration at an acceptable margin. Furthermore, spinner flasks are available in various sizes and impeller shapes depending on the culture size. Previous studies have demonstrated the efficiency of suspension bioreactors for undifferentiated mammalian stem cell expansion [8,9,14,15].

The use of constructs and microcarriers has been proven to aid cell growth in dynamic culture systems. The construct is typically made of polymers and consists of micropores to support the growth of cells. It has been heavily used to assist osteogenic differentiation from adult and embryonic cells [16–19]. On the other hand, microcarriers provide higher surface area-to-volume ratio to accommodate higher

cell densities. It also provides versatility by allowing various surface coatings and treatments to support a wide range of cell growth. Specially conditioned medium or coating, such as murine embryonic fibroblast (MEF) and Matrigel, were typically used to ensure cell adherence to the microcarriers in previous culturing procedures [20,21]. Microcarriers have been demonstrated to be able to support positive cultivation of retinal pigment epithelial [22], adult progenitor [23,24] and human embryonic [20,21,25] cells when they are used in the spinner flask. By varying the spinning rates in the spinner flask, the use of microcarriers in suspension culture covers a wide-range of cell types in culture protocol, making them the frequently-used method for cell growth [26,27].

However, the homogeneous culture condition in the spinner flask is at the expense of hydrodynamic force introduced in the system caused by the rotating impeller. Mechanical force, such as shear stress, could alter the behavior of cell growth; a high shear environment could be damaging to the cells and the microcarriers [28]. Although spinner flasks are widely used in biological applications, the flow characteristics within the system are not well understood. Studies that analyze the underlying flow mechanics in biological applications are limited, especially in the spinner flask. Additionally, hydrodynamic force is often ignored in cell culture protocol and bioreactor design aspects, thus limiting the understanding of how mechanical force affects the cell culture.

Optimization through continuous cell experiment testing would be inefficient and costly. An optical based and therefore non-intrusive flow measurement technique, known as Particle Image Velocimetry (PIV), has been widely utilized in an effort to quantitatively characterize the mechanics behind cell culture. By capturing sequential images of moving seeded particles in the fluid, the displacement of the particles between images can be computed through the use of cross correlation analysis. Having been developed for more than two decades, the technique provides accurate measurements in a variety of flow applications.

Using this technique, Sucosky *et al.* [29] previously measured the flow characteristics around arrays of construct for cartilage culture. Furthermore, Dusting *et al.* [12] presented an extensive flow profile in a disk-driven bioreactor, Meunier and Hourigan [30] investigated the mixing properties, and Mununga *et al.* [31] studied the control of flow in such bioreactors. The characterization of commercial bioreactors has not been conducted until recent years [32–34]; furthermore, only limited mechanical parameters at a few speeds were investigated in these studies. Recently, Gupta *et al.* [35] showed that the high rotational speeds could damage the microcarriers. The study also highlighted the optimum rotational speed corresponds to the highest mouse induced pluripotent cell yield. Understanding the flow properties associated to the culture condition would enable researchers to gain advantage in optimising the culture process [35].

The knowledge gained through flow profiling, together with numerous published cell experiments results, would help define the design parameters and accelerate the improvement of bioreactor design process. This study provides a detailed quantitative investigation of velocity, shear stress and vorticity in the spinner flask through the use of the PIV measurement technique in meridional and azimuthal planes, to extensively highlight the flow feature that may improve cell growth in culture procedure. Although most spinner flasks have fixed impeller positions, some designs allow the change of impeller height. The present study investigates the effect of impeller position on the flow features within the reactor. Additionally, by varying the impeller position and rotational speed, we are able to cover a wide-range of experiment variables that can be of benefit to many research groups. With this

information, the study is aimed at providing a mechanical property datasheet as a reference for previous and future works, to systematically improve the bioreactor design for cell applications.

2. Experimental Section

2.1. Experimental Setup

Figure 1 illustrates the general layout of the experiments. A 100 mL BellCo spinner flask (BellCo Glass Inc., Vineland, NJ, USA), filled with 100 mL of water, was used throughout the experiments. The working water was seeded with 31 μm diameter fluorescent particles, at 1 mg/mL seeding density. The fluid was agitated by a stepper motor (Sanyo Denki America Inc., Torrance, CA, USA), connected through a motion controller (National Instrument North Ryde, New South Wales, Australia) to accurately control the speed of the motor. To ensure a smooth rotation of the impeller, the motor was attached to a worm wheel gear that provides a further reduction factor of 30. The speeds were varied between 10 RPM and 80 RPM, which equates to a Reynolds number (Re) between 668 and 5341. Here, Re is defined as $Re = \Omega R^2/\nu$, where Ω is the angular velocity in radian per second, R is based on the radius of the flat impeller (R = 25.3 mm), and ν is the kinematic viscosity (dynamic viscosity, μ per unit density, ρ) of the water. The flask was placed inside a square tank filled with water to minimize the lensing effect, due to the curvature of the flask wall during the image acquisition process.

Figure 1. Apparatus arrangement for flow imaging in spinner flask. Throughout the experiment, the spinner flask was placed in a glass tank, filled with water to reduce the optical distortion caused by the curvature of the flask. (**a**) To image the flow in the meridional plane, the laser sheet was aligned vertically and positioned at the middle of the flask. (**b**) For azimuthal plane measurement, the laser sheet was aligned horizontally and the position was adjusted at several measurement heights. To allow a better view for the azimuthal measurement, a mirror was placed underneath the flask and the camera captured the images reflected by the mirror. (**c**) The impeller is constructed from a rectangular shape Teflon sheet and a magnetic stirring bar. The angular position is defined as the angular distance from the horizontal datum point to the center of the bar throughout the manuscript.
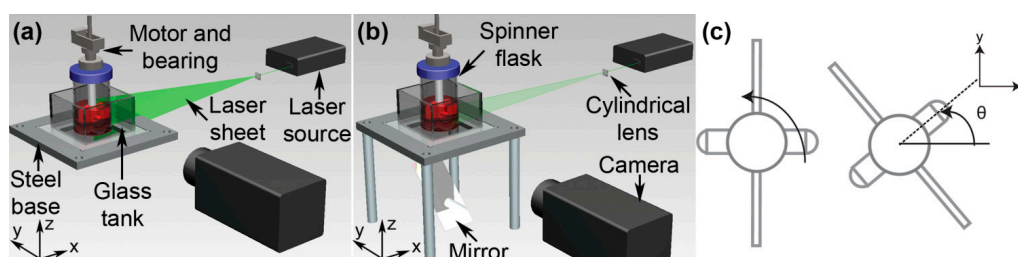

An Nd:YAG laser source and a cylindrical lens were used to create a thin laser sheet that illuminated the imaging plane. For meridional plane analysis, the laser sheet was aligned vertically (Figure 1a), whereas for azimuthal image acquisition procedure, the laser sheet was in a horizontal plane and a mirror was placed underneath the flask to reflect the scattered light in the fluid flow onto the camera sensor as shown in Figure 1b.

A high-speed CMOS camera (Y4, IDT Inc., Tallahassee, FL, USA) fitted with a Nikkor 105 mm f/2.8 G lens (Nikon, Tokyo, Japan) was used throughout the experiment to sequentially capture the scattered light reflected by the seeding particles at 300 µs exposure time. The acquisition rate of the camera was set so that the images were captured at one-degree spatial increments of the impeller. One complete rotation consisted of 360 images and at each speed, 12 sets of data were gathered for averaging purposes. The required acquisition rate can be calculated by multiplying the rotational speed (in RPM) by 6. This means the images were captured between 60 Hz and 480 Hz for 10 RPM and 80 RPM, respectively.

The stepper motor was set to turn in a counter-clockwise direction, viewed from the top. In order to keep track of the impeller position, the angular coordinate system was introduced and is illustrated in Figure 1c. Figure 2 depicts the dimensions of the flask and impeller used throughout the experiments.

Figure 2. Dimensions of the impeller blade and inner wall of the spinner flask bioreactor.
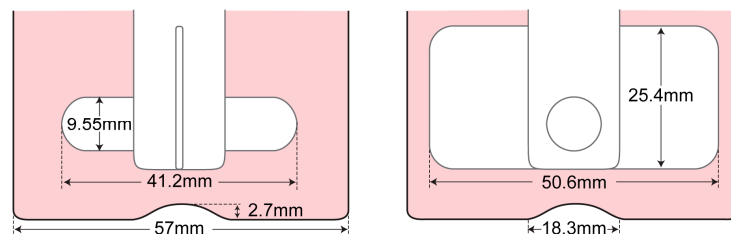
In this study, apart from varying the speed, the impeller height was varied at three positions, defined as low, middle and high as presented in Figure 3. We conducted measurements in the meridional and azimuthal planes. In the azimuthal plane, two main analyses were conducted—the flow profile at the middle height of the stirrer bar, and the fluid- wall interaction at the bottom surface of the flask (Figure 4). To analyze the shear profile at the bottom surface, two measurements at different heights were conducted near the bottom surface. An accurate approximation of shear rate at the bottom surface could be calculated by fitting a parabolic function to the three data points—two experimental measurements plus the no-slip condition at the wall.

Figure 3. Impeller positions in the spinner flask. Throughout the experiment, the impeller height was varied at low, middle and high positions. (**a**) The impeller was positioned at its lowest possible location where the bottom of the impeller touches the bump at the bottom of the flask. (**b**) The impeller was placed at middle height where the distance of the bump to the impeller's bottom edge is similar to the distance of the impeller's top edge to the free surface at 5.5 mm. (**c**) The impeller is in "high" position when the top edge of the impeller is at the free surface and the bottom edge is 11 mm from the bump.
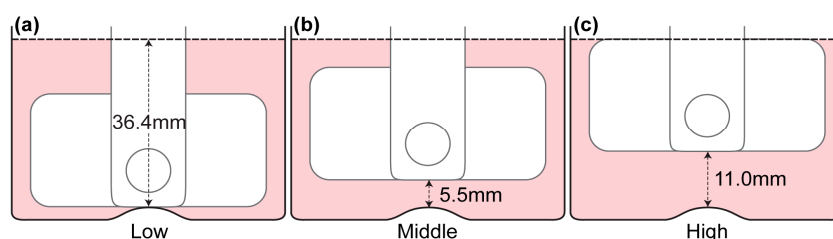
Figure 4. Locations of azimuthal measurements. A measurement was conducted at mid-height of the stirrer bar and two measurements were conducted near the bottom wall of the bioreactor, as represented by the dashed lines. Using the two velocity profiles at $z = 0.75$ mm and $z = 1.25$ mm, a parabolic profile was fitted and the velocity gradient near the bottom wall was estimated.
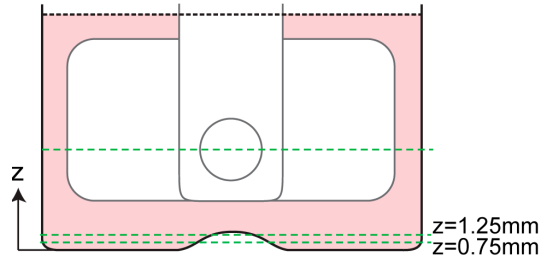
2.2. Data Analysis

In-house PIV software was used to analyze the datasets. The software has been rigorously tested and improved over a number of years [36,37]. To improve the computing efficiency, a mask file was generated to define the area outside of the flask, where no flow existed. This area was excluded from the calculation. The images were divided into 128 by 128 pixel sub-windows and the computation was performed at 8 by 8 pixel spacing, in *x* and *y* directions, correspondingly. A full rotation comprised 360 phases (one phase per one degree spacing). To enhance the signal-to-noise ratio of the analysis, the results were phase-averaged over 12 rotations. Based on the displacement obtained from PIV analysis, gradients were computed, then the shear stress (τ), and vorticity (ω), were calculated using the following equations:

$$\tau_{Meridional} = \mu\left(\frac{\partial W}{\partial x} + \frac{\partial U}{\partial z}\right), \tag{1}$$

$$\tau_{Azimuthal} = \mu\left(\frac{\partial U}{\partial y} + \frac{\partial V}{\partial x}\right), \tag{2}$$

$$\tau_{Bottom\ wall} = \mu\frac{\partial\left(\sqrt{U^2 + V^2}\right)}{\partial z}, \tag{3}$$

$$\omega_{Meridional} = \frac{\partial U}{\partial z} - \frac{\partial W}{\partial x}, \tag{4}$$

where *U*, *V* and *W* are the velocity components in *x*, *y* and *z* directions, respectively. To avoid skewing of the data by outliers, the maximum shear stress was defined as the 99th percentile of the distribution in any given imaged plane.

3. Results and Discussion

The results are split into 3 s—meridional plane, azimuthal plane analysis and flow profile near the bottom surface of the flask. As there are minimal changes to flow structure at different rotational speeds, only one speed of the results is presented for visualization purposes in each section to highlight the main flow feature within the flask, due to the significant number of variables in the study. The analyses mainly focus on velocity profile, shear stress distribution and vorticity. In imaging planes where the impeller was present, the impeller was masked out and excluded in the PIV calculation.

3.1. Fluid Flow in Meridional Plane

Measurements were conducted for three impeller heights and eight rotational speeds at each impeller location in meridional plane. For the purpose of visualization, Figures 5–7 show the velocity, shear and vorticity profiles at 60 RPM rotational speed. The rows and columns present the different angular positions and impeller locations, correspondingly. The impeller rotated into the page in all of results for the meridional plane.

As shown in Figure 5, the rotation of the impeller created significant recirculation behind the flat impeller due to the adverse pressure region behind the impeller paddle. The acceleration of fluid from the top and bottom part of the impeller towards the centre region gives rise to two counter rotating vortices in all impeller arrangements. However, when the impeller is placed at a higher position, the bottom vortex, which rotates in a clockwise direction, becomes more dominant than the top counter clockwise vortex. At 99 degrees, the case of a high position of the impeller records the highest velocity magnitude compared to other arrangements. As the impeller rotates, the velocity magnitude reduces while the vortices travel to the sidewall and away from the impeller towards the top or bottom corner of the imaged window. Although the fluid velocity decreases further downstream of the flat impeller, there is a slight increase in velocity of the top vortex at the high impeller position from 99 degrees to 135 degrees. Additionally, notable flow can be seen at the bottom surface of the bioreactor. In this region, the fluid moves radially inwards towards the centre of the flask before moving upwards. The upward velocity provides lift, ensuring the microcarriers are in suspension in the flask. Unlike the flow in the low and middle impeller positions, the velocity near the bottom surface does not drop significantly throughout the rotation period shown. These results are comparable to the characterisation study in single-use spinner flask, conducted by Kaiser *et al.* [32]. Maximum velocity was obtained at the tip of the flat impeller. Furthermore, the flow moved radially inwards at the bottom of the flask. However, without any additional view in meridional plane at different rotation angles in the study, we are unable to compare the flow features behind the flat impeller. On the other hand, the use of multiple axial impellers in a large scale flask in a study undertaken by Schirmaier *et al.* [38] creates high-velocity flow at the center of the flask. However, without any vector field presented in the study, it is not possible to determine whether the flow is primarily in the vertical or the radial direction.

Figure 5. Evolution of velocity magnitude contour overlaid on the velocity vectors for three impeller positions at 60 RPM. Highest velocity magnitude was achieved at the region downstream of the flat impeller at 99 degrees for all impeller arrangements.
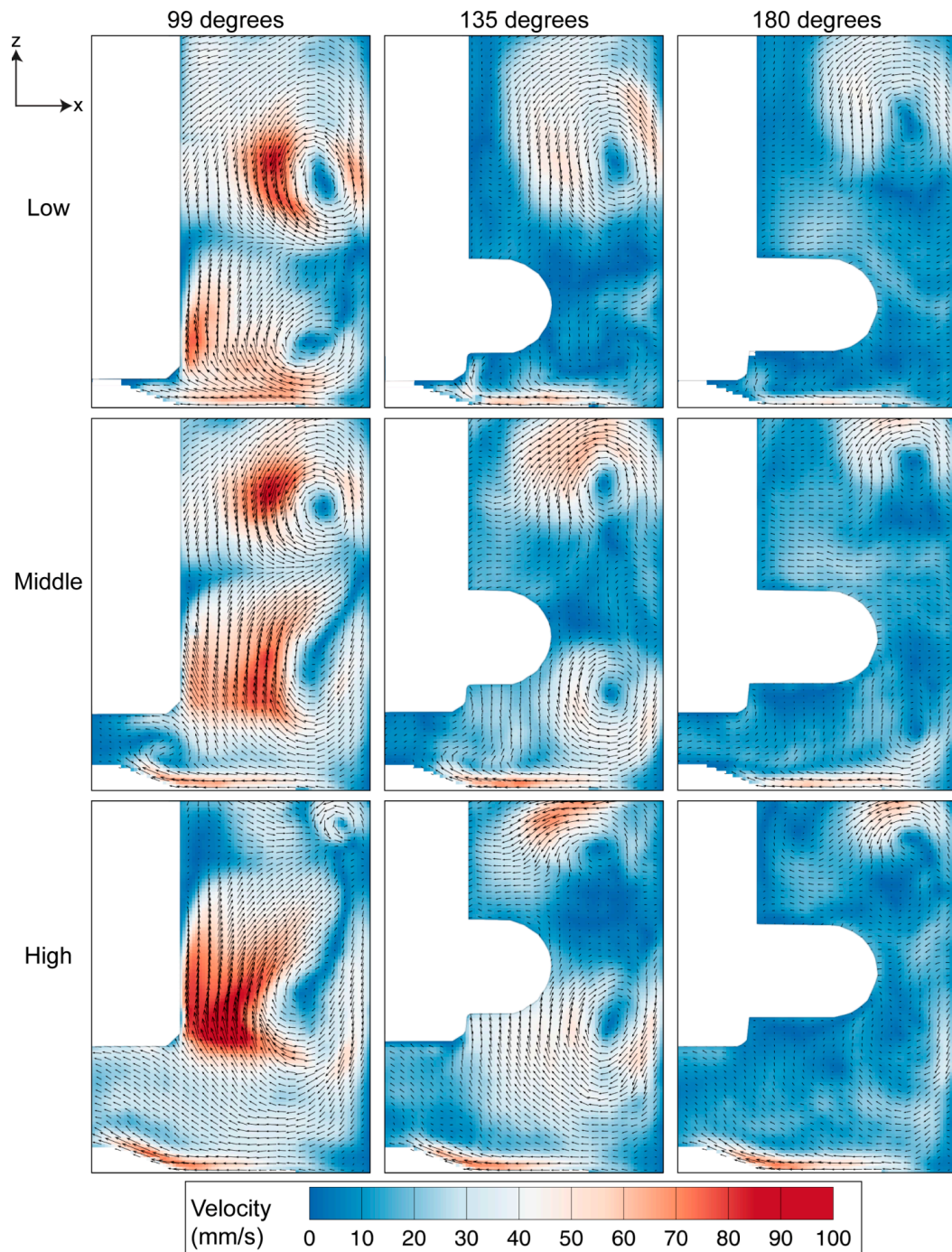
Figure 6. Vorticity evolution for three heights of the impeller, spun at 60 RPM. The magnitude of the vorticity reduces as the impeller rotates from 99 degrees to 180 degrees, with the highest vorticity strength occurring for the high impeller location.
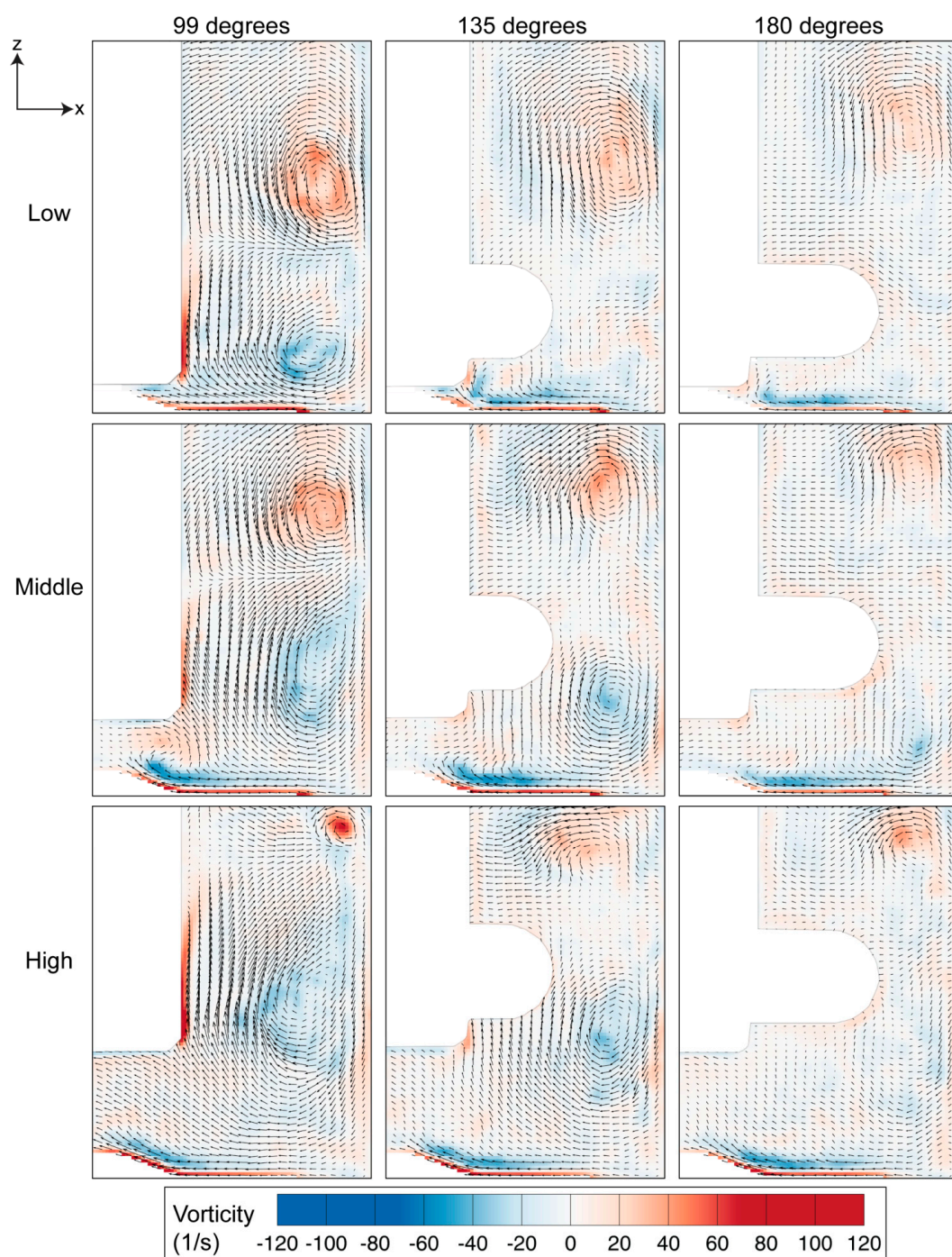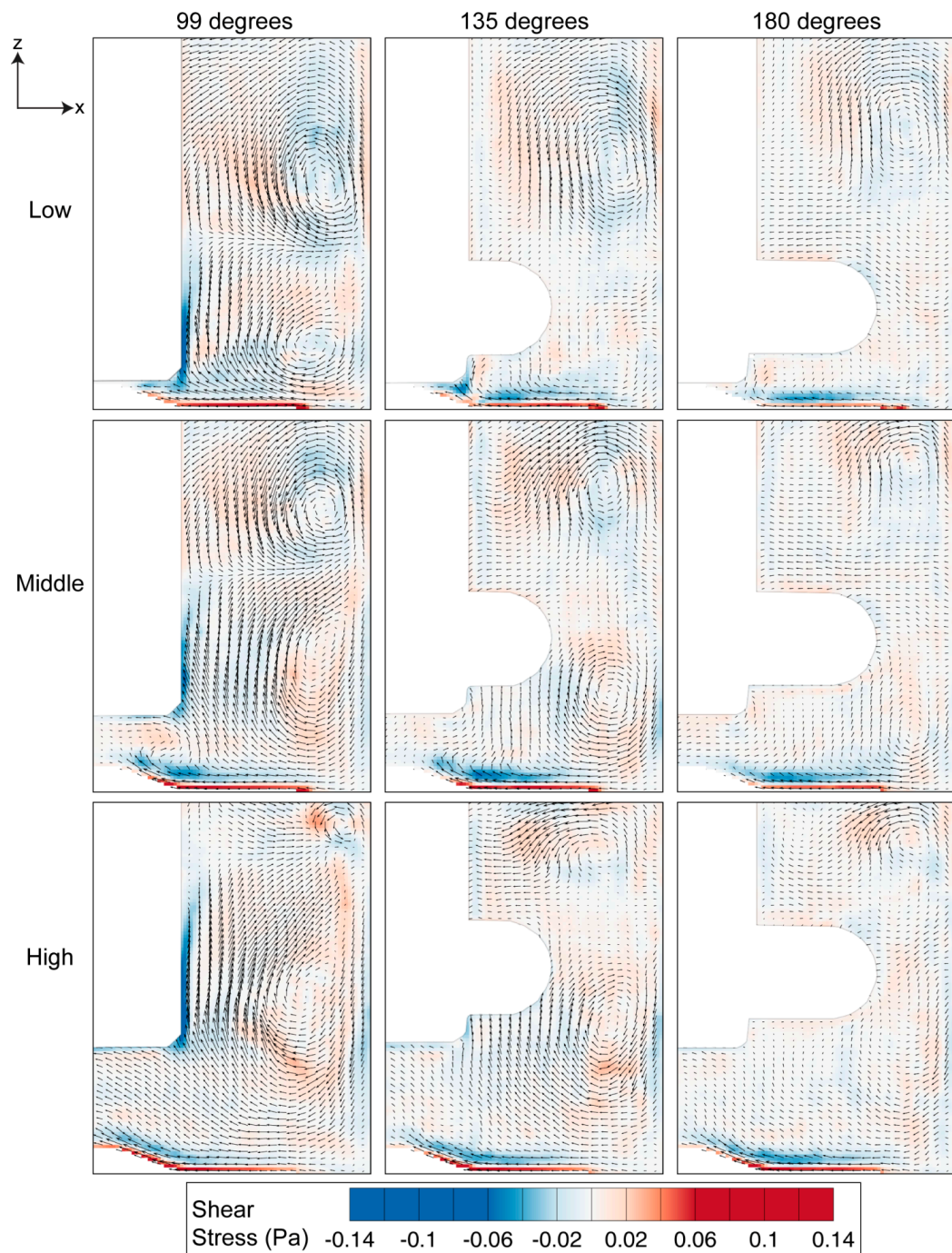
Figure 7. Shear stress distribution at three angular positions for 60 RPM. High stress region can be observed at the bottom wall and near the impeller, caused by the fluid-wall interaction.

Vortices provide a mixing mechanism that creates homogeneous environment in the spinner flask bioreactor. Throughout our analysis, as per convention, counter-clockwise vorticity is defined as positive. The two counter rotating vortices that exist in the flask therefore represent positive and negative vorticity values. The maximum vorticity magnitude occurs at 99 degrees and the magnitude decays as the impeller rotates to 180 degrees. At each impeller arrangement, the positive vorticity above the top half of the impeller is more dominant and clearly visible at 180 degrees compared to the clockwise rotating vortex near the bottom part of the impeller, which was not visible at a similar angular position. Although the size of the top vortex at the high impeller position is small, it has the highest vorticity magnitude that arose, due to the high velocity gradient in that region.

In the meridional plane, the shear stress is significant at the bottom surface of the flask and around the impeller shaft, as illustrated in Figure 7. With the highest fluid velocity occurring at 99 degrees, it is also clear that the magnitude of shear stress at this angular position is the most prominent relative to other angles. Additionally, the figure shows that the shear readings are strongly influenced by the fluid rotation in the lower part of the vessel. However, as the impeller is positioned at higher levels, the vortex is also located farther from the wall. With the vortex developed at a higher location, the fluid near the end wall is not severely affected by the recirculation phenomenon, thus producing lower shear margin at the base. The distribution of stress has not been presented in previous characterization studies [32,38]. The shear stress distribution within the spinner flask presented here would enable researchers to determine the critical location at which the shear stress is significant and its variation at different impeller angular positions.

Figure 8 shows the summary of the shear stress determined in the meridional plane for diverse impeller arrangements and speeds. Overall, it can be seen that the average and maximum shear stresses increase with rotational speed. Although the graphs are slightly different to each other at varying impeller positions, the main feature of the graph is maintained at increasing stirring speed, which confirms the consistency of the measurement. All graphs show similarity by having a sudden increase in shear stress at 90 degrees. At this angular position, the fluid achieves its highest velocity when the flat paddle passes the imaging plane. The rapid increase in velocity generates a high shear stress environment in the flask. Our results show that the middle impeller height has marginally higher mean and maximum stress magnitude. Furthermore, there is a significant drop in shear stress for low impeller alignment after the spike at 90 degrees. The observed behaviour results from the different position of vortices generated at varying impeller height that alters the velocity magnitude at the bottom wall. Although the graphs have some minor feature difference, there was not any prominent dissimilarity in terms of the stress distribution in the meridional flow profile for the given impeller locations.

Figure 8. Shear stress plots for three impeller arrangements and spun at speeds varying from 10 RPM to 80 RPM. Evolution of mean (**a**–**c**) and maximum shear stress (**d**–**f**) for various speeds and rotation angles. In all plots, significant increase in shear stress magnitude was obtained at 90 degrees, an angle at which the flat impeller is in the imaging plane. (**g**–**i**) Distribution functions of shear stress at speeds between 10 RPM and 80 RPM for different impeller heights.
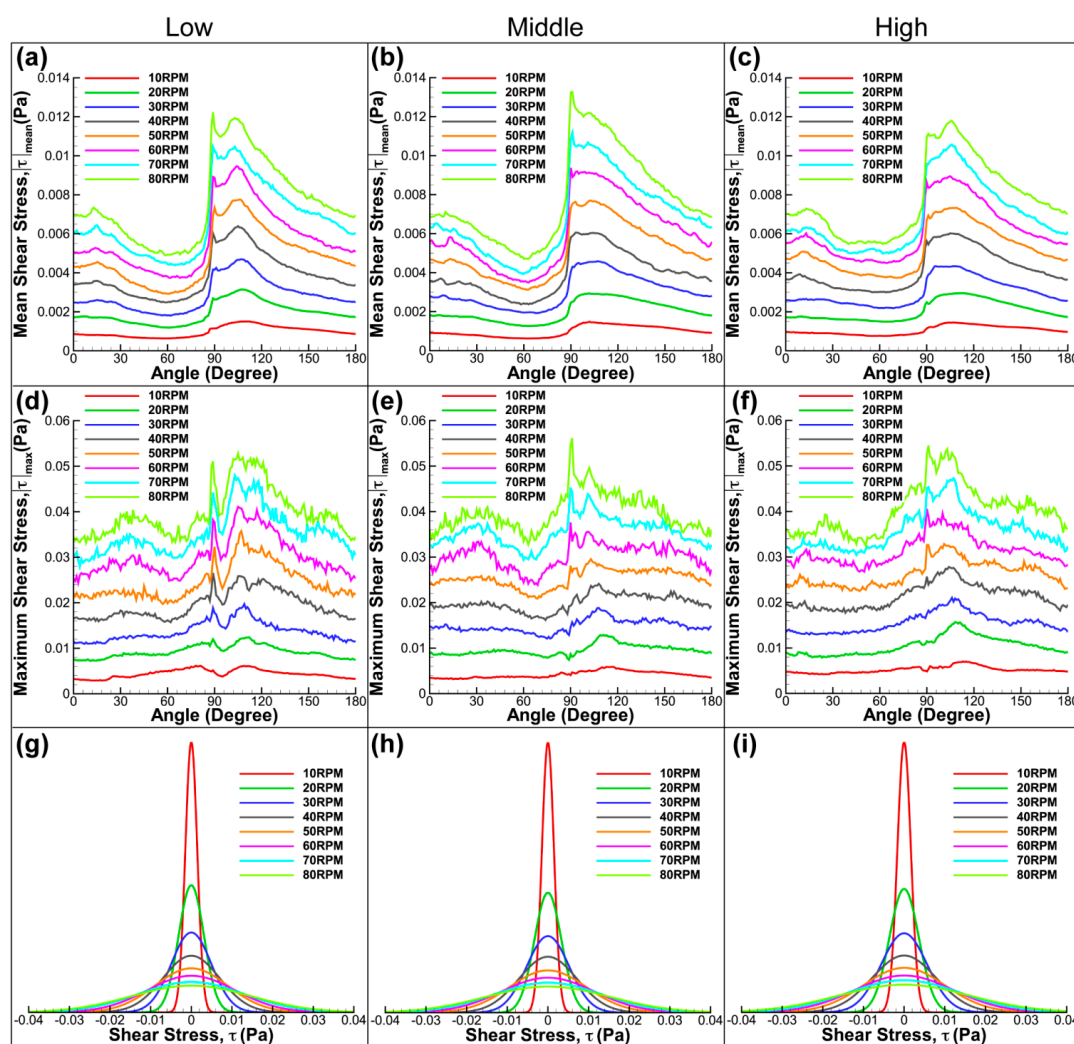
3.2. Fluid Behaviour at Middle Height of the Impeller in Azimuthal Plane

Velocity and shear stress profiles at middle height of the stir bar impeller are presented in Figures 9 and 10, respectively. As the impeller was present in the imaging plane during the image acquisition process, the impeller was masked and removed from the PIV calculation. Figure 9 shows that the fluid flow increases with increasing stirring speed. Due to the fact that the azimuthal velocity is a function of radius and angular speed, it is not surprising to see that the maximum velocity is

located at the tip of the flat paddle, similar to the findings in the literature [32,33]. As the main velocity component in the system, the velocity magnitude in the azimuthal plane is generally far greater than that in the meridional velocity. Minor radial motion can also be seen behind the impeller, which corresponds to the location of recirculation.

Figure 9. Velocity profile in azimuthal plane at middle height of the stirrer bar. The velocity magnitude increases with increasing impeller speed. Highest velocity is observed at the tip of the flat impeller for all rotational speeds.
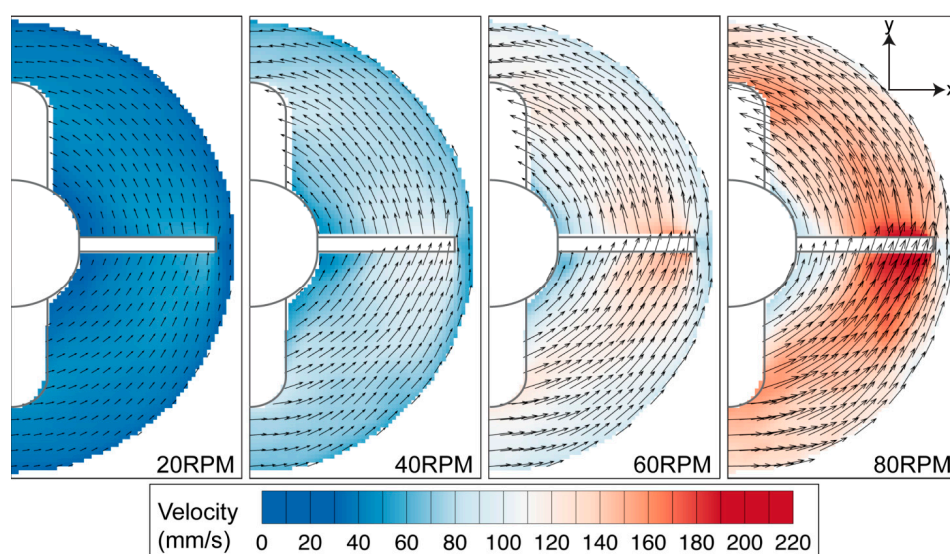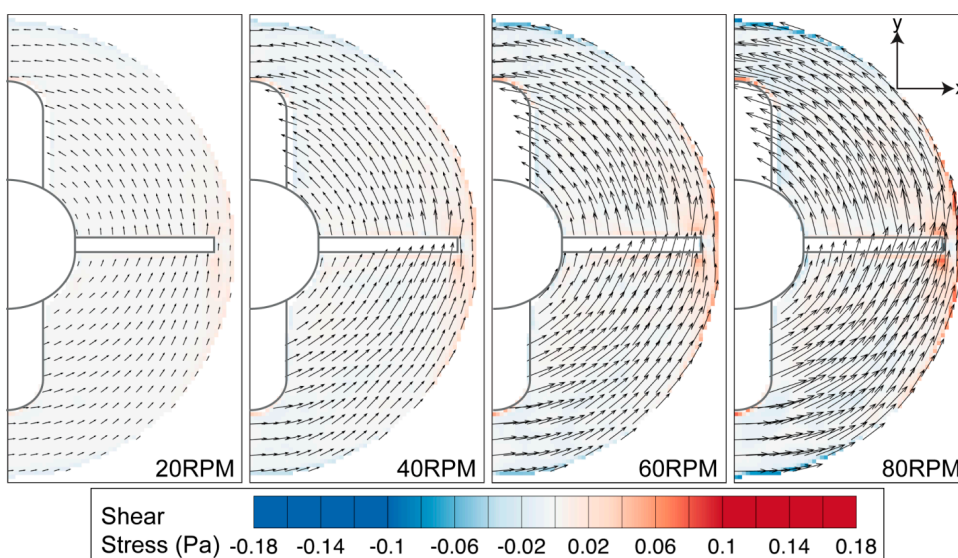

Figure 10. Azimuthal shear stress contour overlaid on velocity vectors. High stress region can be seen near the flask sidewall and around the impeller tip.

The high tangential velocity creates a high velocity gradient at the sidewall, as illustrated in Figure 10. Furthermore, noticeable shear can also be observed at the edge of the stirring bar. Overall, the shear magnitude is greatly dependent on the rotational speed. Figure 11 shows that the maximum shear stress of each speed varies linearly to the stirring rate of the impeller.

Figure 11. Maximum shear stress plot for azimuthal imaging plane at half of the stirrer bar height. The maximum shear stress varies linearly to the rotational speed.
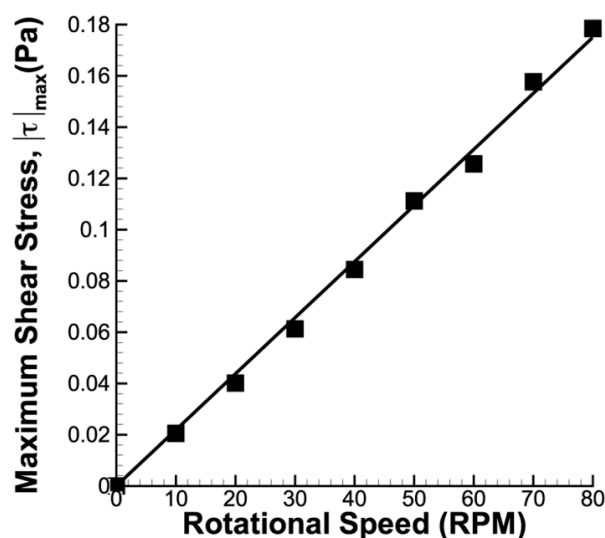
3.3. Fluid–Wall Interaction at the Bottom Surface of the Flask

To estimate the shear stress at the bottom wall, two measurements were conducted at $z = 0.75$ mm and 1.25 mm. The velocity close to the bottom surface was calculated by fitting a parabolic curve to the two velocity profiles, measured at two heights, and the no slip boundary condition at $z = 0$ mm. Using the estimated velocity, the velocity gradient and shear stress between the fluid in azimuthal plane and end wall was calculated. For the purpose of visualization, only the velocity and shear characteristic for 40 RPM is presented. Because the impeller does not present in the imaging plane for this analysis, the impeller is represented as dashed lines to show the rotation phase in each figure.

Figure 12 shows the velocity contour map of the fluid near the bottom surface. Being closer to the boundary, the flow at $z = 0.75$ mm has lower velocity than the flow at $z = 1.25$ mm. Additionally, unlike the flow profile in the middle height of the stirring bar, the vectors in Figure 12 showed that the fluid travels inwards towards the centre of the rotation and the flow then moves upwards in the meridional plane. Thus, higher radial velocity is observed at the bottom of the spinner flask.

Due to the flow in the flask being primarily in the azimuthal direction, the shear stress associated with interaction between the fluid flow and bottom surface, shown in Figure 13, is of a larger scale compared to previous shear analyses in the meridional plane (Figure 7) and at middle-impeller height (Figure 10). Figure 13 shows that vortex development, highlighted in meridional plane characterisation at different impeller heights, has minimal effect on the magnitude of the shear.

Figure 12. Velocity profiles near the bottom wall at 40 RPM spinning rate. The velocity near the wall ($z = 0.75$ mm) is lower than the velocity at location farther from the bottom wall ($z = 1.25$ mm).
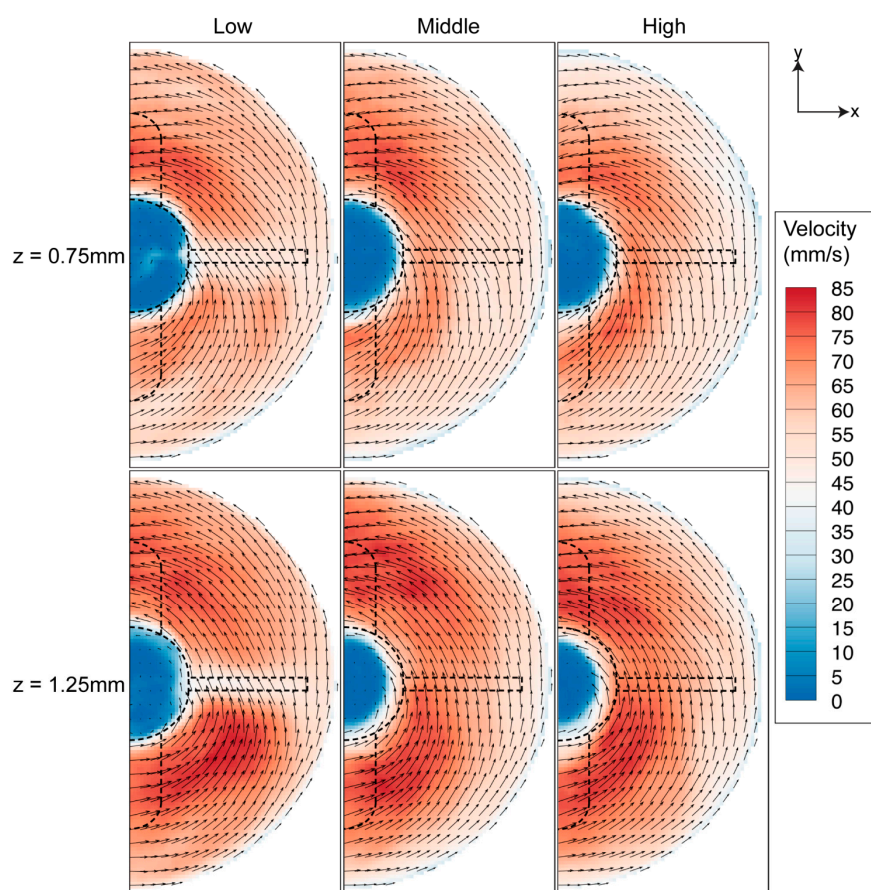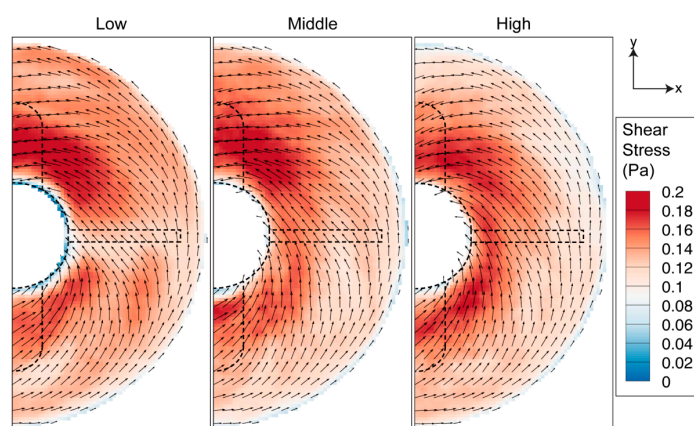

Figure 13. Shear stress contour near the bottom wall for 40 RPM rotational speed. The stress near the wall is higher in magnitude compared to other azimuthal measurement.

In terms of the shear stress magnitude caused by the fluid-wall interaction at the base, both mean and maximum stresses, presented in Figure 14, are significantly larger than those generated in the meridional plane (Figure 8) and fluid-sidewall interaction at the middle of the impeller (Figure 11). The mean and maximum shear stresses showed similar characteristics with lower gradients at lower speeds while evolving to higher gradients at higher speeds. Hemrajani *et al.* (2004) [39] mentioned that turbulent conditions are achieved at Reynolds number higher than 10^4, given that the Reynolds number is defined as Re = $\Omega D^2/\nu$. As the Reynolds number in our study is based on radial length, Re = $\Omega R^2/\nu$, similar conditions are achieved at a Reynolds number of 2500 and higher. The change in gradient may be caused by the transition from a laminar to turbulent flow regime, which occurs at around 37 RPM (Re = 2500) for the given flask dimensions. In the case where the impeller was positioned near the base, the mean and maximum shear stresses were found to be marginally higher than those for the lower impeller locations. In general, the impeller position has minimal effect on the shear stress at the bottom surface of the flask, although the difference in mean shear stress is more significant at higher speeds in the analysis. Overall, the shear stress magnitude is significant at high spinning rates, which will cause damage to the cells and limit the efficiency of the culture.

Figure 14. Shear stress plots for three impeller arrangements at varying impeller speed. The (**a**) mean and (**b**) maximum shear stresses increase with rotational speed. The magnitude obtained for the low impeller position is higher than for the other impeller locations.
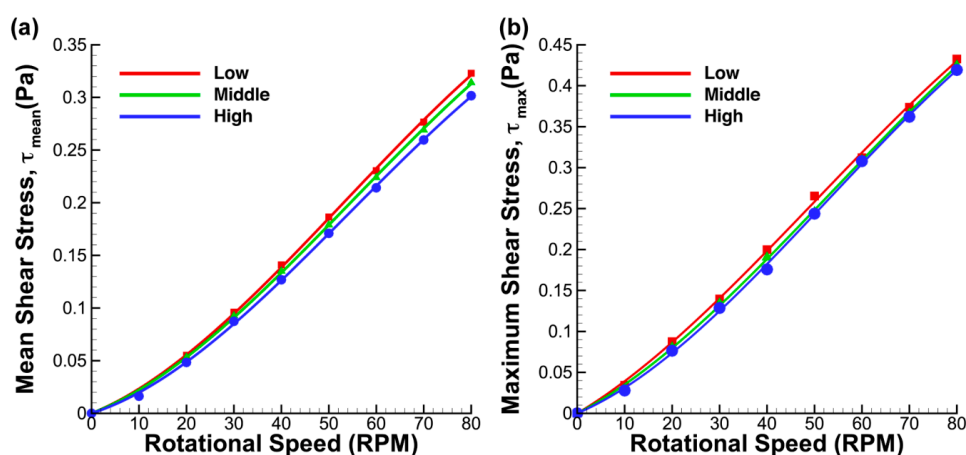

Figure 15 illustrates that the shear stress distribution was also not severely affected by the change in impeller position. However, unlike the shear stress distribution in the meridional plane, the shear stress distribution at the base skewed to higher magnitudes at increasing rotational speed. Due to the fact that the force at the bottom surface was highly dependent on the magnitude of the fluid velocity near the wall, it is not surprising to see that the peak of the distribution shifted to lower value as the impeller was placed at great heights. Microcarriers normally have higher density compared to the working fluid. Thus, they tend to sink and stay at the bottom of the flask. The flow analysis near the bottom wall will enable researchers to quantitatively determine the shear stress that may cause damage to any particular line of cells.

Figure 15. Histograms of shear stress magnitude at three impeller positions. The shear stress readings for (**a**) low, (**b**) middle and (**c**) high were skewed to higher magnitude at increasing rotational speeds.
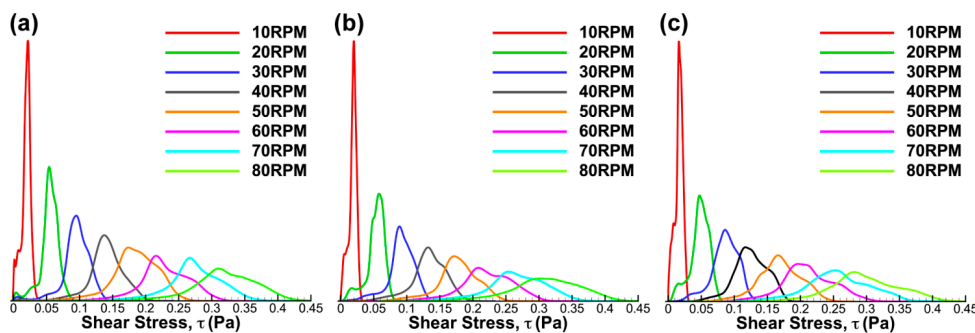
Comparing the stress distributions in this study to the investigations conducted by Kaiser *et al.* [32] and Schirmaier *et al.* [38], it can be deduced that the peak of shear stresses occurred due to fluid-wall interaction at the bottom of the flask. The trend of the histograms agrees with the results obtained in the aforementioned studies.

This study highlights the flow and mechanical characteristics within the spinner flask. Although the required average shear stress for various cell culture procedure and the maximum stress they can withstand are still unknown, given this information from cell culture experiments in a simple shear flow, the required speed for the culture protocol can be determined based on the characterization findings presented in this study. Moreover, the shear margin in many published works can be estimated using the data shown in the current study. The knowledge gained through flow characterization would enable researchers to find the optimum flow condition for cell growth. The optimum flow condition could then be used as design requirement for the development of more efficient bioreactors, tailor-made for specific cell type.

4. Conclusions

This study presents detailed quantitative characterization of the flow in the spinner flask bioreactor for varying impeller vertical position and agitation speed. In all imaging planes, the velocities and shear stresses increase with the spinning rate. In the meridional flow analysis, higher vorticity and more extensive recirculation were obtained when the impeller was placed closer to the upper free surface. The highest shear magnitude was observed near the bottom surface of the flask. The fluid-wall interaction in this region is significantly greater than at the middle height of the impeller. Overall, the impeller position has minimal impact on the shear stress in the bioreactor.

Apart from understanding the flow behavior in the spinner flask bioreactor, the results obtained in this study will enable researchers to quantify the shear stress exerted on cells in culture. Furthermore, the analysis in this study can be used as a datasheet and provide an estimate of the shear stress magnitude and its distribution of the previously published cell studies that utilized similar setup. If the required biomechanical properties for a specific cell lineage are known, the corresponding culture speed can be determined based on the shear stress datasheet for the spinner flask, thus optimizing

the testing phase time. Additionally, these flow parameters can be used as design requirements for the development of more efficient bioreactors, and ultimately improving the efficiency of cell culture. Future work includes systematic optimization studies for different cell types to determine their optimum culture conditions. Moreover, by conducting similar fluid mechanics analysis for different bioreactor designs, it would enable the required biomechanical parameters knowledge for a certain cell type to be transferable to other bioreactors, should a different bioreactor need to be utilized.

Acknowledgments

Author Contributions

M.I. and A.F. conceived and designed the experiments; M.I. performed the experiments and analyzed the data; K.H. and A.F. contributed reagents/materials/analysis tools; M.I., K.H. and A.F. wrote the paper.

Conflicts of Interest

The authors declare no conflict of interest.

References

1. Thomson, J.A.; Itskovitz-Eldor, J.; Shapiro, S.S.; Waknitz, M.A.; Swiergiel, J.J.; Marshall, V.S.; Jones, J.M. Embryonic stem cell lines derived from human blastocysts. *Science* **1998**, *282*, 1145–1147.
2. Dexter, T.M.; Allen, T.D.; Lajtha, L.G.; Schofield, R.; Lord, B.I. Stimulation of differentiation and proliferation of haemopoietic cells *in vitro*. *J. Cell. Physiol.* **1973**, *83*, 461–473.
3. Collins, P.C.; Miller, W.M.; Papoutsakis, E.T. Stirred culture of peripheral and cord blood hematopoietic cells offers advantages over traditional static systems for clinically relevant applications. *Biotechnol. Bioeng.* **1998**, *59*, 534–543.
4. Cabral, J.M.S. *Ex vivo* expansion of hematopoietic stem cells in bioreactors. *Biotechnol. Lett.* **2001**, *23*, 741–751.
5. Goodwin, T.J.; Schroeder, W.F.; Wolf, D.A.; Moyer, M.P. Rotating-wall vessel coculture of small intestine as a prelude to a tissue modelling: Aspects of simulated microgravity. *Proc. Soc. Exp. Biol. Med.* **1993**, *202*, 181–192.
6. Freed, L.E.; Vunjak-Novakovic, G. Microgravity tissue engineering. *In Vitro Cell. Dev. Biol. Anim.* **1997**, *33*, 381–385.
7. Gerecht-Nir, S.; Itskovitz-Eldor, J. Cell therapy using human embryonic stem cells. *Transpl. Immunol.* **2004**, *12*, 203–209.
8. Kallos, M.; Sen, A.; Behie, L. Large-scale expansion of mammalian neural stem cells: A review. *Med. Biol. Eng. Comput.* **2003**, *41*, 271–282.

9. Cabrita, G.J.M.; Ferreira, B.S.; da Silva, C.L.; Goncalves, R.; Almeida-Porada, G.; Cabral, J.M.S. Hematopoietic stem cells: From the bone to the bioreactor. *Trends Biotechnol.* **2003**, *21*, 233–240.

10. Zandstra, P.W.; Bauwens, C.; Yin, T.; Liu, Q.; Schiller, H.; Zweigerdt, R.; Pasumarthi, K.B.S.; Field, L.J. Scalable production of embryonic stem cell-derived cardiomyocytes. *Tissue Eng.* **2003**, *9*, 767–778.

11. Thouas, G.A.; Sheridan, J.; Hourigan, K. A bioreactor model of mouse tumor progression. *J. Biomed. Biotechnol.* **2007**, *2007*, 32754.

12. Dusting, J.; Sheridan, J.; Hourigan, K. A fluid dynamics approach to bioreactor design for cell and tissue culture. *Biotechnol. Bioeng.* **2006**, *94*, 1196–1208.

13. Singh, H.; Teoh, S.H.; Low, H.T.; Hutmacher, D.W. Flow modelling within a scaffold under the influence of uni-axial and bi-axial bioreactor rotation. *J. Biotechnol.* **2005**, *119*, 181–196.

14. Cormier, J.T.; Zur Nieden, N.I.; Rancourt, D.E.; Kallos, M.S. Expansion of undifferentiated murine embryonic stem cells as aggregates in suspension culture bioreactors. *Tissue Eng.* **2006**, *12*, 3233–3245.

15. Mukhopadhyay, A.; Madhusudhan, T.; Kumar, R. Hematopoietic stem cells: Clinical requirements and developments in *ex-vivo* culture. *Adv. Biochem. Eng. Biotechnol.* **2004**, *86*, 215–253.

16. Schroeder, M.; Niebruegge, S.; Werner, A.; Willbold, E.; Burg, M.; Ruediger, M.; Field, L.J.; Lehmann, J.; Zweigerdt, R. Differentiation and lineage selection of mouse embryonic stem cells in a stirred bench scale bioreactor with automated process control. *Biotechnol. Bioeng.* **2005**, *92*, 920–933.

17. Stiehler, M.; Bünger, C.; Baatrup, A.; Lind, M.; Kassem, M.; Mygind, T. Effect of dynamic 3-D culture on proliferation, distribution and osteogenic differentiation of human mesenchymal stem cells. *J. Biomed. Mater. Res. Part A* **2008**, *89A*, 96–107.

18. Zhang, Z.-Y.; Teoh, S.H.; Chong, W.-S.; Foo, T.-T.; Chng, Y.-C.; Choolani, M.; Chan, J. A biaxial rotating bioreactor for the culture of fetal mesenchymal stem cells for bone tissue engineering. *Biomaterials* **2009**, *30*, 2694–2704.

19. Meinel, L.; Karageorgiou, V.; Fajardo, R.; Snyder, B.; Shinde-Patil, V.; Zichner, L.; Kaplan, D.; Langer, R.; Vunjak-Novakovic, G. Bone tissue engineering using human mesenchymal stem cells: Effects of scaffold material and medium flow. *Ann. Biomed. Eng.* **2004**, *32*, 112–122.

20. Nie, Y.; Bergendahl, V.; Hei, D.J.; Jones, J.M.; Palecek, S.P. Scalable culture and cryopreservation of human embryonic stem cells on microcarriers. *Biotechnol. Prog.* **2009**, *25*, 20–31.

21. Phillips, B.W.; Lim, R.Y.M.; Tan, T.T.; Rust, W.L.; Crook, J.M. Efficient expansion of clinical-grade human fibroblasts on microcarriers: Cells suitable for *ex vivo* expansion of clinical-grade hESCs. *J. Biotechnol.* **2008**, *134*, 79–87.

22. Kuriyama, S.; Nakano, T.; Yoshimura, N.; Ohuchi, T.; Moritera, T.; Honda, Y. Mass cultivation of human retinal pigment epithelial cells with microcarrier. *Opthamologica* **1992**, *205*, 89–95.

23. Frauenschuh, S.; Reichmann, E.; Ibold, Y.; Goetz, P.M.; Sittinger, M.; Ringe, J. A microcarrier-based cultivation system for expansion of primary mesenchymal stem cells. *Biotechnol. Prog.* **2007**, *23*, 187–193.

24. Schop, D.; Janssen, F.W.; Borgart, E.; de Bruijn, J.D.; van Dijkhuizen-Radersma, R. Expansion of mesenchymal stem cells using a microcarrier-based cultivation system: Growth and metabolism. *J. Tissue Eng. Regen. Med.* **2008**, *2*, 126–135.

25. Fernandes, A.M.; Marinho, P.A.N.; Sartore, R.C.; Paulsen, B.S.; Mariante, R.M.; Castilho, L.R.; Rehen, S.K. Successful scale-up of human embryonic stem cell production in a stirred microcarrier culture system. *Braz. J. Med. Biol. Res.* **2009**, *42*, 515–522.

26. Frith, J.E.; Thomson, B.; Genever, P.G. Dynamic three-dimensional culture methods enhance mesenchymal stem cell properties and increase therapeutic potential. *Tissue Eng. Part C* **2010**, *16*, 735–749.

27. Alfred, R.; Gareau, T.; Krawetz, R.; Rancourt, D.; Kallos, M. Serum-free scaled up expansion and differentiation of murine embryonic stem cells to osteoblasts in suspension bioreactors. *Biotechnol. Bioeng.* **2010**, *106*, 829–840.

28. Hewitt, C.J.; Lee, K.; Nienow, A.W.; Thomas, R.J.; Smith, M.; Thomas, C.R. Expansion of human mesenchymal stem cells on microcarriers. *Biotechnol. Lett.* **2011**, *33*, 2325–2335.

29. Sucosky, P.; Osorio, D.F.; Brown, J.B.; Neitzel, G.P. Fluid mechanics of spinner flask bioreactor. *Biotechnol. Bioeng.* **2003**, *85*, 34–46.

30. Meunier, P.; Hourigan, K. Mixing in a vortex breakdown flow. *J. Fluid Mech.* **2013**, *731*, 195–222.

31. Mununga, L.; Lo Jacono, D.; Sørensen, J.N.; Leweke, T.; Thomson, M.; Hourigan, K. Control of confined vortex breakdown with partial rotating lids. *J. Fluid Mech.* **2014**, *738*, 5–33.

32. Kaiser, S.C.; Jossen, V.; Schirmaier, C.; Eibl, D.; Brill, S.; van den Bos, C.; Eibl, R. Fluid flow and cell proliferation of mesenchymal adipose-derived stem cells in small-scale, stirred, single-use bioreactors. *Chem. Ing. Tech.* **2012**, *85*, 95–102.

33. Liovic, P.; Sutalo, I.D.; Stewart, R.; Glattauer, V.; Meagher, L. Fluid flow and stresses on microcarriers in spinner flask bioreactors. In Proceedings of the Ninth International Conference on CFD in the Minerals and Process Industries, CSIRO, Melbourne, VIC, Australia, 10–12 December 2012.

34. Ismadi, M.-Z.; Higgins, S.; Samarage, R.; Paganin, D.; Hourigan, K.; Fouras, A. Optimisation of a stirred bioreactor through the use of a novel holographic correlation velocimetry flow measurement technique. *PLoS One* **2013**, *8*, e65714.

35. Gupta, P.; Ismadi, M.-Z.; Verma, P.; Fouras, A.; Jadhav, S.; Bellare, J.; Hourigan, K. Optimisation of agitation speed in spinner flask for microcarrier structural integrity and expansion of induced pluripotent stem cells. *Cytotechnology* **2014**, doi:10.1007/s10616-014-9750-z.

36. Fouras, A.; Lo Jacono, D.; Nguyen, C.V.; Hourigan, K. Volumetric correlation PIV: A technique for 3D velocity vector field measurement. *Exp. Fluids* **2009**, *47*, 569–577.

37. Fouras, A.; Lo Jacono, D.; Hourigan, K. Target-free Stereo PIV: A novel technique with inherent error estimation and improved accuracy. *Exp. Fluids* **2008**, *44*, 317–329.

38. Schirmaier, C.; Jossen, V.; Kaiser, S.C.; Jüngerkes, F.; Brill, S.; Safazi-Nab, A.; Siehoff, A.; van den Bos, C.; Eibl, D.; Eibl, R. Scale-up of adipose tissue-derived mesenchymal stem cell production in stirred single-use bioreactors under low-serum conditions. *Eng. Life Sci.* **2014**, *14*, 292–303.

39. Hemrajani, R.R.; Tatterson, G.B. Mechanically stirred vessels. In *Handbook of Industrial Mixing: Science and Practice*; Paul, E.I., Atiemo-Obeng, V.A., Kresta, S.M., Eds.; John Wiley & Sons, Inc.: Hoboken, NJ, USA, 2004; p. 345.

4.2   Discussion and Conclusion

The present study describes the quantitative flow mechanics in a spinner flask bioreactor between 10RPM (Re = 668) and 80RPM (Re = 5341). The speed margin was chosen due to the high number of suspension culture studies that fell under this parameter. The vertical position of the impeller altered the structure of the flow, especially in the meridional plane. The extensive recirculation in the meridional plane provides an extensive mixing mechanism of the medium in culture procedures. Having flow primarily in the azimuthal direction, the highest shear was recorded at the bottom wall of the flask. It was also found that the impeller position had minimal effect on the magnitude of the stress.

The use of Reynolds number in this study generalises the flow condition and ensures applicability of the results in other systems. Furthermore, the wide range of variables covered in the article will allow an estimate of the shear magnitude in previous culture experiments to be made, thus improving the understanding of the relation between cell growth and mechanical forces associated to the flow within the bioreactor. A study in the next chapter describes the biomechanical parameters in fluid flow for optimum growth of mouse iPS cells and the effect of mechanical force on microcarrier structure.

Chapter 5

Biomechanical Parameters for Induced Pluripotent Stem Cell Culture Application

THE previous chapter underlines the quantitative flow mechanics for various impeller positions and rotational speeds. The results can be used as a datasheet for cell studies. This chapter presents the mechanical parameter characterisation in the spinner flask bioreactor, specifically refined for mouse iPSC culture protocols.

The use of microcarriers has been proven to aid cell growth in dynamic culture systems as explained in section 2.4.4. Microcarriers provide higher surface-area-to-volume ratio to accommodate higher cell densities. It also provides versatility by allowing various surface coatings and treatments to support a wide range of cell growth. However, the effects of stresses within the flow on the microcarriers are unknown. The effect of dynamic force on the structure of microcarriers is described in this chapter. Employing microcarrier culture protocols, this study aims to determine the biomechanical parameters within the flow that correspond to the optimum cell growth.

An article describing an experimental approach of fluid flow characterisation in a 100mL Bellco spinner flask bioreactor is presented. The set up employed in this study is slightly different to the previous chapter. Due to the fragility and sensitivity of mouse iPSCs to dynamic force, only a partial section of the impeller is immersed in the medium. Utilising conventional 2D PIV, several measurements were conducted in azimuthal and meridional planes between 20RPM (Re = 1335) to 45RPM (Re = 3004) rotational speeds, at increments of 5RPM (Re = 334). Similar to the previous chapter, the mechanical parameters, such as velocity, shear stress and vorticity, were

given emphasis. The error bars in the manuscript represent the standard deviation of the results.

The subsequent section explains a parallel study that analysed the impact of rotational speed on the structure of microcarriers. Cells were then grown in a similar setup at different rotational speeds over 7 days. Mouse OG2 iPSCs were used in all cell experiments presented in this thesis. The cells were derived in-house from a single animal, using the same protocol as Tat *et al.* (2010) to ensure consistency of the experiments. Mouse OG2 iPS cells are transgenic induced pluripotent stem cells for which the GFP (Green Fluorescent Protein) expression is controlled by the pluripotent gene Oct4 promoter. The protein in the cells is able to emit fluorescent when they are exposed to fluorescence light as long as they are alive.

In the cell experiments, hemocytometer and trypan blue assay are widely used techniques to count quantitatively the number of cells and determine the cell viability. In this study, the cells were initially washed with PBS and detached from the microcarriers using 1X Tryple Express (Life Technologies, Carlasbad, USA). The microcarrier-cell mixture was then filtered through a 100μm strainer to remove the microcarriers. Then, a small amount cell suspension sample, typically 0.2mL, was mixed with 0.3mL of Hanks Balanced Salt (HBSS) and 0.5mL of 4% Trypan Blue solution (w/v) for a dilution factor of 5. Then, a small amount of cell suspension-trypan blue mixture was pipetted to both chambers of hemocytometer. The cells were then manually counted for each 1mm^2 under a light microscope. With the cover in place, each square had a total volume of 0.1mm^3 or 10^{-4}mL. Knowing the number of total cells in a square (10^{-4}mL), one could simply multiply it to the dilution and conversion factor to get number of cells per mL, as shown in equation below. Using similar method, the viability of a cell protocol could be calculated by counting the number of viable cells (unstained) in each square. By dividing the number of viable cells to the total cell count, the viability fraction was obtained. The procedure was normally repeated and the average is taken as the final value.

$$Cell\ Count/mL = Average\ count\ per\ square\ (Cells/10^{-4}mL) \times Dilution\ Factor \times 10^4$$

(5.1)

$$Cell\ Viability\ (\%) = \frac{Live\ Cell\ Count\ (Cells/mL)}{Total\ Cell\ Count\ (Cells/mL)} \times 100$$

(5.2)

Unlike trypan blue assay, Oct4-GFP expression technique is a qualitative analysis. As mentioned before, the cells used in this study (mouse OG2 iPSCs) have a GFP transgene under the control of the promoter of the pluripotent gene Oct4. The live cells emitted fluorescence under a fluorescence microscope. Due to the simplicity of identifying live and dead cells, Oct4-GFP expression technique provided quick and accurate qualitative results of a sample.

Overall, this study provides insight into biomechanical parameters within the bioreactor and its effect on microcarriers and cell growth. The parameter characterisation will enable researchers to define the required design parameters for future microcarriers and bioreactor developments.

5.1 Article III: Flow Characterisation of A Spinner Flask for Induced Pluripotent Stem Cell Application

The following manuscript was published in *PLoS ONE* in 2014. This work was co-authored by Priyanka Gupta, Andreas Fouras, Paul Verma, Sameer Jadhav, Jayesh Bellare and Kerry Hourigan. The article reproduced in this thesis is directly taken from the published version without alteration.

Declaration

Monash University

Declaration for Thesis Section 5.1

Declaration by candidate

In the case of Section 5.1, the nature and extent of my contribution to the work was the following:

Nature of contribution	Extent of contribution (%)
Conceived, designed and performed experiments. Analysed the data and wrote the manuscript.	80%

The following co-authors contributed to the work. If co-authors are students at Monash University, the extent of their contribution in percentage terms must be stated:

Name	Nature of contribution	Extent of contribution (%) for student co-authors only
P. Gupta	Performed the reference biological experiments	10%
A. Fouras *	Technical advice and revised manuscript	NA
P. Verma	Technical advice and revised manuscript	NA
S. Jadhav	Technical advice	NA
J. Bellare	Technical advice	NA
K. Hourigan	Technical advice and revised manuscript	NA

The undersigned hereby certify that the above declaration correctly reflects the nature and extent of the candidate's and co-authors' contributions to this work*.

Candidate's Signature		Date 01 AUG 2014

Main Supervisor's Signature		Date 01 AUG 2014

PLOS ONE

Flow Characterization of a Spinner Flask for Induced Pluripotent Stem Cell Culture Application

Mohd-Zulhilmi Ismadi[1,2]*, Priyanka Gupta[1,3,4], Andreas Fouras[1,2], Paul Verma[1,5], Sameer Jadhav[4], Jayesh Bellare[4], Kerry Hourigan[1,2]

1 Division of Biological Engineering, Monash University, Melbourne, Victoria, Australia, **2** Department of Mechanical and Aerospace Engineering, Monash University, Melbourne, Victoria, Australia, **3** Department of Chemical Engineering, Monash University, Melbourne, Victoria, Australia, **4** Department of Chemical Engineering, Indian Institute of Technology Bombay, Mumbai, India, **5** South Australian Research and Development Institute, Rosedale, South Australia, Australia

Abstract

We present detailed quantitative measurement analyses for flow in a spinner flask with spinning rates between 20 to 45 RPM, utilizing the optical velocimetry measurement technique of Particle Image Velocimetry (PIV). A partial section of the impeller was immersed in the working fluid to reduce the shear forces induced on the cells cultured on microcarriers. Higher rotational speeds improved the mixing effect in the medium at the expense of a higher shear environment. It was found that the mouse induced pluripotent stem (iPS) cells achieved the optimum number of cells over 7 days in 25 RPM suspension culture. This condition translates to 0.0984 Pa of maximum shear stress caused by the interaction of the fluid flow with the bottom surface. However, inverse cell growth was obtained at 28 RPM culture condition. Such a narrow margin demonstrated that mouse iPS cells cultured on microcarriers are very sensitive to mechanical forces. This study provides insight to biomechanical parameters, specifically the shear stress distribution, for a commercially available spinner flask over a wide range of Reynolds number.

Data Availability: The authors confirm that all data underlying the findings are fully available without restriction. All relevant data are within the paper.

Competing Interests: The authors have declared that no competing interests exist.

Introduction

Neurodegenerative disorders such as Alzheimer's disease, brain and spinal injuries, and Parkinson's disease affect more than 6 million people in North America. The number of cases can be translated to over 150 billion dollars in healthcare costs each year [1]. Methods for repairing and replacing damaged or absent tissues and organs have been of major interest to relieve the immense burden in healthcare expenditure and also to improve quality of human life.

Since the development of pluripotent stem cells, such as embryonic stem (ES) cells and induced pluripotent stem (iPS) cells, the focus in regenerative medicine has shifted from organ transplantation to cell therapy. Due to the stem cells' self-renewing nature and ability to differentiate to various types of cells, the stem cell is the perfect basic material for treatment of degenerative diseases. Scientific research can also benefit from the renewal ability by having a large number of the cells available through the proliferation process.

One of the major shortcomings of stem cell therapy is that it requires a significant number of cells. For example, one to two billion cardiomyocytes are required in order to treat damaged heart tissue after myocardial infarction, and about 1.3 billion insulin-producing β cells are needed to realize insulin independence for diabetes patients [2]. The bioreactor has been used as a device to proliferate cells to larger numbers as well to guide the cells in the differentiation process. As a result, optimizing the bioreactor has been of major research interest [3,4,5] to achieve a high cell number required for therapeutic purposes. Bioreactor design for cell culture varies from the perfusion bioreactor [6,7,8], the rotating wall bioreactor [9,10,11] to the most-commonly used spinner flask bioreactor [12,13,14,15]. It is important that the bioreactor allows control over the characteristics of the serum environment such as pH, oxygen dissolution rate, temperature, nutrient transfer, and mechanical stimulation to ensure repeatability and reproducibility of the cells. However, the optimized condition is highly dependent on the type of the cell. Thus, designing a bioreactor for general cell culture use is a major challenge.

The spinner flask bioreactor is widely used in culture procedure due to its availability, ease of setup and also its ability to provide a homogeneous condition throughout the process. Although it is difficult to design a generic bioreactor for a wide-range of cell types, the spinner flask has been proven to derive a wide range of cells by varying the agitation rates [14,15,16,17,18]. Niebruegge et al. [17] and Zandstra et al. [15] were able to grow cardiomyocytes at 60 RPM. On top of being able to grow multipotent cells, the spinner flask has been demonstrated to be able to grow pluripotent cells. Mouse and human ES cells were successfully grown in a spinner flask at 80 RPM, as shown by
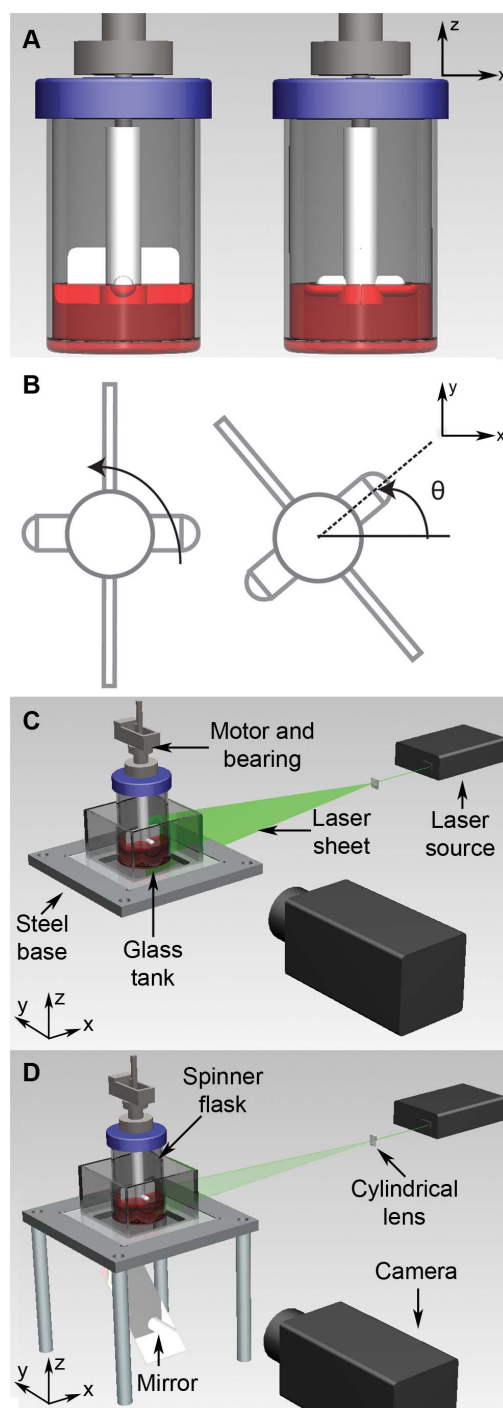
Figure 1. Experimental configuration for PIV measurement in spinner flask bioreactor. A) The impeller consisted of a thin rectangular Teflon sheet and a magnetic stirring bar. The middle height of the magnetic rod was placed at the fluid level throughout the experiment. B) Top view of the impeller. The impeller rotates in counter-clockwise direction throughout the experiment. The spinner flask was placed inside a square tank filled with water to eliminate the lensing effect due to the flask curvature. The working fluid was seeded with 31 µm fluorescent particles and agitated by the impeller driven by a stepper motor. A cylindrical lens was used to create a laser sheet to illuminate the imaging region. The seeded flow was imaged with a high-speed camera (IDT Y4). C) In the meridional plane imaging configuration, the laser sheet was aligned vertically and placed at the center of the flask. D) For measurements in the azimuthal plane, the laser sheet was aligned to the horizontal plane and a mirror was placed underneath the setup to allow view access to the illuminated region.
doi:10.1371/journal.pone.0106493.g001

Schroeder et al. [14] and Cameron et al. [16], respectively. Furthermore, the cell yield can be further enhanced by the introduction of microcarriers, which increase the surface area for cell growth as shown in previous studies [19,20,21,22,23,24].

There is no specific recipe or protocol for cell culture. The procedure to grow cells is different, depending on the type of cells used. Furthermore, there are no specific guidelines in terms of the rotational speed, chemistry and volume of culture medium. In most studies, the location of the impeller is not mentioned. In order to improve the cell culture system as a whole, it is necessary to outline a specific protocol, which would allow optimization of various aspects of cell culture to be done independently.

Flow characterization and hydrodynamic force are aspects that have been overlooked in the past in developing cell culture protocols as well as the bioreactor designs. As these properties are out of the biologists' or cell culturists' area of expertise, most cell studies correlate the number of the cells directly to the stirring rate, without understanding the details of the flow behavior in the reactor. Moreover, the lack of understanding in mechanical interaction with the cells limits the progression of bioreactor technology. Several published studies have attempted to understand the fluid dynamics using experimental and computational methods [25,26,27,28]. However, only a few of these studies examined the importance of hydrodynamic force [25,27]. Furthermore, some studies used a novel type bioreactor as the focal area of analysis while others focused on the flow around a construct or scaffold, rather than profiling the flow in commercially available bioreactors [27,29,30,31]. Recently, a novel holographic technique was developed to characterize the flow condition in the spinner flask [32]. Furthermore, Gupta et al. [33] systematically investigated the effect of rotational speed on microcarrier structures and cell growth. The understanding of fluid mechanics in bioreactors is necessary to provide insights into enhancing the bioreactor efficiency, thus improving the culture process.

This article describes an experimental approach to characterize the fluid dynamics in a 100 mL Bellco spinner flask. The Bellco spinner flask was chosen for this study due to its common impeller design and its frequent use for biological work. Velocimetry techniques have been known to be able to analyze complex flows in diverse applications. In this study, Particle Image Velocimetry (PIV) is chosen to quantitatively describe the meridional and azimuthal flow profiles in the bioreactor.

PIV is a full field, optical-based measurement technique that has been developed for more than twenty years. The technique statistically measures the displacement of the scattered light between consecutive images, captured by a high-speed camera. The scattered light is produced by tracer particles seeded in the
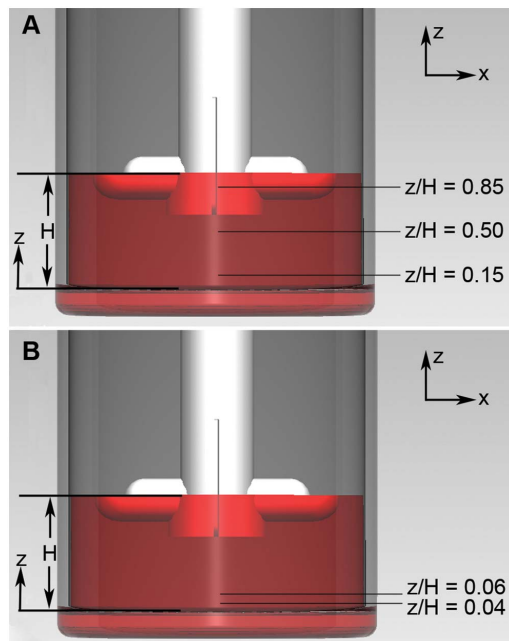
Figure 2. Azimuthal plane measurement locations. A non-dimensional parameter, z/H, is used to show the location of the measurement, where z is the distance from the bottom wall and H is the height of the fluid free surface. In our experiment, H = 19 mm for 50 mL working fluid. A) Three measurements were conducted at z/H = 0.15, 0.50 and 0.85. Velocity, shear stress and vorticity analyses were conducted at each measurement. B) Two measurements were conducted near the bottom wall. A parabolic function was fitted between the measurements at z/H = 0.06 and z/H = 0.04. Then, the velocity gradient near the bottom wall was calculated.
doi:10.1371/journal.pone.0106493.g002

fluid being illuminated by a bright light source, typically a Nd:YAG laser. Assuming the particles follow the fluid flow perfectly, the technique is able to quantitatively characterize the flow with high accuracy through the use of cross-correlation, which provides the distribution of the particle displacement, performed on the discretized images. The highest signal in the cross-correlation map represents the most probable particle displacement between image frames. Knowing the time difference between image frames, the velocity of the flow can be calculated.

This study is aimed at characterizing biomechanical properties associated with cell culture procedures in a commercially available spinner flask to define the design parameters for the bioreactor. It is anticipated that the characterization of frequently used bioreactors would benefit many research groups and, thus, improve the pace in cell protocol and bioreactor design developments. This study outlines extensive shear analysis in a spinner flask at varying rotational speeds, alongside cell culture results with similar experimental parameters.

Methods

Imaging Experimental Setup

The study of flow inside a spinner flask, agitated by a rotating impeller, is presented. The experimental layout is shown in

Figure 1. A 100 mL microcarrier spinner flask (BellCo Glass Inc, USA), with internal diameter of 55 mm, was filled with 50 mL of distilled water. The water was seeded with fluorescent particles having nominal diameter of 31 μm at 1 mg/mL seeding density and which faithfully follow the flow in the flask. The particles were illuminated by a laser sheet generated by a Nd:YAG laser (Darwin $\lambda = 532$ nm) that operates at 40 kHz. For the purpose of this work, the laser was considered to produce a continuous wave illumination. For each measurement, the laser sheet was carefully aligned at the imaging plane in the bioreactor. In order to reduce the lensing effect due to the curvature of the flask wall for the imaging procedure, the flask was placed inside a rectangular tank filled with water. The set-up was mounted on a steel base plate and secured to a precision optical table to eliminate any vibrations.

The flow under study was induced by the rotation of the impeller, driven by a stepper motor (Sanyo Denki America Inc, USA). As shown in Figure 1, the impeller consisted of a flat, rectangular Teflon sheet and a small magnetic stirring bar. In all measurements, the impeller was placed at a height where half of the magnetic rod was immersed in the water as presented in Figure 1A. Such a configuration was chosen to achieve a lower shear environment due to the sensitivity to hydrodynamic forces of the cell types chosen. The motor was run through a motion controller (National Instruments Australia, North Ryde, NSW, Australia), which enabled a maximum of 5.14×10^4 steps per revolution. To ensure a smooth rotation of the impeller at all speeds, the velocity of the motor was further geared down by a factor of 30. The Reynolds number of the flow was defined as Re = $\Omega R^2/\nu$, with Ω being the angular velocity of the impeller, ν being the kinematic viscosity and R being based on the radius of the flat impeller (R = 25.3 mm).

To keep track of the impeller position throughout the measurements, the angular coordinate system was required (see Figure 1B). The stepper motor was set to turn in a counter-clockwise direction from the top view. A horizontal line to the right of the impeller was chosen as the datum line, as depicted by a solid line in Figure 1B. The angular position of the impeller was defined as the angular distance between the datum line to the centerline of the magnetic rod throughout the manuscript.

The flow was visualized with a high-speed CMOS camera (IDT Y4) fitted with a Nikkor 105 mm f/2.8G lens (Nikon, Japan) with an exposure time of 300 μs. The acquisition rate was set so that each image was captured at one-degree rotation spacing. The camera frame rate in Hertz (Hz) can be calculated by multiplying the rotational speed in RPM by 6. This translates to an acquisition rate ranging from 120 Hz for 20 RPM to 270 Hz for 45 RPM. One set of data consisted of 361 images (360 image pairs). Throughout the experiment, 12 sets of data were taken at each speed for averaging purposes. It was ensured that before any image was captured, the setup was left running until steady-state flow was achieved.

To study the flow in the bioreactor, three main analyses were conducted in the meridional and azimuthal planes – the flow profile in the meridional plane, the flow profile in the azimuthal plane, and the fluid interaction at the bottom surface of the flask. In the meridional plane flow measurement, the laser sheet was placed vertically at the center of the flask (Figure 1C). For azimuthal measurement setting, the laser sheet was aligned horizontally and a mirror was placed underneath the tank. In this setup, the camera was placed to capture images reflected by the mirror, as presented in Figure 1D.

A total of six measurements were recorded at each rotational speed. One measurement was conducted in the meridional plane, three measurements at three different heights were conducted in
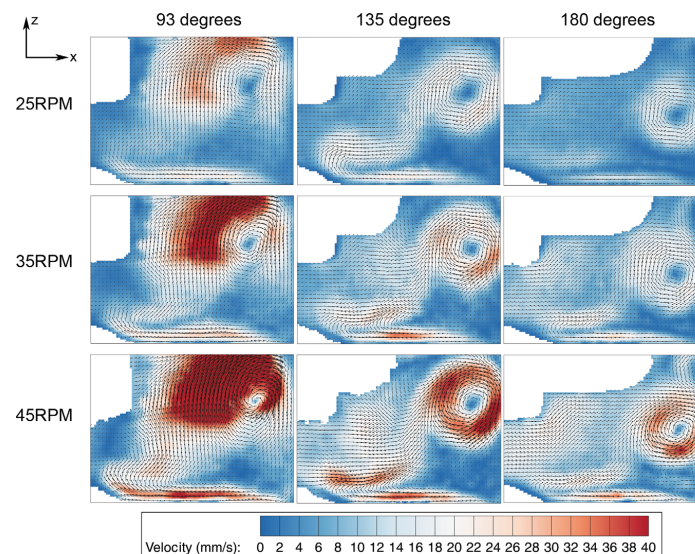
Figure 3. Velocity magnitude contour for flow in spinner flask in meridional plane. The velocity increases with increasing agitation speed. Furthermore, the fluid accelerates radially outwards at highest magnitude behind the flat impeller.
doi:10.1371/journal.pone.0106493.g003

the azimuthal plane (Figure 2A), and finally two measurements near the bottom wall were done in the azimuthal plane (Figure 2B). By having two measurements near the bottom wall plus the non-slip condition at the wall, an accurate approximation

of shear rate was calculated by fitting a parabolic function to the data. The rotational speed was varied between 20 RPM (Re = 1335) and 45 RPM (Re = 3004) at 5 RPM increments.
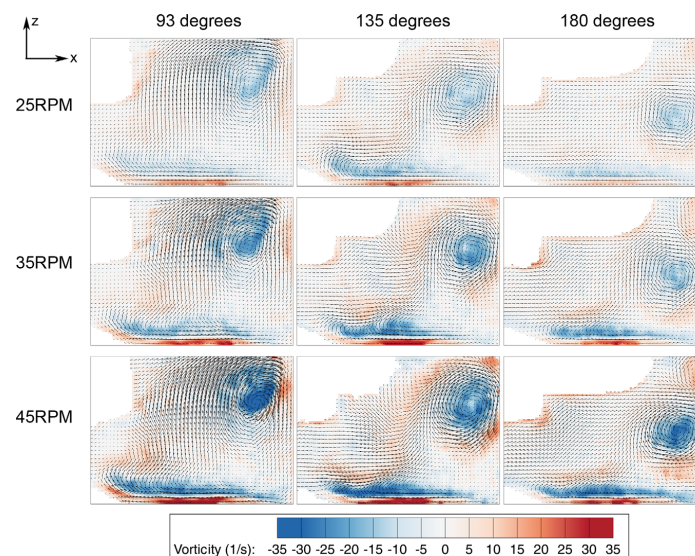

Figure 4. Vorticity evolution at 3 angular positions for 25, 35 and 45 RPM. The main vortex slowly reduces its strength as the plane of measurement shifts from 93 degrees to 135 degrees.
doi:10.1371/journal.pone.0106493.g004
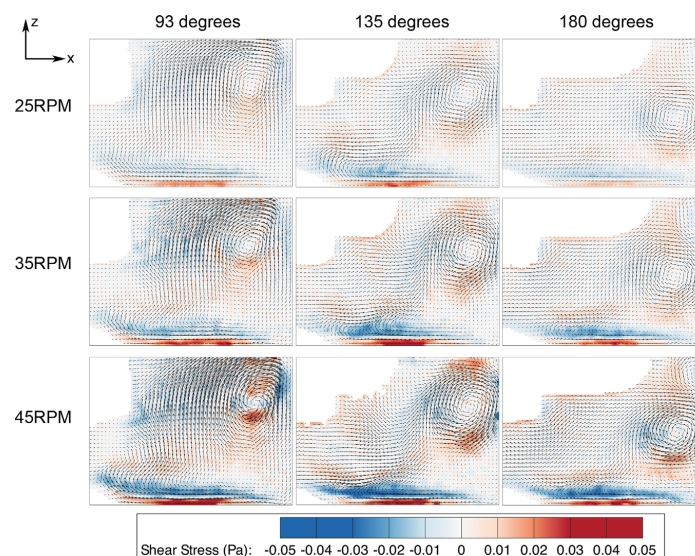
Figure 5. Shear stress distribution in azimuthal plane at varying phases. Significant shear stress can be seen at the bottom wall, caused by a high velocity gradient due to the interaction of the fluid with the wall.
doi:10.1371/journal.pone.0106493.g005
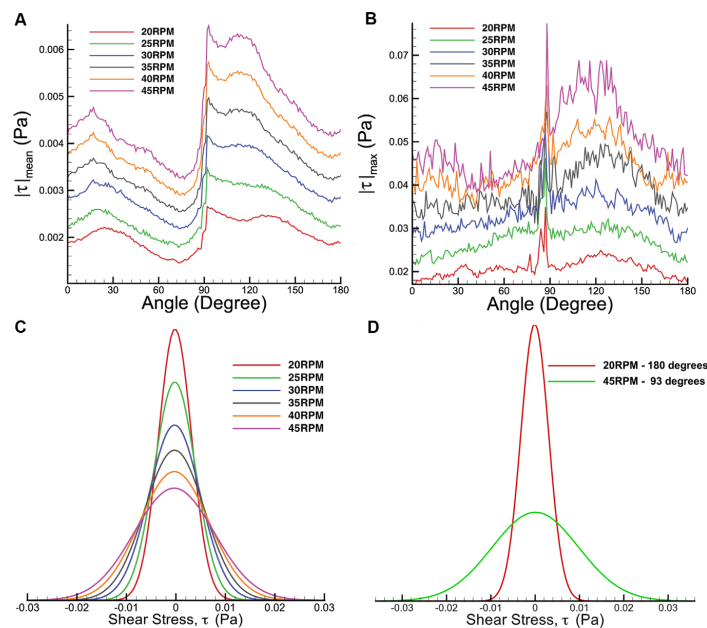
Figure 6. Shear stress distribution for varying rotational phase. A) Mean and B) maximum shear stresses. In both plots, the shear readings spike at 90 degrees, where the flat impeller is in the imaging plane. C) Histogram of shear stress for various speeds between 20 and 45 RPM. D) Shear stress distributions over meridional plane at two extreme cases; 20 RPM at 180 degrees and 45 RPM at 93 degrees.
doi:10.1371/journal.pone.0106493.g006

Flow Characterization of Spinner Flask

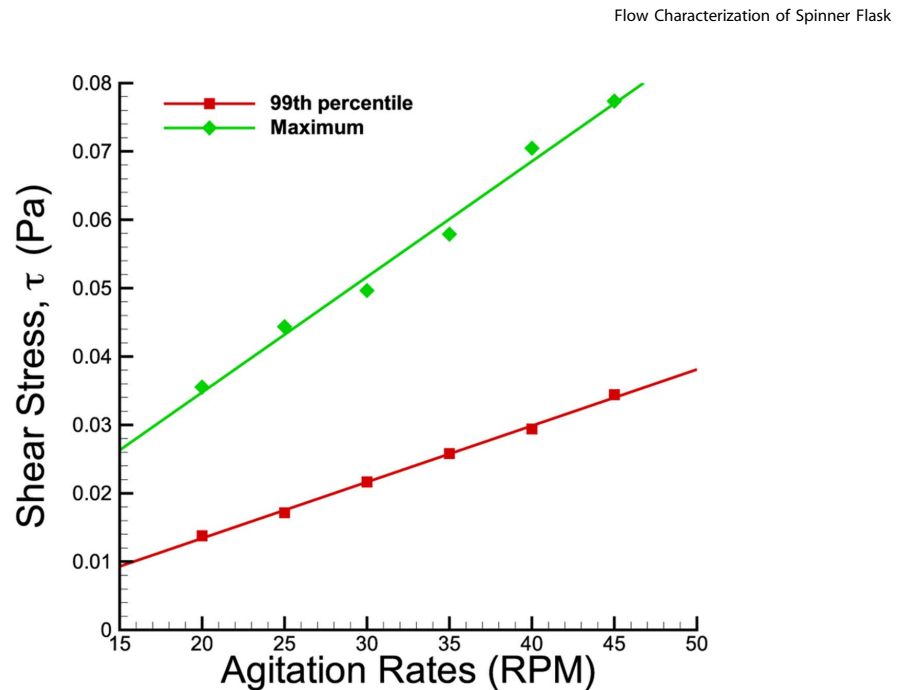**Figure 7. Maximum and 99ᵗʰ percentile shear stress plots in the meridional plane at varying spinning rates.** The plots increase linearly with the agitation rates. However, the shear stress magnitudes at 99ᵗʰ percentile are marginally lower than the maximum values at each speed.
doi:10.1371/journal.pone.0106493.g007

Data Processing

Stationary artifacts were removed to improve the data quality. This was done by performing background subtraction using the local temporal average of the image sequence. A maximum vertical deformation of 0.5 mm was seen at the free surface. To eliminate the discrepancy of the datasets, the top of each image was cropped 0.5 mm. Next, a mask file was generated to remove the impeller (in datasets where the impeller was in the imaging plane) and area outside the flask in the computing analysis. The analysis was performed using in-house PIV software, which has been rigorously tested over a number of years [34,35]. The images were divided into 128×128 pixel interrogation-windows and analysis was conducted at a spacing of 8×8 pixels in x and y directions, respectively. Considering one complete rotation consisted of 360 phases (one degree increment), the results were phase-averaged over the 12-recorded datasets to enhance the accuracy of the measurement. Shear stress, τ, and vorticity, ω, were calculated using the equations shown below,

$$\tau_{Meridional} = \mu\left(\frac{\partial W}{\partial x} + \frac{\partial U}{\partial z}\right), \tag{1}$$

$$\tau_{Azimuthal} = \mu\left(\frac{\partial U}{\partial y} + \frac{\partial V}{\partial x}\right), \tag{2}$$

$$\tau_{Bottom\ wall} = \mu\frac{\partial\left(\sqrt{U^2 + V^2}\right)}{\partial_z}, \tag{3}$$

$$\omega_{Meridional} = \frac{\partial U}{\partial z} - \frac{\partial W}{\partial x}, \tag{4}$$

where μ is the dynamic viscosity of water and U, V, W are the velocity components in the x, y, and z directions, respectively. The coordinate system is shown in Figure 1. Due to the no-slip condition at the bottom surface, the in plane velocity at the wall is zero. In this case, only the z derivative is not zero in general at the bottom wall, which results in equation 3.

Cell Culture Procedure

A parallel cell study was conducted to measure the effect of hydrodynamic force on live mouse OG2 iPS cells, derived according to Tat et al. [36]. Mouse OG2 iPS cells, attached to Cytodex 3 microcarriers, were grown in the spinner flask bioreactor, filled with 50 mL culture medium, in a humidified incubator at 37°C with 5% CO_2 level for 7 days. Due to the sensitivity of the chosen cells to shear conditions, only a partial section of the impeller was immersed in the culture medium, similar to the imaging configuration. The cells were seeded at a density of 2×10^5 cells/mL and for the first 24 hours, no agitation was induced in the system to promote cell attachment to the
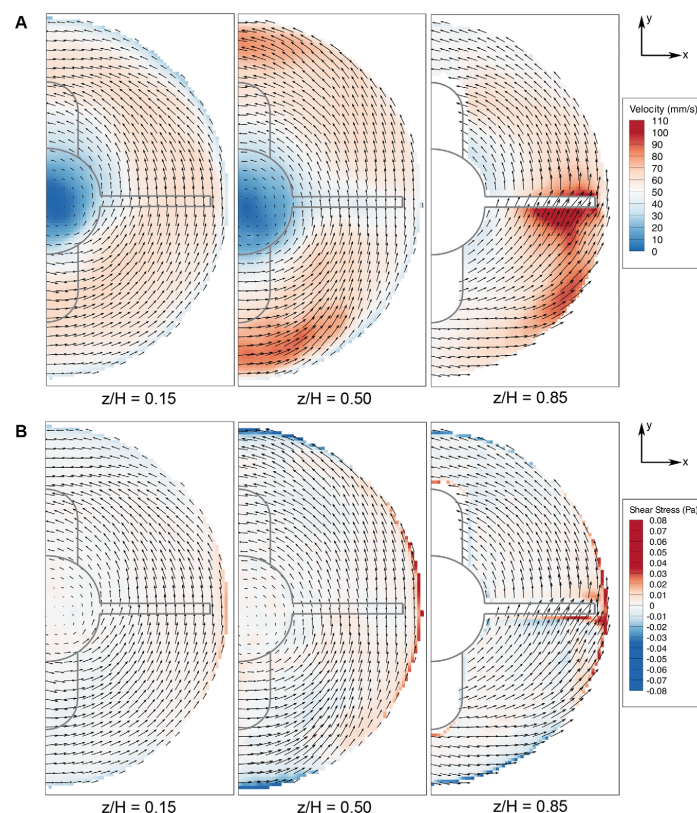
Figure 8. Flow visualization in azimuthal plane. A) Velocity and B) shear stress contours at z/H = 0.15, 0.50 and 0.85. Highest velocity and shear stress magnitudes are achieved around the flat impeller region in the z/H = 0.85 plane. The farthest plane from the impeller shows homogeneous distribution flow characteristics in both velocity and shear plots.
doi:10.1371/journal.pone.0106493.g008

microcarriers. For the next day and onwards, the culture medium was stirred at a specific speed. Throughout the experiments, 50% of the medium was replaced every day. At the end of day 7, viable cells were counted using a haemocytometer after trypan blue staining. The experiments were repeated at various agitation speeds and three repetitions were conducted for each speed. For more details, see Gupta et al. [33,37].

Results and Discussion

Flow profiles in the meridional and azimuthal planes are presented. The impeller and zone outside the flask, where no flow existed, were excluded in the PIV calculation. The analysis was conducted on half of the flask, considering the system has a periodic flow. The studies were split into three sections - meridional plane analysis, azimuthal plane analysis and shear profile analysis at the bottom surface of the flask. In the meridional plane, shear stress and vorticity were characterized as overlaid on the velocity profile. On the other hand, for the azimuthal plane analysis, the vorticity calculation was not shown due to the fluid flow behaving like a solid body rotation, producing minimal variance in vorticity.

Flow Profile in Meridional Plane

The meridional flow profile at various impeller speeds was characterized. In Figure 3, 4 and 5, the columns and rows show the different rotation phases and rotational speeds, respectively. The contour in Figure 3, 4 and 5 illustrate the magnitude of velocities, vorticity and shear stress, correspondingly, overlaid on the velocity vectors. The impeller rotated into the page in all figures. The white area in the figures are the impeller and small bump that were omitted from the PIV calculation. In these figures, only one quarter (90–180 degrees) is shown to highlight the main feature of the fluid behaviour, as there are very minimal changes in flow characteristics beyond 180 degrees.

Based on Figure 3, it can be seen that the velocity magnitude increases with Reynolds number. As the impeller spins, the fluid is accelerated radially outwards towards the sidewall, flowing downwards to the bottom wall. The fluid then travels inwards and goes up at the center of the flask producing a global clockwise flow. At each spin rate, a similar flow structure is obtained and the flow achieved its maximum near the bottom wall and surrounding impeller area, slightly after the flat impeller passed the imaging plane. However, a slight but distinct structure variance can be noticed at 135 degrees between low and high spin rates. At low
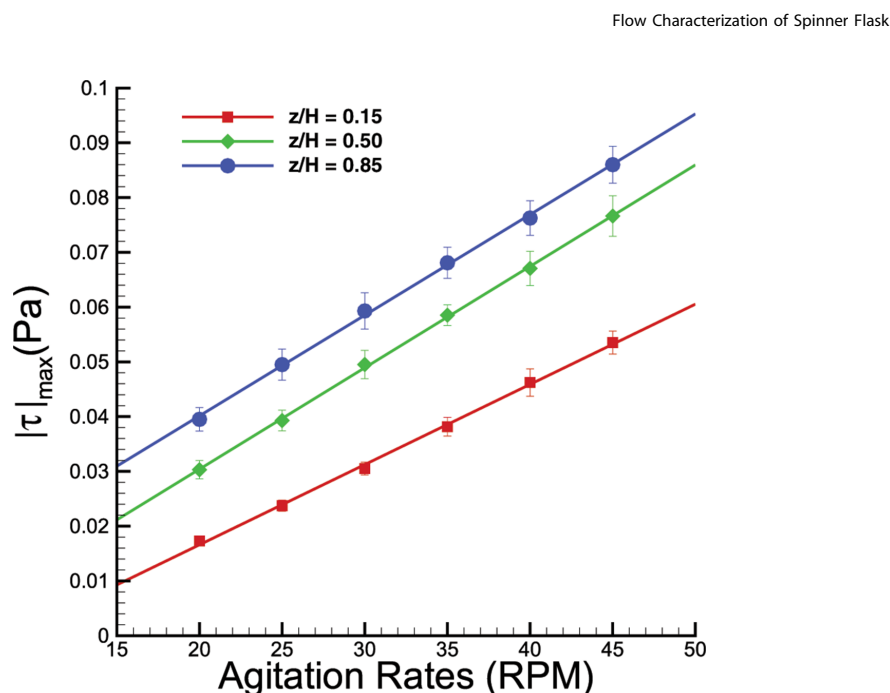
Figure 9. Plots of maximum shear stress when the bioreactor was spun at 20 to 45 RPM. Although at each height the shear varies linearly with the spinning rates, the slopes differ from one to another.
doi:10.1371/journal.pone.0106493.g009

spin rate, the fluid circulates smoothly from bottom surface upwards. In contrast, the fluid is being pushed downwards, producing more abrupt change in direction at high spin rate. Furthermore, higher rotational speed produced higher vertical velocity at the center of the rotation compared to lower spin rates. The vertical velocity provides lift for the microcarriers to keep them in suspension throughout the culture procedure. Some particle settlement was noticed around the bump at 20 RPM.

Vorticity is a quantitative, local measure of circulation. Vortices provide a mixing mechanism in the system to ensure a relatively homogeneous concentration of nutrients in the flask. In the analysis we conducted, a positive value of vorticity represents anti-clockwise circulation and vice-versa. Figure 4 depicts the vorticity contours at various speeds and rotation angles. Overall, the vorticity magnitude increases with increasing rotational speed. Additionally, similar to the velocity profile, vorticity peaks in the region downstream of the flat impeller, in this case, at 93 degrees. The main vortex then translates downwards while showing some reduction in magnitude. At the bottom surface, the vorticity grows as the plane of measurement shifts from from 93 degrees to 135 degrees due to the increment of velocity at that particular area. At 180 degrees, there are small vortices rotating in a counter-clockwise direction above and below the main vortex.

The shear is relatively high in the region close to the bottom surface, with noticable shear around the vortex as illustrated in Figure 5. To understand the shear profile in the meridional plane, the maximum, mean and distribution of shear stress over the meridional plane were plotted and shown in Figure 6. Only the first 180 degrees are given prominence due to the symmetrical geometry of the impeller. In the mean shear stress plot (Figure 6A), the data shows a similar pattern, but with a linearly increasing

magnitude at higher Reynolds numbers. At each spin rate, the highest reading occurs at 90 degrees at the sidewall of the flask. In the maximum shear stress plot in Figure 6B, the measurements are more than 10 times higher than the average shear stress. At each individual spin rate, the shear stress peaks at around 90 degrees, where the highest velocity magnitude is achieved within the rotation phase. The shear stress margin widens at high agitation speeds, which can be seen in the distribution plot in Figure 6C. Additionally, the shear stress distribution for 45 RPM spinning rates specifically at 93 degrees phase angle illustrates wider margin in Figure 6D compared to the overall distribution in Figure 6C at similar speed. The plot demonstrates that the shear stress is significantly higher at 93 degrees. On the other hand, minimal difference is seen at lowest shear stress condition (20 RPM at 180 degrees phase angle) compared to overall shear density plot. The plots at extreme cases shown in Figure 6D highlight the minimum and maximum shear condition over the meridional plane in this experiment.

The maximum and 99th percentile shear stress magnitude corresponding to the agitation rate are plotted in Figure 7. Both plots show increasing linear relationship to the impeller speed. However, the 99th percentile values are noticably lower than the maximum shear stress. The large discrepancies may have been caused by significant shear gradient around the impeller tip at certain phase angle that contributed to the maximum value.

Azimuthal Flow Profile

The azimuthal flow is the primary velocity component in the spinner flask. Similarly, velocity and shear are characterized in this plane. The flow is rotating like a solid body rotation, except for a thin boundary layer around the sidewall, where the no-slip
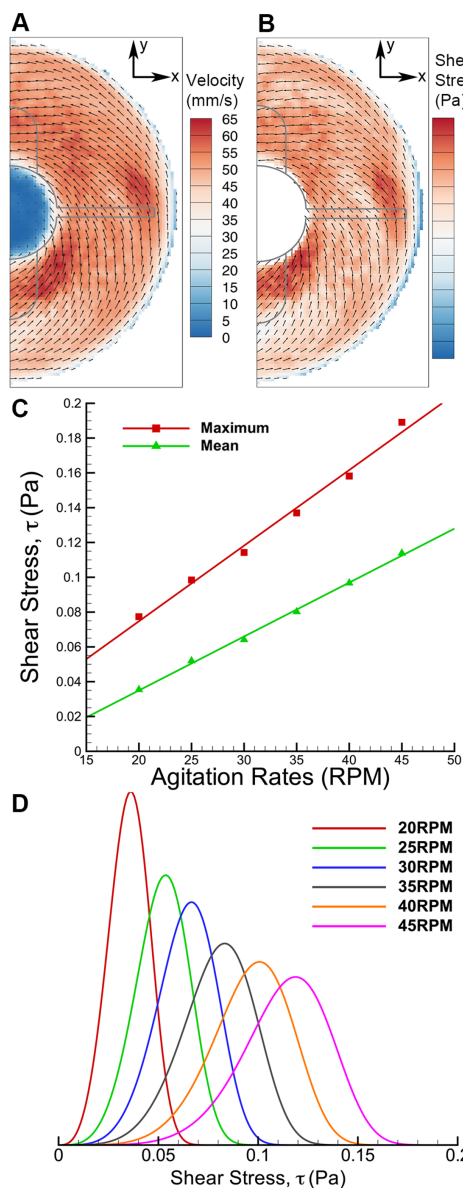
Figure 10. Results of fluid interaction at bottom surface of the flask. A) The velocity distribution at 40 RPM at z/H = 0.04. B) Shear stress near the bottom surface is higher than other azimuthal measurements. C) The mean and maximum shear stress increase linearly to the agitation speed. D) Shear stress distribution is skewed to higher shear magnitude at increasing speed.
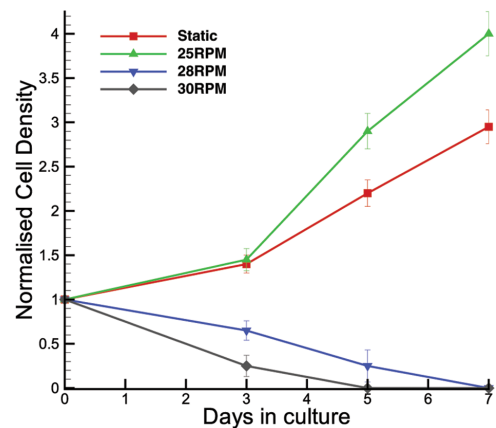doi:10.1371/journal.pone.0106493.g010

Figure 11. Normalized cell count over culture period for static and suspension culture method. A cell count achieved in the 20 RPM bioreactor was superior to the static culture over 7 days. The plot also shows that declining cell counts were obtained for 28 and 30 RPM suspension cell culture.
doi:10.1371/journal.pone.0106493.g011

the velocity and shear profiles for 40 RPM (Re = 2670) are shown. As the flow is in steady state, only one phase is shown at each height that highlights the main flow characteristics in Figure 8.

The velocity magnitude is low at the center of rotation at all heights. In general, it can be seen that the flow is mainly in the tangential direction with a minor radial component (Figure 8A). As the imaging plane gets further away from the impeller, the velocity reduces and a more homogeneous velocity distribution is achieved near the bottom surface. At the highest imaging slice, the highest velocity is recorded near the flat impeller. This is due to the fact that the impeller is within the imaging plane at z/H = 0.85. Unlike at the highest imaging plane, in the middle-height section, the high velocity area is near the magnetic rod. As shown previously in the meridional plane characterization, the circulation travels downwards, which contributed to the high value visualised at z/H = 0.50 near the magnetic rod region. The standard deviation of the velocity measurements varies between 8.01 mm/s to 15.62 mm/s within 20 RPM to 45 RPM speed margin. The largest velocity variation (hence standard deviation) within the imaging plane was recorded at the highest imaging plane, where the measurement made is closest to the impeller. The rotating impeller provides the driving force in the flow and therefore creates high-speed region around it. The lowest standard deviation, achieved at z/H = 0.15, showed that the flow is more homogeneous at a plane far from the impeller.

Figure 8B illustrates the shear stress contour at various heights. At each plane, it can be seen that high shear occurs due to the rapid deceleration of the flow because of the no-slip condition at the sidewall. Additionally, the shear stress is highly dependent on the velocity magnitude. The sidewall shear reading is lowest at z/H = 0.15 and increases at the higher planes due to the greater magnitude of velocities. At the 0.85 height ratio, the sharp edges at the flat impeller provide strong force to agitate the fluid but at the same time it produces a significant velocity gradient, which translates to a substantial shear reading.

The results are summarized in a graph of maximum shear stress versus agitation rate, as shown in Figure 9. Due to the axisymmetric nature of the flow in the azimuthal plane, shear

condition is enforced, the vorticity is almost constant at all imaging planes. Measurements were conducted at three different heights, z/H = 0.15, 0.50 and 0.85. For the purpose of visualization, only

readings over a full rotation can be further averaged to enhance the accuracy of the analysis. The plots show that the shear stress behaves linearly with agitation speed. Presumably, one could extrapolate the graph to obtain an accurate approximation of the shear magnitude for spinning rates outside the margin we tested. The error bars represent the standard deviation of the maximum shear reading of a complete rotation. The shear interaction between the fluid and the bottom surface analysis is presented in the subsequent subsection.

Fluid Interaction at Bottom Surface of the Flask

In order to characterize the shear rate at the bottom surface, two measurements were conducted in azimuthal plane at height ratios of 0.04 and 0.06. Knowing zero velocity at $z = 0$, the gradient close to the bottom surface is calculated based on a parabolic fit between the velocity points at 3 different heights. Figure 10A shows the velocity vector at $z/H = 0.04$. Zero velocities at the center of the rotation are caused by the bump at the bottom of the flask. Furthermore, the vectors also show that the radial velocity component is more prominent than other vectors at higher planes, producing vortex behavior towards the center. The higher radially inward velocities are aligned with the results obtained in meridional imaging.

Although the velocity magnitude is lower than in other azimuthal plane measurements, the shear stress scale at the bottom surface is of significantly higher magnitude than in any previous measurements, as illustrated in Figure 10B and 10C. Unlike the shear stress in previous measurements that arises due to fluid-fluid interaction, the high magnitude of shear stress in Figure 10 is due to the fluid-wall interaction which produces higher shear gradient, resulting in higher shear magnitude. At higher spin rate, the shear distribution is also skewed to a higher value (Figure 10D).

Mouse iPS Cells Proliferation

Figure 11 shows the normalized cell count density over the culture period grown in static culture, at 25 RPM, 28 RPM and 30 RPM agitation rates. It can be seen that the cells cultured at 28 RPM and above suffered an adverse effect on the cell count. Due to the fact that the density difference between Cytodex 3 microcarriers and water is minimal at 0.04 g/mL, it can be assumed that the microcarriers are neutrally buoyant and faithfully follow the fluid flow in the flask. Based on previous results, a spin rate of 28 RPM has its highest shear stress of 0.108 Pa with an average of 0.0592 Pa at the bottom surface of the flask. With declining cell count, it shows that mouse iPS cells are not able to maintain secure attachment to the microcarrriers at such a level of shear stress over the culture period. The plot shows that the highest cell count was obtained at 25 RPM, which translates to a maximum stress of 0.0984 Pa and mean of 0.0520 Pa. Such a flow condition was also able to maintain the cells' pluripotency property [37]. This spin rate was demonstrated to produce a superior yield to the static culture. A low Reynolds number flow condition has a reduced mixing effect that could consequently produce counter-productive results to the cell count. The opposing effects of cell growth within a small shear range show that mouse iPS cells are very susceptible to shear condition. Details of cell morphology analysis can be found in Gupta et al. [33,37]. Negligible suspension at speeds lower than 25 RPM was observed during the experiment. Hence, the culture condition at lower Reynolds number was comparable to static culture. Since the primary culture aim was long-term dynamic culture, 25 RPM was chosen as the minimum speed in the cell study. More experiments need to be conducted using different lines of cells to determine the

optimal mechanical forces required to optimize the cell growth. For any rotational speed using a similar experimental configuration, this study provides a quantitative insight into the fluid dynamics in the spinner flask.

Conclusions

In this study, we have shown extensive flow visualization in a spinner flask at various flow conditions. In the meridional plane point of view, the highest stress was recorded in the region downstream of the flat impeller. The velocity and shear varied linearly with Reynolds number. However, a significantly higher magnitude of shear was recorded in the azimuthal plane. Although higher velocities were obtained in a plane closer to the impeller, the highest velocity gradient occurs at the bottom surface of the flask. A notable value of shear was also present at the edge of the flat impeller. The distribution plots provide insights into how the margin of the mechanical force behaves at different Reynolds number.

It was found that the mouse iPS cells proliferated at their optimum condition at 25 RPM (Re = 1669) spinning rate. Flows at higher spin rates (and therefore Reynolds numbers) were not able to sustain positive growth of the cells. The higher shear stress in the flow had consequently detached the cells from the micro-carriers, causing cell death and adverse cell count. On the other hand, at speeds below 25 RPM, the given setup showed that it was not able to maintain Cytodex 3 microcarrier beads in suspension. Hence, the minimum speed of 25 RPM was chosen since long-term dynamic suspension culture has been the primary aim in this study.

This study has shown that the use of spinner flask was able to increase cell yield compared to static culture. However, the homogeneous flow condition generated through the spinning impeller is at the expense of shear stress in the system. The cell experiment presented in this research served as an example in defining the shear stress condition specifically for mouse OG2 iPS cell culture. Additionally, the flow characterization defines the shear range within the spinner flask for future use.

Future work may include optimization studies for different cell lineages to determine their best culture condition. The results we have presented will enable one to acquire the shear stress distribution within the flask, thus creating a database of the required flow conditions for various cell types. The flow conditions for the cells can then be used as design requirements for the development of more efficient bioreactors. On the other hand, if the optimum biomechanical parameters for certain cell lineage are known, the required speed for the culture procedure can be determined based on the shear stress datasheet for the spinner flask. The flow mechanics knowledge would allow the required culture condition to be transferable to different types of bioreactor, thus reducing the experimental time spent in testing phase, should a different bioreactor needs to be utilized. However, flow characterization for various bioreactor types is required to define the shear margin in each design.

The small range of spin rates at which there was cell growth obtained in the cell culture experiment demonstrates that care should be taken in ensuring the impeller spins at an accurate speed in the cell culture. Furthermore, the use of a reliable and accurate system to drive the impeller will ensure consistency and repeatability, allowing exact replication to be performed by other research groups. This study provides insight into defining the optimum mechanical forces for cell culture procedures, thus providing quantitative parameters for optimizing bioreactor design.

Author Contributions

Conceived and designed the experiments: MI PG AF PV SJ JB KH. Performed the experiments: MI PG. Analyzed the data: MI PG.

References

1. Sen A, Kallos MS, Behie LA (2001) Effects of Hydrodynamics on Cultures of Mammalian Neural Stem Cell Aggregates in Suspension Bioreactors. Ind Eng Chem Res 40: 5350–5357.
2. Kehoe DE, Jing D, Lock LT, Tzanakakis ES (2010) Scalable stirred-suspension bioreactor culture of human pluripotent stem cells. Tissue Eng Part A 16: 405–421.
3. Freed LE, Vunjak-Novakovic G (2000) Tissue engineering bioreactors; Lanza RP, Langer R, Vacanti J, editors. San Diego, USA: Academic Press.
4. Martin I, Wendt D, Heberer M (2004) The role of bioreactors in tissue engineering. Trends Biotechnol 22: 80–86.
5. Shachar M, Cohen S (2003) Cardiac tissue engineering, ex-vivo: Design principles in biomaterials and bioreactors. Heart Fail Rev 8: 271–276.
6. Bancroft GN, Sikavitsas VI, Mikos AG (2003) Technical note: Design of a flow perfusion bioreactor system for bone tissue-engineering applications. Tissue Eng 9: 549–554.
7. Koller MR, Emerson SG, Palsson BO (1993) Large-scale expansion of human stem and progenitor cells from bone marrow mononuclear cells in continuous perfusion cultures. Blood 82: 378–384.
8. Palsson BO, Paek S-H, Schwartz RM, Palsson M, Lee G-M, et al. (1993) Expansion of Human Bone Marrow Progenitor Cells in a High Cell Density Continuous Perfusion System. Nat Biotech 11: 368–372.
9. Freed LE, Vunjak-Novakovic G (1997) Microgravity tissue engineering. In Vitro Cell Dev Biol-Anim 33: 381–385.
10. Gerecht-Nir S, Itskovitz-Eldor J (2004) Cell therapy using human embryonic stem cells. Transpl Immunol 12: 203–209.
11. Goodwin TJ, Schroeder WF, Wolf DA, Moyer MP (1993) Rotating-wall vessel coculture of small intestine as a prelude to a tissue modelling: Aspects of simulated microgravity. Proc Soc Exp Biol Med 202: 181–192.
12. Cabrita GJM, Ferreira BS, Lobato Da Silva C, Goncalves R, Almeida-Porada G, et al. (2003) Hematopoietic stem cells: From the bone to the bioreactor. Trends Biotechnol 21: 233–240.
13. Kallos M, Sen A, Behie L (2003) Large-scale expansion of mammalian neural stem cells: a review. Med Biol Eng Comput 41: 271–282.
14. Schroeder M, Niebruegge S, Werner A, Willbold E, Burg M, et al. (2005) Differentiation and lineage selection of mouse embryonic stem cells in a stirred bench scale bioreactor with automated process control. Biotechnol Bioeng 92: 920–933.
15. Zandstra PW, Bauwens C, Yin T, Liu Q, Schiller H, et al. (2004) Scalable Production of Embryonic Stem Cell-Derived Cardiomyocytes. Tissue Eng 9: 767–778.
16. Cameron CM, Hu W-S, Kaufman DS (2006) Improved development of human embryonic stem cell-derived embryoid bodies by stirred vessel cultivation. Biotechnol Bioeng 94: 938–948.
17. Niebruegge S, Nehring A, Bar H, Schroeder M, Zweigerdt R, et al. (2008) Cardiomyocyte production in mass suspension culture: Embryonic stem cells as a source for great amounts of functional cardiomyocytes. Tissue Eng Part A 14: 1591–1601.
18. Zhang Z-Y, Teoh SH, Chong W-S, Foo T-T, Chng Y-C, et al. (2009) A biaxial rotating bioreactor for the culture of fetal mesenchymal stem cells for bone tissue engineering. Biomaterials 30: 2694–2704.
19. Abranches E, Bekman E, Henrique D, Cabral JMS (2007) Expansion of mouse embryonic stem cells on microcarriers. Biotechnol Bioeng 96: 1211–1221.
20. Fernandes AM, Fernandes TG, Diogo MM, da Silva CL, Henrique D, et al. (2007) Mouse embryonic stem cell expansion in a microcarrier-based stirred culture system. J Biotechnol 132: 227–236.
21. Fok EYL, Zandstra PW (2005) Shear-Controlled Single-Step Mouse Embryonic Stem Cell Expansion and Embryoid Body-Based Differentiation. Stem Cells 23: 1333–1342.
22. Hu W-S, Giard DJ, Wang DIC (1985) Serial propagation of mammalian cells on microcarriers. Biotechnol Bioeng 27: 1466–1476.
23. Kuriyama S, Nakano T, Yoshimura N, Ohuchi T, Moritera T, et al. (1992) Mass cultivation of human retinal pigment epithelial cells with microcarrier. Opthalmologica 205: 89–95.
24. Lock LT, Tzanakakis ES (2009) Expansion and Differentiation of Human Embryonic Stem Cells to Endoderm Progeny in a Microcarrier Stirred-Suspension Culture. Tissue Eng Part A 15: 2051–2063.
25. Kaiser SC, Jossen V, Schirmaier C, Eible D, Brill S, et al. (2012) Fluid flow and cell proliferation of mesenchymal adipose-derived stem cells in small-scale, stirred, single use bioreactors. Chem Ing Tech 85: 95–102.
26. Liovic P, Sutalo ID, Stewart R, Glattauer V, Meagher L (2012) Fluid flow and stresses on microcarriers in spinner flask bioreactors. Ninth International Conference on CFD in the Minerals and Process Industries. CSIRO, Melbourne, Australia.
27. Sucosky P, Osorio DF, Brown JB, Neitzel GP (2003) Fluid mechanics of spinner flask bioreactor. Biotechnol Bioeng 85: 34–46.
28. Venkat RV, Stock R, Chalmers JJ (1996) Study of hydrodynamics in microcarrier culture spinner vessels: A particle tracking velocimetry approach. Biotechnol Bioeng 29: 456–466.
29. Singh H, Teoh SH, Low HT, Hutmacher DW (2005) Flow modelling within a scaffold under the influence of uni-axial and bi-axial bioreactor rotation. J Biotechnol 119: 181–196.
30. Dusting J, Sheridan J, Hourigan K (2006) A fluid dynamics approach to bioreactor design for cell and tissue culture. Biotechnol Bioeng 94.
31. Thouas GA, Sheridan J, Hourigan K (2007) A bioreactor model of mouse tumor progression. J Biomed Biotechnol 2007: 32754.
32. Ismadi M-Z, Higgins S, Samarage R, Paganin D, Hourigan K, et al. (2013) Optimisation of a stirred bioreactor through the use of a novel holographic correlation velocimetry flow measurement technique. PLoS ONE 8: e65714.
33. Gupta P, Ismadi M-Z, Bellare J, Jadhav S, Fouras A, et al. (2014) Optimization of agitation speed in spinner flask for microcarrier survival and expansion of induced pluripotent stem cells. Cytotechnology Available Online.
34. Fouras A, Lo Jacono D, Hourigan K (2008) Target-free Stereo PIV: a novel technique with inherent error estimation and improved accuracy. Exp Fluids 44: 317–329.
35. Fouras A, Lo Jacono D, Nguyen CV, Hourigan K (2009) Volumetric correlation PIV: a technique for 3D velocity vector field measurement. Exp Fluids 47: 569–577.
36. Tat P, Sumer H, Jones KL, Upton K, Verma P (2010) The efficient generation of induced pluripotent stem (iPS) cells from adult mouse adipose tissue-derived and neural stem cells. Cell Transplantation 19: 525–536.
37. Gupta P (2014) Parameter optimization for expansion of pluripotent stem cells [Ph.D Thesis]. Mumbai, India: IITB-Monash Research Academy.

Page | **102**

5.2   Effect of Agitation Speeds Towards Microcarriers Structure.

Prior to cell experiments, the effect of spinning rates on microcarriers were analysed. The microcarriers were placed in the spinner flask bioreactor, at a seeding density of 1mg/mL. Next, the microcarriers were placed in continuous dynamic environment for 48 hours to determine the impact of the dynamic environment towards the structure of the microcarriers. The samples were then observed under a light microscope. For this analysis, the two most prominent microcarrers in cell research were tested - Cytodex 3 and Hillex II; which are dextran- and polystyrene-based microcarriers, respectively.
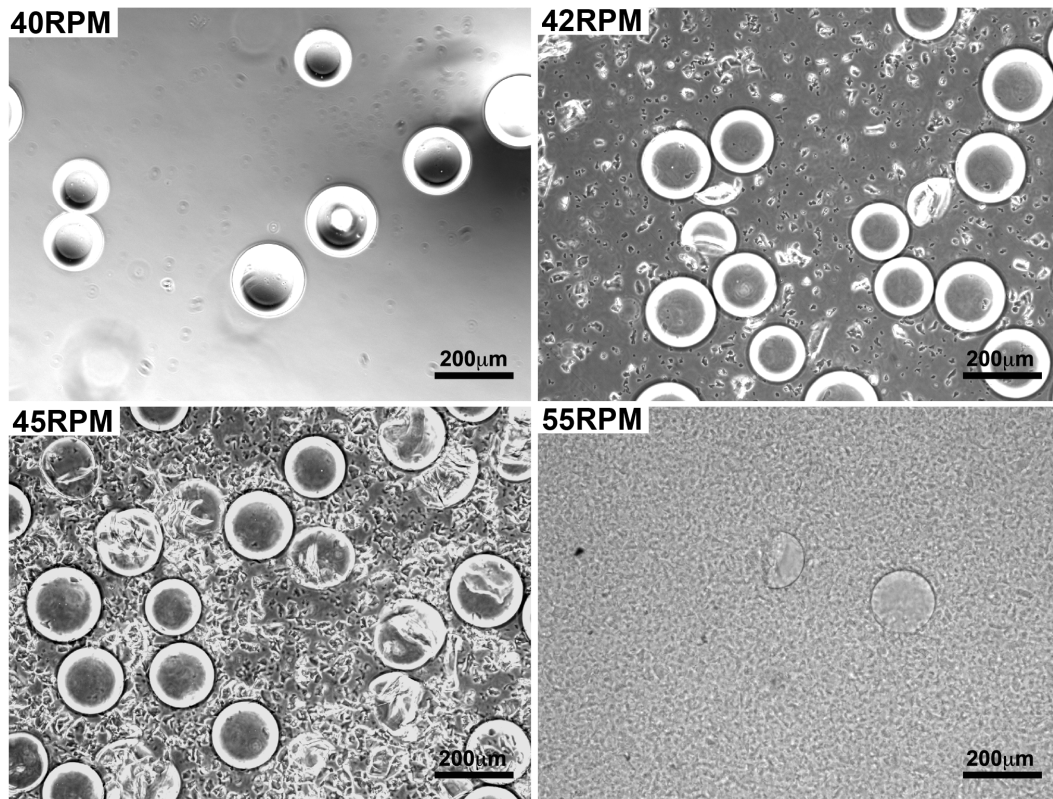
FIGURE 5.1: Phase contrast images of Cytodex 3 microcarriers after being subjected to 2 days of dynamic culture at different speeds. *Scale bar* 200μm

Based on the experiments, it was concluded that the Cytodex 3 microcarriers should be used with the spinner flask at rotational speeds lower than 40RPM (Re = 2671). It was found that the microcarriers structures were not able to withstand the hydrodynamic forces or ballistic impacts at higher speed, as shown in Figure 5.1. These speeds translate to a maximum shear stress of 0.158 Pa with mean stress of 0.097 Pa at the bottom surface. Although the magnitude seems insignificant, it demonstrated

the ability to cause damage to the microcarrier structure over a 48 hour-test period.
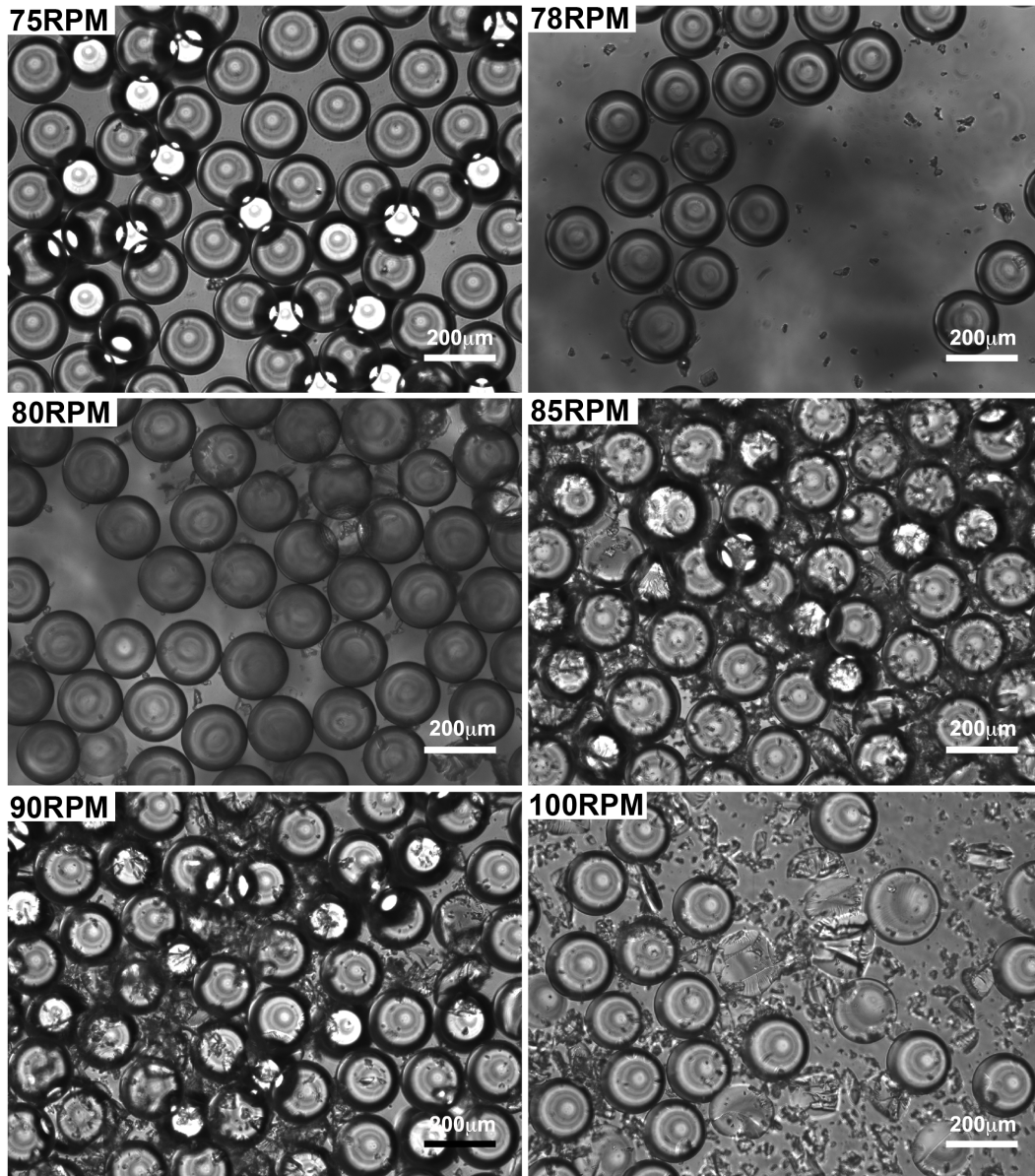
FIGURE 5.2: Images of polystyrene beads (Hillex II) after 48 hours of dynamic suspension in a spinner flask bioreactor at various speeds. *Scale bar* 200μm

Unlike Cytodex 3, Hillex microcarriers were able to withstand larger stress margins. Structure damage was only observed at speeds beginning at 78RPM (Re = 5208), as depicted in Figure 5.2. The fraction of damaged beads increased at higher agitation speeds. The results showed that polystyrene beads are more robust than dextran-based carriers. Focusing solely on the microcarrier structure, it can be concluded that Cytodex 3 and Hillex microcarriers should only be used at maximum speeds of 40RPM (Re = 2671) and 75RPM (Re = 5007), respectively as the damage occurred to the

surface of the microcarriers will not support the growth of the cells.

5.3 Mouse iPSCs Expansion for Different Spinning Rate.

Mouse OG2 iPSCs were expanded in a spinner flask using Cytodex 3 microcarriers over various spinning rates. Before the cells were grown in a dynamic culture, the cells were cultured in a static culture for 24 hours to promote the attachment to the microcarriers. The cells were then grown at different agitation rates for 7 days. The sensitivity of the spinning rate was analysed over the survival of the cells. Oct4-GFP expression method was used to show the live cells distribution at different culture days for three rotation speeds. Detailed cell assays and analyses were also conducted and published in Gupta *et al.* (2014) (Appendix A).
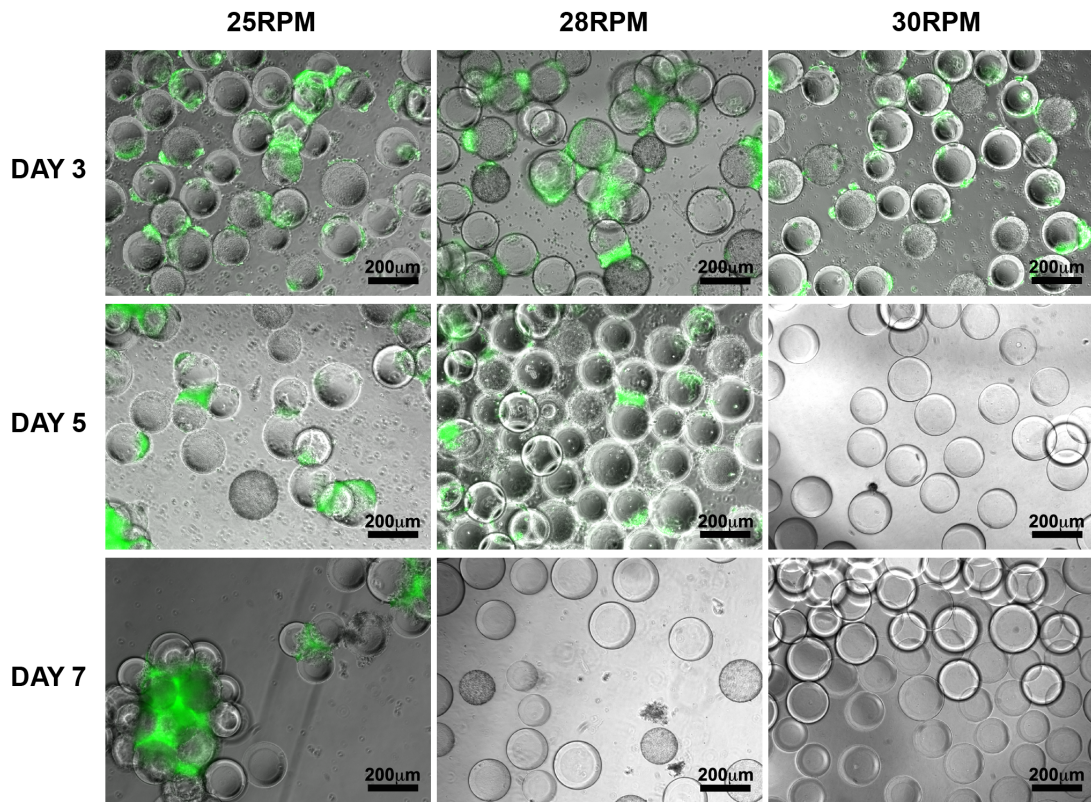
FIGURE 5.3: Mouse iPSCs expansion on Cytodex 3 microcarriers at 25, 28 and 30 RPM imaged on day 3, 5 and 7. *Scale bar* 200µm

Figure 5.3 illustrates microcarriers seeded with mouse iPSCs, overlaid by Oct4-GFP expression which emitted a fluorescent green colour in presence of pluripotent stem cells. At 25RPM (Re = 1669) in the dynamic culture, the cells proliferated healthily around the bead's surface throughout the 7 day culture period. Additionally, at the end of the

culture experiment, it was seen that the cells formed clustered colonies. In contrast, the cell growth declined over time for the 28RPM (Re = 1869) and 30RPM (Re = 2003) suspension cultures. Pluripotent cells were undetected on day 7 and 5 when the samples were cultured at 28RPM and 30RPM, respectively.

5.4 Discussion and Conclusion

This study presents thorough flow field and stress analyses in a spinner flask bioreactor at varying impeller speeds. Using a 50mL culture medium, the impeller was positioned at a height where only half of the impeller bar was immersed in the medium. Such position was aimed to minimise the shear introduced to the dynamic system, while maintaining enough circulation of the medium in providing homogeneous culture environment.

Using a conventional 2-dimensional PIV technique, the flow field was visualised in both meridional and azimuthal planes. Significant recirculation was observed at the region behind the flat impeller in the meridional plane. The recirculation acts as a mixing mechanism of the medium. The highest shear region was measured at the bottom surface of the bioreactor. Due to the flow being dominant in the azimuthal plane, it is not a surprise that the highest shear rate was achieved in this region as a result of the azimuthal flow and wall interaction. Cytodex 3 microcarriers were damaged at speeds higher than 40RPM (Re = 2671) and deemed unsuitable to support cell growth. The optimum growth for mouse iPSCs was achieved at a 25RPM (Re = 1669) suspension culture. At this speed, the maximum shear stress recorded was 0.0984 Pa at the bottom surface of the bioreactor. However, the cells were unable to secure attachments to the microcarrier surfaces at higher speeds, resulting in a decrease in cell counts.

Overall, this research shows that high spinning rates can damage the structure of microcarriers and thus limits the cell growth. Furthermore, the optimum agitation speeds for maximum cell growth, specifically for mouse iPSCs, over 7-day culture period were also found. Unlike traditional cell analyses which are conducted from a biological perspective, this chapter quantitatively characterised the mechanical parameters and highlighted the structure associated to the flow within the spinner flask at the measured planes. The mechanical parameters characterised in this study, alongside the parallel cell work will help researchers to define the design criteria for future bioreactor

development. The next chapter explains a novel imaging technique, called Holographic Correlation Velocimetry (HCV), in an effort to measure instantaneous 3-dimensional flow field in a cuvette and a spinner flask bioreactor.

Chapter 6

Towards 3-dimensional and 3-component Measurement Technique

I N this chapter, a novel imaging technique is proposed to characterise simple flow, such as the flow in a cuvette, as well as complex flows in a spinner flask. The motivation behind the proposed method is to gain understanding of three-dimensional flow behaviour. It is important that the technique is reliable, easy to set up and able to maintain the sterility of the sample. This can be achieved by having an optical-based measurement procedure. There are many qualitative method established for investigating fluid flow. These include flow visualisation method using smoke, dye or bubbles. Quantitative methods are necessary to gain thorough understanding of any flow. Hot-wire Anemometry (HWA), Laser Doppler Anemometry (LDA) and Particle Image Velocimetry (PIV) are a few of the widely used quantitative techniques for flow analysis. However, the anemometry based technique is inefficient and time consuming in characterising volumetric flow as it measures discrete points in the fluid volume. Thus, a velocimetry based technique was chosen to characterise the full field flow in non-intrusive manner.

Conventional PIV measurement techniques measure the velocity field in a single plane. The use of multiple light sheets and cameras provide out-of-plane flow information. However, as a laser sheet is the main light source, the location of the light sheet must be positioned throughout the volume in an effort to obtain volumetric information of the flow. The nature of the configuration imposes difficulties in the experimental procedures.

A correlation-based holographic technique, called Holographic Correlation Velocime-

try (HCV), is presented in this study. Unlike conventional PIV techniques that rely on side scattering in order to visualise the flow profile, the proposed technique utilises an efficient use of light source by employing an in-line collimated laser beam directed towards the camera. Using a single camera arrangement, HCV provides instantaneous 3-dimensional 2-component (3D2C) velocity field through the use of the volumetric correlation function.

The first section of the paper outlines the principle of HCV. The depth information was encoded by the particle diffraction pattern, embedded in the correlation maps. Bigger diffraction rings correspond to farther particle position from the image plane. In order to decode the depth information of the flow, synthetic auto-correlation maps for various particle depths were generated to be used as the calibration. The technique then iteratively used the calibration maps to match the experimental correlation peaks. Synthetic modelling was conducted as a validation of the technique. HCV was then utilised in mapping the flow in a cuvette and also in a commercially-available spinner flask bioreactor using a tomographic arrangement. This study highlights a novel velocimetry technique, which is highly suitable to characterise complex biological flows due to the non-intrusive nature of the technique.

6.1 Article IV: Optimisation of a Stirred Bioreactor through the Use of a Novel Holographic Correlation Velocimetry Flow Measurement Technique

The following manuscript was published online in 2013 in *PLoS ONE*. This work was co-authored by S. Higgins, C. Samarage, D. Paganin, K. Hourigan, and A. Fouras. The article reproduced in this thesis is directly taken from the published version without alteration.

Declaration

Monash University

Declaration for Thesis Section 6.1

Declaration by candidate

In the case of Section 6.1, the nature and extent of my contribution to the work was the following:

Nature of contribution	Extent of contribution (%)
Conceived, designed and performed the experiments, analysed the data, co-wrote the analytical software and wrote the manuscript	35%

The following co-authors contributed to the work. If co-authors are students at Monash University, the extent of their contribution in percentage terms must be stated:

Name	Nature of contribution	Extent of contribution (%) for student co-authors only
S. Higgins	Conceived, designed and performed the experiments, analysed the data, co-wrote analytical software and wrote the manuscript	35%
C. Samarage	Co-wrote the analytical software	20%
D. Paganin	Technical advice, revised manuscript	NA
K. Hourigan	Data interpretation advice, revised manuscript	NA
A. Fouras *	Technical advice, data interpretation advice, revised manuscript	NA

The undersigned hereby certify that the above declaration correctly reflects the nature and extent of the candidate's and co-authors' contributions to this work*.

Candidate's Signature		Date 01 AUG 2014
Main Supervisor's Signature		Date 01 AUG 2014

PLOS | ONE

Optimisation of a Stirred Bioreactor through the Use of a Novel Holographic Correlation Velocimetry Flow Measurement Technique

Mohd-Zulhilmi Ismadi[1,2]*, Simon Higgins[1,2], Chaminda R. Samarage[1,2], David Paganin[3], Kerry Hourigan[1,2], Andreas Fouras[1,2]

1 Department of Mechanical and Aerospace Engineering, Monash University, Melbourne, Victoria, Australia, **2** Division of Biological Engineering, Monash University, Melbourne, Victoria, Australia, **3** School of Physics, Monash University, Melbourne, Victoria, Australia

Abstract

We describe a method for measuring three dimensional (3D) velocity fields of a fluid at high speed, by combining a correlation-based approach with in-line holography. While this method utilizes tracer particles contained within the flow, our method does not require the holographic reconstruction of 3D images. The direct flow reconstruction approach developed here allows for measurements at seeding densities in excess of the allowable levels for techniques based on image or particle reconstruction, thus making it suited for biological flow measurement, such as the flow in bioreactor. We outline the theory behind our method, which we term *Holographic Correlation Velocimetry* (HCV), and subsequently apply it to both synthetic and laboratory data. Moreover, because the system is based on in-line holography, it is very efficient with regard to the use of light, as it does not rely on side scattering. This efficiency could be utilized to create a very high quality system at a modest cost. Alternatively, this efficiency makes the system appropriate for high-speed flows and low exposure times, which is essential for imaging dynamic systems.

Introduction

The advent of stem cell research has opened a new world in cell therapy and revolutionized regenerative medicine [1,2,3,4,5] for many degenerative diseases and injuries [6]. Their ability for self-renewal and differentiation to various cell types makes it an effective option as the basic material for various potential treatments by replenishing damaged cells. Furthermore, the possibility to obtain large amounts of these cells, making full use of their self-renewal nature, can make substantial advancement for scientific research and therapy purposes.

Despite the progress in stem cell research in recent years, technical limitations in scaling-up stem cell cultures represent a challenge in stem cell applications. A controlled, reproducible culture system is needed to expand the cells to adequate quantities for successful clinical implementation of stem cells. Cells are commonly grown in a spinner flask bioreactor. This provides a homogeneous culture environment, thus reducing culture variability. Hydrodynamic shear stress is a significant parameter to be considered in a suspension culture bioreactor. High shear could damage the cell membrane whereas low shear could cause agglomeration, which reduces the culture efficiency. In a suspension bioreactor, hydrodynamic shear stress is varied by the agitation rate and the type of impeller. In order to characterize this parameter, a non-intrusive measurement technique is highly desirable to maintain the sterility of the sample. Velocimetry techniques are widely used for various applications. In particular, Particle Image Velocimetry (PIV) is one of the techniques used for characterizing flow profiles.

Particle Image Velocimetry

There are many qualitative means for investigating fluid flow, including flow visualization methods using smoke, dye, or hydrogen bubbles [7]. To obtain a comprehensive, quantitative understanding of these flows, more sophisticated methods are required. Of these quantitative measurement techniques, the leading three are Hot-wire Anemometry (HWA) [8], Laser Doppler Anemometry (LDA) [9], and Particle Image Velocimetry (PIV) [10]. LDA and HWA are methods that measure discrete points in the fluid volume and may be used in an array or scanned through the flow to record data from throughout the flow volume. This can be a time consuming process and analyzing the discrete data stream from the flow volume may be difficult.

PIV is a full field, image based and therefore non-intrusive flow measurement technique that has been gaining popularity over the last two decades [11]. Tracer particles are introduced into the flow, and the region of interest is illuminated using a laser source (typically a pulsed Nd:YAG laser). A very bright light is required because the method relies on inefficient side scatter of light. Figure 1 shows a typical PIV setup. Assuming that the particles

faithfully follow the flow, consecutive images of the illuminated region are captured using a high-speed digital camera. The images are discretized into sub-regions and a cross-correlation analysis is performed in each sub-region [12]. The cross-correlation is representative of the probability distribution for the displacement of the underlying particle images within the sub-region, and the maximum signal is the most probable displacement between image frames. Since the time between image frames is known, the velocity of the flow captured in the region can be determined. Processing each of the discretized sub-regions results in a detailed velocity field of the flow. In many cases, it is enough to collect these data from a single plane in the flow. In this traditional form, the method provides no out-of-plane flow information. The most common solution to overcome this is stereoscopic PIV [13,14,15]; with two cameras, the local out-of-plane velocity may be calculated. Unfortunately, as laser sheet is the main light source, only a plane of velocity field could be measured at a time. In order to acquire full volumetric flow profile, the position of the light sheet has to be adjusted throughout the volume. Holographic PIV was developed to improve the complex procedure of standard PIV technique in obtaining full field volumetric profile. A number of fully 3D PIV variants have been developed [16] and are briefly described next.

Holographic PIV

Holographic PIV (HPIV) advanced the methods of recording a 3D instantaneous flow field in experimental measurements of fluid flow [17,18]. HPIV started with film-based holography, which involves using a reference beam to project the hologram, followed by a 2D plane detector being moved through the projected hologram to record the particle image field. Meng *et al.* [19] looked at the use of film holography and the emergence of direct Digital HPIV. However, in either case, a method to extract velocity data from holographic images is required. This is commonly conducted using two methods, 3D PIV and Particle Tracking Velocimetry (PTV), both of which require reconstruction

of 3D images before any inter-frame analysis can be performed [20]. We briefly review each method, in the following two sub-sections.

3D PIV. 2D PIV techniques can be readily implemented and adapted for 3D particle fields [21]. In essence, this involves calculation of a spatial 3D cross-correlation using temporally adjacent images, the maximum value of which represents the most common displacement within the 3D sub-region. This requires a highly accurate reconstruction of 3D-images and associated particle images. The reconstructed images often appear exaggerated in the depth direction and this is likely to result in higher ambiguity in the velocity along this axis as described by Pan and Meng [22]. Additions to this method to overcome the loss of accuracy in the depth direction include multi angle in-line holography [20] and multiple off axis holography [23], or a combination of both [17] have been used. However these systems are complex and require accurate calibration and alignment of cameras for corresponding voxel positions [20] and very few groups worldwide utilize this approach.

3D Particle Tracking Velocimetry (PTV). PTV also requires many individual particles to be reconstructed in space and identified in successive frames in order to track them through the flow. Frequently, the seeding density needs to be drastically reduced in order to obtain images in which particles can be unambiguously identified in 3D space. This is because if particles move in front of or behind one another, the tracking position is lost. With low particle seeding density, collecting data at all regions of the measurement volume is time consuming. To improve this, Pu and Meng [23] derived a Concise Cross Correlation and particle pairing algorithm. This study employed a 3D PIV correlation in discretized volumes, subsequently applying particle tracking to particles within the said volume. The dominant source of error in these techniques is the accurate reconstruction of the particles in the 3D volume.

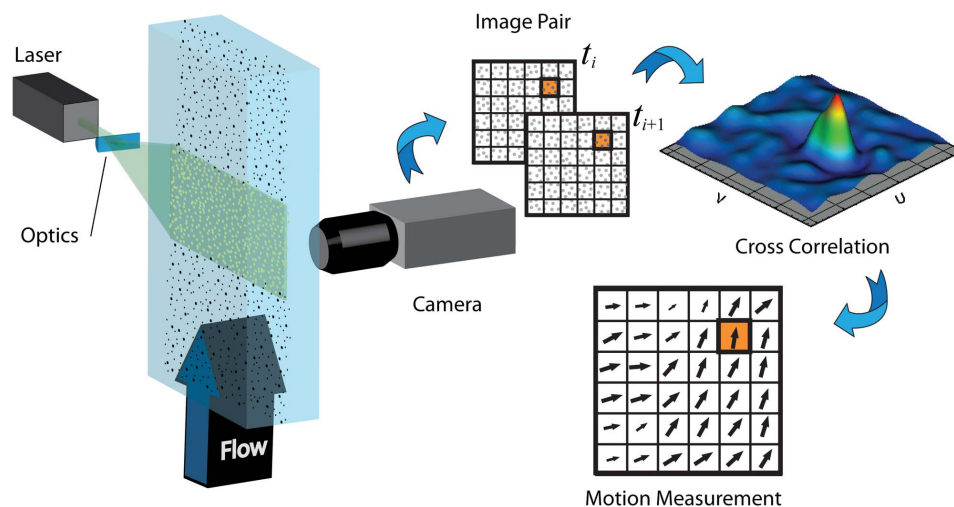**Figure 1. Schematic of conventional 2D PIV.** A laser sheet illuminates tracer particles carried by the fluid flow, yielding image sequences captured with a digital camera. The images are discretized into sub-regions and the correlation between subsequent image sub-regions produces a vector of the local particle motion. From this correlation analysis, the fluid motion can be inferred.
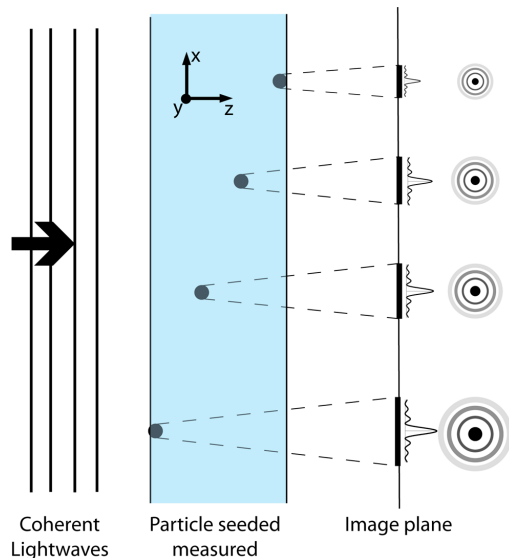doi:10.1371/journal.pone.0065714.g001

Figure 2. Diffraction pattern of the particle at different image plane distances. As coherent light is scattered by particles, they produce a diffraction image of the particle, which in the far field transversely scales with distance from the image plane. Particle nearer to the image plane produce diffraction rings that are transversely compressed relative to the rings produced by particles further from the image plane. The measured volume gives a speckle pattern comprised of all the overlapping rings.
doi:10.1371/journal.pone.0065714.g002

Holographic Correlation Velocimetry

In the present study, an alternative approach for volumetric flow measurement is proposed. The proposed holographic technique utilizes a correlation-based analysis to produce the full 3D velocity field without the need for first reconstructing 3D images. This method reduces the amount of processing for digital inline holographic reconstruction and 3D velocity mapping. The method does not use complicated calibration and can be performed with relatively low powered lasers. Due to Mie scattering, forward scattered light is several orders of magnitude brighter compared with side scatter [24]. The efficient use of light with the in-line system allows for high-speed flows to be investigated, which is something highly sought-after in many fields of research. This technique has been titled Holographic Correlation Velocimetry (HCV). This article describes the use of HCV to map the flow in a cuvette as well as the full 3-dimensional field of flow in a conventional bioreactor spinner flask using a tomographic arrangement.

Methods

Description of Holographic Correlation Velocimetry

Encoding the depth information. Unlike PTV, the technique described in this paper is based on a cross-correlation analysis. Fouras *et al.* [25] developed a technique by which the depth information in a seeded flow was encoded by the point spread function of the lens used in cross correlation space to form the images. Cross correlation is a statistical measure of multiple particles, without tracking individual particles. The cross correla-

tion can accurately encode the depth position even in the presence of variable particle diameter. In HCV, the depth information of the particles is encoded by the particle diffraction pattern, embedded in correlation maps, that varies with the propagation distance, z. Figure 2 illustrates the concept of how the depth information is encoded. When the Fresnel number, $N_F = a^2/(\lambda z)$ – where a, is the seed-particle diameter and λ, is the radiation wavelength – is much less than unity, Fraunhofer diffraction is applicable [26]. Given the scaling of the Fraunhofer pattern is in direct proportion to z, similar sized particles at different distances from the image plane yield diffraction patterns that are transversely scaled with respect to one another. Hence, the change in the appearance of a given particle's diffraction pattern is principally due to its distance from the image plane.

This method utilizes the first Born approximation that states that the optical energy density contained in the scattered beam, Ψ_s, must be significantly less than that contained in the unscattered beam, Ψ_o, at each point within the scattering volume: [26].

$$|\psi_S| << |\psi_O|. \qquad (1)$$

For this to hold, the ratio of total illuminated area of particles to the total area must be significantly less than 1:

$$\frac{N\pi r^2}{A} << 1, \qquad (2)$$
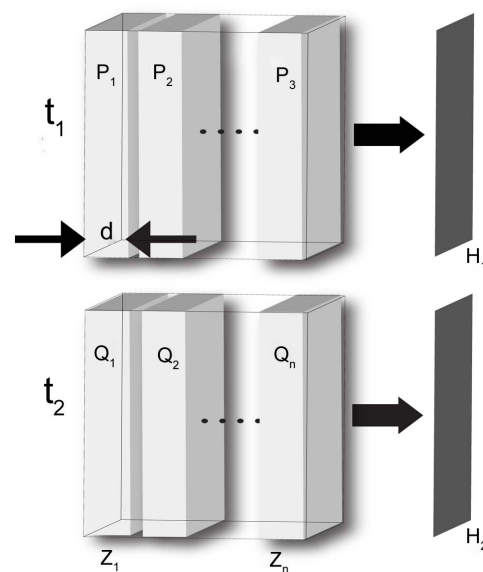
Figure 3. Two holographic images H$_1$ and H$_2$, at two successive time points, t$_1$ and t$_2$ for a range of z. P_i represents the inline hologram due to slice z_i at $t=t_1$, and Q_i is similarly defined at $t=t_2$. Under the assumption of weak scattering by each slab, and neglecting both interference between adjacent particles and an irrelevant additive constant, $H_1 = \sum_i P_i$ and $H_2 = \sum_i Q_i$.
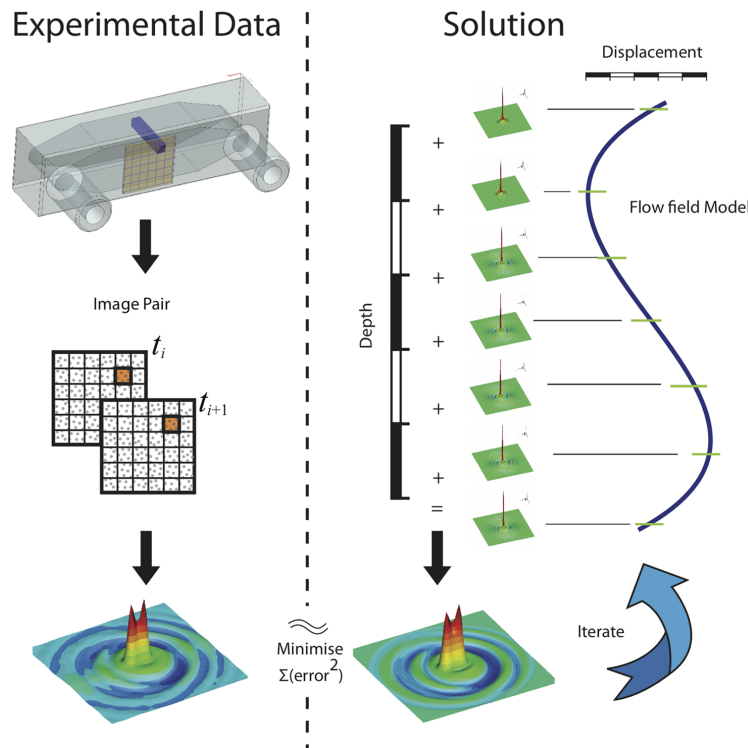doi:10.1371/journal.pone.0065714.g003

Figure 4. Graphical representation of the Holographic Correlation Velocimetry (HCV) algorithm. The algorithm solves for the 3-dimensional flow field by iteratively reconstructing the volumetric cross-correlation until the residual of the reconstructed cross-correlation and the measured cross-correlation reaches an acceptable level.
doi:10.1371/journal.pone.0065714.g004

where N is the number of particles, r is the radius of the particles and A is the total area. Since the number of particles, N, is given by the ratio of the volume of the particles to the volume of a single particle, we obtain the following inequality as a sufficient condition for the applicability of the first Born approximation:

$$\frac{T\phi}{r} << \frac{4}{3},$$

(3)

where T and ϕ represent the sample thickness and particle volume fraction, respectively. For our situation, we have $T = 10$ mm, $\phi = 2.9 \times 10{-}5$ and $r = 5$ μm; this yields $T\phi/r = 0.058$, which clearly satisfies inequality (3). Hence the first Born approximation is applicable to our analysis.

Figure 3 shows two inline holograms, H_1 and H_2, of a volume at two closely-spaced successive time points, t_1 and t_2, over a range of z. P_i and Q_i represent sub images of H_1 and H_2 that would be formed if only the particles within the slab z_i were imaged. Under the first Born approximation [27], H_1 is the sum of all P_i and H_2 is the sum of all Q_i. The current method is based on the key assumption that the cross-correlation of the full projected images is equal to the sum of the cross-correlations of sub image pairs. This proposition assumes that the particles are randomly distributed within the measurement volume. This requires that the packing fraction not approach levels that require organized packing or

alignment of the particles. A basic proof of this can be formulated as follows with an asterisk (*) denoting a two-dimensional discrete convolution:

$$\sum_{i=1}^{N}(P_i * Q_i) = \sum_{i=1}^{N}\sum_{j=1}^{N}(P_i * Q_i).$$

(4)

Since the particles are randomly distributed, there is no interparticle correlation between adjacent slabs,

$$P_i * Q_j = 0 \text{ for } i \neq j,$$

(5)

hence,

$$H_1 * H_2 = \sum_{i=1}^{N}(P_i * Q_i).$$

(6)

A limitation with current techniques is the particle concentration, whereby high levels of particle seeding can lead to challenges in reconstructing the particle image positions. However, with HCV, a higher level of seeding aids in improving the quality of the cross-
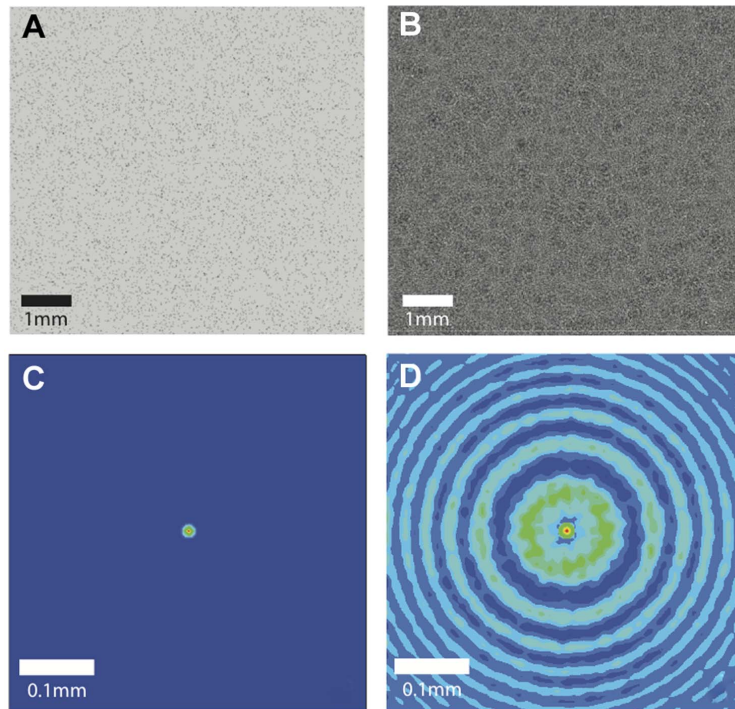
Figure 5. Synthetic image data of particle fields (A, B) and the averaged spatial auto-correlation of the corresponding inline holograms (C, D). The data in A and C represents particles imaged at contact (i.e. $z = 0$), while the particles in B and D are at 20 mm propagation ($\lambda = 532$ nm).
doi:10.1371/journal.pone.0065714.g005

correlation that has the depth information readily encoded. This result can be achieved because the spatial relationship is larger than the correlation length.

Decoding the depth information. Under the above model for holographically encoding the depth information in the seeded flow, we can formulate an approach by which over a specified

depth, we may model a full cross-correlation function for the entire volume.

As customary in PIV, the projected holographic images are discretized into sub-regions. Within each sub-region (which is 2D in the projected image domain), an analytical model of the flow is developed in which the velocity of the flow is specified as a function of z. In this case, we have chosen to use an Akima spline
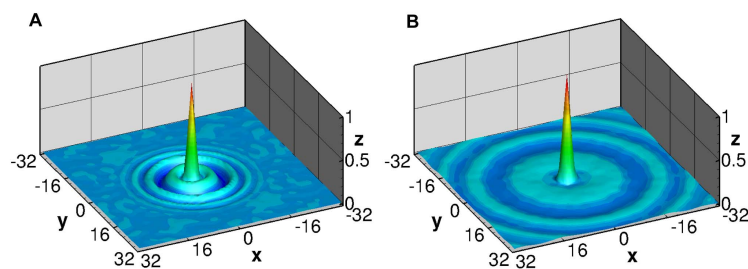
Figure 6. Two, 64×64 pixel normalized, auto-correlation maps from synthetic holographic calibration images of particles having a nominal diameter of 10 μm in a single plane. A) Correlation map corresponds to a propagation distance of 3 mm to the image plane. B) Correlation map at 14 mm propagation distance shows wider diffraction ring pattern. At 0 mm there are no rings visible in the auto correlation. The position and subsequent summation of this calibration map is used to replicate the data correlation maps yielding the velocity direction and intensity at different depths in the flow.
doi:10.1371/journal.pone.0065714.g006
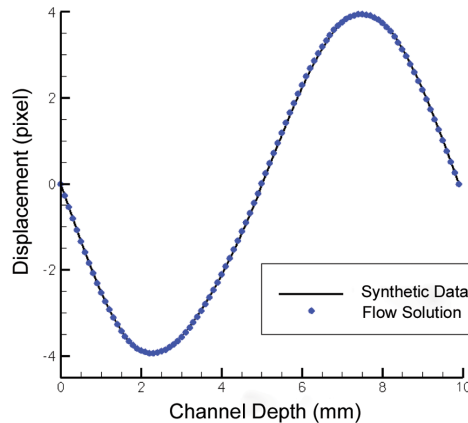
Figure 7. A plot of synthetic flow measurement experiments. The synthetic data (the simulated shear flow between two infinite plates) is shown as a continuous line, with the recovered function indicated by dots. The solution resolved both positive and negative velocity directions from individual cross-correlation maps as illustrated in Figure 8. The normalized RMS difference between the synthetic data and the flow solution is 0.72%.
doi:10.1371/journal.pone.0065714.g007

[28] as this model. From the known velocity field, the probability distribution function (PDF) is readily calculated. It is well known that the cross-correlation is the convolution of the auto correlation (AC) and the probability distribution function for the displacement [25,29,30]:

$$CC = AC * PDF \qquad (7)$$

Since the auto correlation varies with z, we invoke equation (7) to give:

$$CC = \sum_{z=1}^{n} [AC(z) * PDF(z)] \qquad (8)$$

$AC(z)$ can be evaluated analytically, or, in the laboratory by imaging a monolayer of particles at several z locations; we

therefore have a methodology for constructing the cross-correlation map for any given flow field.

Based on this model, we can iteratively reconstruct the 3D velocity field by minimizing the error between the full cross-correlation map from the flow model described above, and the 2D cross-correlation map, obtained for the same sampling region with standard PIV. The modal velocity is measured with standard PIV and contains information that incorporates the velocities of the volume. It is used as the initial velocity estimate for the iterative solver. We use a Levenberg-Marquardt non-linear least-squares solver [19,20] to perform the error minimization. Figure 4 is an illustration of this iterative process which is implemented in HCV. The Levenberg-Marquardt solver minimizes the residual error between the measured cross-correlation data and the current estimate. The solution is deemed to have converged when the sum-of-squares error changes by less than one part in 10^9.

Once the in-plane flow has been reconstructed, the out-of-plane flow can be calculated with the assumption that the fluid is incompressible, the volume is fixed, and the flow obeys the law of continuity.

Modelling

Synthetic image generation. To validate the method described in previous section, computer modeling was conducted via generation of synthetic holographic images of particles. These particles are displaced by a known velocity function between successive images. This simulates a flow field of particles in a laboratory fluid flow. There is complete control over the refractive indices and the noise component to the images. The synthetic images are generated with equations from Widjaja & Soontaranon [31] and Tyler & Thompson [32] that are used for holographic particle size analysis and utilize the first Born approximation insofar as they neglect multiple scattering between distinct particles. The parameters for these synthetic images were: 532 nm illumination, 105 mm objective lens, 5000 particles of 10 μm diameter particles per image, and an image of 1024×1024 pixels with pixel size 7.4 μm. The technique uses the diffraction rings, caused by the particles, to record the motion between series of images with depth information included in terms of diffraction. These images are discretized into sub-regions and cross-correlations are generated between successive image pairs. These correlation maps are then decoded in order to determine the velocity through the depth of the discretized sub-regions.

Figure 5 contains synthetically generated images of particle fields (A, B) and the averaged spatial auto-correlation of their corresponding inline holograms (C, D). The data in A and C represent particles imaged at the contact plane (i.e. $z = 0$), while
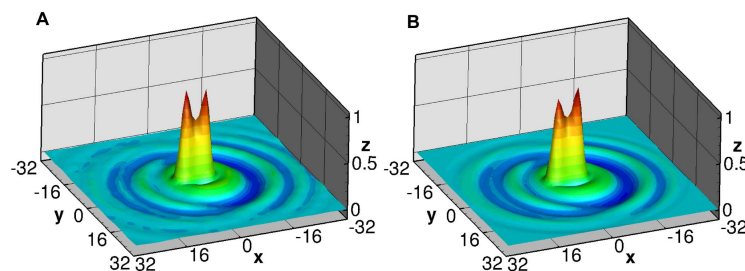

Figure 8. Two, 64×64 pixel normalized, cross-correlation maps for synthetic experiments. A) Cross-correlation of two synthetic image sub-regions. B) Cross-correlation from the combination of calibration maps with the flow model solution.
doi:10.1371/journal.pone.0065714.g008
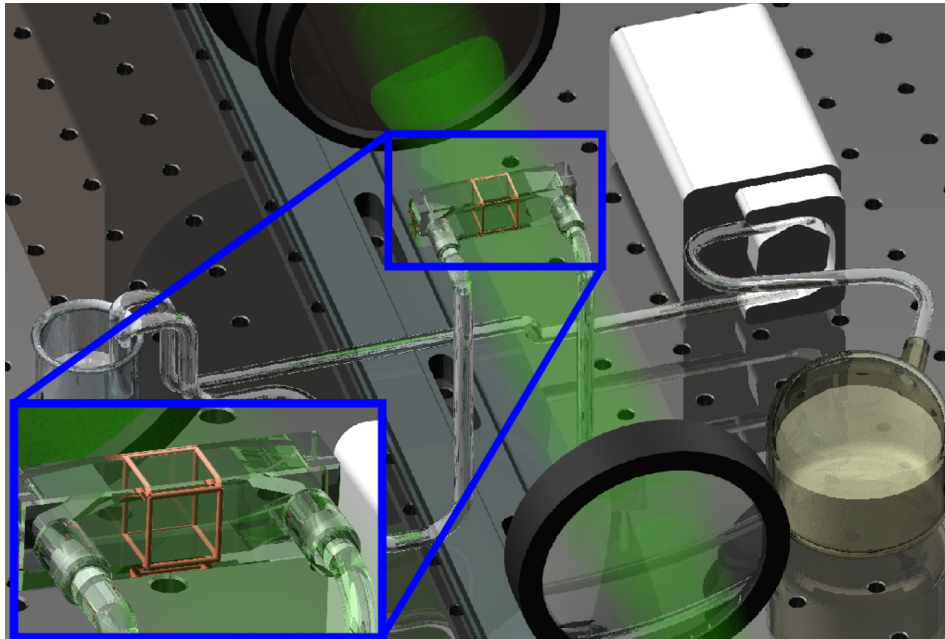
Figure 9. Experimental setup for Holographic Correlation Velocimetry. Shown are the laser, optics, camera, lens, and flow cell attached to the peristaltic pump. A Nd:YLF laser (Darwin 532 nm) was used to generate the inline illumination. This was projected through the Flow Cell (Hellma® 137-QS, 10 mm), which was filled with glycerin mixed with 10 μm glass particles. This seeded flow was imaged with a CMOS camera (IDT Y4) with a 200 mm macro lens (Nikon) set with the focal plane 5 mm from the front of the flow cell for optimized propagation. This flow was maintained with a peristaltic pump through a muffler to remove pulsatility and into an open reservoir. The inset shows the region that is being measured with HCV.
doi:10.1371/journal.pone.0065714.g009

the particles in B and D are at 20 mm propagation distance. Figure 6 shows two example cross-correlation functions of the inline holograms of single-layer particle fields at a small propagation distance and medium propagation distance.

Results of synthetic simulation. The results for the synthetic modelling shown in this paper are generated by representing the variation of velocity field in the depth direction with a cubic polynomial. Figure 7 shows the flow input function with 100 data points for the solution fitting function. These data

Figure 10. An illustration of the flow channel with the velocity field contour in-situ. The inlet and outlet are shown on the near surface of the (Hellma®) manufactured from fused Quartz (SUPRASIL®). The square cross section of the channel is 9 mm×10 mm ±0.01 mm.
doi:10.1371/journal.pone.0065714.g010

Page | **118**

Figure 11. Reconstruction of the out-of-plane velocity magnitude of a single slice of the measured flow within the 9 mm×10 mm flow cell. As the flow enters from the top of the cell ($z = 10$ mm) in a jet like fashion, the momentum carries fluid towards the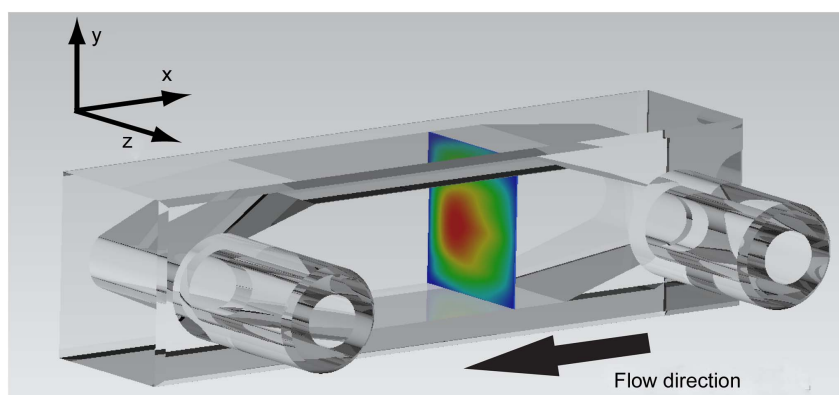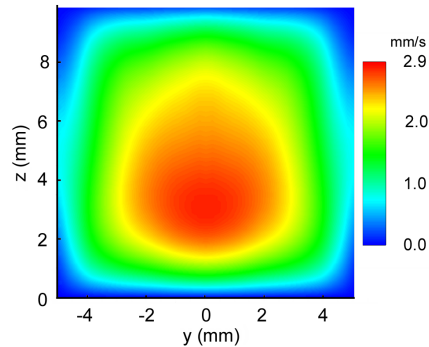 bottom of the cell ($z = 0$ mm). The peak velocity magnitude is therefore not on the centerline, but closer to the bottom. The flow is symmetric about the centerline at $y = 0$ mm, as expected with the cell geometry.
doi:10.1371/journal.pone.0065714.g011

Figure 12. Reconstructed 3D vector field of the fluid flow within the measurement volume. There are approximately 400,000 vectors (colored with velocity magnitude) in the solution. For the sake of clarity, vector resolution has been decreased in x and y-axes.
doi:10.1371/journal.pone.0065714.g012

points are the velocity at each of these channel depth locations. Figure 8 gives a side-by-side comparison of a single correlation function from the input synthetic data field and from the output model solution. It can be seen clearly that the model adequately approximates the synthetic data. This flow has been chosen due to its complexity with particles in different depth planes moving in opposite directions, thereby stretching and spreading the correlation map. Nevertheless, the algorithm is able to fit the calibration maps to the data and solve for the correct flow. The initial guess provided to the solver for this experiment was an all-zero or null field. In the simple parabolic case, there may be several similar solutions and hence convergence may be more difficult. But in these cases, this is compensated for by the capacity to supply a good initial approximation for the 3D HCV. This is done from 2D PIV analysis of the same image data sets used for the HCV analysis. With promising results in the synthetic case studies, experimental work was then conducted. The next section outlines the use of HCV for flow in a Flow Cell cuvette (Hellma) as well as the advancement of this method into a tomographic set up in visualizing flow in a thicker sample such as that in a spinner flask bioreactor.

Experiments and Results

Flow in Cuvette

Experimental set up. A Nd:YLF laser (Darwin $\lambda = 532$ nm) was used to generate collimated inline illumination. The laser operates at 40 kHz, which for the purposes of this work can be considered to be continuous wave illumination. This was projected through the Flow Cell (Hellma®137-QS, 10 mm) filled with glycerin seeded with glass particles having a nominal diameter of 10 μm. The particles have a size distribution with 10% having a diameter less than 3.45 μm, 50% less than 9.1 μm and 90% less than 20.31 μm. The holograms of these particles were imaged with a CMOS camera (IDT Y4) with a 200 mm lens (Nikon Corporations, Japan) set with its focal plane 5 mm from the front of the flow cell to allow optimal propagation for the near particles compared to the particles on the far side of the channel. The lens
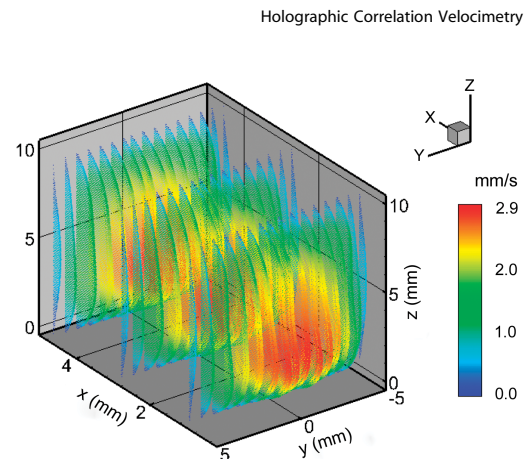
utilized the largest aperture (f-number – f/4.0) to relay light to the CCD. Any alteration in the f-number would alter the required exposure time, as the exposure time is proportional to the square of the f-number. Each image records a volume containing in the order of 2.3×10^4 particles, which satisfies the first Born approximation.

The flow of particles was maintained with a peristaltic pump through a muffler (to remove pulsatility) into an open reservoir as illustrated in Figure 9. The Reynolds number represents the ratio of momentum to viscous forces and is given by $Re = (\rho u D)/\mu$, where ρ is the density, u is a representative velocity, D is the representative length scale and μ is the dynamic viscosity. The Reynolds number of this flow based on the inlet diameter of 2 mm is 1.77. The cross section of the channel is 9 mm×10 mm. The exposure time for the CMOS chip was 762 μs at a 50 Hz frame rate. As the system is based on in-line holography, it is very
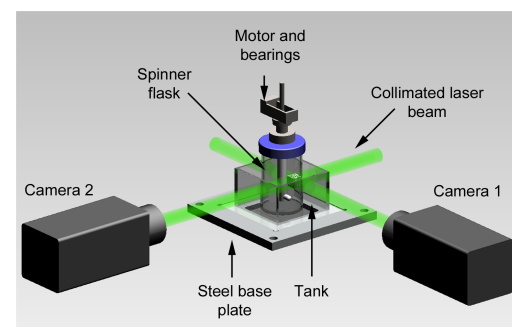
Figure 13. Experimental arrangements for imaging flow in spinner flask bioreactor. The flask was placed inside a rectangular housing filled with water to minimize refraction of laser light. The fluid in the spinner flask was seeded with 10 μm glass particles and stirred by a stepper motor. Two beams illuminated the seeded flow and imaged by two high-speed CMOS cameras (IDT Y4), placed orthogonal to each other to map full 3D velocity profile of the flow.
doi:10.1371/journal.pone.0065714.g013
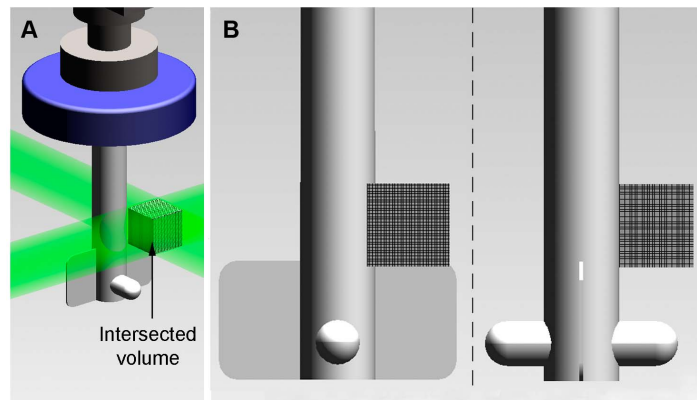
Figure 14. Detailed view of the measured volume. A) Isometric view of the region-of-interest. The intersected volume of the beams is in the size of 11 mm×11 mm×11 mm. B) The beams and the cameras were positioned slightly above the flat impeller shown as the shaded area in the figure.
doi:10.1371/journal.pone.0065714.g014

efficient with regard to the use of light, as it does not rely on side scattering. Most other volumetric measuring systems rely on off-axis or side-scattered light, which requires high power lasers. This efficiency makes the system appropriate for high-speed flows and lower exposure times. Once the images are captured, the analysis is completed on a PC. The calibration images that are used for the algorithm to solve the model for the flow were acquired at 100 depth positions.

Data treatment. Images are first filtered to remove stationary artifacts. This background subtraction was performed using the local temporal average of the image sequence. The images are discretized into sub-regions and the cross-correlation map between images frames is computed for each discrete sub-region. These correlation maps have been time averaged as described by Meinhart *et al.* [33]. It has been shown that averaging the correlation maps results in an improved signal to noise ratio by increasing the effective seeding density of the data set [34]. The averaging was performed on the same sub-regions over 400 frames using moving average technique. This system results in a maximum frame rate of 1000 frames per second; this corresponds to 2.5 independent measurements per second. Consider that the dataset consisted of 1000 images; the first average was conducted from image 1 to image 400. Then, another independent average was calculated based on image 401 to image 800. Those averages should be similar as measurements were conducted to steady-state flow. A further increase in temporal resolution is possible by reducing the number of averages, but with the compromise of reduced signal to noise ratio.

This averaging method gives rise to an apparent increase in seeding density. As this is achieved through temporal averaging in the correlation space this does not affect actual seeding density and
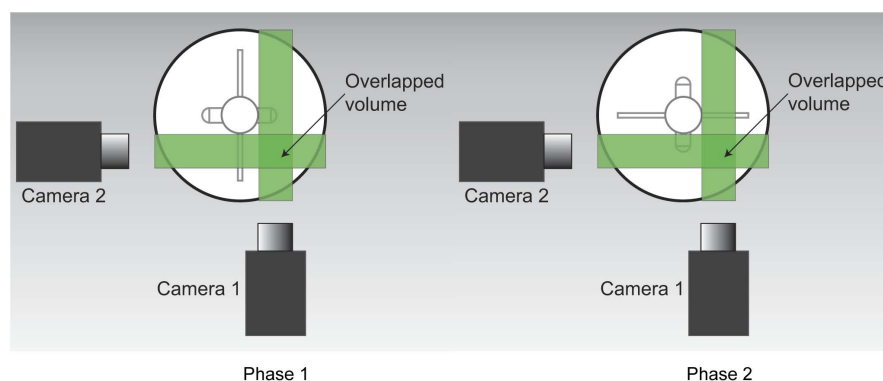

Figure 15. Two phases at which images were captured at each rotation for 50 rpm and 60 rpm as the impeller was spinning in counter-clockwise direction. In Phase 1, consecutive images were captured when the flat paddle was perpendicular to camera 2. On the other hand, Phase 2 captured images when the impeller is 90 degrees out-of-phase to Phase 1.
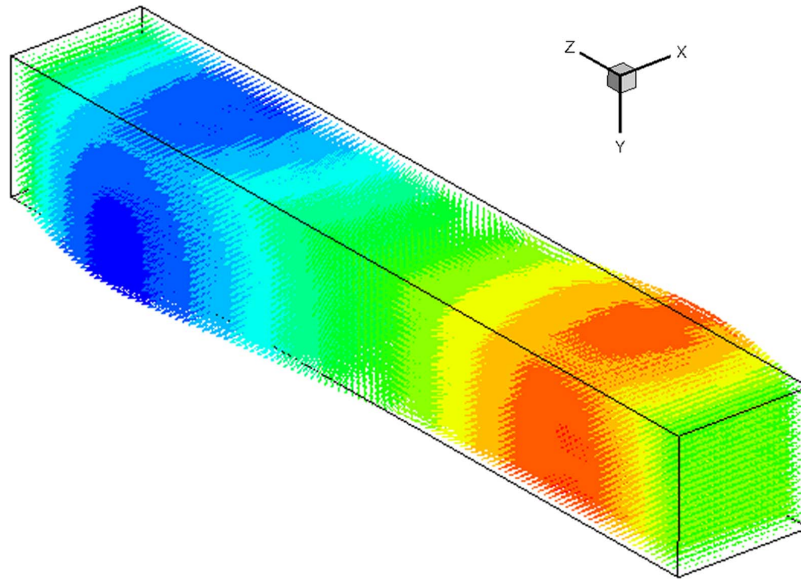doi:10.1371/journal.pone.0065714.g015

Figure 16. A reconstructed 3D volume (11 mm×11 mm×55 mm), based on images captured with one camera. Two velocity components (u and v) were solved for each camera. At this stage, the velocity along the z-axis (w) was still unsolved. The z-component velocity was acquired from another camera where a full 3D3C vector field can be created at the overlapped volume with reconstruction algorithm.
doi:10.1371/journal.pone.0065714.g016

furthermore the validity of the first Born approximation is still upheld in our analysis.

The image sub-regions of 64×64 pixels were evaluated with a spacing of 16×16 pixels in x and y. This achieves an overlap of 75%, which has been shown to be optimal [35]. These correlations are produced using a zero padded fast Fourier transform (FFT) function to prevent any wrapping effects over the 64 pixels sub-region of the diffraction fringes from the particles at long propagation distances.

We found that utilizing experimental calibration images introduced noise to the solution. This noise was removed by using synthetic, noise free calibration images generated from first-principle AC maps. This has been implemented in the analysis throughout the rest of this paper. The use of experimental calibration images would be very useful for calibration of flows using poly-dispersed particles or other seeding particles that are harder to model such as red blood cells [36]. The process is simply implemented by placing a sample of the seeding particles in the working fluid on a glass slide that is traversed through the measurement depth.

The 2D PIV results that reveal the modal velocity of the flow field are used to give the first approximation of the solution to the least-squares solver. This allows the algorithm to rapidly converge at an accurate local minimum in what is a very large parameter space.

Results. Figure 10 shows a single slice of the flow in the channel displayed for orientation and context. It is necessary to note that the highest flow rate is toward the back wall on the opposite side of the inlet and outlet ports. The plane shown is towards the inlet port that is in effect acting like a jet into a volume. With this in mind, it can be understood that because the fluid has momentum as it exits the jet, it will be carried to the back

wall and then through the channel. Figure 11 shows contours for the magnitude of velocity in a single slice of the reconstructed flow field. On the z axis zero is the back wall and we see that the flow is predominantly faster in the lower half of the channel. The flow is extremely symmetrical, which is to be expected from the inlet port being on the centerline of the channel. The corners of the channel clearly illustrate very slow flow occurring here. Again, this is expected in the area where the two walls meet and there is a high drag on the fluid.

To best illustrate that the full 3D volume of the flowing fluid is reconstructed, Figure 12 shows the vectors of over 400,000 points. The spacing between these points is 0.2 mm in the x and y plane and 0.1 mm in the z or depth direction. The vector color is velocity magnitude and there is a single slice of the velocity contour levels. Next, the technique was expanded using tomographic set up to image rotational flow in a bioreactor spinner flask.

Tomographic- HCV for Flow in a Spinner Flask

Experimental set up. This experiment used similar laser and optics set up as in the previous experiment. Figure 13 shows the general layout of the experiment. In order to gain full 3D measurement in the system, two orthogonal beams were projected through the 100 mL microcarrier spinner flask (BellCo Glass Inc, USA), having internal diameter 55 mm. The flask was filled with a 100 mL distilled water seeded with glass particles having nominal diameter of 10 μm at $5×10^{-4}$ g/mL seeding density. The flask was placed inside a rectangular housing, which was also filled with water and has flat exterior faces to prevent the lensing effect due to curved flask surface during the imaging process. The set-up was mounted on a steel base plate and secured to a precision optical table to eliminate any vibrations. The data were recorded with a
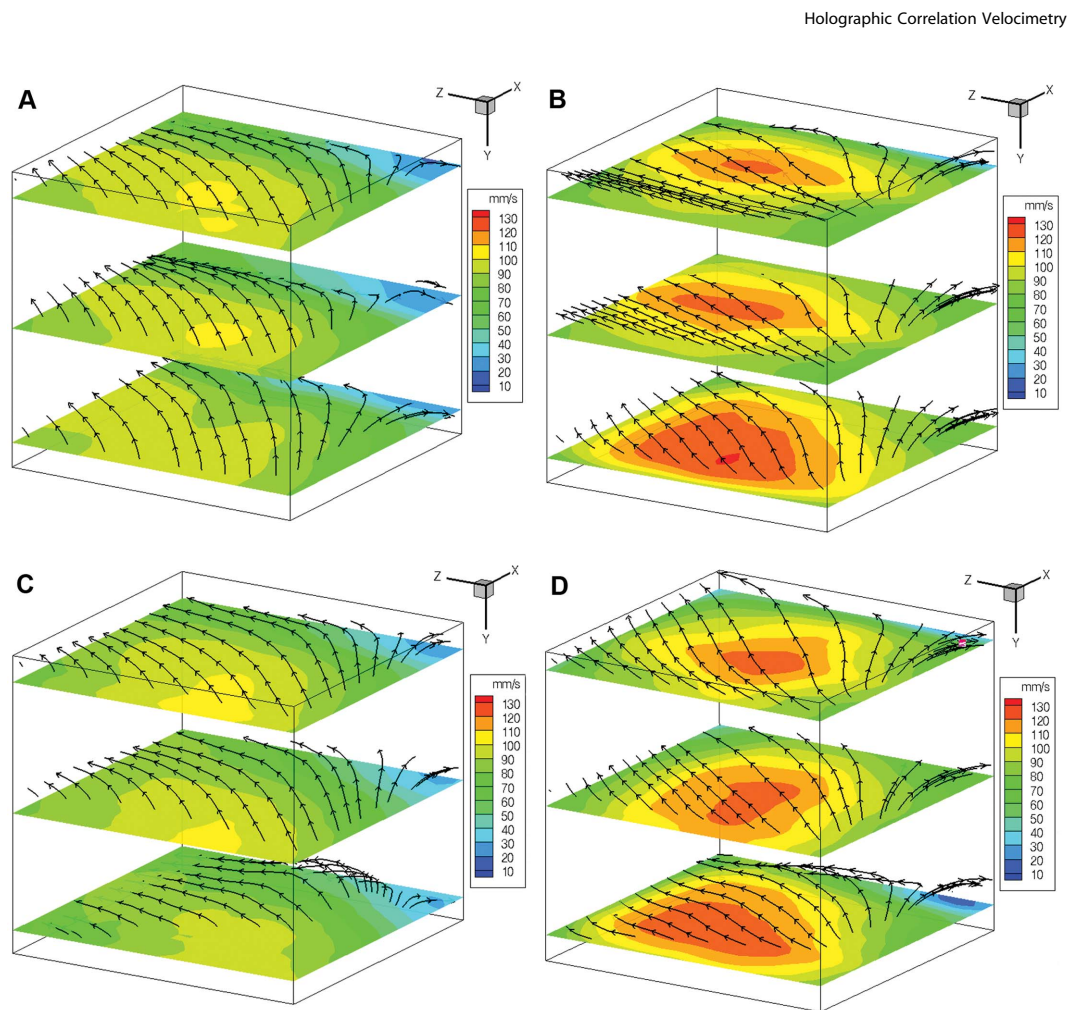
Figure 17. Reconstructed 3D vector field in spinner flask bioreactor in Phase 1 (A, B) and Phase 2 (C, D) regions. A, C) As the flow stirred at 50 rpm (Re = 3338), the intersected volume vector field showed that the flow enters from negative x-plane and exits at positive z-plane. B, D) The fluid enters the volume at higher speed as the flow was agitated at 60 rpm (Re = 4006).
doi:10.1371/journal.pone.0065714.g017

CMOS camera (IDT Y4) fitted with Nikkor 105 mm f/2.8G lens (Nikon, Japan) at a rate of 450 Hz with exposure time of 54 μs. Due to the nature of the impeller's opaque material that impeded the field of view, the beam and camera were positioned slightly on top of the impeller for the imaging procedures as shown in Figure 14. Furthermore, each camera captured two consecutive images when the impeller was at a similar position each rotation. 50 pairs of images were taken for averaging purposes.

The flow of particles in the spinner flask was induced with the rotation of the impeller, driven by a stepper motor (Sanyo Denki America Inc, USA) run through a motion controller (National Instruments Australia, North Ryde, NSW, Australia), enabling 5.12×10^{4} steps per revolution. The velocity of the motor was further reduced by a factor 30 through the use of a worm gear, which allows a smooth rotation of the disk at all speeds. The Reynolds number of the flow $Re = \Omega R^{2}/\nu$, ν being the kinematic

viscosity (dynamic viscosity, μ per density, ρ) of the water, was based on the radius of the flat impeller (R = 25.3 mm) and rotational velocity, Ω of 5.24 rad/s (50 rpm) or 6.28 rad/s (60 rpm), which translates to Reynolds numbers of 3338 and 4006, respectively. It is important to note that most stirred vessel achieved turbulent condition at Reynolds number higher than 10^{4}, having the Reynolds number defined as $Re = \Omega D^{2}/\nu$ [37]. As most fluid mechanics journals used radius as the length scale rather than diameter, the Reynolds number defined in this manuscript is 4 times lower than the Reynolds number utilizing a diameter length scale. The calibration images used in the algorithm to solve the depth of the flow were obtained at 120 depth positions at 32-pixel spacing. Due to the tomographic set-up of the experiment, two sets of data were obtained at one time, one for each camera, from which the overlapped volume was reconstructed to achieve 3D measurement. For each speed, two

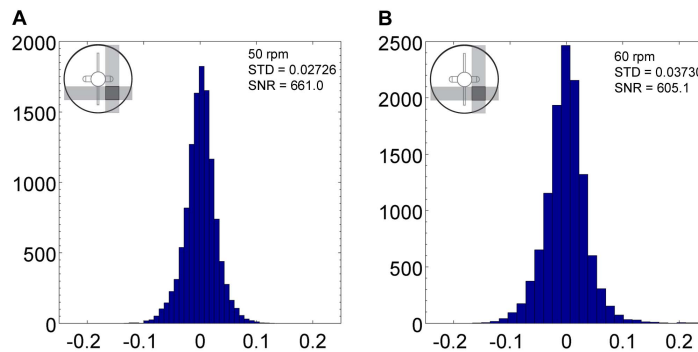**Figure 18. Probability density function of reconstructed volume divergence for flow in spinner flask stirred at 50 rpm (A) and 60 rpm (B) at Phase 1.**
doi:10.1371/journal.pone.0065714.g018

phases were recorded separately to map the flow in the spinner flask as shown in Figure 15. Flow profiles in front and behind the flat impeller were reconstructed for each spinning rate producing four measurements in total.

Data treatment. Each set of data captured by each camera were analysed separately before they were combined to create the volumetric flow profile. Filtering procedures were completed as before. The averaging was performed over 50 pairs of images captured at the same time of each phase. In the analysis, the images were divided into smaller sub-regions in the size of 128×128 pixels. The spacing in x and y dimensions was 32×32 pixels, allowing 75% overlap as the previous experiment. In this experiment, the calibration images were different than previous experiment. Due to thicker depth of the flask, the calibration images is carried out from 5 mm to 60 mm projection (55 mm thick). The calibration images used the diffraction pattern to solve the depth location (z-axis) of particles in the 2D images from the experiment.

In order to obtain full field 3-dimensional flow patterns, 2 sets of 3D-2-component (3D2C), 90-degree to each other were combined and reconstructed at the overlapped volume. The redundant parameter of each data set (y-direction) was used as a measure to quantify the divergence at every node. Due to the incompressible nature of water, the divergence must be zero. Therefore, in this case, the divergence was a measure of how the values from 2 separate data sets conform to each other.

Results. By having 2 cameras, one camera could capture images in x-y plane while reconstructing the depth in the z-axis, whereas another camera, positioned 90 degrees to the first camera, could capture images in the z-y plane and decode the depth in the x-axis. Figure 16 shows the remodeled volume developed from data gathered in camera 1. It can be seen this configuration is able to capture important features of the flow. As the impeller is spinning in the counter-clockwise direction, the fluid closer to the camera moves in the positive x-direction whereas the fluid further in the depth (z-axis) moves in the negative x-direction.

To create the flow field in the overlapped volume, the start and end of the depth slice for each camera were selected to define the overlapped boundaries of the region. The spacing of layers in the depth has to be similar to the horizontal spacing in order to match each node and ensure accuracy of the reconstructed volume. In this experiment, 32-pixel spacing was chosen in every direction. Based on the captured information, a 3D vector field was mapped, as shown in Figure 17, and the probability density function (PDF) of vector divergence was plotted (Figures 18 and 19).

Figure 17 depicts slices of streamlines and velocity contours of the volume. Some points are omitted in the figure to enhance clarity. The top layer is closer to the free surface whereas the
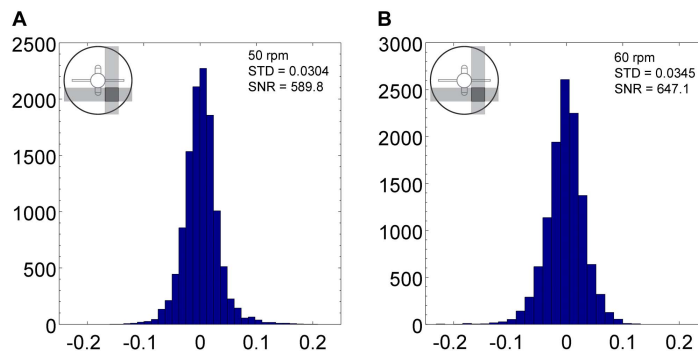

Figure 19. Probability density function of 11638 nodes at Phase 2 region, rotated at 50 rpm (A) and 60 rpm (B).
doi:10.1371/journal.pone.0065714.g019

bottom layer is closer to the impeller. As the impeller rotates, it can be seen from the streamlines that the flow rotates and exits at the positive z-plane. In Phase 1, high velocity occurs at the entrance of the volume as the flat paddle impeller pushes the liquid into the imaging region. Lowest velocity occurs near the wall region due to the no slip boundary condition with slight recirculation at the edge. At 60 rpm, the fluid flow had higher velocity with less curvature profile near the free surface. Overall, there was only minor change in the flow topology at this phase.

On the other hand, Phase 2 flow shows some change in topology near the impeller region. The change in height is the trail caused by the flat impeller's movement. The fluid is forced to flow up and around the flat paddle as it rotates, causing some change in height downstream.

In order to measure the accuracy of the measurement, histograms of the calculated divergence at each node were created for each data set. The standard deviation of the divergence and the signal to noise ratio (SNR) were calculated to determine the statistical variation of the measured divergence and the strength of the proposed technique in measuring the displacement, respectively. SNR is defined by the ratio of maximum magnitude over standard deviation of divergence in the volume as presented in equation (9). Figures 18 and 19 show the divergence histogram for total of 11638 nodes of each volume. All tests show normal distribution profile. The lowest SNR occurred for the 50 rpm data set at Phase 2 with a value of 589.8. The high signal strength in relation to noise demonstrates that the measurement technique is reliable as volumetric velocimetry measurement technique.

$$SNR = \frac{\max\left(\sqrt{\Delta x^2 + \Delta y^2 + \Delta z^2}\right)}{\sigma_{div}} \qquad (9)$$

$$\sigma_{div} = stdev\left(\frac{\partial \Delta x}{\partial x} + \frac{\partial \Delta y}{\partial y} + \frac{\partial \Delta z}{\partial z}\right) \qquad (10)$$

Discussion

This study has shown clearly the applicability of HCV in characterizing volumetric flow field. We have demonstrated that the use of HCV can characterize both 2D flow in a cuvette, as well as 3D flow in a spinner flask. This measurement technique is superior to normal stereoscopic PIV, where one layer is measured at one time thus imposing difficulty in the experimental procedure. By decoding the depth based on the diffraction ring in the correlation function, 3D2C measurement field was obtained from 2D images. By having another set of data orthogonal to each other, a full 3D3C flow field was achieved. As the light source is inline with the sensor, a high Reynolds number flow could be characterized due to the efficient use of light. Additionally, as the proposed technique is an optical based measurement, high Reynolds number flow can be characterized by increasing the frame rate at which the camera is acquiring the data. The technique is not only limited to low Reynolds number flow, but rather limited to the maximum acquisition rate of the camera.

This non-intrusive measurement technique presented is suitable for biological flow analysis which sterility is one of the main concerns. Unlike normal flow characterization techniques that involve the use of probes, which have to be immersed in the medium, HCV is an optical-based measurement using a laser and a camera. It allows the medium and cells to be kept isolated in the spinner flask, hence maintaining sterility during the measurement procedure. The volumetric field enables biologists to gain understanding in cell growth and therefore illustrate the important parameters for the proliferation process. The high SNR magnitude proved the reliability in the measurement.

Conclusion

In this paper, an improved approach for volumetric flow measurement has been developed, in which the correlations of inline holograms can be successfully used to generate a full 3D velocity field of a seeded fluid. It has been shown that these correlations have encoded depth information, providing the velocity at different depths within the fluid. This method allows flow reconstruction without the need to holographically reconstruct the 3D image. Holographic Correlation Velocimetry (HCV) allows for the direct measurement of the velocity field at all depth locations through the use of the volumetric correlation function. Not reconstructing the 3D particle field offers advantages over other HPIV and Digital HPIV systems by directly producing velocity data from 2D images. This approach allows the use of seeding densities in excess of maximum levels for other techniques. Since it does not rely on side scattering, the system makes very efficient use of available light. This efficiency could be utilized to create a high quality system at a modest cost. Alternatively, this efficiency allows low exposure times and the dynamic measurement of high speed flows.

We have shown that this novel technique is able to characterize 3D2C flow in a cuvette and in a spinner flask bioreactor at high signal-to-noise ratio. The laminar flow in a cuvette, with Re = 1.77 showed a maximum velocity of 2.9 mm/s. We have also shown the flexibility of this technique in tomographic set up in the spinner flask experiment. Maximum velocities of 100 mm/s and 130 mm/s were achieved at Reynolds numbers of 3338 and 4006, respectively. The non-intrusive nature of this technique ensures the sterility and suitability for biological flow characterization especially in cell culture procedure. Future work would involve defining the mechanical parameters associated in the process by using this technique. Mixing ability and shear stress are two main considerations that would improve the culture protocol and bioreactor design.

Acknowledgments

Author Contributions

Conceived and designed the experiments: MI SH. Performed the experiments: MI SH. Analyzed the data: MI SH CS. Contributed reagents/materials/analysis tools: MI SH CS DP AF. Wrote the paper: MI SH CS DP KH AF. Designed the analytical software: MI SH CS DP AF.

References

1. Hentze H, Graichen R, Colman A (2007) Cell therapy and the safety of embryonic stem cell-derived grafts. Trends in Biotechnology 25: 24–32.
2. Ho H-Y, Li M (2006) Potential application of embryonic stem cells in Parkinson' Âôs disease: drug screening and cell therapy. Regenerative Medicine 1: 175–182.
3. Hoffman LM, Carpenter MK (2005) Characterization and culture of human embryonic stem cells. Nature Biotechnology 23: 699–708.
4. Lyon A, Harding S (2007) The potential of cardiac stem cell therapy for heart failure. Current Opinion in Pharmacology 7: 164–170.

Page | **124**

5. Mountford JC (2008) Human embryonic stem cells: origins, characteristics and potential for regenerative therapy. Transfusion Medicine 18: 1–12.

6. Smith AG (2003) Embyo-derived stem cells: Of mice and men. Annual Review of Cell and Developmental Biology 17: 435–462.

7. Mahir N, Rockwell D (1996) Vortex formation from a forced system of two cylinders.1. Tandem arrangement. Journal of Fluids and Structures 10: 473–489.

8. Comte-Bellot G (1976) Hot-wire anemometry. Annual Review of Fluid Mechanics 8: 209–231.

9. Tropea C (1995) Laser-Doppler anemometry - recent developments and future challenges. Measurement Science & Technology 6: 605–619.

10. Adrian RJ (1991) Particle-imaging techniques for experimental fluid-mechanics. Annual Review of Fluid Mechanics 23: 261–304.

11. Adrian RJ (2005) Twenty years of particle image velocimetry. Experiments in Fluids 39: 159–169.

12. Willert CE, Gharib M (1991) Digital particle image velocimetry. Experiments in Fluids 10: 181–193.

13. Arroyo MP, Greated CA (1991) Stereoscopic particle image velocimetry. Measurement Science & Technology 2: 1181–1186.

14. Fouras A, Dusting J, Hourigan K (2007) A simple calibration technique for stereoscopic particle image velocimetry. Experiments in Fluids 42: 799–810.

15. Fouras A, Lo Jacono D, Hourigan K (2008) Target-free Stereo PIV: a novel technique with inherent error estimation and improved accuracy. Experiments in Fluids 44: 317–329.

16. Arroyo MP, Hinsch KD (2008) Recent developments of PIV towards 3D measurements. Particle Image Velocimetry: New Developments and Recent Applications 112: 127–154.

17. Barnhart DH, Adrian RJ, Papen GC (1994) Phase-conjugate holographic system for high-resolution particle-image velocimetry. Applied Optics 33: 7159–7170.

18. Hinsch KD (2002) Holographic particle image velocimetry. Measurement Science & Technology 13: R61-R72.

19. Meng H, Pan G, Pu Y, Woodward SH (2004) Holographic particle image velocimetry: from film to digital recording. Measurement Science & Technology 15: 673–685.

20. Soria J, Atkinson C (2008) Towards 3C–3D digital holographic fluid velocity vector field measurement - tomographic digital holographic PIV (Tomo-HPIV). Measurement Science & Technology 19: 12.

21. Ooms T, Koek W, Westerweel J (2008) Digital holographic particle image velocimetry: eliminating a sign-ambiguity error and a bias error from the measured particle field displacement. Measurement Science & Technology 19: 074003.

22. Pan G, Meng H (2001) Digital in-line holographic PIV for 3D particulate flow diagnostics. PIV '01: 4th International Symposium on Particle Image Velocimetry Göttingen, Germany. 17–19.

23. Pu Y, Meng H (2000) An advanced off-axis holographic particle image velocimetry (HPIV) system. Experiments in Fluids 29: 184–197.

24. Raffel M, Willert CE, Wereley ST, Kompenhans J (2007) Particle Image Velocimetry: A Practical Guide. Berlin, Heidelberg, New York: Springer.

25. Fouras A, Lo Jacono D, Nguyen CV, Hourigan K (2009) Volumetric correlation PIV: a new technique for 3D velocity vector field measurement. Experiments in Fluids 47: 569–577.

26. Born M, Wolf E (1999) Principles of Optics, seventh (expanded edition). Cambridge: Cambridge University Press.

27. Cowley JM (1995) Diffraction physics. Amsterdam: Elsevier

28. Akima H (1970) A new method of interpolation and smooth curve fitting based on local procedures. Journal of the Acm 17: 589–602.

29. Fouras A, Dusting J, Lewis R, Hourigan K (2007) Three-dimensional synchrotron X-ray particle image velocimetry. Journal of Applied Physics 102: 064916.

30. Dubsky S, Jamison RA, Irvine SC, Siu KKW, Hourigan K, et al. (2010) Computed tomographic X-ray velocimetry. Applied Physics Letters 96: 023702.

31. Widjaja J, Soontaranon S (2009) All wavelet analysis of in-line particle holograms. Optics and Lasers in Engineering 47: 1325–1333.

32. Tyler GA, Thompson BJ (1976) Fraunhofer holography applied to particle-size analysis - reassessment. Optica Acta 23: 685–700.

33. Meinhart CD, Wereley ST, Santiago JG (2000) A PIV algorithm for estimating time-averaged velocity fields. Journal of Fluids Engineering-Transactions of the Asme 122: 285–289.

34. Samarage C, Carberry J, Hourigan K, Fouras A (2012) Optimisation of temporal averaging processes in PIV. Experiments in Fluids 52: 617–631.

35. Theunissen R, Scarano F, Riethmuller ML (2007) An adaptive sampling and windowing interrogation method in PIV. Measurement Science & Technology 18: 275–287.

36. Nguyen CV, Carberry J, Fouras A (2011) Volumetric-correlation PIV to measure particle concentration and velocity of micro flows. Experiments in Fluids.

37. Hemrajani RR, Tatterson GB (2004) Mechanically Stirred Vessels. In: Paul EL, Atiemo-Obeng VA, Kresta SM, editors. Handbook of Industrial Mixing: Science and Practice. USA: John Wiley & Sons, Inc. 345.

6.2   Discussion and Conclusion

This study outlines a novel correlation-based volumetric measurement technique. The technique is capable of quantifying a 3D2C vector field of a flow. With a simpler experimental setup, the technique provides an advantage superior to conventional scanning PIV. Correlation patterns for various distances from the image plane was computationally generated and used as a calibration map. Using the given calibration map as a reference, the technique can accurately solve the in-plane velocity components for the given volume.

The technique has been proven applicable for characterising complex flow such as the flow in the spinner flask bioreactor. The use of HCV in a tomographic setup to obtain a 3D3C vector field of the flow proves the versatility of the technique. Although in the presented manuscript, this technique is limited by the optical access obstructed by the impeller in the spinner flask bioreactor, HCV is highly applicable for other types of bioreactors, such as spinning lid bioreactors. The use of the proposed volumetric measurement technique is not limited to bioreactor flows. It can also be used for other fields, such as measuring blood flow, industrial and aeronautical flows, to name a few. This technique will allow one to gain and strengthen the knowledge of the underlying mechanics in the respective field.

Chapter 7

Conclusions

T HIS thesis has presented an experimental fluid mechanics perspective in the study of bioreactor flows. The results presented in this study, utilising dye visualisation and laser velocimetry imaging techniques, was able to uncover the flow behaviour and provide qualitative and quantitative insights into the biomechanical considerations for cell culture procedures. This chapter outlines a general summary of studies included in this thesis as well as several future work recommendations. Finally, the concluding remarks end this chapter.

7.1 Final Conclusions

Flows in rotating lid and spinner flask bioreactors were studied through the application of experimental fluid dynamics. The experimental techniques uncovered the practical flow in the bioreactors. The use of dye visualisation, planar Particle Image Velocimetry, and a novel 3D imaging technique known as Holographic Correlation Velocimetry enabled the depiction of the flow features, while concurrently providing the ability to quantify related properties within the bioreactors. The extensive characterisation gives insight into the relationship between fluid dynamics and cell culture. Additionally, such qualitative and quantitative understandings could define the bioreactor design requirements, thus accelerating the development of improved bioreactors for biomedical applications in both industrial or research capacities.

In Chapter 3, the effect of dye density variation on the vortex breakdown structure and stability was analysed experimentally in a rotating top lid cylinder. The sinking velocity of dense dye, which counteracts the global recirculation, induced the stagnation point formation at the bottom of vortex breakdown. The critical Reynolds number (Re) was reduced by a factor of two for a 0.02% density difference. In contrast, a light dye

leads to a new structure where the jet of dye pierces through the breakdown bubbles without destroying them, proving the robustness of vortex breakdown to disturbance. The new regime was observed at density differences of 0.03% and higher. The low-shear condition at the vortex breakdown is highly suitable environment for cell culture. The use of microcarriers in a rotating lid bioreactor would create a behaviour similar to the dense dye experiment. The microcarriers are expected to accumulate and thicken at the centre of the container, near the stagnation point of the vortex breakdown. The new structure of a light jet penetrating through the vortex breakdown could be used to feed the cells located in the bubble without having to put a probe close to the cells. This could benefit the suspension cell culture.

The flow characteristics in spinner flask bioreactor were quantified using 2D PIV in meridional and azimuthal planes. The velocities and shear stresses steadily increase with the spinning rate as highlighted in Chapter 4 and 5. The low pressure behind the flat impeller creates vortices, which ensure the fluid within the bioreactor is thoroughly mixed. As the main flow is in the azimuthal direction, the bottom surface of the flask recorded the highest shear magnitude as a result of the interaction between moving fluids and the no-slip boundary condition at the wall. The impact of flow environment on microcarriers and cell growth was investigated in Chapter 5. Cytodex 3 and Hillex II microcarriers were damaged at speeds higher than 40RPM (Re = 2671) and 70RPM (Re = 4674), correspondingly. The damaged microcarriers were not able to support cell growth. Mouse OG2 induced pluripotent cells showed the highest cell count at 25RPM (Re = 1669). Lower speeds were not able to maintain the suspension of the microcarriers and cells in the spinner flask. With a partial section of the impeller immersed in the medium to reduce the shear magnitude in the system, the lift force to keep the microcarriers in suspension was reduced. Over 7 days, mouse iPSCs showed the highest cell count in flask spun at 25RPM. At this speed, the maximum shear stress recorded was 0.0984 Pa at the bottom surface of the bioreactor.

The development of improved, correlation-based, volumetric flow measurement technique allows complex 3-dimensional flow to be characterised with a high level of detail. The depth information, coded in the correlation patterns, allows flow reconstruction without the need to holographically reconstruct the 3D image, proving it superior to digital holographic PIV measurement techniques. The direct arrangement of the light source to the camera enables an efficient use of the available light which improves the

capability of the technique to capture images at low exposure times for dynamic measurement of high speed flows. The high signal-to-noise ratio obtained in experiments demonstrated the reliability of HCV in measuring laminar (Re = 1.77) and turbulent (Re = 3338 and 4006) flows in a cuvette and a spinner flask, respectively.

In summary, the studies presented in this thesis highlight the importance of fluid mechanics in bioreactor culture procedure. To date, the analyses conducted form one of the most extensive and advanced experimental characterisation works on bioreactor flows. The novel contributions demonstrated in the study are summarised as followings:

- The effect of varying the density in rotating top bioreactor has been visualised experimentally. The introduction of higher density fluid to the flow induced the vortex breakdown formation and altered the critical Reynolds number. Additionally, a new structure was seen piercing through the vortex breakdown with the introduction of a less dense fluid. The low-shear mixing conditions in vortex breakdown can be highly beneficial for *in vitro* suspension culture applications.

- The flow fields within the bioreactor have been extensively quantified. The flow features and stress distributions near the impeller, sidewall, and bottom wall in meridional and azimuthal planes at different Reynolds numbers are described. The fluid-wall interaction at the bottom surface of the flask created the highest shear magnitude in the bioreactor. The highest velocity achieved at the edge of the impeller in the azimuthal plane also produced a high shear region. The recirculation behind the flat impeller facilitates the mixing in the system.

- A novel Holographic Correlation Velocimetry imaging technique was proposed and tested experimentally. Three-dimension two-component flow was measured with the efficient use of light without relying on the side scattering, such as required in conventional laser velocimetry technique. The utility of HCV was demonstrated in imaging the flow in a spinner flask bioreactor.

- The systematic approach in defining the biomechanical characteristics using non-dimensional functions ensures the applicability of the results to various applications. The input parameters in previous and future cell studies can be correlated to the experimental results presented in this thesis to estimate the required conditions for cell culture. The wide range of parameters covered in this study can

be used as a reference datasheet for various input speeds in cell experiments, as well as an aid in the development of new suspension bioreactors.

7.2   Recommendations for Future Study

Suspension cell culture using bioreactors has demonstrated great promise in enhancing cell growth compared with other types of bioreactors. However, further research is necessary to improve our understanding of cell mechanics in order for a highly-efficient bioreactor to be realised. Future study suggestions are described by the following:

- The potential use of rotating lid bioreactors should be investigated. *In vitro* cell experiments should be conducted to gauge vortex breakdown feasibility in supporting cell growth in the region.

- Numerical modeling should be done to check for the effect of possible rig imperfection.

- The database of characterised culture conditions can be expanded by conducting similar characterisations for various types of bioreactors and input parameters.

- The sensitivity and impact of possible changes during practical applications need to be examined. As the cell mass and volume increase over time, this may vary the stress at which the cells are exposed to. Furthermore, the effect of dead cells in the system and media replenishment may require further investigation.

- Further investigation of the correlation of shear stress to cell growth is required, especially at a subcellular level. An independent experiment that quantifies relations of shear to cell count would be ideal in order to define the design requirement of suspension bioreactors. These parameters can help the development of a generalist bioreactor that could support the culture of various cell lines.

7.3   Concluding Remarks

The studies presented in this thesis contribute further insight concerning the flow dynamics in rotating lid and spinner flask bioreactors. Defining the role of fluid dynamics in biological flows, specifically for cell culture protocols has been the main focus of this thesis. Extensive experimental flow characterisation was demonstrated, which could serve as an example for future biomechanical characterisation studies. The parametric

generalisation of the studies would allow quantitative measurement results to be used as a database for previous and future cell works. The outcome of the study, along with the results from various cell experiments, provides specification for bioreactor design requirements. These parameters could assist in the development of next-generation bioreactors and contribute to the advancement of cell culture processing technologies. Improved, more efficient bioreactors would allow stem cells to be cultured in a more efficient manner and achieve a higher cell yield. Large numbers of cells available, will allow stem cell therapy to be realised for the treatment of tissues, damaged through injury or degenerative diseases, which affects millions of patients and costs the healthcare sector billions of dollars. The realisation of cell therapy has the capacity to relieve an immense burden in healthcare expenditure and more importantly, to improve the quality of life for many.

Bibliography

ABRANCHES, E., BEKMAN, E., HENRIQUE, D. & CABRAL, J. M. 2007 Expansion of mouse embryonic stem cells on microcarriers. *Biotechnology and Bioengineering* **96** (6), 1211–1221.

ADRIAN, R. J. 1991 Particle-imaging techniques for experimental fluid mechanics. *Annual Review of Fluid Mechanics* **23**, 261–304.

ADRIAN, R. J. 2005 Twenty years of particle image velocimetry. *Experiments in Fluids* **39**, 159–169.

AKASHA, A. A., SOTIRIADOU, I., DOSS, M. X., HALBACH, M., WINKLER, J., BAUNACH, J. J., KATSEN-GLOBA, A., ZIMMERMANN, H., CHOO, Y., HESCHELER, J. & SACHINIDIS, A. 2008 Entrapment of embryonic stem cells-derived cardiomyocytes in macroporous biodegradable microspheres: preparation and characterization. *Cellular Physiology and Biochemistry* **22** (5–6), 665–672.

AKIMA, H. 1970 A new method of interpolation and smooth curve fitting based on local procedures. *Journal of the ACM* **17** (4), 589–602.

AKIYAMA, Y., HONMOU, O., KATO, T., UEDE, T., HASHI, K. & KOCSIS, J. D. 2001 Transplantation of clonal neural precursor cells derived from adult human brain establishes functional peripheral myelin in the rat spinal cord. *Experimental Nuerology* **167** (1), 27–39.

ALFRED, R., GAREAU, T., KRAWETZ, R., RANCOURT, D. & KALLOS, M. 2010 Serum-free scaled up expansion and differentiation of murine embryonic stem cells to osteoblasts in suspension bioreactors. *Biotechnology and Bioengineering* **106**, 829–840.

ALVIANO, F., FOASSATI, V., MARCHIONNI, C., ARPINATI, M., BONSI, L., FRANCHINA, M., LANZONI, G., CANTONI, S., CAVALLINI, C., BIANCHI, F., TAZZARI, P. L., PASQUINELLI, G., FORONI, L., VENTURA, C., GROSSI, A. & BAGNARA, G. P. 2007 Term amniotic membrane is a high throughput source for multipotent mesenchymal stem cells with the ability to differentiate into endothelial cells in vitro. *BMC Developmental Bilogy* **7** (1), 11.

AMIT, M., CHEBATH, J., MARGULETS, V., LAEVSKY, I., MIROPOLSKY, Y., SHARIKI, K., PERI, M., BLAIS, I., SLUTSKY, G., REVEL, M. & ITSKOVITZ-ELDOR, J. 2010 Suspension culture of undifferentiated human embryonic and induced pluripotent stem cells. *Stem Cell Reviews and Reports* **6** (2), 248–259.

AMIT, M., MARGULETS, V., SEGEV, H., SHARIKI, K., LAEVSKY, I., COLEMAN, R. & ITSKOVITZ-ELDOR, J. 2003 Human feeder layers for human embryonic stem cells. *Biology of Reproduction* **68** (6), 2150–2156.

AMIT, M., SHARIKI, C., MARGULETS, V. & ITSKOVITZ-ELDOR, J. 2004 Feeder and serum-free culture system for human embryonic stem cells. *Biology of Reproduction* **70** (3), 837–845.

ARROYO, M. P. & GREATED, C. A. 1991 Stereoscopic particle image velocimetry. *Measurement Science and Technology* **2**, 1181–1186.

ARROYO, M. P. & HINSCH, K. D. 2008 Recent developments of PIV towards 3D measurements. In *Particle Image Velocimetry: New Developments and Recent Applications* (ed. A. Schröder & C. E. Willert), pp. 127–154. Springer, Heidelberg.

ARSENIJEVIC, Y., VILLEMURE, J.-G., BRUNET, J.-F., BLOCH, J. J., DÉGLON, N., KOSTIC, C., ZURN, A. & AEBISCHER, P. 2001 Isolation of multipotent neural precursors residing in the cortex of the adult human brain. *Experimental Neurology* **170** (1), 48.

ATKINSON, C., STANISLAS, M. & SORIA, J. 2011 Two and three-dimensional geometry of low speed streaks in wall-bounded turbulence using tomographic PIV. *9th International Symposium of PIV (Kobe, Japan)* pp. –.

AWAD, H. A., BUTLER, D. L., BOIVIN, G. P., SMITH, F. N., MALAVIYA, P., HUIBREGTSE, B. & CAPLAN, A. I. 1999 Autologous mesenchymal stem cell-mediated repair of tendon. *Tissue Engineering* **5** (3), 267–277.

BAIN, G., KITCHENS, D., YAO, M., HUETTNER, J. E. & GOTTLIEB, D. I. 1995 Embryonic stem cells express neuronal properties in vitro. *Developmental Biology* **168** (2), 342–357.

BAKSH, D., SONG, L. & TUAN, R. S. 2007 Adult mesenchymal stem cells: characterization, differentiation, and application in cell and gene therapy. *Journal of Cellular and Molecular Medicine* **8** (3), 301–316.

BALSAM, L. B., WAGERS, A. J., CHRISTENSEN, J. L., KOFIDIS, T., WEISSMAN, I. L. & ROBBINS, R. C. 2004 Haematopoietic stem cells adopt mature haematopoietic fates in ischaemic myocardium. *Nature* **428** (6983), 668–673.

BANCROFT, G. N., SIKAVITSAS, V. I. & MIKOS, A. G. 2003 Technical note: Design of a flow perfusion bioreactor system for bone tissue-engineering applications. *Tissue Engineering* **9** (3), 549–554.

BANFI, A., BIANCHI, G., NOTARO, R., LUZZATTO, L., CANCEDDA, R. & QUARTO, R. 2002 Replicative aging and gene expression in long-term cultures of human bone marrow stromal cells. *Tissue Engineering* **8** (6), 901–910.

BARDY, J., CHEN, A. K., LIM, Y. M., WU, S., WEI, S., WEIPING, H., CHAN, K., REUVENY, S. & OH, S. K. W. 2013 Microcarrier suspension cultures for high-density expansion and differentiation of human pluripotent stem cells to neural progenitor cells. *Tissue Engineering Part C: Methods* **19** (2), 166–180.

BARNHART, D. H., ADRIAN, R. J. & PAPEN, G. C. 1994 Phase-conjugate holographic system for high-resolution particle-image velocimetry. *Applied Optics* **33**, 7159–7170.

BARRANDON, Y. & GREEN, H. 1987 Three clonal types of keratinocyte with different capacities for multiplication. *Proceedings of National Academic of Sciences* **84** (8), 2302–2306.

BARRY, F., BOYNTON, R. E., LIU, B. & MURPHY, J. M. 2001 Chondrogenic differentiation of mesenchymal stem cells from bone marrow: Differentiation-dependent gene expression of matrix components. *Experimental Cell Research* **268** (2), 189–200.

BASHIR, A., GRAY, M. L., HARTKE, J. & BURSTEIN, D. 1999 Nondestructive imaging of human cartilage glycosaminoglycan concentration by MRI. *Magnetic Resonance in Medicine* **41**, 857–865.

BAUWENS, C., YIN, T., DANG, S., PEERANI, R. & ZANDSTRA, P. W. 2005 Development of a perfusion fed bioreactor for embryonic stem cell-derived cardiomyocyte generation: Oxygen-mediated enhancement of cardiomyocyte output. *Biotechnology and Bioengineering* **90** (4), 452–461.

BENJAMIN, T. B. 1962 Theory of the vortex breakdown phenomenon. *Journal of Fluid Mechanics* **14**, 593–629.

BETRE, H., ONG, S. R., GUILAK, F., CHILKOTI, A., FERMOR, B. & SETTON, L. A. 2006 Chondrocytic differentiation of human adipose-derived adult stem cells in elastin-like polypeptide. *Biomaterials* **27** (1), 91–99.

BHATTACHARYA, S. & PAL, A. 1962 Axisymmetric vortex breakdown in a filled cylinder. *International Journal of Engineering Science* **36**, 555.

BJÖRKLUND, L. M., SÁNCHEZ-PERNAUTE, R., CHUNG, S., ANDERSSON, T., CHEN, I. Y. C., MCNAUGHT, K. S. P., BROWNELL, A.-L., JENKINS, B. G., WAHLEST-

EDT, C., KIM, K.-S. & ISACSON, O. 2002 Embryonic stem cells develop into functional dopaminergic neurons after transplantation in a parkinson rat model. *Proceedings of the National Academy of Sciences* **99** (4), 2344–2349.

BLANPAIN, C. & FUCHS, E. 2006 Epidermal stem cells of the skin. *Annual Review of Cell and Developmental Biology* **22**, 339–373.

BORN, M. & WOLF, E. 1999 *Principles of Optics*, 7th edn. Cambridge: Cambridge University Press.

BRØNS, M., SHEN, W. Z., SØRENSEN, J. N. & ZHU, W. J. 2007 The influence of imperfections on the flow structure of steady vortex breakdown bubbles. *Journal of Fluid Mechanics* **578**, 453–466.

BRØNS, M., THOMPSON, M. & HOURIGAN, K. 2009 Dye visualization near a three-dimensional stagnation point: application to the vortex breakdown bubble. *Journal of Fluid Mechanics* **622**, 177–194.

BROUARD, M. & BARRANDON, Y. 2003 Controlling skin morphogenesis: hope and despair. *Current Opinion in Biotechnology* **14** (5), 520–525.

BROWN, G. L. & LOPEZ, J. M. 1990 Axisymmetric vortex breakdown. Part 2: Physical mechanism. *Journal of Fluid Mechanics* **221**, 553.

BROXMEYER, H. E., DOUGLASS, G. W., HANGOC, G., COOPER, S., BARD, J., ENGLISH, D., ARNY, M., THOMAS, L. & BOYSE, E. A. 1989 Human umbilical cord blood as a potential source of transplantable hematopoietic stem/progenitor cells. *Proceedings of the National Academy of Sciences* **86** (10), 3828–3832.

BRUDER, S. P., FINK, D. J. & CAPLAN, A. I. 2004 Mesenchymal stem cells in bone development, bone repair, and skeletal regeneration therapy. *Journal of Cellular Biochemistry* **56** (3), 283–294.

BUCHANAN, N. A., ATKINSON, C., JEREMY, M. C. & SORIA, J. 2011 Tomographic particle image velocimetry investigation of the flow in a modeled human carotid artery bifurcation. *Experiments in Fluids* **50**, 1131–1151.

BUCHHOLZ, D. E., HIITA, S. T., ROWLAND, T. J., FRIEDRICH, A. M., HINMAN, C. R., JOHNSON, L. V. & CLEGG, D. O. 2009 Derivation of functional retinal pigmented epithelium from induced pluripotent stem cells. *Stem Cells* **27** (10), 2427–2.

BUCKLEY, R. H., SCHIFF, S. E., SCHIFF, R. I., MARKERT, M. L., WILLIAMS, L. W., ROBERTS, J. L., MYERS, L. A. & WARD, F. E. 1999 Hematopoietic stem-cell transplantation for the treatment of severe combined immunodeficiency. *New England Journal of Medicine* **340** (7), 508–516.

BURGGRAF, O. R. & FOSTER, M. R. 1977 Continuation or breakdown in tornado-like vortices. *Journal of Fluid Mechanics* **80** (4), 685–703.

BUTTERY, L. D. K., BOURNE, S., XYNOS, J. D., WOOD, H., HUGHES, F. J., HUGHES, S. P. F., EPISKOPOU, V. & POLAK, J. M. 2001 Differentiation of osteoblasts and in vitro bone formation from murine embryonic stem cells. *Tissue Engineering* **7** (1), 89–99.

CABRAL, J. M. S. 2001 *Ex vivo* expansion of hematopoietic stem cells in bioreactors. *Biotechnology Letters* **23**, 741–751.

CABRITA, G. J. M., FERREIRA, B. S., SILVA, C. L. D., GONCALVES, R., ALMEIDA-PORADA, G. & CABRAL, J. M. S. 2003 Hematopoietic stem cells: From the bone to the bioreactor. *Trends in Biotechnology* **21**, 233–240.

CAMERON, C. M., HU, W. S. & KAUFMAN, D. S. 2006 Improved development of human embryonic stem cell-derived embryoid bodies by stirred vessel cultivation. *Biotechnology and Bioengineering* **94** (5), 938–948.

CANNIZZARO, C., TANDON, N., FIGALLO, E., PARK, H., GERECHT, S., RADISIC, M., ELVASSORE, N. & VUNJAK-NOVAKOVIC, G. 2007 Practical aspects of cardiac tissue engineering with electrical stimulation. *Methods in Molecular Medicine* **140**, 291–307.

CAPLAN, A. I. & BRUDER, S. P. 2001 Mesenchymal stem cells: building blocks for molecular medicine in the 21st century. *Trends in Molecular Medicine* **7** (6), 259–264.

CARPENTER, M. K., CUI, X., HU, Z.-Y., JACKSON, J., SHERMAN, S., SEIGER, Å. & WAHLBERG, L. U. 1999 In vitro expansion of a multipotent population of human neural progenitor cells. *Experimental Neurology* **158** (2), 265–278.

CHAMBERS, I. 2004 The molecular basis of pluripotency in mouse embryonic stem cells. *Cloning and Stem Cells* **6** (4), 386–391.

CHENG, Y., TORREGROSA, M. M., VILLEGAS, A. & DIEZ, F. J. 2011 Time resolved scanning PIV measurements at fine scales in a turbulent jet. *International Journal of Heat and Fluid Flow* **32** (3), 708–718.

CLAUSE, K. C., TINNEY, J. P., LIU, L. J., GHARAIBEH, B., HUARD, J., KIRK, J. A., SHROFF, S. G., FUJIMOTO, K. L., WAGNER, W. R., RALPHE, J. C., KELLER, B. B. & TOBITA, K. 2010 A three-dimensional gel bioreactor for assessment of cardiomyocyte induction in skeletal musclederived stem cells. *Tissue Engineering Part C Methods* **16** (3), 375–385.

COLLINS, P. C., MILLER, W. M. & PAPOUTSAKIS, E. T. 1998 Stirred culture of peripheral and cord blood hematopoietic cells offers advantages over traditional static systems for clinically relevant applications. *Biotechnology and Bioengineering* **59** (5), 534–543.

COMTE-BELLOT, G. 1976 Hot-wire anemometry. *Annual Review of Fluid Mechanics* **8** (1), 209–231.

CONTI, L., POLLARD, S. M., GORBA, T., REITANO, E., TOSELLI, M., BIELLA, G., SUN, Y., SANZONE, S., YING, Q.-L., CATTANEO, E. & SMITH, A. 2005 Niche-independent symmetrical self-renewal of a mammalian tissue stem cell. *PLOS Biology* **3** (9), 283.

CORMIER, J. T., ZUR NIEDEN, N. I. & KALLOS, M. S. 2006 Expension of undifferentiated murine embryonic stem cells as aggregates in suspension culture bioreactors. *Tissue Engineering* **12**, 3233–3245.

COWLEY, J. M. 1995 *Diffraction Physics*. Amsterdam: Elsevier.

CRANE, J. F. & TRAINOR, P. A. 2006 Neural crest stem and progenitor cells. *Annual Review of Cell and Developmental Biology* **22**, 267–286.

DANI, C., SMITH, A. G., DESSOLIN, S., LEROY, P., STACCINI, L., VILLAGEOIS, P., DARIMONT, C. & AILHAUD, G. 1997 Differentiation of embryonic stem cells into adipocytes in vitro. *Journal of Cell Science* **110**, 1279–1285.

DAVIES-JONES, R. P. 1983 Tornado dynamics. In *Thunderstorms: A social, scientific and technological documentary* (ed. E. Kessler), , vol. 2, p. 297. Nolan: University of Oklahoma Press.

DAVISSON, T., SAH, R. L. & RATCLIFFE, A. 2002 Perfusion increases cell content and matrix synthesis in chondrocyte three-dimensional cultures. *Tissue Engineering* **8** (5), 807–816.

DAY, T. F., GUO, X., GARRETT-BEAL, L. & YANG, Y. 2005 Wnt/β-catenin signaling in mesenchymal progenitors controls osteoblast and chondrocyte differentiation during vertebrate skeletogenesis. *Developmental Cell* **8** (5), 739–750.

DEXTER, T. M., ALLEN, T. D., LAJTHA, L. G., SCHOFIELD, R. & LORD, B. I. 1973 Stimulation of differentiation and proliferation of haemopoietic cells *in vitro*. *Journal of Cell Physiology* **82** (3), 461–474.

DHARA, S. K. & STICE, S. L. 2008 Neural differentiation of human embryonic stem cells. *Journal of Cellular Biochemistry* **105** (3), 633–640.

DUBSKY, S., JAMISON, R. A., IRVINE, S. C., SIU, K. K. W., HOURIGAN, K. & FOURAS, A. 2010 Computed tomographic x-ray velocimetry. *Applied Physics Letters* **96** (2), 023702.

DUNCAN, S. A., NAVAS, M. A., DUFORT, D., ROSSANT, J. & STOFFEL, M. 1998 Regulation of a transcription factor network required for differentiation and metabolism. *Science* **281** (5377), 692–695.

DUSTING, J., SHERIDAN, J. & HOURIGAN, K. 2006 A fluid dynamics approach to bioreactor design for cell and tissue culture. *Biotechnology and Bioengineering* **94** (6), 1196–1208.

ELLIS, M., JARMAN-SMITH, M. & CHAUDHURI, J. 2005 Bioreactor systems for tissue engineering: A four-dimensional challenge. In *Bioreactors for Tissue Engineering* (ed. J. Chaudhuri & M. Al-Rubeai), pp. 1–18. Springer Netherlands.

ELSINGA, G. E., KUIK, D. J., VAN OUDHEUSDEN, B. W. & SCARANO, F. 2007 Investigation of the three-dimensional coherent structures in a turbulent boundary layer. *45th AIAA Aerospace Science Meeting (Reno, NV, USA)* pp. –.

ELSINGA, G. E., SCARANO, F., WIENEKE, B. & VAN OUDHEUSDEN, B. W. 2006 Tomographic particle image velocimetry. *Experiments in Fluids* **41**, 933–947.

ENGLUND, U., BJÖRKLUND, A., WICTORIN, K., LINDVALL, O. & KOKAIA, M. 2002 Grafted neural stem cells develop into functional pyramidal neurons and integrate into host cortical circuitry. *Proceedings of the National Academy of Sciences* **99** (26), 17089–17094.

ERICKSON, G. R., GIMBLE, J. M., FRANKLIN, D. M., RICE, H. E., AWAD, H. & GUILAK, F. 2002 Chondrogenic potential of adipose tissue-derived stromal cells *in Vitro* and *in Vivo*. *Biochemical and Biophysical Research Communications* **290** (2), 763–769.

ESCUDIER, M. 1988 Vortex breakdown: Observations and explainations. *Progress in Aerospace Sciences* **25** (2), 189–229.

ESCUDIER, M. P. 1984 Observations of the flow produced in a cylindrical container by a rotating endwall. *Experiments in Fluids* **2**, 189–196.

EVANS, M. J. & KAUFMAN, M. H. 1981 Establishment in culture of pluripotential cells from mouse embryos. *Nature* **292** (5819), 154–156.

FALER, J. H. & LEIBOVICH, S. 1978 An experimental map of the internal structure of a vortex breakdown. *Journal of Fluid Mechanics* **86**, 313–335.

FERNANDES, A. M., FERNANDES, T. G., DIOGO, M. M., DA SILVA, C. L., HENRIQUE, D. & CABRAL, J. M. S. 2007 Mouse embryonic stem cell expansion in a microcarier-based stirred culture system. *Journal of Biotechnology* **132** (2), 227–236.

FERNANDES, A. M., MARINHO, P. A., SARTORE, R. C., PAULSEN, B. S., MARIANTE, R. M., CASTILHO, L. R. & REHEN, S. K. 2009 Successful scale-up of human embryonic stem cell production in a stirred microcarrier culture system. *Brazilian Journal of Medical and Biological Research* **42** (6), 515–522.

FISHMAN, J. A. & RUBIN, R. H. 1998 Infection in organ-transplant recipients. *New England Journal of Medicine* **338**, 1741–1751.

FOK, E. Y. L. & ZANDSTRA, P. W. 2005 Shear-controlled single-step mouse embryonic stem cell expansion and embryoid body-based differentiation. *Stem Cells* **23** (9), 1333–1342.

FONG, W. J., TAN, H. L., CHOO, A. & OH, S. K. 2005 Perfusion cultures of human embryonic stem cell. *Bioprocess and Biosystem Engineering* **27** (6), 381–387.

FORSYTH, N. R., MUSIO, A., VEZZONI, P., SIMPSON, A. H., NOBLE, B. S. & MCWHIR, J. 2006 Physiologic oxygen enhances human embryonic stem cell clonal recovery and reduces chromosomal abnormalities. *Cloning and Stem Cells* **8** (1), 16–23.

FORTIER, L. A., NIXON, A. J., WILLIAMS, J. & CABLE, C. S. 1998 Isolation and chondrocytic differentiation of equine bone marrow-derived mesenchymal stem cells. *American journal of veterinary research* **59** (9), 1182–1187.

FOURAS, A., DUSTING, J. & HOURIGAN, K. 2007a A simple calibration technique for stereoscopic particle image velocimetry. *Experiments in Fluids* **42**, 799–810.

FOURAS, A., DUSTING, J., LEWIS, R. & HOURIGAN, K. 2007b Three-dimensional synchrotron X-Ray Particle Image Velocimetry. *Journal of Applied Physics* **102**, 064916.

FOURAS, A., LO JACONO, D. & HOURIGAN, K. 2008 Target-free stereo PIV: a novel technique with inherent error estimation and improved accuracy. *Experiments in Fluids* **44**, 317–329.

FOURAS, A., LO JACONO, D., NGUYEN, C. V. & HOURIGAN, K. 2009 Volumetric correlation PIV: a new technique for 3D velocity vector field measurement. *Experiments in Fluids* **47**, 569–577.

FRAICHARD, A., CHASSANDE, O., BILBAUT, G., DEHAY, C., SAVATIER, P. & SAMARUT, J. 1995 *In vitro* differentiation of embryonic stem cells into glial cells and functional neurons. *Journal of Cell Science* **108**, 3181–3188.

Frauenschuh, S., Reichmann, E., Ibold, Y., Goetz, P. M., Sittinger, M. & Ringe, J. 2007 A microcarrier-based cultivation system for expansion of primary mesenchymal stem cells. *Biotechnology Progress* **23** (1), 187–193.

Freed, L. E. & Vunjak-Novakovic, G. 1997 Microgravity tissue engineering. *In Vitro Cellular & Developmental Biology - Animal* **33**, 381–385.

Freed, L. E. & Vunjak-Novakovic, G. 2000 Tissue engineering bioreactors. In *Principles of Tissue Engineering* (ed. R. P. Lanza, R. Langer & J. Vacanti), pp. 143–156. Academic Press.

Frith, J. E., Thomson, B. & Genever, P. G. 2010 Dynamic three-dimensional culture methods enhance mesenchymal stem cell properties and increase therapeutic potential. *Tissue Engineering Part C: Methods* **16**, 735–749.

Fromstein, J. D., Zandstra, P. W., Alperin, C., Rockwood, D., Rabolt, J. F. & Woodhouse, K. A. 2008 Seeding bioreactor-produced embryonic stem cell-derived cardiomyocytes on different porous, degradable, polyurethane scaffolds reveals the effect of scaffold architecture on cell morphology. *Tissue Engineering Part A* **14** (3), 369–378.

Gallaire, F., Chomaz, J. M. & Huerre, P. 2004 Closed-loop control of vortex breakdown: a model study. *Journal of Fluid Mechanics* **511**, 67–93.

Gallico, G. G., O'Connor, N. E., Compton, C. C., Kehinde, O. & Green, H. 1984 Permanent coverage of large burn wounds with autologous cultured human epithelium. *New England Journal of Medicine* **311** (7), 448–451.

Galmiche, M. C., Koteliansky, V. E., Briere, J., Herve, P. & Charbord, P. 1993 Stromal cells from human long-term marrow cultures are mesenchymal cells that differentiate following a vascular smooth muscle differentiation pathway. *Blood* **82** (1), 66–76.

Gelfat, A. Y., Bar-Yoseph, P. Z. & Solan, A. 2001 Three-dimensional instability of axisymmetric flow in a rotating lid-cylinder enclosure. *Journal of Fluid Mechanics* **438**, 363–377.

Gerecht-Nir, S., Cohen, S. & Itskovitz-Eldor, J. 2004 Bioreactor cultivation enhances the efficiency of human embryoid body (hEB) formation and differentiation. *Biotechnology and Bioengineering* **86** (5), 493–502.

Gillogly, S. D., Voight, M. & Blackburn, T. 1998 Treatment of articular cartilage defects of the knee with autologous chondrocyte implantation. *Journal of Orthopedic and Sports Physical Therapy* **28** (4), 241–253.

GOODWIN, T. J., PREWETT, T. L., WOLF, D. A. & SPAULDING, G. F. 1993a Reduced shear stress: A major component in the ability of mammalian tissues to form three-dimensional assemblies in simulated microgravity. *Journal of Cellular Biochemistry* **51** (3), 301–311.

GOODWIN, T. J., SCHROEDER, W. F., WOLF, D. A. & MOYER, M. P. 1993b Rotating-wall vessel coculture of small intestine as a prelude to tissue modeling: Aspects of simulated microgravity. *Proceedings of the Society for Experimental Biology and Medicine* **202** (2), 181–192.

GRAY, M. L., PIZZANELLI, A. M., LEE, R. C., GRODZINSKY, A. J. & SWANN, D. A. 1989 Kinetics of the chondrocyte biosynthetic response to compressive load and release. *Biochimica et Biophysica Acta (BBA) - General Subjects* **991** (3), 415–425.

GRIGORIADIS, A. E., HEERSCHE, J. N. & AUBIN, J. E. 1981 Differentiation of muscle, fat, cartilage, and bone from progenitor cells present in a bone-derived clonal cell population: effect of dexamethasone. *a* **1** (1), 2139–2151.

GUILAK, F., LOTT, K. E., AWAD, H. A., CAO, Q., HICOK, K. C., FERMORE, B. & GIMBLE, J. M. 2006 Clonal analysis of the differentiation potential of human adipose-derived adult stem cells. *Journal of Cellular Physiology* **206** (1), 229–237.

GUPTA, A. K., LILLEY, D. G. & SYRED, N. 1985 *Swirl Flows*. Abacus Press, Tunbridge Wells, Kent.

GUPTA, P., ISMADI, M.-Z., BELLARE, J., JADHAV, S., FOURAS, A., VERMA, P. & HOURIGAN, K. 2014 Optimization of agitation speed in spinner flask for microcarrier survival and expansion of induced pluripotent stem cells. *Cytotechnology* (In Press).

HALL, M. G. 1972 Vortex breakdown. *Annual Review of Fluid Mechanics* **4**, 195–218.

HAMAZAKI, T., IIBOSHI, Y., OKA, M., PAPST, P. J., MEACHAM, A. M., ZON, L. I. & TERADA, N. 2001 Hepatic maturation in differentiating embryonic stem cells in vitro. *FEBS Letters* **497** (1), 15–19.

HANNA, J., WERNIG, M., MARKOULAKI, S., SUN, C.-W., MEISSNER, A., CASSADY, J. P., BEARD, C., BRAMBRINK, T., WU, L.-C., TOWNES, T. M. & JAENISCH, R. 2007 Treatment of sickle cell anemia mouse model with ips cells generated from autologous skin. *Science* **318** (5858), 1920–1923.

HARRIS, D. T. & ROGERS, I. 2007 Umbilical cord blood: a unique source of pluripotent stem cells for regenerative medicine. *Current Stem Cell Research Therapy* **2** (4), 301–309.

HARVEY, J. K. 1962 Some observations of the vortex breakdown phenomenon. *Journal of Fluid Mechanics* **14**, 585.

HEGERT, C., KRAMER, J., HARGUS, G., MÜLLER, J., GUAN, K., WOBUS, A. M., MÜLLER, P. K. & ROHWEDEL, J. 2002 Differentiation plasticity of chondrocytes derived from mouse embryonic stem cells. *Journal of Cell Science* **115** (23), 4617–4628.

HEMRAJANI, R. R. & TATTERSON, G. B. 2004 Mechanically stirred vessels. In *Handbook of Industrial Mixing: Science and Practice* (ed. E. L. Paul, V. A. Atiemo-Obeng & S. M. Kresta), p. 345. USA: John Wiley & Sons, Inc.

HENTZE, H., GRAICHEN, R. & COLMAN, A. 2007 Cell therapy and the safety of embryonic stem cell-derived grafts. *Trends in Biotechnology* **25** (1), 24–32.

HERRADA, M. A. & SHTERN, V. 2003 Control of vortex breakdown by temperature gradients. *Physics of Fluids* **15**, 3468.

HEWITT, C. J., LEE, K., NIENOW, A. W., THOMAS, R. J., SMITH, M. & THOMAS, C. R. 2011 Expansion of human mesenchymal stem cells on microcarriers. *Biotechnology Letters* **33**, 2325–2335.

HINSCH, K. D. 2002 Holographic particle image velocimetry. *Measurement Science and Technology* **13** (7), R61–R72.

HO, H.-Y. & LI, M. 2006 Potential application of embryonic stem cells in Parkinson's disease: Drug screening and cell therapy. *Regenerative Medicine* **1** (2), 175–182.

HOFFMAN, L. M. & CARPENTER, M. K. 2005 Characterization and culture of human embryonic stem cells. *Nat Biotech* **23** (6), 699–708.

HU, W.-S., GIARD, D. J. & WANG, D. I. C. 1985 Serial propagation of mammalian cells on microcarriers. *Biotechnology and Bioengineering* **27** (10), 1466–1476.

HUA, J., QIU, P., ZHU, H., CAO, H., WANG, F. & LI, W. 2011 Multipotent mesenchymal stem cells (MSCs) from human umbilical cord: Potential differentiation of germ cells. *African Journal of Biochemistry Research* **5** (4), 113–123.

HUBBELL, J. A. 2003 Materials as morphogenetic guides in tissue engineering. *Current Opinion in Biotechnology* **14** (5), 551–558.

HUNZIKER, E. B. 2001 The development, structure and repair of articular cartilage. *Osteoarthritis and Cartilage* **10**, 432–463.

HUSAIN, H., SHTERN, V. & HUSAIN, F. 2003 Control of vortex breakdown by addition of near-axis swirl. *Physics of Fluids* **15**, 271.

Hwang, N. S., Kim, M. S., Sampattavanich, S., Baek, J. H., Zhang, Z. & Elisseeff, J. 2006 Effects of three-dimensional culture and growth factors on the chondrogenic differentiation of murine embryonic stem cells. *Stem Cells* **24** (2), 284–291.

Ismadi, M.-Z., Higgins, S., Samarage, R., Paganin, D., Hourigan, K. & Fouras, A. 2013 Optimisation of stirred bioreactor through the use of a novel holographic correlation velocimetry flow measurement technique. *PLoS ONE* **8** (e65714).

Ito, K. & Sieber-Blum, M. 1991 In vitro clonal analysis of quail cardiac neural crest development. *Developmental Biology* **148** (1), 95–106.

Itskovitz-Eldor, J., Schuldiner, M., Karsenti, D., Eden, A., Yanuka, O., Amit, M., Soreq, H. & Benvenisty, N. 2005 Differentiation of human embryonic stem cells into embryoid bodies compromising the three embryonic germ layers. *Molecular medicine* **6** (2), 88–95.

Jiang, Y., Jahagirdar, B. N., Reinhardt, R. L., Schwartz, R. E., Keene, C. D., Ortiz-Gonzalez, X. R., Reyes, M., Lenvik, T., Lund, T., Blackstad, M., Du, J., Aldrich, S., Lisberg, A., Low, W. C., Largaespada, D. A. & Verfaillie, C. M. 2002a Pluripotency of mesenchymal stem cells derived from adult marrow. *Nature* **418**, 41–49.

Jiang, Y., Vaessen, B., Lenvik, T., Blackstad, M., Reyes, M. & Verfaillie, C. M. 2002b Multipotent progenitor cells can be isolated from postnatal murine bone marrow, muscle, and brain. *Experimental Hematology* **30** (8), 869–904.

Jørgensen, B., Sørensen, J. & Aubry, N. 2010 Control of vortex breakdown in a closed cylinder with a rotating lid. *Theoretical and Computational Fluid Dynamics* pp. 483–496.

Kaczmarek, L., Finbow, M., Revel, J. P. & Strumwasser, F. 1979 The morphology and coupling of *aplysia* bag cells within the abdominal ganglion and in cell culture. *Journal of Neurobiology* **10**, 535–550.

Kaiser, S. C., Jossen, V., Schirmaier, C., Eible, D., Brill, S., van den Bos, C. & Eible, R. 2012 Fluid flow and cell proliferation of mesenchymal adipose-derived stem cells in small-scale, stirred, single-use bioreactors. *Chemie Ingenieur Technik* **85** (1–2), 95–102.

Kak, A. C. & Slaney, M. 1988 *Principles of computerised tomographic imaging*. New York: Institute of Electrical and Electronics Engineers (IEEE).

Kallos, M., Sen, A. & Behie, L. 2003 Large-scale expansion of mammalian neural stem cells: a review. *Medical and Biological Engineering and Computing* **41** (3), 271–282.

Kattman, S. J., Huber, T. L. & Keller, G. M. 2006 Multipotent FLK-1+ cardiovascular progenitor cells give rise to the cardiomyocyte, endothelial, and vascular smooth muscle lineages. *Developmental Cell* **11** (5), 723–732.

Kaufman, D. S., Hanson, E. T., Lewis, R. L., Auerbach, R. & Thomson, J. A. 2001 Hematopoietic colony-forming cells derived from human embryonic stem cells. *Proceedings of the National Academy of Sciences* **98** (19), 10716–10721.

Kehat, I., Kenyagin-Karsenti, D., Snir, M., Segev, H., Amit, M., Gepstein, A., Livne, E., Binah, O., Itskovitz-Eldor, J. & Gepstein, L. 2001 Human embryonic stem cells can differentiate into myocytes with structural and functional properties of cardiomyocytes. *The Journal of Clinical Investigation* **108** (3), 407–414.

Kehoe, D. E., Jing, D., Lock, L. T. & Tzanakakis, E. S. 2010 Scalable stirred-suspension bioreactor culture of human pluripotent stem cells. *Tissue Engineering Part A* **16** (2), 405–421.

Keller, G. 2005 Embryonic stem cell differentiation: emergence of a new era in biology and medicine. *Genes & Development* **19**, 1129–1155.

Keller, G., Kennedy, M. & Papayannopoulou, T. 1993 Hematopoietic commitment during embryonic stem cell differentiation in culture. *Molecular and Cellular Biology* **13**, 473–486.

Kennea, N. L. & Mehment, H. 2002 Neural stem cells. *The Journal of Pathology* **197** (4), 536–550.

Kern, S., Eichler, H., Stoeve, J., Klüter, H. & Bieback, K. 2006 Comparative analysis of mesenchymal stem cells from bone marrow, umbilical cord blood, or adipose tissue. *Stem Cells* **24** (5), 1294–1301.

Khalil, S., Hourigan, K. & Thompson, M. C. 2006 Effects of axial pulsing on unconfined vortex breakdown. *Physics of Fluids* **18**, 038102.

Kim, J. B., Zaehres, H., Wu, G., Gentile, L., Ko, K., Sebastiano, V., Araúzo-Bravo, M. J., Ruau, D., Han, D. W., Zenke, M. & Schöle, H. R. 2008 Pluripotent stem cells induced from adult neural stem cells by reprogramming with two factors. *Nature* **454**, 646–650.

Kim, S. K. & Chung, S. K. 2004 An investigation on airflow in disordered nasal cavity and its corrected models by tomographic PIV. *Measurement Science and Technology* **15**, 1090–1096.

Kohlman, D. L. & Wentz, W. H. 1971 Vortex breakdown on slender sharp-edged wings. *Journal of Aircraft* **8** (3), 151–161.

Koller, M. R., Emerson, S. G. & Palsson, B. O. 1993 Large-scale expansion of human stem and progenitor cells from bone marrow mononuclear cells in continuous perfusion cultures. *Blood* **82** (2), 378–384.

Kramer, J., Hegert, C., Guan, K., Wobus, A. M., Müller, P. K. & Rohwedel, J. 2000 Embryonic stem cell-derived chondrogenic differentiation in vitro: activation by BMP-2 and BMP-4. *Mechanisms of Development* **92** (2), 193–205.

Krause, D. S. 2002 Plasticity of marrow-derived stem cells. *Gene Therapy* **9** (11), 754–758.

Kuriyama, S., Nakano, T., Yoshimura, N., Ohuchi, T., Moritera, T. & Honda, Y. 1992 Mass cultivation of human retinal pigment epithelial cells with microcarrier. *Opthamologica* **205** (2), 89–95.

Laflamme, M. A., Chen, K. Y., Naumova, A. V., Muskheli, V., Fugate, J. A., Dupras, S. K., H. Reinecke, C. X., Hassanipour, M., Police, S., O'Sullivan, C., Collins, L., Chen, Y., Minami, E., Gill, E. A., Ueno, S., Yuan, C., Gold, J. & Murray, C. E. 2007 Cardiomyocytes derived from human embryonic stem cells in pro-survival factors enhance function of infarcted rat hearts. *Nature Biotechnology* **25**, 1015–1024.

Langer, R. S. & Vacanti, J. P. 1999 Tissue engineering: the challenges ahead. *Scientific American* **280** (4), 86–89.

Lee, C. R., Grodzinsky, A. J., Hsu, H.-P., Martin, S. D. & Spector, M. 2000a Effects of harvest and selected cartilage repair procedures on the physical and biochemical properties of articular cartilage in the canine knee. *Journal of Orthopaedic Research* **18** (5), 790–799.

Lee, C. R., Grodzinsky, A. J., Hsu, H.-P., Martin, S. D. & Spector, M. 2000b Effects of harvest and selected cartilage repair procedures on the physical and biochemical properties of articular cartilage in the canine knee. *Journal of Orthopaedic Research* **18** (5), 790–799.

Lee, D. A. & Bader, D. L. 2005 Compressive strains at physiological frequencies influence the metabolism of chondrocytes seeded in agarose. *Journal of Orthopaedic Research* **15** (2), 181–188.

Lee, O. K., Kuo, T. K., Chen, W.-M., Lee, K.-D., Hsieh, S.-L. & Chen, T.-H. 2004 Isolation of multipotent mesenchymal stem cells from umbilical cord blood. *Blood* **103** (5), 1669–1675.

Leibovich, S. 1978 The structure of vortex breakdown. *Annual Review of Fluid Mechanics* **10**, 221–246.

Li, X.-H., Yu, X.-Y., Lin, Q.-X., Deng, C.-Y., Shan, Z.-X., Yang, M. & Lin, S.-G. 2007 Bone marrow mesenchymal stem cells differentiate into functional cardiac phenotypes by cardiac microenvironment. *Journal of Molecular and Cellular Cardiology* **42** (2), 295–303.

Li, X.-J., Du, Z.-W., Zarnowska, E. D., Pankratz, M., Hansen, L. O., Pearce, R. A. & Zhang, S.-C. 2005 Specification of motoneurons from human embryonic stem cells. *Nature Biotechnology* **23** (2), 215–221.

Lindvall, O., Kokaia, Z. & Martinez-Serrano, A. 2004 Stem cell therapy for human neurodegenerative disorders how to make it work. *Nature Medicine* **10**, S42–S50.

Liovic, P., Sutalo, I. D., Stewart, R., Glattauer, V. & Meagher, L. 2012 Fluid flow and stresses on microcarriers in spinner flask bioreactors. In *Ninth International Conference on CFD in the Minerals and Process Industries*. Melbourne, Australia: CSIRO.

Lo Jacono, D., Sørensen, J. N., Thompson, M. C. & Hourigan, K. 2008 Control of vortex breakdown in a closed cylinder with a small rotating rod. *Journal of Fluids and Structures* **24**, 1278–1283.

Lock, L. T. & Tzanakakis, E. S. 2009 Expansion and differentiation of human embryonic stem cells to endoderm progeny in a microcarrier stirred-suspension culture. *Tissue Engineering Part A* **15** (8), 2051–2063.

Loh, Y.-H., Argawal, S., Park, I.-H., Urbach, A., Huo, H., Heffner, G. C., Kim, K., Miller, J. D., Ng, K. & Daley, G. Q. 2009 Generation of induced β pluripotent stem cells from human blood. *Blood* **113**, 5476–5479.

Lopez, J. M. 1990 Axisymmetric vortex breakdown. Part 1: Confined swirling flow. *Journal of Fluid Mechanics* **221**, 533–552.

Lopez, J. M. & Perry, A. D. 1992 Axisymmetric vortex breakdown. Part 3: Onset of periodic flow and chaotic advection. *Journal of Fluid Mechanics* **234**, 449–471.

Lowson, M. V. & Riley, A. J. 1995 Vortex breakdown control by delta wing geometry. *Journal of Aircraft* **32** (4), 832–838.

Ludwieg, H. 1962 Zur erklarung der instabilitat der uber angestellten delta-flugeln auftretenden freien wirbelkerne. *Z. Flugwiss* **10**, 242–249.

LUDWIG, T. E., LEVENSTEIN, M. E., JONES, J. M., BERGGREN, W. T., MITCHEN, E. R., FRANE, J. L., CRANDALL, L. J., DAIGH, C. A., CONARD, K. R., PIEKARCZYK, M. S., LLANAS, R. A. & THOMSON, J. A. 2006 Derivation of human embryonic stem cells in defined conditions. *Nature Biotechnology* **24**, 185–187.

LUGT, H. J. & ABBOUD, M. 1987 Axisymmetric vortex breakdown in a container with a rotating lid. *Journal of Fluid Mechanics* **179**, 179–190.

LUMELSKY, N., BLONDEL, O., LAENG, P., VELASCO, I., RAVIN, R. & MCKAY, R. 2001 Differentiation of embryonic stem cells to insulin-secreting structures similar to pancreatic islets. *Science* **292**, 1389–1394.

LYON, A. & HARDING, S. 2007 The potential of cardiac stem cell therapy for heart failure. *Current Opinion in Pharmacology* **7** (2), 164–170.

MACKAY, A. M., BECK, S. C., MURPHY, J. M., BARRY, F. P., CHICHESTER, C. O. & PITTENGER, M. F. 2007 Chondrogenic differentiation of cultured human mesenchymal stem cells from marrow. *Tissue Engineering* **4** (4), 415–428.

MAHIR, N. & ROCKWELL, D. 1996 Vortex formation from a forced system of two cylinders. Part 1: Tandem arrangement. *Journal of Fluids and Structures* **10** (5), 473–489.

MALTSEV, V. A., ROHWEDEL, J., HESCHELER, J. & WOBUS, A. M. 1993 Embryonic stem cells differentiate in vitro into cardiomyocytes representing sinusnodal, atrial and ventricular cell types. *Mechanisms of Development* **44** (1), 41–50.

MARTIN, G. R. 1981 Isolation of a pluripotent cell line from early mouse embryos cultured in medium conditioned by teratocarcinoma stem cells. *Proceedings of the National Academy of Sciences* **78** (12), 7634–7638.

MARTIN, I., WENDT, D. & HEBERER, M. 2004 The role of bioreactors in tissue engineeirng. *Trends in Biotechnology* **22**, 80–86.

MAUCK, R. L., YUAN, X. & TUAN, R. S. 2006 Chondrogenic differentiation and functional maturation of bovine mesenchymal stem cells in long-term agarose culture. *Osteoarthritis and Cartilage* **14** (2), 179–189.

MAURITZ, C., K., S., REPPEL, M., NEEF, S., HESCHELER, K. J., HASENFUSS, G., MARTIN, U., MAIER, L. S., NGUEMO, F., MENKE, S. & HAUSTEIN, M. 2008 Generation of functional murine cardiac myocytes from induced pluripotent stem cells. *Circulation* **118** (5), 507–517.

MCDONALD, J. W., LIU, X. Z., QU, Y., LIU, S., MICKEY, S. K., TURETSKY, D., GOTTLIEB, D. I. & CHOI, D. W. 1999 Transplanted embryonic stem cells survive,

differentiate and promote recovery in injured rat spinal cord. *Nature Medicine* **5**, 1410–1412.

MEINEL, L., KARAGEORGIOU, V., FAJARDO, R., SNYDER, B., SHINDE-PATIL, V., ZICHNER, L., KAPLAN, D., LANGER, R. & VUNJAK-NOVAKOVIC, G. 2004 Bone tissue engineering using human mesenchymal stem cells: Effects of scaffold material and medium flow. *Annals of Biomedical Engineering* **32** (1), 112–122.

MEINHART, C. D., WERELEY, S. T. & SANTIAGO, J. G. 2000 A PIV algorithm for estimating time-averaged velocity fields. *Journal of Fluids Engineering* **122** (2), 285–289.

MENG, H., PAN, G., PU, Y. & WOODWARD, S. H. 2004 Holographic particle image velocimetry: from film to digital recording. *Measurement Science and Technology* **15**, 673–685.

MEUNIER, P. & HOURIGAN, K. 2013 Mixing in a vortex breakdown flow. *Journal of Fluid Mechanics* **731**, 195–222.

MIAO, Z., JIN, J., CHEN, L., ZHU, J., HUANG, W., ZHAO, J., QIAN, H. & ZHANG, X. 2006 Isolation of mesenchymal stem cells from human placenta: comparison with human bone marrow mesenchymal stem cells. *Cell Biology International* **30** (9), 681–687.

MINAS, T. & NEHRER, S. 1997 Current concepts in the treatment of articular cartilage defects. *Orthopedics* **20** (6), 525–538.

MORRISON, S. J., WANDYCZ, A. M., HEMMATI, H. D., WRIGHT, D. E. & WEISSMAN, I. L. 1997 Identification of a lineage of multipotent hematopoietic progenitors. *Development* **124** (10), 1929–1939.

MOUNTFORD, J. C. 2008 Human embryonic stem cells: Origins, characteristics and potential for regenerative therapy. *Transfusion Medicine* **18** (1), 1–12.

MUKHOPADHYAY, A., MADHUSUDHAN, T. & KUMAR, R. 2005 Hematopoietic stem cells: Clinical requirements and developments in *ex vivo* culture. *Advances in Biochemichel Engineering / Biotechnology* **86**, 215–253.

MUMMERY, C., WARD-VAN OOSTWAARD, D., DOEVENDANS, P., SPIJKER, R., VAN DEN BRINK, S., HASSINK, R., VAN DER HEYDEN, M., , OPTHOF, T., PERA, M., DE LA RIVIERE, A. B., PASSIER, R. & TERTOOLEN, L. 2003 Differentiation of human embryonic stem cells to cardiomyocytes: Role of coculture with visceral endoderm-like cells. *Circulation* **107**, 2733–2740.

MUNUNGA, L., HOURIGAN, K. & THOMPSON, M. C. 2004 Confined flow vortex breakdown control using a small rotating disk. *Physics of Fluids* **16** (12), 4750–4753.

Mununga, L., Lo Jacono, D., Sørensen, J. N., Leweke, T., Thomson, M. & Hourigan, K. 2014 Control of confined vortex breakdown with partial rotating lids. *Journal of Fluid Mechanics* **738**, 5–33.

Muotri, A. R., Nakashima, K., Toni, N., Sandler, V. M. & Gage, F. H. 2005 Development of functional human embryonic stem cell-derived neurons in mouse brain. *Proceedings of the National Academy of Sciences* **102** (51), 18644–18648.

Neitzel, G. P. 1988 Streak-line motion during steady and unsteady axisymmetric vortex breakdown. *Physics of Fluids* **41**, 958–960.

Nguyen, C. V., Carberry, J. & Fouras, A. 2012 Volumetric-correlation PIV to measure particle concentration and velocity of micro flows. *Experiments in Fluids* **52** (3), 663–677.

Nie, Y., Bergendahl, V., Hei, D. J., Jones, J. M. & Palecek, S. P. 2009 Scalable culture and cryopreservation of human embryonic stem cells on microcarriers. *Biotechnology Progress* **25** (1), 20–31.

Niebruegge, S., Nehring, A., Bär, H., Schroeder, M., Zweigerdt, R. & Lehmann, J. 2008 Cardiomyocyte production in mass suspension culture: Embryonic stem cells as a source for great amounts of functional cardiomyocytes. *Tissue Engineering Part A* **14** (10), 1591–1601.

Novara, M., Batenburg, K. J. & Scarano1, F. 2010 Motion tracking-enhanced MART for tomographic PIV. *Measurement Science and Technology* **21**, 035401.

Odorico, J. S., Kaufman, D. S. & Thomson, J. A. 2001 Multilineage differentiation from human embryonic stem cell lines. *Stem Cells* **19** (3), 193–204.

Oh, S. & Choo, A. 2006 Human embryonic stem cell technology: Large scale cell amplification and differentiation. *Cytotechnology* **50** (1), 181–190.

Oh, S. K., Chen, A. K., Mok, Y., Chen, X., Lim, U. M., Chin, A., Choo, A. B. & Reuveny, S. 2009 Long-term microcarrier suspension cultures of human embryonic stem cells. *Stem Cell Research* **2** (3), 219–230.

Oh, S. K. W., Fong, W. J., Teo, Y., Tan, H. L., Padmanabhan, J., Chin, A. C. P. & Choo, A. B. H. 2005 High density cultures of embryonic stem cells. *Biotechnology and Bioengineering* **91** (5), 523–533.

Ohgushi, H. & Caplan, A. I. 1999 Stem cell technology and bioceramics: from cell to gene engineering. *Journal of Biomedical Materials Research* **48** (6), 913–927.

OKABE, S., FORSBERG-NILSSON, K., SPIRO, A. C., SEGAL, M. & MCKAY, R. D. G. 1996 Development of neuronal precursor cells and functional postmitotic neurons from embryonic stem cells *in vitro*. *Mechanisms of Development* **59** (1), 89–102.

OKI, K., TATARISHVILI, J., WOOD, J., KOCH, P., WATTANANIT, S., MINE, Y., MONNI, E., TORNERO, D., AHLENIUS, H., LADEWIG, J., BRÚSTLE, O., LINDVALL, O. & KOKAIA, Z. 2012 Human-induced pluripotent stem cells form functional neurons and improve recovery after grafting in stroke-damaged brain. *Stem Cells* **30** (6), 1120–1133.

OOMS, T. A., CHAN, V., WESTERWEEL, J., KOEK, W., BHATTACHARYA, N. & BRAAT, J. 2008 Holographic PIV system using bacteriorhodopsin (bR) film. In *Particle Image Velocimetry: New Developments and Recent Applications* (ed. A. Schröder & C. E. Willert), pp. 171–189. Springer, Heidelberg.

ORLIC, D., KAJSTURA, J., CHIMENTI, S., JAKONIUK, I., ANDERSON, S. M., LI, B., PICKEL, J., MCKAY, R., NADAL-GINARD, B., BODINE, D. M., LERI, A. & ANVERSA, P. 2001 Bone marrow cells regenerate infarcted myocardium. *Nature* **410** (6829), 701–705.

OWENS, D. M. & WATT, F. M. 2003 Contribution of stem cells and differentiated cells to epidermal tumours. *Nature Reviews Cancer* **3**, 444–451.

PALSSON, B. O., PAEK, S.-H., SCHWARTZ, R. M., PALSSON, M., LEE, G.-M., SILVER, S. & EMERSON, S. G. 1993 Expansion of human bone marrow progenitor cells in a high cell density continuous perfusion system. *Nature Biotechnology* **11** (3), 368–372.

PAN, G. & MENG, H. 2001 Digital in-line holographic PIV for 3D particulate flow diagnostics. In *4th International Symposium on Particle Image Velocimetry*, pp. 17–19. Göttingen, Germany.

PAYA, C., HUMAR, A., DOMINGUEZ, E., WASHBURN, K., BLUMBERG, E., ALEXANDER, B., FREEMAN, R., HEATON, N., PESCOVITZ, M. D. & VALGANCICLOVIR SOLID ORGAN TRANSPLANT STUDY GROUP 2004 Efficacy and safety of valganciclovir vs. oral ganciclovir for prevention of cytomegalovirus disease in solid organ transplant recipients. *American Journal of Transplantation* **4**, 611–620.

PFEFFER, M. A. & BRAUNWALD, E. 1990 Ventricular remodeling after myocardial infarction. *Circulation* **80** (4), 1161–1172.

PHILLIPS, B. W., LIM, R. Y., TAN, T. T., RUST, W. L. & CROOK, J. M. 2008 Efficient expansion of clinical-grade human fibroblasts on microcarriers: Cells suitable for *ex vivo* expansion of clinical-grade hescs. *Journal of Biotechnology* **134** (1–2), 79–87.

PITTENGER, M. F., MACKAY, A. M., BECK, S. C., HAISWAL, R. K., DOUGLAS, R., MOSCA, J. D., MOORMAN, M. A., D. W. SIMONETTI, CRAIG, S. & MARSHAK, D. R. 1999 Multilineage potential of adult human mesenchymal stem cells. *Science* **284** (5411), 143–147.

PONTICIELLO, M. S., SCHINAGL, R. M., KADIYALA, S. & BARRY, F. P. 2000 Gelatin-based resorbable sponge as a carrier matrix for human mesenchymal stem cells in cartilage regeneration therapy. *Journal of Biomedical Materials Research* **52** (2), 246–255.

POUNGVARIN, N. 1998 Stroke in the developing world. *Lancet* **352 Suppl 3**, 19–22.

PRAEMER, A., FURNER, S. & RICE, D. P. 1999 *Musculoskeletal Conditions in the United States*. American Academy of Orthopaedic Surgeons.

PU, Y. & MENG, H. 2000 An advanced off-axis holographic particle image velocimetry (HPIV) system. *Experiments in Fluids* **29**, 184–197.

RAFFEL, M., WILLERT, C. E., WERELEY, S. T. & KOMPENHANS, J. 2007 *Particle Image Velocimetry: A Practical Guide*, 2nd edn. Heidelberg, Germany: Springer-Verlag.

RAIBLE, D. W. & EISEN, J. S. 1994 Restriction of neural crest cell fate in the trunk of the embryonic zebrafish. *Development* **120**, 495–503.

REUBINOFF, B. E., PERA, M. F., FONG, C.-Y., TROUNSON, A. & BONGSO, A. 2000 Embryonic stem cell lines from human blastocysts: somatic differentiation in vitro. *Nature Biotecnology* **18** (4), 399–404.

REYES, M., DUDEK, A., JAHAGIRDAR, B., KOODIE, L., MARKER, P. H. & VERFAILLIE, C. M. 2002 Origin of endothelial progenitors in human postnatal bone marrow. *Journal of Clinical Investigation* **109** (3), 337–382.

RICHARDS, M., FONG, C. Y., CHAN, W. K., WONG, P. C. & BONGSO, A. 2002 Human feeders support prolonged undifferentiated growth of human inner cell masses and embryonic stem cells. *Nature Biotechnology* **20** (9), 933–936.

ROBINS, J. C., AKENO, N., MUKHERJEE, A. & DALAL, R. R. 2005 Hypoxia induces chondrocyte-specific gene expression in mesenchymal cells in association with transcriptional activation of Sox9. *Bone* **37** (3), 313–322.

RODRIGUEZ, A.-M., ELABD, C., AMRI, E.-Z., AILHAUD, G. & DANI, C. 2005 The human adipose tissue is a source of multipotent stem cells. *Biochimie* **87** (1), 125–128.

Rohwedel, J., Maltsev, V., Bober, E., Arnold, H. H., Hescheler, J. & Wobus, A. M. 1994 Muscle cell differentiation of embryonic stem cells reflects myogenesis in vivo: Developmentally regulated expression of myogenic determination genes and functional expression of ionic currents. *Developmental Biology* **164** (1), 87–101.

Ronnenberg, B. 1977 Ein selbstjustierendes 3-Komponenten-LDA nach dem Vergleighstrahlverfaren, angewendt für Untersuchungen in einer stationären zylindersymmetrischen Drehströmung mit einem Rühckströmgebiet. *Technical Report Bericht 20, Max-Planck-Institut für Strömungsforschung, Göttingen* .

Sah, R. L.-Y., Kim, Y.-J., Grodzinsky, J.-Y. H. D. A. J., Plass, A. H. K. & Sandy, J. D. 1989 Biosynthetic response of cartilage explants to dynamic compression. *Journal of Orthopaedic Research* **7** (5), 619–636.

Samarage, C., Carberry, J., Hourigan, K. & Fouras, A. 2012 Optimisation of temporal averaging processes in PIV. *Experiments in Fluids* **52**, 617–631.

Sarpkaya, T. 1971 On stationary and travelling vortex breakdowns. *Journal of Fluid Mechanics* **45**, 545–559.

Schop, D., Janssen, F. W., Borgart, E., de Bruijn, J. D. & van Dijkhuizen-Radersma, R. 2008 Expansion of mesenchymal stem cells using a microcarrier-based cultivation system: growth and metabolism. *Journal of Tisse Engineering and Regenerative Medicine* **2** (2–3), 126–135.

Schröder, A., Geisler, R., Elsinga, G. E., Scarano, F. & Dierksheide, U. 2008 Investigation of a turbulent spot and a tripped turbulent boundary layer flow using time-resolved tomographic PIV. *Experiments in Fluids* **44** (2), 305–316.

Schroeder, M., Biebruegge, S., Werner, A., Willbold, E., Burg, M., Ruediger, M., Field, L. J., Lehmann, J. & Zweigerdt, R. 2005 Differentiation and lineage selection of mouse embryonic stem cells in a stirred bench scale bioreactor with automated process control. *Biotechnology and Bioengineering* **92** (7), 920–933.

Schuldiner, M., Yanuka, O., Itskovitz-Eldor, J., Melton, D. A. & Benvenisty, N. 2000 Effects of eight growth factors on the differentiation of cells derived from human embryonic stem cells. *Proceedings of the National Academy of Sciences* **97** (21), 11307–11312.

Schwartz, R. M., Palsson, B. O. & Emerson, S. G. 1991 Rapid medium perfusion rate significantly increases the productivity and longevity of human bone marrow cultures. *Proceedings of the National Academy of Sciences* **88** (15), 6760–6764.

SEN, A., KALLOS, M. S. & BEHIE, L. A. 2001 Effects of hydrodynamics on cultures of mammalian neural stem cell aggregates in suspension bioreactors. *Industrial and Engineering Chemistry Research* **40** (23), 5350–5357.

SHACHAR, M. & COHEN, S. 2003 Cardiac tissue engineering, ex-vivo: design principles in biomaterials and bioreactors. *Heart Failure Reviews* **8**, 271–276.

SHEN, Q., GODERIE, S. K., JIN, L., KARANTH, N., SUN, Y., ABRAMOVA, N., VINCENT, P., PUMIGLIA, K. & TEMPLE, S. 2004 Endothelial cells stimulate self-renewal and expand neurogenesis of neural stem cells. *Science* **304** (5675), 1338–1340.

SHENGHUI, H., NAKADA, D. & MORRISON, S. J. 2009 Mechanisms of stem cell self-renewal. *Annual Review of Cell and Developmental* **25**, 377–406.

SILVA, G. V., LITOVSKY, S., ASSAD, J. A., SOUSA, A. L., MARTIN, B. J., VELA, D., COULTER, S. C., LIN, J., OBER, J., VAUGHN, W. K., BRANCO, R. V., OLIVEIRA, E. M., HE, R., GENG, Y. J., WILLERSON, J. T. & PERIN, E. C. 2005 Mesenchymal stem cells differentiate into an endothelial phenotype, enhance vascular density, and improve heart function in a canine chronic ischemia model. *Circulation* **111** (2), 150–156.

SINGH, A., SURI, S., LEE, T., CHILTON, J. M., COOKE, M. T., CHEN, W., FU, J., STICE, S. L., LU, H., McDEVITT, T. C. & GARCIA, A. J. 2013 Adhession strength-based, label free isolation of human pluripotent stem cells. *Nature Methods* **10**, 438–444.

SINGH, H., TEOH, S. H., LOW, H. T. & HUTMACHER, D. W. 2005 Flow modelling within a scaffold under the influence of uni-axial and bi-axial bioreactor rotation. *Journal of Biotechnology* **119**, 181–196.

SMITH, A. G. 2003 Emryo-derived stem cells: Of mice and men. *Annual Review of Cell and Developmental Biology* **17** (1), 435–362.

SOLCHAGA, L. A., DENNIS, J. E., GOLDBERG, V. M. & CAPLAN, A. I. 1999 Hyaluronic acid-based polymers as cell carriers for tissue-engineered repair of bone and cartilage. *Journal of Orthopaedic Research* **17** (2), 205–213.

SORIA, J. & ATKINSON, C. 2008 Towards 3C-3D digital holographic fluid velocity vector field measurement - tomographic digital holographic PIV (Tomo-HPIV). *Measurement Science and Technology* **19** (7), 074002.

SPOHN, A., MORY, M. & HOPFINGER, E. J. 1998 Experiments on vortex breakdown in a confined flow generated by a rotating disc. *Journal of Fluid Mechanics* **370**, 73–99.

SQUIRE, H. B. 1962 Analysis of the vortex breakdown phenomenon. part 1. *Aerospace Department, Imperial College, London, Rep. 102* .

STADTFELD, M., BRENNAND, K. & HOCHEDLINGER, K. 2008 Reprogramming of pancreatic cells into induced pluripotent stem cells. *Current Biology* **18** (12), 890–894.

STIEHLER, M., BÜNGER, C., BAATRUP, A., LIND, M., KASSEM, M. & MYGIND, T. 2008 Effect of dynamic 3-D culture on proliferation, distribution and osteogenic differentiation of human mesenchymal stem cells. *Journal of Biomedical Materials Research Part A* **89A**, 96–107.

SUCOSKY, P., OSORIO, D. F., BROWN, J. B. & NEITZEL, G. P. 2003 Fluid mechanics of spinner flask bioreactor. *Biotechnology and Bioengineering* **85**, 34–46.

SULLIVAN, G. J., HAY, D. C., PARK, I.-H., FLETCHER, J., HANNOUN, Z., PAYNE, C. M., DALGETTY, D., BLACK, J. R., ROSS, J. A., SAMUEL, K., WANG, G., DALEY, G. Q., LEE, J.-H., CHURCH, G. M., FORBES, S. J., IREDALE, J. P. & WILMUT, I. 2010 Generation of functional human hepatic endoderm from human induced pluripotent stem cells. *Hepatology* **51** (1), 329–335.

SWITOWSKI, A., PENG, J., LIU, Q., MALI, P., RAO, M. S., CHENG, L. & ZENG, X. 2010 Efficient generation of functional dopaminergic neurons from human induced pluripotent stem cells under defined conditions. *Stem Cells* **28** (10), 1893–1904.

TAKAHASHI, K., TANABE, K., OHNUKI, M., NARITA, M., ICHISAKA, T., TOMODA, K. & YAMANAKA, S. 2007 Induction of pluripotent stem cells from adult human fibroblasts by defined factors. *Cell* **131** (5), 861–872.

TAN, B. T., LIOW, K. Y. S., MUNUNGA, L., THOMPSON, M. C. & HOURIGAN, K. 2009 Simulation of the control of vortex breakdown in a closed cylinder using a small rotating disk. *Physics of Fluids* **21**, 024104.

TAT, P., SUMER, H., JONES, K. L., UPTON, K. & VERMA, P. 2010 The efficient generation of induced pluripotent stem (iPS) cells from adult mouse adipose tissue-derived and neural stem cells. *Cell Transplantation* **19**, 525–536.

TENG, Y. D., LAVIK, E. B., QU, X., PARK, K. I., OUREDNIK, J., ZURAKOWSKI, D., LANGER, R. & SYNDER, E. Y. 2002 Functional recovery following traumatic spinal cord injury mediated by a unique polymer scaffold seeded with neural stem cells. *Proceedings of the National Academy of Sciences* **99** (5), 3024–3029.

THEUNISSEN, R., SCARANO, F. & RIETHMULLER, M. L. 2007 An adaptive sampling and windowing interrogation method in PIV. *Measurement Science and Technology* **18**, 275–287.

THOMPSON, M. C. & HOURIGAN, K. 2003 The sensitivity of steady vortex breakdown bubbles in confined cylinder flows to rotating lid misalignment. *Journal of Fluid Mechanics* **496**, 129–138.

THOMSON, J. A., ITSKOVITZ-ELDOR, J., SHAPIRO, S. S., WAKNITZ, M. A., SWIERGIEL, J. J., MARSHALL, V. S. & JONES, J. M. 1998 Embryonic stem cell lines derived from human blastocysts. *Science* **282** (5391), 1145–1147.

THOUAS, G. A., SHERIDAN, J. & HOURIGAN, K. 2007 A bioreactor model of mouse tumor progression. *Journal of Biomedicine and Biotechnology* **9**, 32754.

TOMA, C., PITTENGER, M. F., CAHILL, K. S., BYRNE, B. J. & KESSLER, P. D. 2002 Human mesenchymal stem cells differentiate to a cardiomyocyte phenotype in the adult murine heart. *Circulation* **105**, 93–98.

TOMA, J. G., AKHAVAN, M., FERNANDES, K., BARNABÉ-HEIDER, F., SADIKOT, A., KAPLAN, D. R. & MILLER, F. D. 2001 Isolation of multipotent adult stem cells from the dermis of mammalian skin. *Nature Cell Biology* **3** (9), 778–784.

TORRES, M. 1998 The use of embryonic stem cells for the genetic manipulation of the mouse. *Current Topics in Developmental Biology* **36**, 99–114.

TROPEA, C. 1995 Laser-doppler anemometry - recent developments and future challenges. *Measurement Science and Technology* **6** (6), 605–619.

TROPEL, P., PLATET, N., PLATEL, J.-C., NOËL, D., ALBRIEUX, M., BENABID, A.-L. & BERGER, F. 2006 Functional neuronal differentiation of bone marrow-derived mesenchymal stem cells. *Stem Cells* **24** (12), 2868–2876.

TYLER, G. A. & THOMPSON, B. J. 1976 Fraunhofer holography applied to particle-size analysis - A reassessment. *Optica Acta* **23** (9), 685–700.

UCHIO, Y., OCHI, M., TOYODA, T., YAO, J. Q. & SEEDHOM, B. B. 2000 Different effect of static and cyclic hydrostatic pressure on proteoglycan biosynthesis of articular chondrocytes between subpopulations. *Transactions of the Orthopaedic Research Society* **25**, 648–.

VALENTINE, D. T. & JAHNKE, C. C. 1994 Flow induced in a cylinder with both ends walls rotating. *Physics of Fluids* **6**, 2702.

VAN WEZEL, A. L. 1967 Growth of cell-strains and primary cells on micro-carriers in homogeneous culture. *Nature* **216** (5110), 64–65.

VARANI, J., BENDELOW, M. J., CHUN, J. H. & HILLEGAS, W. A. 1986 Cell growth on microcarriers: comparison of proliferation on and recovery from various substrates. *Journal of Biological Standardization* **14** (4), 331–336.

VARANI, J., DAME, M., BEALS, T. F. & WASS, J. A. 1983 Growth of three established cell lines on glass microcarriers. *Biotechnology and Bioengineering* **25** (5), 1359–1372.

VARANI, J., DAME, M., REDISKE, J., BEALS, T. F. & HILLEGAS, W. 1985 Substrate-dependent differences in growth and biological properties of fibroblasts and epithelial cells grown in microcarrier culture. *Journal of Biological Standardization* **13** (1), 67–76.

VENKAT, R. V., STOCK, R. & CHALMERS, J. J. 1996 Study of hydrodynamics in microcarrier culture spinner vessels: A particle tracking velocimetry approach. *Biotechnology and Bioengineering* **29**, 456–466.

VOGEL, H. U. 1968 Experimentelle ergebnisse über die laminare Strömung in einem zylindrischen Gehaüse mit darin rotierender Scheibe. *Technical Report Bericht 6, Max-Planck-Institut für Strömungsforschung, Göttingen* .

WANG, S. & RUSAK, Z. 1997 The dynamics of a swirling flow in a pipe and transition to axisymmetric vortex breakdown. *Journal of Fluid Mechanics* **340**, 177–223.

WATT, F. M. 2001 Stem cell fate and patterning in mammalian epidermis. *Current Opinions in Genetics and Development* **11** (4), 410–417.

WEISS, S., DUNNE, C., HWESON, J., WOHL, C., WHEATLEY, M., PETERSON, A. C. & REYNOLDS, B. A. 1996 Multipotent CNS stem cells are resent in the adult mammalian spinal cord and ventricular neuroaxis. *The Journal of Neuroscience* **16** (23), 7599–7609.

WESTERLUND, U., MOE, M. C., VARGHESE, M., BERG-JOHNSEN, J., OHLSSON, M., LANGMOEN, I. A. & SVENSSON, M. 2003 Stem cells from the adult human brain develop into functional neurons in culture. *Experimental Cell Research* **289** (2), 378–283.

WIDJAJA, J. & SOONTARANON, S. 2009 All wavelet analysis of in-line particle holograms. *Optics and Lasers in Engineering* **47**, 1325–1333.

WILLERT, C. 1997 Stereoscopic digital particle image velocimetry for application in wind tunnel flows. *Measurement Science and Technology* **8**, 1465–1479.

WILLERT, C. E. & GHARIB, M. 1991 Digital particle image velocimetry. *Experiments in Fluids* **10**, 181–193.

WISLET-GENDEBIEN, S., HANS, G., LEPRINCE, P., RIGO, J.-M., MOONEN, G. & ROGISTER, B. 2005 Plasticity of cultured mesenchymal stem cells: Switch from nestin-positive to excitable neuron-like phenotype. *Stem Cells* **23** (3), 392–402.

WORTH, N. A. & NICKELS, T. B. 2008 Acceleration of tomo-PIV by estimating the initial volume intensity distribution. *Experiments in Fluids* **48**, 847–856.

XU, C., INOKUMA, M. S., DENHAM, J., GOLDS, K., KUNDU, P., GOLDS, J. D. & CARPENTER, M. K. 2001 Feeder-free growth of undifferentiated human embryonic stem cells. *Nature Biotechnology* **19** (10), 971–974.

XU, C., ROSLER, E., JIANG, J., LEBKOWSKI, J. S., GOLD, J. D., O'SULLIVAN, C., DELAVAN-BOORSMA, K., MOK, M., BRONSTEIN, A. & CARPENTER, M. K. 2005a Basic fibroblast growth factor supports undifferentiated human embryonic stem cell growth without conditioned medium. *Stem Cells* **23** (3), 315–323.

XU, R. H., PECK, R. M., LI, D. S., FENG, X., LUDWIG, T. & THOMSON, J. A. 2005b Basic FGF and suppression of BMP signaling sustain undifferentiated proliferation of human ES cells. *Nature Methods* **2** (3), 185–190.

XU, W., ZHANG, X., QIAN, H., ZHU, W., SUN, X., HU, J., ZHOU, H. & CHEN, Y. 2004 Mesenchymal stem cells from adult human bone marrow differentiate into a cardiomyocyte phenotype in vitro. *Experimental Biology and Medicine* **229** (7), 623–631.

YAMAMOTO, K., SOKABE, T., WATABE, T., MIYAZONO, K., YAMASHITA, J. K., OBI, S., OHURA, N., MATSUSHITA, A., KAMIYA, A. & ANDO, J. 2005 Fluid shear stress induces differentiation of FLK-1-positive embryonic stem cells into vascular endothelial cells *in vitro*. *American Journal of Physiology. Heart and Circulatory Physiology* **288** (4), H1915–1914.

YEN, B. L., HUANG, H.-I., CHIEN, C.-C., JUI, H.-Y., KO, B.-S., YAO, M., SHUN, C.-T., YEN, M.-L., LEE, M.-C. & CHEN, Y.-C. 2005 Isolation of multipotent cells from human term placenta. *Stem Cells* **23** (1), 3–9.

YING, Q.-L., NICHOLS, J., CHAMBERS, I. & SMITH, A. 2003 BMP induction of Id proteins suppresses differentiation and sustains embryonic stem cell self-renewal in collaboration with STAT3. *Cell* **115** (3), 281–292.

YU, J., VODYANIK, M. A., SMUGA-OTTO, K., ANTOSIEWICZ-BOURGET, J., FRANE, J. L., TIAN, S., NIE, J., JONSDOTTIR, G. A., RUOTTI, V., STEWART, R., SLUKVIN, I. I. & THOMSON, J. A. 2007 Induced pluripotent stem cell lines derived from human somatic cells. *Science* **318** (5858), 1317–1920.

YU, P., LEE, T. S., ZENG, Y. & LOW, H. T. 2006 Effects of conical lids on vortex breakdown in an enclosed cylindrical chamber. *Physics of Fluids* **18**, 117101.

ZANDSTRA, P. W., BAUWENS, C., YIN, T., LIU, Q., SCHILLER, H., ZWEIGERDT, R., PASUMARTHI, K. B. S. & FIELD, L. J. 2003 Scalable production of embryonic stem cell-derived cardiomyocytes. *Tissue Engineering* **9** (4), 767–778.

ZHANG, J., WILSON, G. F., SOERENS, A. G., KOONCE, C. H., YU, J., PALECEK, S. P. & THOMSON, J. A. 2009a Functional cardiomyocytes derived from human induced pluripotent stem cells. *Circulation Research* **104**, e30–e41.

ZHANG, M., MAL, N., KIEDROWSKI, M., CHACKO, M., ASKARI, A. T., POPOVIC, Z. B., KOC, O. N. & PENN, M. S. 2007 SDF-1 expression by mesenchymal stem cells results in trophic support of cardiac myocytes after myocardial infarction. *The FASEB Journal* **21** (12), 3197–3207.

ZHANG, Z. Y., TEOH, S. H., CHONG, W. S., FOO, T. T., CHNG, Y. C., CHOOLANI, M. & CHAN, J. 2009b A biaxial rotating bioreactor for the culture of fetal mesenchymal stem cells for bone tissue engineering. *Biomaterials* **30** (14), 2694–2704.

ZHAO, F. & MA, T. 2005 Perfusion bioreactor system for human mesenchymal stem cell tissue engineering: Dynamic cell seeding and construct development. *Biotechnology and Bioengineering* **91** (4), 482–493.

ZHAO, L.-R., DUAN, W.-M., REYES, M., KEENE, C. D., VERFAILLIE, C. M. & LOW, W. C. 2002 Human bone marrow stem cells exhibit neural phenotypes and ameliorate neurological deficits after grafting into the ischemic brain of rats. *Experimental Neurology* **174** (1), 11–20.

ZUK, P. A., ZHU, M., ASHJIAN, P., DE UGARTE, D. A., HUANG, J. I., MIZUNO, H., ALFONSO, Z. C., FRASER, J. K., BENHAIM, P. & HEDRICK, M. H. 2002 Human adipose tissue is a source of multipotent stem cells. *Molecular Biology of the Cell* **13** (12), 4279–4295.

ZUK, P. A., ZHU, M., MIZUNO, H., HUANG, J., FUTRELL, J. W., KATZ, A. J., BENHAIM, P., LORENZ, H. P. & HEDRICK, M. H. 2001 Multilineage cells from human adipose tissue: Implications for cell-based therapies. *Tissue Engineering* **7** (2), 211–228.

ZUR NIEDEN, N., KEMPKA, G., RANCOURT, D. & AHR, H.-J. 2005 Induction of chondro-, osteo- and adipogenesis in embryonic stem cells by bone morphogenetic protein-2: Effect of cofactors on differentiating lineages. *BMC Developmental Biology* **5** (1).

ZUR NIEDEN, N. I., CORMIER, J. T., RANCOURT, D. E. & KALLOS, M. S. 2007 Embryonic stem cells remain highly pluripotent following long-term expansion as aggregates in suspension bioreactors. *Journal of Biotechnology* **129**, 421–432.

ᴢᴜʀ Nɪᴇᴅᴇɴ, N. I., Kᴇᴍᴘᴋᴀ, G. & Aʜʀ, H. J. 2003 In vitro differentiation of embryonic stem cells into mineralized osteoblasts. differentiation. *Differentiation* **71** (1), 18–27.

Appendix A

Optimisation of Agitation Speed in Spinner Flask for Microcarrier Structural Integrity and Expansion of Induced Pluripotent Stem Cells

The following manuscript was published online in 2014 in *Cytotechnology*. This journal is a parallel study of Chapter 5 and was authored by P. Gupta, M.-Z. Ismadi, P. Verma, A. Fouras, S. Jadhav, J. Bellare and K. Hourigan. The article reproduced in this thesis is directly taken from the published version without alteration.

ORIGINAL RESEARCH

Optimization of agitation speed in spinner flask for microcarrier structural integrity and expansion of induced pluripotent stem cells

**Priyanka Gupta · Mohd-Zulhilmi Ismadi ·
Paul J. Verma · Andreas Fouras ·
Sameer Jadhav · Jayesh Bellare · Kerry Hourigan**

Abstract In recent times, the study and use of induced pluripotent stem cells (iPSC) have become important in order to avoid the ethical issues surrounding the use of embryonic stem cells. Therapeutic, industrial and research based use of iPSC requires large quantities of cells generated in vitro. Mammalian cells, including pluripotent stem cells, have been expanded using 3D culture, however current limitations have not been overcome to allow a uniform, optimized platform for dynamic culture of pluripotent stem cells to be achieved. In the current work, we have expanded mouse iPSC in a spinner flask using Cytodex 3 microcarriers. We have looked at the effect of agitation on the microcarrier survival and optimized an agitation speed that supports bead suspension and iPS cell expansion without any bead breakage. Under the optimized conditions, the mouse iPSC were able to maintain their growth, pluripotency and differentiation capability. We demonstrate that microcarrier survival and iPS cell expansion in a spinner flask are reliant on a very narrow range of spin rates, highlighting the need for precise control of such set ups and the need for improved design of more robust systems.

Keywords Microcarrier · Induced pluripotent stem cells · Spinner flask

P. Gupta (✉)
IITB Monash Research Academy, Mumbai, India
▓▓▓▓▓▓▓▓▓▓▓▓▓▓▓▓▓▓▓▓▓▓

P. Gupta · S. Jadhav · J. Bellare
Department of Chemical Engineering, IIT Bombay,
Mumbai, India

S. Jadhav
▓▓▓▓▓▓▓▓▓▓▓▓▓▓

J. Bellare
▓▓▓▓▓▓▓▓▓▓

P. Gupta
Department of Chemical Engineering, Monash
University, Melbourne, VIC, Australia

P. Gupta · M.-Z. Ismadi · P. J. Verma · K. Hourigan
Division of Biological Engineering, Monash University,
Melbourne, VIC, Australia

M.-Z. Ismadi
▓▓▓▓▓▓▓▓▓▓▓▓▓▓

P. J. Verma
▓▓▓▓▓▓▓▓▓▓▓▓▓▓▓▓▓▓

K. Hourigan
▓▓▓▓▓▓▓▓▓▓▓▓▓

M.-Z. Ismadi · A. Fouras · K. Hourigan
Department of Mechanical and Aerospace Engineering,
Monash University, Melbourne, VIC, Australia

A. Fouras
▓▓▓▓▓▓▓▓▓▓▓▓▓

P. J. Verma
South Australian Research and Development Institute,
Rosedale, SA, Australia

 Springer

Introduction

The unique properties of unlimited self renewal and differentiation into all types of cells have made pluripotent stem cells exciting tools for tissue engineering, regenerative medicine and drug screening. The discovery of iPSC has allowed scientists to harness and utilize these cells without the ethical dilemma associated with ESC (Takahashi and Yamanaka 2006). However, practical use in cellular therapy requires cell numbers ranging typically between several thousands to a few billions. For example, it is estimated that on average approximately 4.0×10^{10} cells would be required to treat each patient requiring cardiomyocyte replacement. This roughly equates to 1,144 T-175 flasks per patient, making it an impossible task (Want et al. 2012). The use of large scale culture systems or bioreactors is a necessity for such purposes. Apart from scaling up of culture, the use of bioreactors also allows better aeration, facilitates proper nutrient supply to cells, reduces consumable costs and supports long term culture of cells. Spinner flasks are one of the oldest and most widely used reactor systems and have been used extensively for the expansion of mouse as well as human ESC. Both mouse and human ESC have been expanded as aggregates in spinner flasks (Fok and Zandstra 2005; Cormier et al. 2006; Abbasalizadeh et al. 2012; Krawetz et al. 2010; Steiner et al. 2010). Extensive study in the field of large scale expansion of ES cells has given rise to novel and better systems for these cells but the field of dynamic culture of iPS cells has just started. Recently, efforts have also been made to expand iPSC in spinner flasks as aggregates (Fluri et al. 2012; Olmer et al. 2010, 2012; Shafa et al. 2012). However, expansion as aggregates is associated with some disadvantages. The formation of aggregates may lead to concentration gradients of nutrients and oxygen, resulting in their uneven distribution. In case of larger aggregates, this may even result in improper waste removal along with cell death and necrosis at the centre. The use of microcarriers in conjunction with spinner flasks has been deemed to be a suitable alternative to aggregate expansion of pluripotent cells. A successful microcarrier expansion is dependent on several factors including the type of carrier used, the cell line being expanded, the spinner flask set up, the position of the impeller and the spin rate (revolutions per minute—RPM) used. It is well known that the sensitivity of the cells to the spinning is of utmost importance, but it is equally important to know the tolerance level of the microcarriers themselves. Extensive studies have been conducted for expansion of both mouse and human ESC using microcarriers. But the range of RPM used varies widely across the literature along with the type of carrier used. The success of the carriers also varied with the cell line in question, even for the same cell type. Commercially available microcarriers—such as Cultisphere S, Cytodex 3, Solohill carriers and Hillex II have been widely used for the expansion of ESC, with Cytodex 3 being the most common. The speed used for mouse ESC, varies between 40 and 70 RPM (Fok and Zandstra 2005; Abranches et al. 2007; Alfred et al. 2011; Fernandes et al. 2007; Marinho et al. 2010; Storm et al. 2010; Tielens et al. 2007), while the range for human ESC lies within 24–80 RPM (Storm et al. 2010; Chen et al. 2011; Fernandes et al. 2009; Kehoe et al. 2010; Leung et al. 2011; Lock and Tzanakakis 2009; Marinho et al. 2013; Nie et al. 2009; Oh et al. 2009; Phillips et al. 2008; Serra et al. 2010). iPSC are by nature, delicate, making their large scale culture in spinner flasks using microcarriers a much more difficult proposition. Until now, very few groups have tried to use microcarriers for the expansion of iPSC. Kehoe et al. (2010) have shown some preliminary data in their review article. Recently, Bardy et al. (2013) have expanded iPSC on microcarriers, followed by their differentiation into neural progenitor cells. However, prior to spinner flask culture, they had to adapt the iPSC to expansion on the carriers in static culture. Also, in both these cases, the carriers were coated with Matrigel, which was already well known for supporting the growth of pluripotent stem cells in the absence of feeder cells. Similar to the studies with ESC, the spinner flask spin rate for these two studies varied considerably.

The experimental limitations associated with any type of dynamic culture bring into the forefront the need to integrate engineering aspects such as fluid mechanics with biology. Our group has worked towards this aspect of spinner flask culture for some time now with the earliest work reported in 2006 (Dusting et al. 2006). In this work, a detailed study of the flow dynamics within a prototype reactor system similar to a spinner flask was undertaken for the first time, and it highlighted the need for similar studies to understand the shear stress and flow structures that affect microcarrier breakage, cell attachment and

expansion. A similar study involving cell growth in a stirred bioreactor was also carried out, integrating theoretical modeling and experimental results (Thouas et al. 2007). More recently, efforts were also made to understand the mixing properties of flow within a cylindrical system similar to a spinner flask (Meunier and Hourigan 2013). Currently, a new holographic technique for visualization of flow within a spinner flask has been developed in our laboratory (Ismadi et al. 2013). This particular technique can be used for a deeper understanding of fluid flow and carrier dispersement within a spinner flask, providing us with in depth knowledge of the system and design guidelines.

In this current work, we have expanded mouse iPSC in a spinner flask using Cytodex 3, without any prior coating of the carriers. Although widely used for ES cells, this is the first time Cytodex 3 has been used for iPS cells. We have used the cells directly from their 2D feeder dependent culture, thus testing their adaptability to a change in culture condition. We have also studied the effect of different spin rates covering the entire range published till date, related to Cytodex 3 microcarriers and iPSC. Our work highlights the presence of very specific spin rate ranges for: carrier breakage; survival of the carriers but with no cell attachment; short term cell attachment and survival; non suspension of carriers; and finally, an optimized spin rate for carrier suspension without breakage and long term attachment and expansion of iPSC. The results can also be used to corroborate future fluid dynamic modeling and visualization of the current system.

Materials and methods

Cell culture

Mouse OG2 iPSC were generated previously in the lab (Tat et al. 2010) and were regularly maintained on mitomycin C inactivated feeder cells using ES media containing DMEM, 15 % fetal bovine serum, $1\times$ Glutamax, $1\times$ non essential amino acid, $1\times$ Pen/Strep Solution, 0.1 mM β-mercaptoethanol and 1,000 U/ml LIF solution (Merck-Millipore, Billerica, MA, USA). The cells were incubated in a humidified incubator at 37 °C with 5 % CO_2. Unless otherwise mentioned, all media materials were purchased from Invitrogen (Life Technologies, Carlsbad, CA, USA). The iPSC used

have a GFP transgene under the control of the promoter of the pluripotent gene Oct4.

Spinner flask culture

Based on the available literature on expansion of ES cells on carriers, Cytodex 3 and Hillex II were selected for a preliminary study on iPS cell attachment on these two carriers. This study demonstrated that the iPS cell line used for our main study displayed better cell attachment and expansion on Cytodex 3 (data not shown). Hence Cytodex 3 was chosen for the spinner flask culture.

100 ml spinner flasks from Bellco Biotechnology (Bellco Glass, Inc., Vineland, NJ, USA) were used with a final media volume of 50 ml. The spinner flasks were coated with SigmaCote (Sigma Aldrich, St. Louis, MO, USA) prior to usage. Cytodex 3 carriers (GE Health Care, Little Chalfont, UK) equivalent to a surface area of 200 cm^2/flask were weighed, hydrated using PBS and sterilized by autoclaving as per manufacturer's instructions. The carriers were equilibrated prior to use by incubating them in culture medium for around 1 h. A seeding density of 2×10^5 cells/ml was used for each flask. The cells were inoculated with the carriers in a low adherence 10 cm dish for about 24 h in order to facilitate cell attachment. After 24 h, carriers with cells were transferred to the spinner flasks and the culture volume was adjusted to 50 ml. The impeller was adjusted after initial trial and error experiments in such a way that the stirrer was half immersed, in order to minimise mechanical damage to the carriers as well as the cells as far as possible. We observed more carrier breakage if the impeller was submerged too much and if the motor rotation was not smooth. The spinner flask's impeller was directly connected to a stepper motor using a custom-made coupling shaft (Fig. 1). The speed of the motor was precisely regulated with a motion controller (National Instrument, Clayton, VIC, Australia). The iPSC were expanded for 7 days in the spinner flask with 50 % medium replacement every day.

Control

As control, the iPSC were grown on 0.1 % gelatin coated 24 well plates (Corning (Corning, NY, USA), Sigma-Aldrich, St Louise, USA) in the same seeding density. The medium was changed at the same frequency as the spinner flasks.
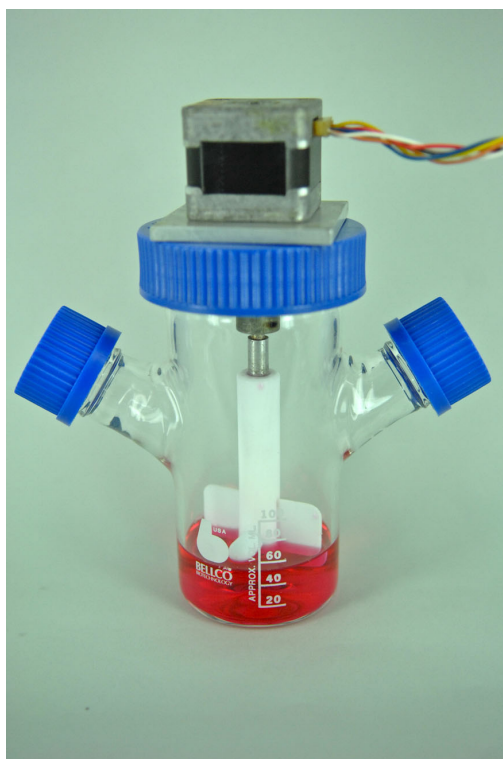
Fig. 1 Spinner flask set up with the impeller directly connected to a stepper motor

Cell count and microscopy

Samples of microcarriers (1 ml) were taken on days 3, 5 and 7 and viewed under a microscope. The cells were then washed with PBS and trypsinized using 1X Tryple Express (Life Technologies, Carlasbad, USA) for cell detachment. Microcarriers with cells were incubated at 37 °C for about 5 minutes to facilitate cell detachment. The suspension was then filtered through a 100 μm strainer to remove the microcarriers. Cell counts and cell viability were recorded using a haemocytometer and trypan blue assay. On each occasion the sampling and counting were done in duplicates.

Spontaneous differentiation

The differentiation capability of the cells was measured by in vitro EB formation. After 7 days of culture, iPSC from the control set up, as well as the

spinner flask culture, were seeded on low-adherence 6 well plates (Nunc, Sigma-Aldrich, St. Louis, USA) with mouse embryonic fibroblasts (mEF) medium at a seeding density of 50,000 cells/well. Medium was changed on alternate days. After 10 days of culture, the EBs were collected and the presence of cells of the three germ layers was ascertained by RT-PCR and immunostaining.

RT-PCR analysis

Cells for RT-PCR analysis were snap frozen on dry ice and stored at −80 °C until analysis. Oct 4, Nanog and c-myc genes were anlaysed for pluripotency while Nestin, Brachyury and Fox A2 were analysed for measuring the cells' differentiation capability. β actin was used as the house keeping gene in all cases (Primers are listed in Table 1). RNA was isolated from the cells using RNeasy Mini kit (Qiagen, Hilden, Germany) according to the manufacturer's instructions. Isolated RNA was cleaned using Ambion RNA Turbo DNAfree kit (Invitrogen) to remove any contaminating genomic DNA. Cleaned RNA was quantified using NanoDrop ND-1000 (NanoDrop Technologies, Wilmington, DE, USA). cDNA synthesis was carried out using Superscript III kit (Invitrgen) following the manufacturer's instructions. To verify the procedures, RT-PCR for β-actin was carried out after RNA clean up and cDNA synthesis. The PCR amplification included a total 35 cycles of denaturation at 95 °C for 30 s, followed by annealing at appropriate temperature for 30 s and extension at 72 °C for 1 min with an initial denaturation step at 95 °C for 4 min and a final extension step at 72 °C for 10 min. The PCR products were run on a 1 % agarose gel at 80 V. Gels were visualised using the Bio Rad Universal Hood II GelDoc system (Bio Rad Laboratories Inc., Hercules, CA, USA) and images were taken using Quantity One (version 4.6.3) software.

Immunostaining

Cells on microcarriers were fixed using 4 % paraformaldehyde followed by permeabilization and blocking using 0.1 % Triton X and 2 % BSA in PBS, respectively. Subsequently, the cells were incubated overnight with primary antibodies against SSEA-1 and Nanog. Next day, the cells were stained with appropriate secondary antibodies that were rhodamine

Cytotechnology

Table 1 Primer sequences for genes used in pluripotency and differentiation capability analysis

Gene	Primer Sequence
β-actin	F: GGA ATC CTG TGG CAT CCA TGA AAC
	R: AAA ACG CAG CTC AGT AAC AGT CCG
Oct 3/4	F: TCT TTC CAC CAG GCC CCC GGC TC
	R: TGC GGG CGG ACA TGG GGA GAT CC
Nanog	F: TCA AGG ACA GGT TTC AGA AGC A
	R: GCT GGG ATA CTC CAC TGG TG
c-myc	F: AAG TTT GAG GCA GCA GTT AAA ATT ATG GCT GAA
	R: TGA CCT AAC TCG AGG AGG AGC TGG AAT C
Nestin	F: TCT GGA AGT CAA CAG AGG TGG
	R: ACG GAG TCT TGT TCA CCT GC
Brachyury	F: CAT GTA CTC TTT CTT GCT GG
	R: GGT CTC GGG AAA GCA GTG GC
Fox A2	F: TGG TCA CTG GGG ACA AGG GAA
	R: GCA ACA ACA GCA ATA GAG AAC

conjugated for SSEA-1 and Alexa Fluor 594 conjugated for Nanog, following which the cells were subjected to nuclear staining with Hoechst 33342. Cells were also trypsinized for detachment from the microcarriers following the previously mentioned protocol after 7 days of culture and seeded on to 24 well plates for 3 days followed by staining for SSEA 1 and Nanog markers as per the aforementioned protocol.

EBs were stained for Brachyury, Nestin and FoxA2 markers following the same protocol. The secondary antibodies for all three markers were conjugated with Alexa Fluor 594.

Scanning electron microscopy

After 7 days of culture, the cells on microcarriers were fixed with 3 % gluteraldehyde, followed by drying using graded ethanol. This was followed by chemical drying using a transition from 100 % ethanol to 100 % Hexamethyldisilazane (HMDS) through a graded series of ethanol–HMDS mixture, ending at 100 % HMDS. The samples were then sputter coated and imaged using Hitachi S570 scanning electron microscope (Hitachi, Tokyo, Japan).

Pluripotency marker fluorescence intensity quantification

At the end of 7 days of culture, the cells were trypsinized using the previously mentioned protocol

and re-plated on gelatin coated Optilux opaque wall plates for 6–8 h to allow attachment, following which they were fixed using 4 % paraformaldehyde. The cells were then permeabilized using 0.1 % Triton X followed by blocking with 2 % BSA for 30 min. The cells were then incubated overnight with mouse IgM anti SSEA 1 antibody (Merck-Millipore) at 4 °C. After washing, the cells were incubated with anti mouse—IgM rhodamine (Chemicon International, Merck-Millipore) for 1 h followed by 30 min incubation with 1 µg/ml Hoechst 3342 solution. The fluorescence intensity for the pluripotency gene SSEA 1 was measured using an Array Scan High Content Screening instrument (Thermo Scientific, Waltham, MA, USA).

Effect of spin rate on microcarriers

In order to study the effect of different spin rates on Cytodex 3 microcarriers (1.5 mg/ml), the carriers were suspended in PBS in spinner flasks for 2 days at various RPMs. After 2 days, 1 ml of the suspension was taken out and studied under microscope.

Results

Effect of spin rate on microcarrier breakage

Proper attachment and expansion of iPSC in spinner flasks is dependent on the survival of the microcarriers
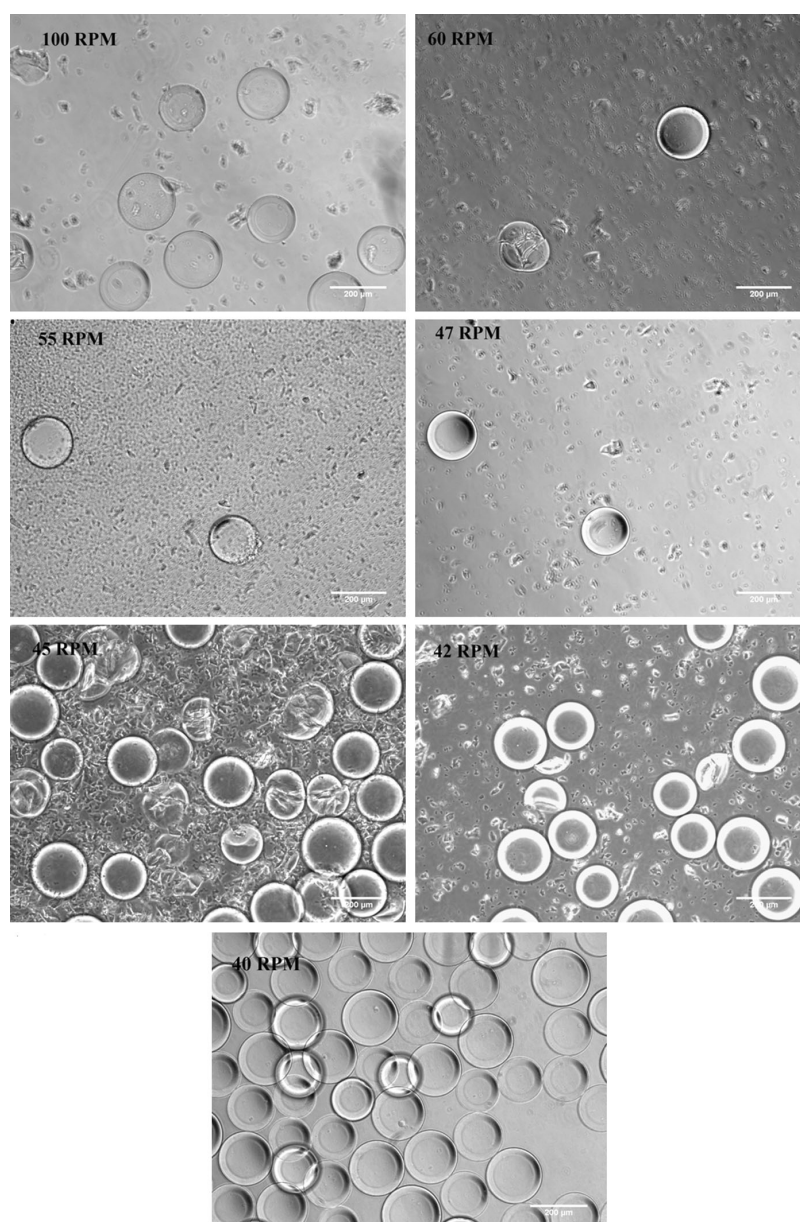
Fig. 2 Effect of different spin rates on Cytodex 3 microcarriers. Carriers were put in a spinner flask and kept in dynamic motion for 2 days. Samples were then taken out and observed under a phase contrast microscope. *Scale bar* 200 μm. The threshold level of tolerance for Cytodex 3 was found to be at 40 RPM

themselves. We were interested in studying the effect of different speeds on the Cytodex 3 microcarriers. The aim was to find out the maximum speed that the carriers can tolerate within the spinner flask without any breakage. 100 RPM was taken as the upper limit based on literature survey along with set ups at 60, 55, 47, 45, 42 and 40 RPM. As seen in Fig. 2, spin rates between 42 &100 RPM resulted in the breakage of the
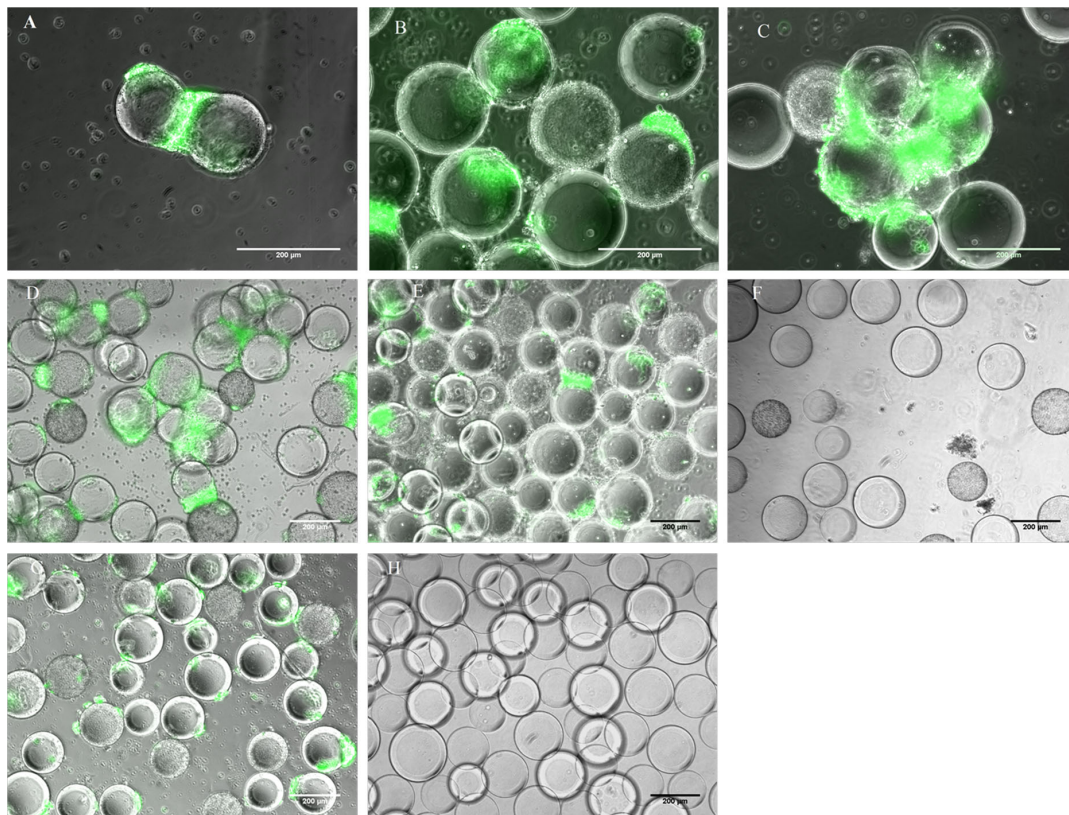
Fig. 3 Expansion of mouse iPSC on Cytodex 3 carriers at different spin rates over days 3, 5 and 7. **A–C** 25RPM, **D–F** 28 RPM, **G**, **H** 30 RPM. **A**, **D**, **G** day 3, **B**, **E**, **H** day 5, **C**, **F** day 7. *Scale bar* 200 μm

Cytodex 3 carriers after 2 days in the spinner flask. However, at 40 RPM, no carrier breakage was observed. 40 RPM was thus optimal as far as being the highest RPM that the Cytodex 3 carriers could tolerate.

The proper suspension of microcarriers in the spinner flask was also considered to be an important aspect for long term culture of cells in a dynamic environment. For this purpose we also looked at the suspension of Cytodex 3 carriers at lower spin rates (data not shown). It was observed that the suspension of the carriers was negligible at 20 RPM and below.

Based on these results, spin rates between 25 and 40 RPM were tested for attachment and expansion of mouse iPSC in spinner flask using Cytodex 3 micro-carriers. The aim was to find a spin rate at which the carriers were properly suspended and at the same time supported long term cell expansion.

Attachment and expansion of iPSC in spinner flask at different spin rates

Similar to any mammalian cell line, the mouse iPSC will have a threshold spin rate in terms of cell attachment, expansion and pluripotency maintenance. Based on the above results, we looked at attachment and expansion of mouse iPSC on Cytodex 3 carriers at 40, 30, 28 and 25 RPM in order find out the optimum spin rate for their long term expansion.

Cells and microcarriers were put in spinner flasks after 18–24 h of static attachment and subjected to 7 days spinning. Samples were drawn and imaged
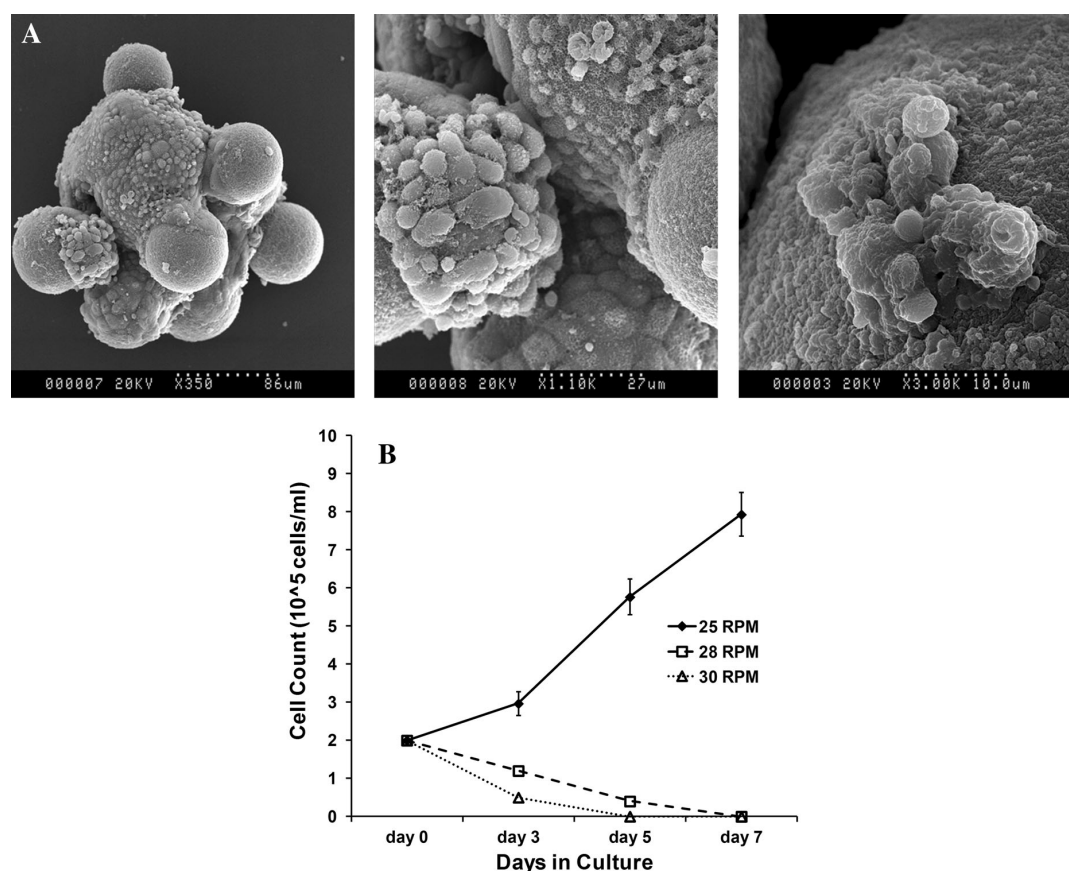
Fig. 4 Cell attachment and expansion on microcarriers. **A** Scanning electron microscopy (SEM) images of cells growing on Cytodex 3 microcarriers at the end of 7 days culture in spinner flask at 25 RPM. **B** Density of mouse IPSC on days 3, 5 and 7 at RPMs 25 (*filled diamond with solid line*), 28 (*open square with dashed line*) and 30 (*open triangle with dotted line*). Based on the preliminary data from microscopy and cell count, 25 RPM was deemed to be the best possibility and the set up was repeated n = 3 times to validate its reproducibility for all experiments

daily while a cell count was performed on days 3, 5 and 7.

It was observed that at 40 RPM the cells detached within 24 h of spinner flask culture and thus it was deemed unfit for further studies. Microscopic images showed cell attachment at 28 (Fig. 3D–F) and 30 RPM (Fig. 3G, H) in the initial culture days, but they were not able to support long term cell culture.

On the other hand, at 25 RPM cell expansion was observed till day 7. Cells were able to grow on the surface of microcarriers but they also showed some amount of 'bead bridging', due to the tendency of iPSC to form clustered colonies. The small

hydrodynamic forces at the low RPMs were not able to prevent bead bridging. The Oct4-GFP expression of the cells on the carriers suggested that the cells were able to maintain their pluripotency (Fig. 3A–C).

Scanning electron microscopy images of cells on Cytodex 3 carriers at the end of 7 days culture shows cell attachment, spreading and expansion on the microcarriers (Fig. 4A). Cell count data also supported the microscopy observation (Fig. 4B). At 25 RPM, cell density increased from 2×10^5 cells/ml to around 8×10^5 cells/ml at the end of 7 days giving rise to a total cell number of 40×10^6 while the total cell number in the control set up was 6×10^6. However, at 28 and 30 RPM, the cell number

Fig. 5 Pluripotency analysis of cells cultured in spinner flask. **A** Reverse transcription–polymerase chain reaction analysis of pluripotency markers on days 3, 5, 7 for 25, 28 and 30 RPM cultures. Analysis of static culture cells at the same time points was considered as control. β actin was considered as the house keeping gene. **B** Quantitative analysis of pluripotency by comparing average SSEA 1 fluorescence intensity/cell between static culture and dynamic culture (25 RPM) at the end of 7 days. Experiments were repeated for n = 3 times and data represents mean ± SEM
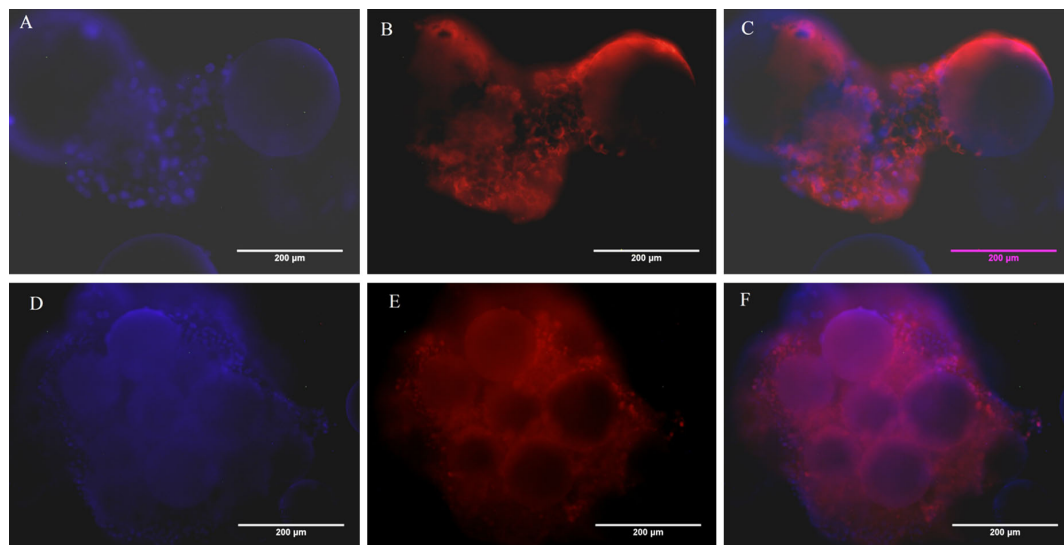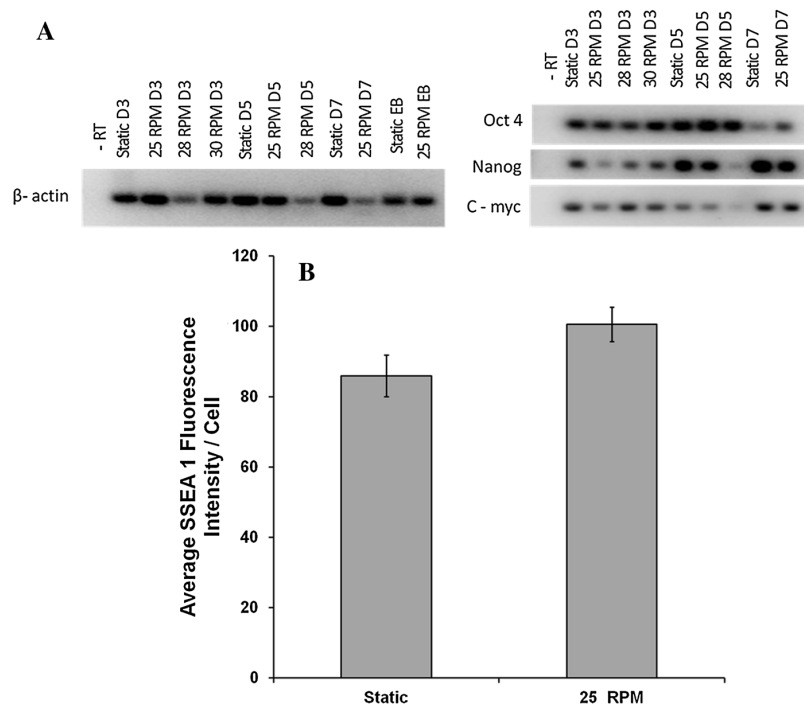
Fig. 6 Immunostaining of fixed cells on microcarriers at the end of 7 days culture at 25 RPM. (**A, D**) Nuclei were stained blue with Hoechst, (**B**) SSEA 1 postive cells stained red, (**C**) SSEA 1 staining merged image, (**E**) Nanog positive cells stained red, (**E**) Nanog staining merged image. *Scale bar* 200 μm
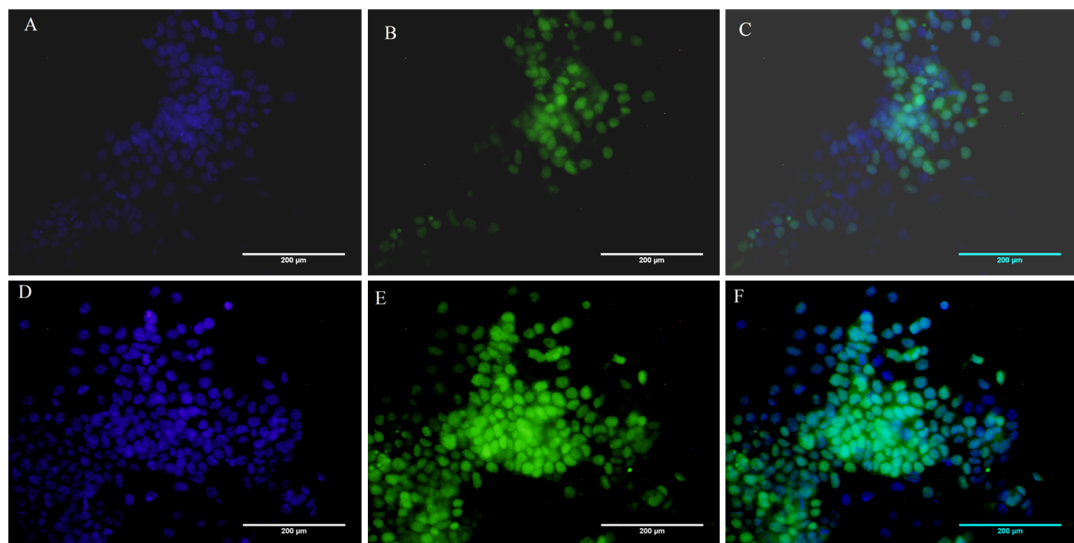
Fig. 7 Oct4-GFP immunofluorescence of cells from day 7 culture at 25 RPM. Cells were replated and imaged after 3 days of culture. (**A**, **D**) Hoechst staining for nuclei, (**B**, **E**) Oct4-GFP positive cells, (**C**, **F**) Merged images. *Scale bar* 200 μm
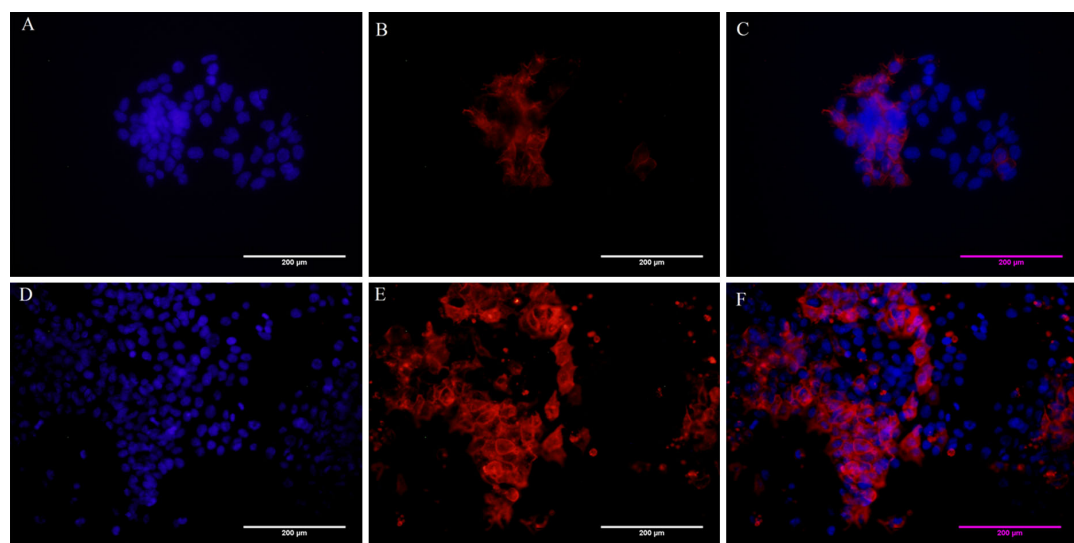
Fig. 8 SSEA 1 immunostaining of cells from day 7 culture at 25 RPM. Cells were replated and imaged after 3 days of culture. (**A**, **D**) Hoechst staining for nuclei, (**B**, **E**) SSEA-1 positive cells stained red, (**C**, **F**) Merged images. *Scale bar* 200 μm

decreased over time. Cell count became negligible between days 4 and 6 for both 28 and 30 RPM. The ability of the iPSC to expand in the spinner flasks highlights their adaptability to changed culture conditions.

Cell pluripotency

Along with cell attachment and expansion, the maintenance of pluripotency of the mouse iPSC was also considered to be an important aspect for dynamic
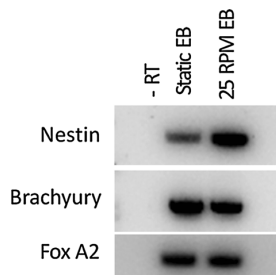
Fig. 9 Reverse transcription–polymerase chain reaction for 3 germ layers marker on day 10 EBs; Ectoderm (Nestin), Mesoderm (Brachyury) and Endoderm (FoxA2). Static culture EBs were considered as control. β actin was used as the house keeping gene (data shown in Fig. 5A)

culture optimization. RT-PCR analysis for cells collected on days 3, 5 and 7 of culture at 25, 28, and 30 RPM was carried out to ascertain their pluripotency. As shown in Fig. 5A, it was observed that Oct 4, Nanog and c-myc expressions were present in all cases although Nanog and c-myc were very low for cells expanded at 28 RPM on day 5. This suggested that although cells were present on day 5 at 28 RPM, their pluripotency was negatively affected.

Quantitative analysis of SSEA-1 fluorescence intensity was carried out after 7 days of culture at 25 RPM and was compared to static culture. Figure 5B shows average fluorescence intensity per/cell due to SSEA 1 marker. Although not significant, the intensity in the control culture was slightly less than that of the 25 RPM culture cells.

SSEA 1 and Nanog immunostaining was carried out after 7 days of culture at 25 RPM for cells fixed directly on carriers. Figure 6 demonstrates that miPS cell cultured on microcarriers in a spinner flask for 7 days at 25 RPM stained positive for both SSEA 1 and Nanog.

SSEA 1 staining was also carried out for replated cells after 7 days of spinner flask culture, along with Oct4-GFP live cell imaging. Cells from static culture worked as a control for comparison purpose in this case (Figs. 7, 8). Pluripotency was largely maintained by the cells for both the control and 25 RPM cultures although loss of a small fraction of SSEA 1 marker and Oct4-GFP was also observed, suggesting some loss of pluripotency. However, this could be due to the cells being re-plated on 2D gelatin coating and not a direct effect of dynamic culture itself.

Flow cytometric analysis of Oct4-GFP showed that around 96 ± 2 % cells for static culture and around 90 ± 2 % cells in case of dynamic culture (25 RPM) maintained the GFP fluorescence at the end of 7 days (data not shown).

In vitro differentiation

Spontaneous in vitro differentiation capability of the mouse iPSC after dynamic culture was tested by EB formation using suspension culture method. Cells were collected at the end of 7 days of culture and EBs were formed in low adherence culture plates using media without LIF. EBs were collected on day 10 for immunostaining and RT-PCR analysis. Cells from static culture were used as a control. Cells from both static culture and dynamic culture (at 25RPM) were able to form embryoid bodies. RT-PCR analysis (Fig. 9) shows the presence of all three germ layer markers at the end of 10 days. Immunostaining of EBs also shows the presence of 3 germ layer markers (Fig. 10).

Discussion and conclusion

The ethical issues associated with the use of ESC have led to extensive research in the field of iPSC. Scaling up of pluripotent stem cell culture from the bench top to a reactor system is essential before these cells can be used for various applications. A spinner flask in conjunction with microcarriers has been widely used for large scale expansion of pluripotent stem cells. Efforts have been made for culturing of ESC (both mouse and human) in such a set up since 2005 (Fok and Zandstra 2005) but until now, a uniform system with optimized parameters for the expansion of a specific cell type is yet to be achieved. The available reports on large scale expansion of ES cells differ widely in terms of many variables including the type of microcarrier used and the agitation rate. Also, the relevant studies have considered only the effect of a dynamic culture system on the cells and not on the microcarriers being used despite the existence of a threshold tolerance of carriers themselves.

The use of dynamic culture systems like spinner flasks for the expansion of iPSC is still in its nascent stage and similar to the ES cells, a versatile culture system is yet to be achieved. To date, three groups

Fig. 10 Embryoid body immunostaining for detection of 3 germ layers marker. **A**, **C**, **E** EB from static culture, **B**, **D**, **F** EB from 25 RPM dynamic culture. *Scale bar* 200 μm

Cytotechnology
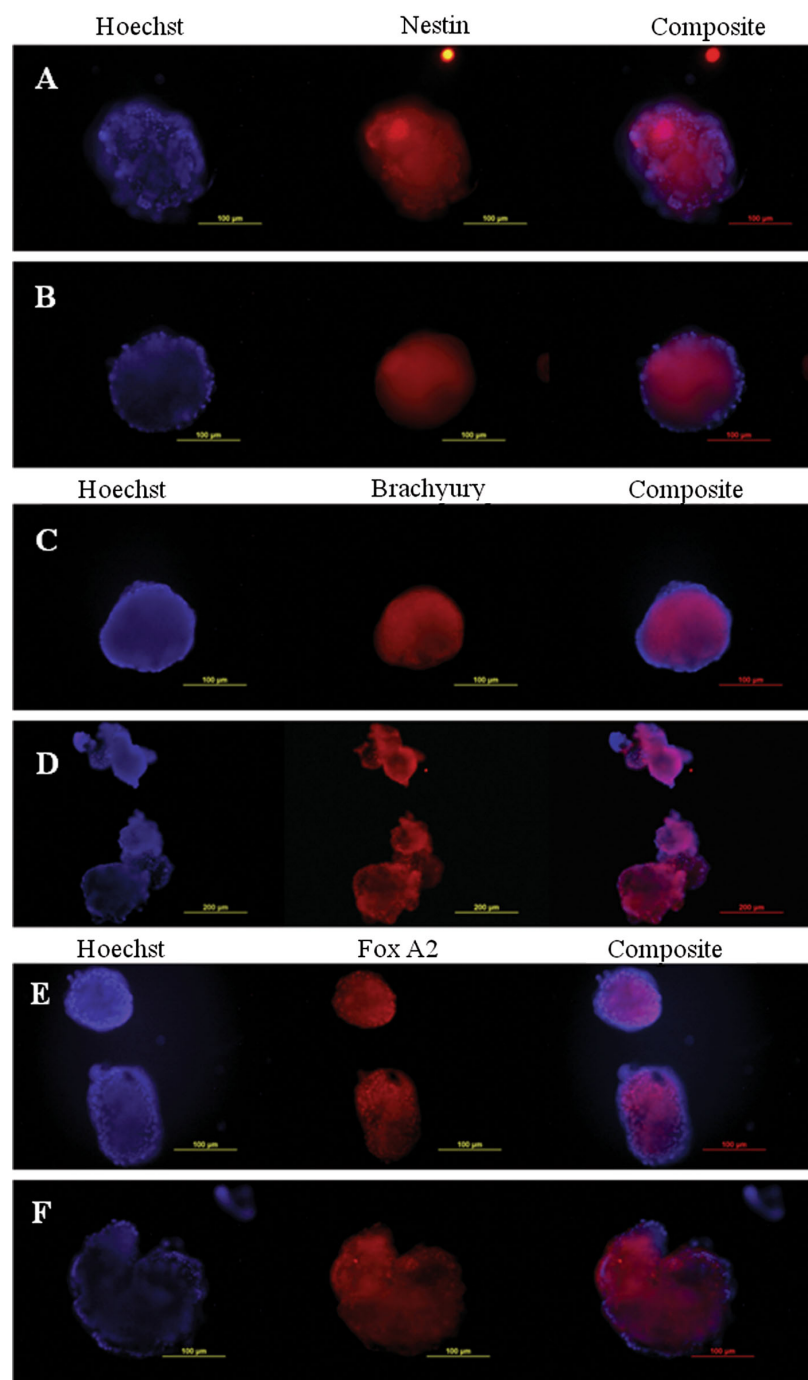
have attempted the expansion iPSC as aggregates in spinner flask or stirred bioreactor and all three have used different agitation rates (Fluri et al. 2012; Olmer et al. 2012; Shafa et al. 2012). The use of microcarrier for iPSC expansion has been reported by only two groups: Kehoe et al. (2010) mentioned iPSC expansion in a review article, while recently, Bardy et al. (2013) looked at the expansion of iPSC and its neural differentiation. Surprisingly, both these groups had used the same type of carrier (with Matrigel coating) for the expansion of human iPSC but the agitation rates used were very different. Amongst the commercially available microcarriers, Cytodex 3 is one of the most widely used carriers for the expansion of both human and mouse ESC, but the present study is the first where these have been used for expansion of iPSC.

Specifically, we have attempted to study the expansion of mouse iPSC on Cytodex 3 microcarriers in a spinner flask. We have looked at the effect of different agitation rates not only on the attachment and expansion of iPSC but also on the microcarriers. We were also able to expand these cells directly off the feeder on to Cytodex 3 without any prior coating of the carriers.

As hypothesized, it was seen that the Cytodex 3 indeed has an agitation tolerance threshold above which there was extensive carrier breakage. 40 RPM was found to be the maximum agitation rate that these carriers could tolerate. Breakage was observed upwards of 42 RPM. Since Cytodex 3 has been previously used at higher spin rates for cell expansion, it is possible that the effect of agitation rate on microcarriers is also dependent on the reactor set up itself. Thus, it is evident that similar studies for other carriers and different set-ups are essential to determine their future use in pluripotent stem cell expansion.

Based on the carrier study, spin rates of 40 RPM and below were tested for iPSC expansion. Agitation rates between 28 and 40 RPM were unable to support long term cell attachment and expansion, with cell detachment being directly proportional to the agitation rate. At 40 RPM, cells detached within 24 h while for 30 and 28 RPM, the cell number showed a steady decline with time, with complete detachment taking place between days 4 and 6. The 25 RPM flow, on the other hand, was able to support the attachment and expansion of the cells for 7 days. The shear stress at 25 RPM varies at different points in the spinner flask with

a maximum stress of 0.0984 Pa and mean of 0.0520 Pa (Ismadi et al. 2014, Submitted). The above observations are interesting, since they show that the range of agitation speed that can support iPSC expansion is very narrow, and hence requires very precise control in dynamic cultures for future work with such cell lines. Maintenance of pluripotency and differentiation capability of these cells during spinner flask expansion is highly important. Immunostaining, RT-PCR analysis of cells from the dynamic culture system and of EBs formed from the cells prove that the miPSC were able to maintain their pluripotency and differentiation capability after spinner flask culture.

Taken together, 25 RPM was found to be the optimum agitation rate for the expansion of miPSC in the spinner flask while maintaining all their essential characteristics. Our findings are in line with Bardy et al. (2013) who had also used a 25 RPM system for the expansion of hiPSC and their neural differentiation on DE-53 microcarriers. The spinner flask used by this group was the same as ours but it is possible that the impeller height may have been different. Given the remarkably small range of spin rates found to be viable for iPSC proliferation and microcarrier integrity, the present work also highlights the need for precise speed and set up control for spinner flasks and their extensive study prior to being used for dynamic culture of pluripotent stem cells.

References

Abbasalizadeh S, Larijani MR, Samadian A, Baharvand H (2012) Bioprocess development for mass production of size-controlled human pluripotent stem cell aggregates in stirred suspension bioreactor. Tissue Eng Part C Methods 18:831–851. doi:10.1089/ten.TEC.2012.0161

Abranches E, Bekman E, Henrique D, Cabral JM (2007) Expansion of mouse embryonic stem cells on microcarriers. Biotechnol Bioeng 96:1211–1221. doi:10.1002/bit.21191

Alfred R, Radford J, Fan J, Boon K, Krawetz R, Rancourt D, Kallos MS (2011) Efficient suspension bioreactor expansion of murine embryonic stem cells on microcarriers in serum-free medium. Biotechnol Prog 27:811–823. doi:10.1002/btpr.591

Bardy J, Chen AK, Lim YM, Wu S, Wei S, Weiping H, Chan K, Reuveny S, Oh SK (2013) Microcarrier suspension cultures for high-density expansion and differentiation of human pluripotent stem cells to neural progenitor cells. Tissue Eng Part C Methods 19:166–180. doi:10.1089/ten.TEC.2012.0146

Chen AK, Chen X, Choo AB, Reuveny S, Oh SK (2011) Critical microcarrier properties affecting the expansion of undifferentiated human embryonic stem cells. Stem Cell Res 7:97–111. doi:10.1016/j.scr.2011.04.007

Cormier JT, Nieden NIZ, Rancourt DE, Kallos MS (2006) Expansion of undifferentiated murine embryonic stem cells as aggregates in suspension culture bioreactors. Tissue Eng 12:3233–3245. doi:10.1089/ten.2006.12.3233

Dusting J, Sheridan J, Hourigan K (2006) A fluid dynamics approach to bioreactor design for cell and tissue culture. Biotechnol Bioeng 94:1196–1208. doi:10.1002/bit.20960

Fernandes AM, Fernandes TG, Diogo MM, da Silva CL, Henrique D, Cabral JM (2007) Mouse embryonic stem cell expansion in a microcarrier-based stirred culture system. J Biotechnol 132:227–236. doi:10.1016/j.jbiotec.2007.05.031

Fernandes AM, Marinho PA, Sartore RC, Paulsen BS, Mariante RM, Castilho LR, Rehen SK (2009) Successful scale-up of human embryonic stem cell production in a stirred microcarrier culture system. Braz J Med Biol Res 42(6):515–522

Fluri DA, Tonge PD, Song H, Baptista RP, Shakiba N, Shukla S, Clarke G, Nagy A, Zandstra PW (2012) Derivation, expansion and differentiation of induced pluripotent stem cells in continuous suspension cultures. Nat Methods 9:509–516. doi:10.1038/nmeth.1939

Fok EY, Zandstra PW (2005) Shear-controlled single-step mouse embryonic stem cell expansion and embryoid body-based differentiation. Stem Cells 23:1333–1342. doi:10.1634/stemcells.2005-0112

Ismadi MZ, Higgins S, Samarage CR, Paganin D, Hourigan K, Fouras A (2013) Optimisation of a stirred bioreactor through the use of a novel holographic correlation velocimetry flow measurement technique. PLoS ONE 8:e65714. doi:10.1371/journal.pone.0065714

Ismadi ZM, Gupta P, Fouras A, Verma P, Jadhav S, Bellare J, Hourigan K (2014) Flow characterization of spinner flask for induced pluripotent stem cell culture application. Plos One (Submitted)

Kehoe DE, Jing D, Lock LT, Tzanakakis ES (2010) Scalable stirred-suspension bioreactor culture of human pluripotent stem cells. Tissue Eng Part A 16:405–421. doi:10.1089/ten.TEA.2009.0454

Krawetz R, Taiani JT, Liu S, Meng G, Li X, Kallos MS, Rancourt DE (2010) Large-scale expansion of pluripotent human embryonic stem cells in stirred-suspension bioreactors. Tissue Eng Part C Methods 16:573–582. doi:10.1089/ten.TEC.2009.0228

Leung HW, Chen A, Choo AB, Reuveny S, Oh SK (2011) Agitation can induce differentiation of human pluripotent

stem cells in microcarrier cultures. Tissue Eng Part C Methods 17:165–172. doi:10.1089/ten.TEC.2010.0320

Lock LT, Tzanakakis ES (2009) Expansion and differentiation of human embryonic stem cells to endoderm progeny in a microcarrier stirred-suspension culture. Tissue Eng Part A 15:2051–2063. doi:10.1089/ten.tea.2008.0455

Marinho PA, Fernandes AM, Cruz JC, Rehen SK, Castilho LR (2010) Maintenance of pluripotency in mouse embryonic stem cells cultivated in stirred microcarrier cultures. Biotechnol Prog 26:548–555. doi:10.1002/btpr.328

Marinho PA, Vareschini DT, Gomes IC, Paulsen Bda S, Furtado DR, Castilho Ldos R, Rehen SK (2013) Xeno-free production of human embryonic stem cells in stirred microcarrier systems using a novel animal/human-component-free medium. Tissue Eng Part C Methods 19:146–155. doi:10.1089/ten.TEC.2012.0141

Meunier P, Hourigan K (2013) Mixing in a vortex breakdown flow. J Fluid Mech 731:195–222. doi:10.1017/jfm.2013.226

Nie Y, Bergendahl V, Hei DJ, Jones JM, Palecek SP (2009) Scalable culture and cryopreservation of human embryonic stem cells on microcarriers. Biotechnol Prog 25:20–31. doi:10.1002/btpr.110

Oh SK, Chen AK, Mok Y, Chen X, Lim UM, Chin A, Choo AB, Reuveny S (2009) Long-term microcarrier suspension cultures of human embryonic stem cells. Stem Cell Res 2:219–230. doi:10.1016/j.scr.2009.02.005

Olmer R, Haase A, Merkert S, Cui W, Palecek J, Ran C, Kirschning A, Scheper T, Glage S, Miller K, Curnow EC, Hayes ES, Martin U (2010) Long term expansion of undifferentiated human iPS and ES cells in suspension culture using a defined medium. Stem Cell Res 5:51–64. doi:10.1016/j.scr.2010.03.005

Olmer R, Lange A, Selzer S, Kasper C, Haverich A, Martin U, Zweigerdt R (2012) Suspension culture of human pluripotent stem cells in controlled, stirred bioreactors. Tissue Eng Part C Methods 18:772–784. doi:10.1089/ten.TEC.2011.0717

Phillips BW, Horne R, Lay TS, Rust WL, Teck TT, Crook JM (2008) Attachment and growth of human embryonic stem cells on microcarriers. J Biotechnol 138:24–32. doi:10.1016/j.jbiotec.2008.07.1997

Serra M, Brito C, Sousa MF, Jensen J, Tostoes R, Clemente J, Strehl R, Hyllner J, Carrondo MJ, Alves PM (2010) Improving expansion of pluripotent human embryonic stem cells in perfused bioreactors through oxygen control. J Biotechnol 148:208–215. doi:10.1016/j.jbiotec.2010.06.015

Shafa M, Sjonnesen K, Yamashita A, Liu S, Michalak M, Kallos MS, Rancourt DE (2012) Expansion and long-term maintenance of induced pluripotent stem cells in stirred suspension bioreactors. J Tissue Eng Regen Med 6:462–472. doi:10.1002/term.450

Steiner D, Khaner H, Cohen M, Even-Ram S, Gil Y, Itsykson P, Turetsky T, Idelson M, Aizenman E, Ram R, Berman-Zaken Y, Reubinoff B (2010) Derivation, propagation and controlled differentiation of human embryonic stem cells in suspension. Nat Biotechnol 28:361–364. doi:10.1038/nbt.1616

Storm MP, Orchard CB, Bone HK, Chaudhuri JB, Welham MJ (2010) Three-dimensional culture systems for the

expansion of pluripotent embryonic stem cells. Biotechnol Bioeng 107:683–695. doi:10.1002/bit.22850

Takahashi K, Yamanaka S (2006) Induction of pluripotent stem cells from mouse embryonic and adult fibroblast cultures by defined factors. Cell 126:663–676. doi:10.1016/j.cell.2006.07.024

Tat PA, Sumer H, Jones KL, Upton K, Verma PJ (2010) The efficient generation of induced pluripotent stem (iPS) cells from adult mouse adipose tissue-derived and neural stem cells. Cell Transplant 19:525–536. doi:10.3727/096368910X491374

Thouas GA, Sheridan J, Hourigan K (2007) A bioreactor model of mouse tumor progression. J Biomed Biotechnol 2007:32754. doi:10.1155/2007/32754

Tielens S, Declercq H, Gorski T, Lippens E, Schacht E, Cornelissen M (2007) Gelatin-based microcarriers as embryonic stem cell delivery system in bone tissue engineering: an in vitro study. Biomacromolecules 8:825–832. doi:10.1021/bm060870u

Want AJ, Nienow AW, Hewitt CJ, Coopman K (2012) Large-scale expansion and exploitation of pluripotent stem cells for regenerative medicine purposes: beyond the T flask. Regen Med 7:71–84. doi:10.2217/rme.11.101